

**Active and passive soft matter:
crystal growth, confinement,
and swimming**

Inaugural-Dissertation
zur Erlangung des Doktorgrades
der Mathematisch-Naturwissenschaftlichen Fakultät
der Heinrich-Heine-Universität Düsseldorf

vorgelegt von
Sven van Teeffelen
aus Essen

September 2008

Aus dem Institut für Theoretische Physik II: Weiche Materie
der Heinrich-Heine-Universität Düsseldorf.

Gedruckt mit der Genehmigung
der Mathematisch-Naturwissenschaftlichen Fakultät
der Heinrich-Heine-Universität Düsseldorf

Referent: Prof. Dr. Christos N. Likos
Koreferent: Prof. Dr. Hartmut Löwen
Koreferent: Prof. Pedro Tarazona

Tag der mündlichen Prüfung: 10. November 2008

©Sven van Teeffelen 2008
All Rights Reserved.

The work described in this thesis has been published in a number of papers, which constitute the following self-contained chapters:

- **Chapter 3:** Sven van Teeffelen, Norman Hoffmann, Christos N. Likos, and Hartmut Löwen, “Density functional theory of freezing for soft interactions in two dimensions,” *Europhys. Lett.* *75* (2006), 583 (preprint: arXiv:cond-mat/0604422).
- **Chapter 4:** Sven van Teeffelen, Hartmut Löwen, and Christos N. Likos, “Crystallization of magnetic dipolar monolayers: a density functional approach,” *J. Phys.: Condens. Matter* *20* (2008), 404217 (preprint: arXiv:0804.3299).
- **Chapter 5:** Hartmut Löwen, Christos N. Likos, Lahcen Assoud, Ronald Blaak, and Sven van Teeffelen, “Critical nuclei and crystallization in colloidal suspensions,” *Philos. Mag. Lett.* *87* (2007), 847 .
- **Chapter 6:** Sven van Teeffelen, Christos N. Likos, and Hartmut Löwen, “Colloidal crystal growth at externally imposed nucleation clusters,” *Phys. Rev. Lett.* *100* (2008), 108302 (preprint: arXiv:0802.2235).
- **Chapter 7:** Sven van Teeffelen, Angel J. Moreno, and Christos N. Likos, “Cluster crystals in confinement,” *submitted to Soft Matter, currently with referees* (preprint: arXiv:0808:1363).
- **Chapter 8:** Sven van Teeffelen and Hartmut Löwen, “Dynamics of a Brownian circle swimmer,” *Phys. Rev. E* *78* (2008), 020101(R) (selected for publication in the September 2008 issue of the Virtual Journal of Nano Science & Technology (<http://www.vjnano.org/>); preprint: arXiv:0803.2008).

The author was also involved in the following publications, which are not part of this thesis:

- Rik Wensink, Hartmut Löwen, Marin Rex, Christos N. Likos, and Sven van Teeffelen, “Long-time self-diffusion of Brownian Gaussian-core particles,” *Computer Physics Communications* *79* (2008), 77 (preprint: arXiv:0710.3111).
- Urs Zimmermann, Sven van Teeffelen, and Hartmut Löwen, “Ballistic motion of a Brownian circle swimmer in circular confinement,” in preparation.
- Sven van Teeffelen, “Freezing of ultrasoft repulsive particles into cluster crystals with non-Bravais lattice geometries,” in preparation.
- Sven van Teeffelen, Hartmut Löwen, Rainer Backofen, and Axel Voigt, “Comparison between dynamical density functional and phase field crystal theory for colloidal solidification,” in preparation.

Summary

This thesis deals with equilibrium and dynamical properties of *colloidal dispersions*. It contains three parts, each concerned with a different colloidal system: in the first part, we present results from classical density functional theory (DFT), dynamical density functional theory (DDFT), and Brownian dynamics (BD) computer simulations on crystallization of a colloidal suspension of paramagnetic spheres on a planar interface that carry a magnetic-field-induced dipole moment, directed perpendicular to the interface. The equilibrium system is completely characterized by the long-range dipole-dipole interactions. The phase behavior is addressed by two different approximations to the DFT, an extended form of the approach by Ramakrishnan and Yussouff (RY) and the extended modified weighted density approximation. Both approaches, which are exact up to third order in the functional expansion of the excess free energy about a fluid with uniform density, are superior to their simpler second-order counterparts. Subsequently, the relaxation dynamics of crystal growth and melting is studied by means of DDFT with the RY density functional as an input and with BD computer simulations. To study the growth scenario, a crystalline cluster of few particles is tagged in an equilibrated fluid at a low magnetic field, before instantaneously increasing the field, which renders the fluid undercooled, and letting the particles free at the same time. Observed is a two-stage process, consisting of a fast relaxation towards a cutout of the stable bulk crystal, which then either collapses or serves as a heterogeneous nucleation seed for further crystal growth, depending on the quench depth and on the structure of the incipient cluster.

The second part deals with crystallization in slit-pore confinement of a model system of particles interacting via ultrasoft repulsive pair potentials representing, e.g., amphiphilic dendrimers in solution, which is addressed with an accurate mean-field DFT and BD computer simulations. The particles are shown to freeze into cluster crystals either from the middle of the slit towards the walls or vice versa, depending on the particle-wall interaction. For large wall-wall separations, a continuous growth of the fluid or solid layer on either wall, upon approaching the bulk freezing line, indicates complete wetting in both cases. The continuous growth is interrupted by capillary melting or freezing.

The third part is devoted to the dynamics of an active, self-propelled, colloidal rod in two dimensions, which serves as a simplified model to study the motion of, e.g., bacteria, spermatozoa, or artificial nano-swimmers close to planar walls. The self-propulsion is modeled through a constant force in the rod orientation and a constant torque, both yielding motion along circles rather than along straight lines; we therefore designate the particle a “Brownian circle swimmer.” The motion in the bulk is examined by integrating analytically the Langevin equations of motion, whereas the motion in linear, confining channels is assessed by a non-Hamiltonian rate theory and BD computer simulations. A sliding mode close to the channel wall leads to a huge acceleration as compared to the bulk motion, which can further be enhanced by an optimum torque-to-force ratio.

Zusammenfassung

Die vorliegende dreiteilige Arbeit beschäftigt sich sowohl mit Gleichgewichts- als auch dynamischen Eigenschaften dreier verschiedener kolloidaler Suspensionen. Im ersten Teil analysieren wir mit den Methoden der klassischen Dichtefunktionaltheorie (DFT), der dynamischen Dichtefunktionaltheorie (DDFT) und mit Computer-Simulationen der Brownschen Dynamik (BD) die Kristallisation einer Suspension von paramagnetischen Kugeln auf einer Grenzfläche, die einem senkrecht zur Grenzfläche stehenden magnetischen Feld ausgesetzt sind. Das Gleichgewichtsphasenverhalten, das vollständig durch die langreichweitige Dipol-Dipol-Wechselwirkung und die thermodynamischen Zustandsgrößen charakterisiert ist, wird durch zwei verschiedene DFT-Näherungen ermittelt, zum einen durch eine erweiterte Form der Näherung von Ramakrishnan und Yussouff (RY) und zum anderen durch eine sogenannte *extended modified weighted density*-Näherung. Beide Methoden stimmen bis zur dritten Ordnung mit der Funktionalentwicklung der Exzess-Freien Energie in den lokalen Dichteschwankungen bezüglich einer Flüssigkeit mit konstanter Dichte exakt überein und sind ihren einfacheren, lediglich bis zur zweiten Ordnung übereinstimmenden Vorgängern überlegen. Anschließend betrachten wir die Relaxationsdynamik von schmelzenden und wachsenden Kristallen mit Hilfe der DDFT und mit BD-Simulationen, erstere auf Basis der RY-Näherung. Um das Wachstumsverhalten zu untersuchen, ordnen wir wenige Teilchen in einer bei niedrigem magnetischen Feld im thermodynamischen Gleichgewicht befindlichen Flüssigkeit zu einem Kristalliten an, dessen Zeitentwicklung wir nach einer instantanen Erhöhung der Feldstärke in der umgebenden, dann metastabilen bzw. unterkühlten Flüssigkeit beobachten. Der Relaxationsprozess besteht im wesentlichen aus zwei Schritten: Auf sehr kurzer Zeitskala relaxiert der zuvor festgehaltene Kristallit zu einem Ausschnitt eines thermodynamisch stabilen, unendlich ausgedehnten Kristalls. Anschließend wächst oder kollabiert die kristalline Konfiguration, je nach originärer Geometrie und je nach Stärke des magnetischen Feldes.

Im zweiten Teil der Arbeit untersuchen wir die Kristallisation einer weiteren kolloidalen Suspension zwischen zwei repulsiven oder attraktiven, planaren Wänden. Das System, dessen Teilchen über sehr weiche, beschränkte Potentiale miteinander wechselwirken, modelliert in einfacher Weise beispielsweise eine Lösung von amphiphilen Dendrimeren. Mit Hilfe der hier sehr akuraten *mean-field*-Näherung der DFT und BD-Simulationen finden wir, dass die Teilchen sich bei niedrigen Temperaturen zu sogenannten *Cluster*-Kristallen ordnen, in denen jeweils mehrere Teilchen die Position eines einzigen Gittervektors annehmen. Die Teilchen kristallisieren entweder zunächst in der Mitte der Pore und erst dann an den Wänden, oder gerade andersherum, je nach der Form der Wand-Teilchen-Wechselwirkung. Im Fall großer Wand-Wand-Abstände wachsen die flüssigen oder kristallinen Lagen beim Annähern an den Einfrierübergang kontinuierlich von beiden Wänden in die Mitte, was auf eine vollständige Benetzung durch die jeweilige Phase hindeutet. Das Wachstum wird schließlich durch die Kapillarkondensation der kristallinen oder flüssigen Phase unterbrochen.

Im dritten und letzten Teil geht es schließlich um die Dynamik eines aktiven, selbst angetriebenen, kolloidalen Stäbchens in zwei Dimensionen, das als ein vereinfachtes Model für die Bewegung von Bakterien, Spermien, oder künstlichen Nano-Schwimmern in der Nähe planarer Oberflächen dienen kann. Der Selbstantrieb wird durch eine konstante Kraft in Richtung der Stäbchenorientierung und ein konstantes Drehmoment modelliert, die zusammen zu einer zirkulären Bewegung des Teilchens führen; das Stäbchen wird daher auch als “Brownscher Kreisschwimmer” bezeichnet. Ohne Anwesenheit eines äußeren Potentials, d.h., in der homogenen, ausgedehnten Flüssigkeit, lassen sich die Langevin-Bewegungsgleichungen analytisch integrieren. Für die Analyse der Bewegung in linearen, einschränkenden Kanälen bedienen wir uns einer nicht-Hamiltonschen Ratentheorie und Computer-Simulationen, die übereinstimmend eine deutlich schnellere diffusive Bewegung als in der ausgedehnten Flüssigkeit vorhersagen. Die beschleunigte Bewegung wird durch einen metastabilen, stationären Zustand des Gleitens entlang einer der beiden Wände bedingt und kann durch eine Optimierung des Verhältnisses von Vorwärtskraft und Drehmoment noch gesteigert werden.

Acknowledgements

First, I would like to express my gratitude to my advisers Hartmut Löwen and Christos Likos. Hartmut and Christos have both been great mentors and it was a pleasure to work with them. During the last three years I was in the fortunate position to have them almost at any time available for the numerous requests for a “minute” of discussion, which most often became a very lively and fruitful talk of half an hour or longer. Thank you for the immeasurable host of ideas, comments, discussions, hints, and further support. I also very much enjoyed the great deal of both diverting chitchat and serious talking on and beyond physics—with Hartmut, during extensive lunch and coffee breaks, and with Christos, on his frequent ways between the office and the printer room, not to forget the late-night chats by email. It has been a pleasure!

Second, I thank my present and former colleagues in the Löwen-Likos lab for providing an excellent and most pleasant atmosphere. The partly endless coffee breaks have made my stay in the institute a very enjoyable time. Ansgar and Jo, thank you for your patience with all my smaller and bigger Linux- and other problems. Ronald, thanks for the many major or minor issues, with which I could bother you. It was good to have you as a reliable problem-solver and -listener just two doors away. Martin K. and Aaron, I owe you a very special thanks for critically proof-reading parts of this manuscript. Federica, I am still missing the special Italian air in our office. A special thanks goes to a group of “peers,” for being there in times of prosperity and misery; Adam, Martin R., Richard, Heike, Aaron, I am fortunate to have you as colleagues and friends—not to mention the many discussions, comments, assistance, etc., that were of invaluable help. To all the others, who I can not name here, thanks for making my stay as pleasant as it could be.

Outside the lab, I am grateful to have friends that distract me from physics or not. Again, I can not name all here, but among those in Düsseldorf, my flatmates Anna and Mirko and my friend Vittorio from one floor up deserve a special mentioning, as they made my time on the Rhine very livable.

Finally, and most importantly I want to thank my family for their constant and unmeasurable support and encouragement at every stage of my life.

Contents

Summary	v
Zusammenfassung	vii
Acknowledgements	ix
Introduction	1
1 Classical density functional theory of freezing	9
1.1 The variational principle	10
1.2 Two hierarchies of correlation functions	12
1.3 Approximate density functionals and an excursion to the homogeneous liquid state	14
1.4 Approximate density functionals for freezing	16
1.5 The search for the optimum crystalline density	19
1.6 Discussion	19
1.6.1 Ergodicity breaking and omitted fluctuations	20
1.6.2 Density functional theory in two dimensions	22
1.6.3 The canonical vs the grand canonical ensemble	23
2 Colloids in nonequilibrium	25
2.1 Langevin dynamics	26
2.2 Dynamical density functional theory	28
2.2.1 Derivation of the dynamical equation	28
2.2.2 Approximate density functionals in the DDFT	32
2.2.3 The adiabatic approximation	34
2.2.4 Crystal growth and melting	35
2.2.5 Further applications and extensions	38
2.3 Nonequilibrium rate theory for a Brownian swimmer	39
2.3.1 The Langevin and the Smoluchowski-Perrin equations for a self-propelled rod	42
2.3.2 Hopping between the sliding modes	43
2.3.3 The escape rate	45

2.3.4	The probability distribution	46
2.3.5	An approximate treatment of the escape rate	47
2.3.6	Discussion	49
3	Density functional theory of freezing for soft interactions in two dimensions	53
4	Crystallization of magnetic dipolar monolayers: a density functional approach	63
4.1	Introduction	63
4.2	Modified weighted-density approximation and its extension to third-order correlation functions	66
4.3	Application of the different approximations to the DFT to freezing of monodisperse two-dimensional liquids	68
4.4	The dipolar system	71
4.5	Results	77
4.5.1	Gaussian profiles, no vacancies	77
4.5.2	Gaussian profiles, allowing for vacancies	85
4.5.3	Free minimization	85
4.6	Discussion and concluding remarks	90
5	Critical nuclei and crystallization in colloidal suspensions	91
5.1	Introduction	91
5.2	Homogeneous nucleation of colloidal melts under shear	92
5.3	Dynamical density functional theory	93
5.4	Application of DDFT to gradual versus sudden solid heating	95
5.5	Relation to phase-field models	97
5.6	Conclusions	98
6	Colloidal crystal growth at externally imposed nucleation clusters	99
7	Cluster crystals in confinement	109
7.1	Introduction	109
7.2	The model: ultrasoft, repulsive particles	111
7.3	Density functional theory	113
7.4	Simulation	114
7.5	The bulk phase diagram	115
7.6	Repulsive slit pores	119
7.7	Attractive walls	131
7.8	Conclusions	139
8	Dynamics of a Brownian circle swimmer	141
	Bibliography	150

Introduction

The work at hand deals with different systems of what is generally referred to as *soft colloidal matter* [132, 136, 157] and is dedicated to the question of how these systems behave in and out of equilibrium. Soft matter comprises a vast number of everyday realizations, such as paint, food, pharmaceuticals, biological cells, etc. [136], which—despite their many structural and dynamical differences—have in common that their behavior is governed by one or several mesoscopic length scales,¹ which lie in the range of $1\text{ nm} - 10\text{ }\mu\text{m}$ [132, 247]. Such a length scale typically becomes manifest in the size of the systems’ relevant constituents; the latter can be simple colloidal particles with only translational and rotational degrees of freedom (rigid colloidal bodies such as spheres, rods, or platelets), or more complex entities, which possess many internal, thermally activated degrees of freedom such as polymers, proteins, membranes, etc. [136, 157, 167]. The colloidal particles are typically immersed in a viscous molecular solvent (aqueous or organic), i.e., there is a large separation of length- and time-scales between the solvent and the colloidal entities (eventually, with those of colloidal subdomains, e.g., polymer monomers, in between).

The presence of different length and time scales, which span many orders of magnitude, is the key source of the host of diverse, exciting physical phenomena, which make soft matter a fascinating field of physics. For a theoretical description, however, this complexity is also a great challenge, as, on the one hand, a first principles, “ab initio” approach from the microscopic scale is impossible, but, on the other hand, it is most often also not so obvious which of the small and intermediate scales can be ignored or treated on a coarse level, and which have to be taken into account explicitly. Therefore, the first and most important task is often to choose a proper way of bridging the gap from the microscopic to the mesoscopic scale; the solution to this problem does not only depend on the particular system under study but also on the physical question posed. For the equilibrium problems, we base our studies on the concept of effective interactions [157, 247], which amounts to integrating out the small scale degrees of freedom in the partition sum; this treatment leads to a mesoscopic Hamiltonian, which contains only the center-of-mass coordinates of the colloids as variables, plus potentially further internal degrees of freedom. In fact,

¹Our use of the term “mesoscopic” is different from the more common one, implying the scales in which quantum-mechanical effects are significant. On the contrary, the length scale considered here is way larger than the thermal de Broglie wavelength, rendering quantum effects negligible.

colloidal fluids or solids are therefore to be regarded self-similar to so-called *simple* liquids or solids, which are not immersed in a solvent but are described by the same Hamiltonian—up to a different prefactor setting the energy scale. Note, however, that the experimentally realized effective interaction potentials in soft matter are by far richer and more diverse than atomic or molecular interaction potentials, which are dictated by the electronic structure. For the non-equilibrium problems, our studies are based on the concept of overdamped Langevin dynamics [67, 247], in which the solvent is treated as a heat bath, exerting both friction and random forces onto the colloids, which are related via Einstein fluctuation-dissipation relations. Once the relevant equations of motion or a Hamiltonian are formulated, a second step to bridge the gap between the meso- and the macro-scale can be pursued. In the present thesis we will be mainly concerned with this second step, which is still demanding, in particular when the underlying equations still contain a lot of micro- or mesoscopic details.

Soft matter systems are not only interesting to study in themselves, e.g., for their vast importance in nature or technology, but they are also most appealing to serve as *model systems* for the study of very general physical problems, such as the equilibrium phenomena of critical behavior, wetting, or freezing, and as the non-equilibrium phenomena of nucleation, crystal growth, spinodal decomposition, or glass formation. This latter attractiveness has two reasons: first, the important observables are often accessible experimentally by relatively simple means for the relatively large length and time scales, which is in contrast to atomic or molecular systems. For example, μm -sized colloidal particles can be tracked individually with confocal light microscopes even in three spatial dimensions [285]. At the same time, colloids are small and light enough to be thermally excited² and therefore to be addressed by classical statistical mechanics and thermodynamics. Second, the interaction potentials between the particles and also with external fields can in many experiments be tailored according to the individual needs, e.g., to study certain aspects of a system isolated from others. This is achieved, e.g., by changing the solvent, the shape, or the architecture of the colloidal particles, or even by manipulating single particle trajectories with laser tweezers [285].

In the thesis at hand the reader will encounter soft-matter systems carrying characteristics of both kinds, pure model systems and systems of direct relevance in nature or technology. The first system under study, paramagnetic colloids at an interface, which are additionally exposed to an external magnetic field [307], and the second system, a special class of amphiphilic dendrimers [192] in slit-pore confinement, fall into the former category of model systems. The two setups are

²A more quantitative criterion for thermal excitability is that the relevant deterministic forces F_i (e.g., due to gravity, electric or magnetic fields, and van der Waals interactions) should at typical inter-particle distances not by far outrange the Brownian force $k_B T \sigma$, where k_B is Boltzmann's constant, T the absolute temperature, and σ a characteristic length [247]. However, as the inter-particle forces depend on separation and, e.g., the van-der-Waals force diverges at contact, a more careful assessment is typically necessary.

exploited for a systematic study of equilibrium crystallization (Chapters 3, 4, and 7) and non-equilibrium crystal growth and melting (Chapters 5 and 6). Although we put both of these systems into the first category, future relevance in nanotechnology of adsorption, photonic crystals, etc., is not ruled out, of course. A quite different, third system studied in Chapter 8 is a particularly designed, rodlike nano-swimmer in two spatial dimensions, i.e., an active particle, which moves through a quiescent solvent by *self-propulsion*. This system has certainly model character, but is also highly relevant for the understanding of the motion of, e.g., bacteria or spermatozoa close to planar walls [71].

The first and major part of this thesis, comprising Chapters 3-7, is devoted to the theoretical modeling and understanding of the liquid-solid phase transition of the first two soft matter systems in the bulk and in slit-pore confinement; our treatment includes both the equilibrium phase behavior and the non-equilibrium relaxation processes driving a system from one state to the other, i.e., crystal growth and melting.³ In fact, an understanding of the underlying equilibrium phase diagram in the bulk is an essential prerequisite for the modeling of more complex, broken-symmetry problems in confinement or in non-equilibrium. Our focus lies in this work on the systematic treatment of those situations, in which liquid and solid domains are either in coexistence, or in competition, one eventually growing at the expense of the other. Both of these situations involve stationary or moving interfaces between the domains. A theory, which has proved to be very reliable for the study of many colloidal systems in situations of the former kind, i.e., systems displaying liquid-solid coexistence, is *classical density functional theory* (DFT) [85, 165, 263]. This approach to bridge the aforementioned gap between the meso- and the macro-scale for systems in equilibrium regards the solid as a strongly modulated fluid, i.e., a fluid, in which the density modes have condensed. DFT is therefore able to treat the liquid and the solid state within the same *density field*, which provides the ensemble averaged probability density to find a particle at a certain point in space. The theory, which is reviewed with a focus on applications to crystallization in Chapter 1, is particularly appealing, because it is rigorously derivable from statistical mechanics. However, in most practical situations of strongly correlated fluids, including most problems involving freezing, some *ad hoc* approximations have to be made. Still, DFT has made remarkably correct predictions for the equilibrium phase behavior of many systems, including the ones studied in the work at hand.

The first soft-matter system to be examined in the realm of crystallization consists of monodisperse, paramagnetic colloids, which are confined to a planar interface and additionally exposed to an external magnetic field that is directed perpendicular to the interface [307]. As these colloids are perfectly modeled by point-like magnetic dipoles, free of additional parameters, in the strong-field limit, the system

³We will in this thesis not be concerned with the subject of spontaneous homogeneous or heterogeneous nucleation [257], although Chapter 6 can be regarded in the realm of the latter phenomenon (see also Subsections 1.6.1 and 2.2.4).

marks an ideal setup for qualitatively and quantitatively comparative studies between experiment, computer simulations and theory. In Chapters 3 and 4 we put forward different approximations to the DFT to predict very accurately the bulk phase diagram of the system.⁴ The approximations made, comprise an extension of the approach by Ramakrishnan and Yussouff [226] to third-order correlation functions and a so-called *extended modified weighted density approximation*, which was originally developed in three spatial dimensions [158, 159] (cf. Subsections 1.3-5). Next to an accurate prediction of the phase diagram, the work laid out in these two Chapters was also motivated by two other quite distinct reasons: first—quite a technical point—this work demonstrates the importance of explicit inclusion of triplet correlation functions in the approximate density functionals of long-range, inverse-power pair potentials in two spatial dimensions; the necessity of such an inclusion had already been demonstrated in three dimensions [158] but the translation to two dimensions was by far not clear *a priori*. Second, these two Chapters constitute an important part of the foundations for a study of the non-equilibrium processes of crystal growth and melting of the same system in Chapters 5 and 6, which we shortly comment upon in the following paragraph.

Crystal growth and melting have been studied extensively by different complementary means, experiments [5, 215, 304], computer simulations [15], and phenomenological theories [104]. Regarding the theory side, many groups were for a long time rather concerned with simple liquids, in which latent heat is a key quantity ruling the dynamics of crystals in contact with their melt. Only few phenomenological theories have been designed for the study of colloidal crystal growth or melting [78, 79, 105, 296], in which the conserved particle density is the important rate-determining quantity (see also the discussion in Section 2.2.4). However, these models, which are typically based on a Landau-Ginzburg kind of Hamiltonian, need phenomenological mobilities as an input. Instead, we rely in Chapters 5 and 6 on a more microscopic theory, which is based on the Langevin equations of motion for overdamped particles and on classical density functional theory, and is therefore referred to as *dynamical density functional theory* (DDFT) [10, 179]. The theory, which is reviewed in Section 2.2, provides an equation of motion for the time-dependent, ensemble averaged one-particle density of a system; the latter can be regarded as an extension of the equilibrium density field in DFT to a time-dependent field in DDFT. However, this extension is by no means straightforward nor is it derived, at least in principle, rigorously from the foundations of statistical mechanics, as is DFT. Instead, a crucial *ad hoc* approximation is made, which amounts to approximate generally time-dependent correlation functions by equilibrium equivalents. This so-called *adiabatic* approximation, which was originally introduced by Enskog [82], is extensively discussed in Subsection 2.2.3. Still, DDFT

⁴Having said this, we note that the actual phase transition in two dimensions is incorrectly predicted to be first order due to the inherent mean-field character of any approximation to the DFT, whereas it actually consists of two continuous transitions with a narrow hexatic phase in between (cf. the introduction of Chapter 1 and Subsection 1.6.2).

has proved to very accurately predict the non-equilibrium dynamics of many soft-matter systems (see Subsection 2.2.5). The same theory is therefore put forward as the first full microscopic approach to the dynamics of crystallization in Chapters 5 and 6.

The particular physical problems studied within this thesis are limited to homogeneous melting on the one hand (Chapter 5), and to the growth of eventually strained crystalline clusters of few particles into an undercooled melt on the other hand (Chapter 6), both after an instantaneous change of the magnetic field from a high to a low value or vice versa, which is equivalent to an instantaneous change of temperature everywhere in the system. In the growth case, which is also regarded in the realm of recent studies on heterogeneous crystal nucleation [104, 105, 257], interesting dynamics are observed on different time scales, which are also confirmed by extensive Brownian dynamics computer simulations. Next to the setups studied in this thesis, many other problems are still to be treated or await completion. Among them is a systematic study of the short- and long-time dynamics of planar crystal fronts. This in principle straightforward, though computationally time-consuming, problem is currently studied with DDFT and with the more coarse-grained *phase field crystal* (PFC) model [78, 79] in collaboration with R. Backofen and A. Voigt. The reason for this comparative study is two-fold: first, within a truncated density expansion the PFC model can in principle be derived from DDFT, but is based on certain strong approximations (cf. Subsection 2.2.4); a quantitative comparison is therefore on order. Second, the PFC model certainly has the advantage to be computationally faster than DDFT, which offers the assessment of larger length and time scales. A prudent separation of application domains is therefore highly desirable. The studies on the two-dimensional model system discussed here may also be regarded as a forerunner of more demanding studies in three spatial dimensions, where even complementary experimental approaches are still at their infancy [285].

The second model system under study in Chapter 7 are amphiphilic dendrimers [192] in slit-pore confinement. The equilibrium system is studied with a density functional approach, which can therefore be partly regarded as a preparatory work for an application of DDFT to the dynamics of crystallization in three spatial dimensions. However, in this work we are only concerned with the static behavior in equilibrium, first in the bulk, and then in confinement, which we treat with mean-field density functional theory (cf. Subsections 1.3-5), backed by computer simulations. Both the bulk and the confined cases are already intricate in themselves for several reasons. First, and different from the system of paramagnetic colloids above, where the setup of a Hamiltonian of point-like dipoles without loss of microscopic information was straightforward, bridging the gap between the micro- and the meso-scale is here pursued via a much coarser, effective Hamiltonian. After averaging over the polymeric degrees of freedom, the dendrimers are regarded as spherical objects, which interact with each other via a special class of *ultrasoft*, repulsive pair potentials. The latter are bounded and therefore allow for a complete overlap of two or more dendrimers' centers of mass at the expense of a finite interac-

tion energy [192]. The ability to overlap, which is due to their polymeric nature, is one of the prerequisites for the formation of so-called *cluster crystals*, in which several particles share the same lattice site in a crystal of almost density-independent lattice spacing [161, 190]. Note that the theoretical model is based on the strong assumption of pairwise additive interactions between the dendrimers, which is believed to hold in a regime of small to intermediate average densities, but still awaits testing with computer simulations or experiments. In this work, we regard the model Hamiltonian as given even for arbitrarily high densities and leave the examination of model distortions due to many-body interactions to a future study. The at first sight counter-intuitive phenomenon of cluster crystallization, which is absent for unbounded, “conventional,” repulsive pair interactions,⁵ is the second reason for our special interest. An astonishing finding, which to our knowledge has not been reported for other systems, is the prevalence of the unexpected hexagonally close packed lattice at the freezing transition. From the theory point of view, the bulk model system is well understood; whether the assumption of pair-additivity prevails also for large number densities, remains to be tested, however.

In the second part of Chapter 7 we go beyond the infinite bulk system and regard the symmetry-broken states of different planar confinements. In a systematic fashion we study the effect of the wall-particle interactions and the wall-wall separation on the freezing behavior. We show that for repulsive walls the system freezes from the middle, whereas for attractive ones crystallization sets in at the walls and proceeds to the middle. For large wall-wall-separations we find continuous growth of a fluid or crystalline layer on the wall, depending on the wall-particle interaction, which is interrupted by capillary melting or freezing close to the bulk crystallization transition. An asymptotic scaling analysis of the width of the liquid or crystalline films growing at the walls indicates complete wetting in both cases. As in the bulk case, the theoretical studies are backed by computer simulations. In summary, the system of dendrimers and the simplified model system of ultrasoft, spherical particles are ideal candidates to study different further phenomena of crystallization, as in particular the latter is easily accessible by theoretical means and computer simulations. The still missing link to the “real” world is, however, an experimental realization through dendrimers or possibly other complex molecules.

The third model system under study in Chapter 8, which is also addressed at extent in Section 2.3, is an active colloidal particle in two dimensions, which is self-propelled by an internal motor. On average, the rodlike particle performs a circular motion, which is eventually perturbed by Brownian kicks of the embedding solvent; we therefore refer to the particle as a “Brownian circle swimmer.” Despite its colloidal characteristic of performing overdamped, Brownian motion in a quiescent solvent it is quite different from the other two models, introduced above. At first, the particle is *active*, i.e., it is out of equilibrium by construction; in fact, the

⁵Clustering in systems interacting via unbounded pair potentials is observed in the special case of additional short-range attractions and long-range repulsions [258].

self-propulsion is modeled through a non-Hamiltonian force driving the swimmer in the direction of its orientation and a non-Hamiltonian torque, which together induce the circular motion. Second, we are here only concerned with the single-particle properties instead of collective phenomena induced by the presence of many particles. This latter restriction may, however, be overcome in a future study. And third, the model particle is a colloidal rod, i.e., even without the self-propulsion it has an internal orientation, which becomes manifest through anisotropic interaction potentials and friction coefficients. The study of this seemingly complex model is motivated by a large number of experiments of diverse Brownian swimmers, ranging from Bacteria and spermatozoa to catalytically driven nanorods, active, anisotropic colloidal particles and vibrated granulates (see Chapter 8 for a list of references), which under certain conditions swim in circles rather than along straight lines. As an example we mention here the bacterium *Escherichia coli* [24], which swims in circles close to planar walls.

In the first part of Chapter 8, we present the averaged position and the mean-square-displacement of the swimmer in the bulk, which is obtained exactly by integrating the Langevin equations of motion; it is shown that the averaged position falls on a *spira mirabilis*, and that the mean-squared displacement displays a crossover from an oscillatory ballistic to a diffusive behavior. In the second part, we identify the modes of propagation of a circle swimmer in confining channels with repulsive walls using Brownian dynamics computer simulations and a non-Hamiltonian rate theory, which is introduced at extent in Section 2.3. In channel confinement, an efficient stable sliding mode is identified for an optimum torque-to-force ratio that strongly enhances the long-time diffusion along the channel, and might once be exploited for sorting of bacteria with microfluidic devices. If the channel is asymmetric, the sliding mode leads to ballistic long-time motion.

The thesis is roughly divided into two parts: in a first part, comprising Chapters 1 and 2, the relevant theoretical methods are introduced, their application to the respective problem is discussed, and their use in the past is shortly reviewed. In a second part, comprising Chapters 3-8, the physical problems under study are presented in the form of self-contained chapters, which have already been published or submitted to different physical journals. In particular, we start in Chapter 1 with a review of classical DFT in equilibrium, where a special focus is put on crystallization. In Chapter 2 we are concerned with the theoretical approaches of DDFT and non-Hamiltonian rate theories to non-equilibrium, overdamped, Brownian dynamics. Chapters 3 and 4 are devoted to the equilibrium properties of paramagnetic colloids on an interface, where Chapter 4 is basically an extended version of Chapter 3, with some comments and details excluded, however. Non-equilibrium properties of the same system are assessed with DDFT in Chapters 5 and 6. Chapter 5 covers melting,⁶ whereas Chapter 6 is devoted to the growth dynamics of small crystalline

⁶The same chapter also includes a short section on nucleation under shear in a different model system by Ronald Blaak and Hartmut Löwen.

clusters into the undercooled melt. Crystallization in slit pores of the second model system, cluster-forming dendrimers, is assessed in Chapter 7. Finally, in Chapter 8, the dynamics of a single, active colloidal particle in two dimensions is studied with a non-Hamiltonian rate theory.

Chapter 1

Classical density functional theory of freezing

A large part of the thesis at hand is devoted to the equilibrium crystallization of colloidal liquids in the bulk (Chapters 3 and 4) and in confinement (Chapter 7). There is to date only one microscopic theory capable to describe the solid and the liquid state within the same framework [165, 209, 263], which is classical density functional theory (DFT) [85, 87, 117, 299, 300]. Classical DFT is a liquid-based approach which regards the solid as a strongly inhomogeneous fluid with frozen-in density modes. The way for this viewpoint was paved by Kirkwood and Monroe [144] already in 1941. However, the approach was put on solid grounds and applied to hard-sphere freezing only in 1979 by Ramakrishnan and Yussouff [226] and further reformulated by Haymet and Oxtoby [119, 209, 213]. As a liquid-based approach, DFT stands in contrast to crystal-based elasticity theory [35, 265] originally dating back as far as to Born in 1939 [34], which regards the liquid state simply as a collapsed crystal. In two spatial dimensions, where “true” long-range translational order is lost according to the Mermin-Wagner theorem [185] and only rotational order persists on large scales [91, 92], Kosterlitz, Thouless, Halperin, Nelson and Young [113, 146, 200, 265, 305] have established a famous theory for crystal melting, which is a two-stage process via an intermediate hexatic phase. To date, there is no approximation of DFT capable of reproducing these features. Still, it is common belief that even in two dimensions DFT of freezing gives good results on small to intermediate length scales (i.e., within the “crystalline domains”) and away from the Kosterlitz-Thouless transition (for a discussion see Subsection 1.6.1 and also Chapter 3). The capability of DFT to describe the liquid and the solid state through the same density field is not only relevant for equilibrium fluids, but is also of great advantage for the study of crystallization *dynamics*; this will become evident in Chapter 2, where static DFT is extended to a dynamical theory for nonequilibrium Brownian motion, e.g., for colloidal crystal relaxation and melting (cf. Chapter 5), and crystal growth (cf. Chapter 6).

The formalism of classical DFT has been established by Ebner *et al.* [76] in the late 70's. However, it is based on an equivalent framework for the electron density in an interacting electron gas by Hohenberg and Kohn [127] and also by Mermin [184], already developed in 1964. Since classical DFT has been used to study liquids and crystals in equilibrium for many years already, there are excellent reviews and textbooks describing the theory [85, 87, 117] and its application to crystallization [165, 209, 210, 263]. We therefore restrict ourselves here to a sketch of the important relations, approximations and implications, mainly following the reviews by Evans [85] and Singh [263]. In the first part of this chapter (Section 1.1), we sketch the basic relations leading to a variational principle for the grand potential Ω of a fluid in thermodynamic equilibrium in terms of the average one-particle density $\rho(\mathbf{r})$. In order to exploit the desired variational principle, the corresponding grand-canonical functional $\tilde{\Omega}[\rho(\mathbf{r})]$ is needed, which, for most fluids of interacting particles, can be obtained only approximatively. This is the actual challenge in DFT. We will therefore establish a hierarchy of correlation functions in Section 1.2, before turning to different approximations of the density functional relevant for homogeneous and inhomogeneous density fields in Section 1.3. In Section 1.4, we will name those approximations applied to freezing of colloidal systems in this thesis, and we will discuss their advantages and disadvantages compared to other approaches. For detailed derivations and discussions of the different approaches used we refer the reader to the relevant Chapters 3, 4, and 7. In Section 1.6, we discuss some subtleties of approximate density functional approaches to freezing, in particular the mean-field-like character of most density functionals, which leads to the omission of important fluctuations in continuous symmetry breaking phase transitions and in two dimensions.

1.1 The variational principle

We restrict our study to monodisperse systems of particles with mass m in a volume \mathcal{V} , which, in equilibrium, are completely characterized by a N -particle Hamiltonian

$$H_N = H_{\text{kin}} + U + H_{\text{ext}} . \quad (1.1)$$

where

$$H_{\text{kin}} = \sum_i \frac{\mathbf{p}_i^2}{2m}; \quad U \equiv U(\mathbf{r}_1, \dots, \mathbf{r}_N); \quad H_{\text{ext}} = \sum_i V(\mathbf{r}_i) . \quad (1.2)$$

Here, \mathbf{p}_i , \mathbf{r}_i are the momentum and position of the particle i , and the sum runs over all N particles $i = 1 \dots N$. U is the potential energy of interaction of the particles, and V is an external potential.

In the grand canonical ensemble, the equilibrium probability density for N particles is defined by

$$w_0 = \Xi^{-1} \exp[-\beta(H_N - \mu N)] , \quad (1.3)$$

where μ is the chemical potential and $\beta = 1/k_B T$, with k_B Boltzmann's constant and T the temperature. The grand partition function Ξ guarantees normalization of thermodynamic averages with respect to w_0 , which we denote by $\langle \dots \rangle$ (e.g., $\langle 1 \rangle = 1$). It follows that the thermodynamic average of the one-particle density operator $\hat{\rho}(\mathbf{r}) = \sum_i \delta(\mathbf{r} - \mathbf{r}_i)$,

$$\rho_0(\mathbf{r}) = \langle \hat{\rho}(\mathbf{r}) \rangle, \quad (1.4)$$

can be regarded as a unique functional of the probability density w_0 .¹ Having introduced the necessary quantities and notions of statistical mechanics, we come now to the two basic theorems of DFT:

First, it can also be shown that the inverse relation holds, i.e., that w_0 is a unique functional of ρ_0 , $w_0 \equiv w_0[\rho_0]$ (for a proof see, e.g., Appendix 1 of ref. [85]). This is the first fundamental theorem. The proof proceeds by showing that $V(\mathbf{r})$ is a unique functional of w_0 , which in turn implies that for any one-particle density $\rho(\mathbf{r})$ there exists exactly one external potential $V[\rho]$, which renders $\rho(\mathbf{r})$ an equilibrium density, i.e., $\rho(\mathbf{r}) = \langle \hat{\rho}(\mathbf{r}) \rangle_\rho$, where the subscript “ ρ ” denotes the average with respect to $w_0[\rho]$. Therefore, the important functional

$$F_{\text{intr}}[\rho] = \langle H_{\text{kin}} + U + \beta^{-1} \ln w_0[\rho] \rangle_\rho, \quad (1.5)$$

which will turn out to be the “intrinsic” part of the Helmholtz free energy, is a unique functional of ρ .

Second, it can be shown that the functional

$$\tilde{\Omega}[\rho] = F_{\text{intr}}[\rho] + \int d\mathbf{r} \rho(\mathbf{r})(V(\mathbf{r}) - \mu) \quad (1.6)$$

is minimized by the equilibrium density $\rho_0(\mathbf{r})$, where it takes the value of the grand potential $\Omega \equiv -\beta^{-1} \ln \Xi$, i.e.,

$$\left[\frac{\delta \tilde{\Omega}[\rho]}{\delta \rho} \right]_{\rho_0} = 0, \quad (1.7)$$

$$\tilde{\Omega}[\rho_0] = \Omega. \quad (1.8)$$

Eqs. (1.7) and (1.8) constitute the second fundamental theorem of DFT and also the essential variational principle allowing for the determination of the equilibrium state of any nonequilibrium fluid. However, so far F_{intr} is unknown, and we will dedicate a large part of this chapter to finding approximate forms of this functional. From Eqs. (1.6) and (1.8) it is now clear that $F_{\text{intr}}[\rho_0]$ is the intrinsic Helmholtz free energy. The *total* Helmholtz free energy F is obtained from Eq. (1.8) by a simple Legendre transform:

$$F = F_{\text{intr}}[\rho_0] + \int d\mathbf{r} \rho_0(\mathbf{r})V(\mathbf{r}). \quad (1.9)$$

¹To what extent ρ_0 remains a unique functional of w_0 in approximate density functional approaches, particularly in the context of spontaneous symmetry breaking, will be discussed in Subsection 1.6.1.

For a noninteracting fluid/gas with $U = 0$, the intrinsic free energy can be calculated exactly. F_{intr} then reduces to

$$F_{\text{id}}[\rho_0] = \int d\mathbf{r} \rho_0(\mathbf{r}) [\ln(\rho_0(\mathbf{r})\Lambda^D) - 1] , \quad (1.10)$$

where $\Lambda = h(\beta/2m\pi)^{1/2}$ is the thermal de Broglie wavelength and D the space dimension. We therefore define the excess part of the intrinsic Helmholtz free energy

$$F_{\text{ex}} = F_{\text{intr}} - F_{\text{id}} , \quad (1.11)$$

which is solely caused by the mutual interactions of the particles.

1.2 Two hierarchies of correlation functions

Two hierarchies of correlation functions can be established from the functionals $\tilde{\Omega}$ and F_{ex} , respectively. First, $\tilde{\Omega}$ is the generating functional for a hierarchy of *density-density correlation functions*

$$H^{(n)}(\mathbf{r}_1, \dots, \mathbf{r}_n) \equiv \langle [\hat{\rho}(\mathbf{r}_1) - \rho_0(\mathbf{r}_1)] \cdots [\hat{\rho}(\mathbf{r}_n) - \rho_0(\mathbf{r}_n)] \rangle = \frac{\delta^n \beta \tilde{\Omega}[\rho_0]}{\delta \beta u(\mathbf{r}_1) \cdots \delta \beta u(\mathbf{r}_n)} , \quad n \geq 2 , \quad (1.12)$$

where $u(\mathbf{r}) = \mu - V(\mathbf{r})$ is the intrinsic chemical potential. Eq. (1.12) implies that if $\tilde{\Omega}$ is known exactly, all structural properties of the liquid can be determined by successive functional differentiation. Second, a hierarchy of *direct correlation functions* can be established by functional differentiation of F_{ex} with respect to density:

$$c^{(n)}[\rho; \mathbf{r}_1, \dots, \mathbf{r}_n] \equiv -\beta \frac{\delta^n F_{\text{ex}}[\rho]}{\delta \rho(\mathbf{r}_1) \cdots \delta \rho(\mathbf{r}_n)} , \quad n \geq 1 . \quad (1.13)$$

The variational principle, Eq. (1.7), can now be recast into the form

$$\rho_0(\mathbf{r}) = \Lambda^{-D} \exp(\beta(\mu - V(\mathbf{r})) + c^{(1)}[\rho; \mathbf{r}]) , \quad (1.14)$$

which is the basis of an iterative numerical scheme to find $\rho_0(\mathbf{r})$, if the effective one-body potential $c^{(1)}[\rho; \mathbf{r}]$ is known. Eq. (1.14) will be explicitly used in Chapter 7. We will also come back to this relation further down.

It can be shown that the second-order correlation functions of each of these hierarchies can be related to each other via the Ornstein-Zernike or OZ equation

$$h(\mathbf{r}, \mathbf{r}') = c^{(2)}(\mathbf{r}, \mathbf{r}') + \int d\mathbf{r}'' c^{(2)}(\mathbf{r}, \mathbf{r}'') \rho_0(\mathbf{r}'') h(\mathbf{r}'', \mathbf{r}') , \quad (1.15)$$

where we defined $c^{(2)}(\mathbf{r}, \mathbf{r}') \equiv c^{(2)}[\rho_0; \mathbf{r}, \mathbf{r}']$ and replaced $H^{(2)}(\mathbf{r}, \mathbf{r}')$ by the dimensionless *total correlation function* $h(\mathbf{r}, \mathbf{r}')$, defined as

$$h(\mathbf{r}, \mathbf{r}') = [\rho_0(\mathbf{r})\rho_0(\mathbf{r}')]^{-1} [H^{(2)}(\mathbf{r}, \mathbf{r}') - \rho_0(\mathbf{r})\delta(\mathbf{r} - \mathbf{r}')] . \quad (1.16)$$

Similar relations can be established for higher-order direct and total correlation functions [291]. For uniform fluids ($\rho_0(\mathbf{r}) = \rho_0$), Eq. (1.15) reduces to the well known OZ equation for fluids

$$h(r) = c_0^{(2)}(r) + \rho_0 \int d\mathbf{r}' h(r') c_0^{(2)}(|\mathbf{r} - \mathbf{r}'|) , \quad (1.17)$$

where we introduced the subscript “0” on the direct pair-correlation function to denote that the density field is flat. Due to translational and rotational symmetry, h and $c_0^{(2)}$ now only depend on the distance r between two coordinates.² The Fourier transform of Eq. (1.17), $\tilde{h}(k)$, is connected to the static structure factor

$$S(k) = 1 + \rho_0 \tilde{h}(k) = [1 - \rho_0 \tilde{c}_0^{(2)}(k)]^{-1} , \quad (1.18)$$

which can be measured in scattering experiments [117, 224]. Here, $\tilde{c}_0^{(2)}(k)$ denotes the Fourier transform of the direct pair correlation function. A whole branch of physics, liquid state integral equation theory, is dedicated to the closure of Eq. (1.17) through appropriate constitutive equations [117]. The resulting, often very accurate pair correlation functions frequently serve as expansion kernels for perturbative and non-perturbative approaches to the excess free energy functional $F_{\text{ex}}[\rho]$ of inhomogeneous fluids in terms of density modulations $\Delta\rho(\mathbf{r}) = \rho(\mathbf{r}) - \rho$ about a reference fluid with constant density ρ ; we therefore give a short excursion to the field of liquid state integral equation theory in Section 1.3, which is also based on DFT. Starting from a reference fluid with an arbitrary inhomogeneous density field $\rho_i(\mathbf{r})$, the excess free energy functional of a fluid with density $\rho(\mathbf{r})$ can be obtained by functional integration and making use of the hierarchy of direct correlation functions, Eq. (1.13):

$$\begin{aligned} \beta F_{\text{ex}}[\rho] &= \beta F_{\text{ex}}[\rho_i] - \int d\mathbf{r} \Delta\rho(\mathbf{r}) \int_0^1 d\alpha c^{(1)}[\rho_\alpha; \mathbf{r}] \\ &= \beta F_{\text{ex}}[\rho_i] - \int d\mathbf{r} \Delta\rho(\mathbf{r}) \left\{ c^{(1)}[\rho_i; \mathbf{r}] \right. \\ &\quad \left. + \int d\mathbf{r}' \Delta\rho(\mathbf{r}') \int_0^1 d\alpha (1 - \alpha) c^{(2)}[\rho_\alpha; \mathbf{r}, \mathbf{r}'] \right\} , \end{aligned} \quad (1.19)$$

where $\Delta\rho(\mathbf{r}) = \rho(\mathbf{r}) - \rho_i(\mathbf{r})$ and $\rho_\alpha(\mathbf{r}) = \alpha\rho(\mathbf{r}) + (1 - \alpha)\rho_i(\mathbf{r})$. Eq. (1.19) is the basis for many approximate density functionals (see Section 1.4). The replacement of

²The effective one-body potential reduces to the constant excess chemical potential, $\beta^{-1}c_0^{(1)} = -\mu_0^{\text{ex}}$.

lower- by higher-order correlation functions [in the step from the first to the second line of Eq. (1.19)] can in principle be continued *ad infinitum*. For homogeneous fluids and for $\rho_i = 0$, Eq. (1.19) reduces to an integral of the compressibility $\chi_T = \rho_0^{-1} \beta S(k \rightarrow 0)$, which is the susceptibility related to density-density fluctuations, with $S(k)$ from Eq. (1.18).

1.3 Approximate density functionals and an excursion to the homogeneous liquid state

Before we proceed to different approximations to the DFT of inhomogeneous fluids, we throw a short glance at how to close the OZ equation, (1.17), for homogeneous fluids. We will restrict ourselves here to systems of particles interacting via pairwise-additive forces only, i.e.,

$$U(\mathbf{r}_1, \dots, \mathbf{r}_N) = \frac{1}{2} \sum_{i,j(i \neq j)} \phi(|\mathbf{r}_i - \mathbf{r}_j|), \quad (1.20)$$

which are embedded in a uniform external potential $V(\mathbf{r}) = 0$. To lowest order in density ρ_0 , the pair correlation function $c_0^{(2)}(r) \simeq f(r)$ is given by the *Mayer function* $f(r) = \exp[-\beta\phi(r)] - 1$, which reduces to $c_0^{(2)}(r) \simeq -\beta\phi(r)$ in the limit of small $\beta\phi$. This is in accordance with the well-known first-order virial expansion. In the context of DFT, the latter asymptotics is obtained from the following idea, originally formulated by Percus [218]: the radial distribution function $g(r) = h(r) + 1$ of a homogeneous fluid with constant density $\rho(\mathbf{r}) = \rho$ is equal to the inhomogeneous (radially isotropic) one-particle density $\rho_0(r)$ of the same system with one particle held fixed at the origin, i.e., with an external potential $V(r) = \phi(r)$. The assumption that the perturbation due to ϕ is small and therefore that the response of the density change $\Delta\rho(\mathbf{r}) = \rho_0(\mathbf{r}) - \rho$ is linear,

$$\Delta\rho(\mathbf{r}) \simeq \int d\mathbf{r}' H^{(2)}(|\mathbf{r} - \mathbf{r}'|) \beta\phi(r'), \quad (1.21)$$

(the Yvon equation [117]), together with Eq. (1.17), lead to the *mean-field* approximation (MFA), $c_0^{(2)}(r) \simeq -\beta\phi(r)$. Clearly, this simple relation holds at large distances r , where $\phi(r)$ is small. Interestingly, the same relation is recovered at *all* distances r for a special class of particles interacting via short-range, *bounded* pair potentials in the limit of a diverging temperature $(\beta\phi)^{-1} \gg 1$ and density $\rho\sigma^D \gg 1$, where σ is the range of the potential, keeping the ratio T/ρ finite [1, 106–108, 150, 191]: This is phenomenologically understood by reckoning that in this limit, in which ϕ is much smaller than the average potential energy per particle caused by all the other particles and smaller than the thermal energy, the excess free energy becomes completely energy-dominated, i.e.,

$$F_{\text{ex}}[\rho(\mathbf{r})] \simeq U[\rho] = \frac{1}{2} \iint d\mathbf{r} d\mathbf{r}' \rho(\mathbf{r}) \rho(\mathbf{r}') \phi(|\mathbf{r} - \mathbf{r}'|). \quad (1.22)$$

Functional differentiation according to Eq. (1.13) leads to the mean-field result $c^{(2)}[\mathbf{r}, \mathbf{r}'; \rho] = -\beta\phi(|\mathbf{r} - \mathbf{r}'|)$ for any density field $\rho(\mathbf{r})$. Concomitantly, all higher-order correlation functions vanish. We will exploit Eq. (1.22) in Chapter 7. Note that the MFA breaks down for pair interactions with a divergence at the origin.

Returning to “usual” fluids, a better approximation to the functional and to the correlation functions is obtained by expanding F_{ex} around a fluid of constant density ρ in terms of $\Delta\rho = \rho(\mathbf{r}) - \rho$, which in turn is due to the test particle at the origin (instead of expanding $\Delta\rho$ in terms of ϕ , as in the MFA, above):

$$\beta F_{\text{ex}}[\rho(\mathbf{r})] = \beta F_{\text{ex}}(\rho) - \sum_{n=1}^{\infty} \frac{1}{n!} \int_V d\mathbf{r}_1 \dots d\mathbf{r}_n c_0^{(n)}(\mathbf{r}_1, \dots, \mathbf{r}_n; \rho) \Delta\rho(\mathbf{r}_1) \dots \Delta\rho(\mathbf{r}_n). \quad (1.23)$$

Truncating the expansion at second order, $n \leq 2$, employing the variational principle to the respective grand potential functional according to Eq. (1.14) (with constrained density $\int d\mathbf{r} \Delta\rho(\mathbf{r}) = 0$) together with the OZ equation lead to the *hypernetted-chain* or HNC approximation, $c_0^{(2)}(r) = h(r) - \ln[h(r) + 1] - \beta\phi(r)$. The latter relation constitutes a closure relation to the OZ equation. Solution of the two equations for h and $c_0^{(2)}$ typically requires the application of an iterative, numerical scheme (see Chapter 4). Various other closure relations to the OZ equation are obtained by expanding different functionals in $\Delta\rho$, the second most famous closure being the Percus-Yevick approximation (an expansion of $\exp[c^{(1)}(\mathbf{r})]$ in $\Delta\rho$), which can also be obtained by functional differentiation of the *fundamental measure* functional [240, 243, 271]. Employing a diagrammatic description in terms of Mayer-bonds, the different approaches to the correlation functions can be recast into (infinite) sums of diagrams, being therefore highly non-perturbative. Still, the HNC and PY approximations entail equations of state reproducing correctly the second and third virial coefficients. Whereas the HNC approximation gives good (quantitative) results for long-range interacting particles the PY approximation serves well rather for short-range, hard-core potentials. However, both approximations are thermodynamically inconsistent in giving rise to different pressures upon either integrating the isothermal compressibility [based on $\tilde{c}_0^{(2)}(k=0)$] or employing the virial equation of state [based on $h(r)$] [117]. A somewhat arbitrary, but computationally feasible “mixture” of the two, guaranteeing thermodynamic consistency, which we make use of for dipolar particles in two dimensions ($\phi(r) \sim r^{-3}$) in Chapters 3-6, is an ansatz by Rogers and Young [239] (for the functional form see Chapter 4).

Similarly to the pair correlation functions, three-particle and even higher-order correlation functions can in principle be calculated via generalized, higher-order OZ equations [291] and potential closure relations. However, this task rapidly becomes difficult and in practice often unfeasible. Therefore, typical approaches are based on first- and second-order correlation functions. Famous approaches are by Kirkwood [143], Barrat *et al.* [20], and Denton *et al.* [63] (see Chapter 4 for details on the latter two).

1.4 Approximate density functionals for freezing

Within the density functional formalism bulk freezing sets in once a periodically modulated density field, $\rho(\mathbf{r}) = \rho(\mathbf{r} + \mathbf{R})$, with \mathbf{R} a lattice vector of the “optimum” crystal lattice, becomes a stable solution to the variational equations (1.7) or (1.14). Before coming to the search for the optimum lattice in the following chapter, we discuss here the usability of different already and yet to be introduced approximations to the DFT for the theoretical treatment of freezing. The simplest approximation to the excess free energy functional is the MFA, Eq. (1.22). Used for the test-particle treatment of homogeneous liquids above, it does also serve for the prediction of freezing for particles interacting via pair potentials with negative Fourier amplitudes [160]. It turns out that this functional, applied to a special class of cluster-forming particles, which interact via repulsive, *bounded* pair potentials with negative Fourier components (for details of the model, see Section 7.2), leads to a very accurate bulk phase diagram already for intermediate temperatures, $\beta\phi \approx 1$, and densities, $\rho\sigma^D \approx 1$, including a first-order liquid-solid transition and a subsequent solid-solid transition [161, 162, 188, 190, 191]. In Chapter 7, we will extend previous studies in scrutinizing the behavior of particles with a similar interaction potential in slit-pore confinement, i.e., in an inhomogeneous external potential $V(\mathbf{r})$ representing two parallel, infinite planar walls. The external potential partly breaks the symmetry of the underlying fluid and leads to wall-induced prefreezing and pre-melting, complete wetting of the respective crystalline or liquid phase, and capillary freezing or melting.

For unbounded potentials, the MFA-DFT is not a good approximation, as it already fails to give converging free energies per particle in the homogeneous liquid state. One step further goes the expansion of $F_{\text{ex}}[\rho]$ in terms of the density differences $\Delta\rho(\mathbf{r})$ about a reference fluid at constant density ρ , according to Eq. (1.23). The application of this approach to freezing goes back to a work by Ramakrishnan and Yussouff [226] in 1979; the approach was reformulated in the familiar density functional language in 1981 by Haymet and Oxtoby [119]. For practical reasons (i.e., due to limited knowledge of higher than second-order correlation functions of the fluid) they truncated the expansion at $n = 2$; it is therefore also referred to as *second-order* theory (SOT). We will extend their approach by taking third-order correlation functions of the fluid into account [i.e., $n = 3$ in Eq. (1.23)], consequently referred to as *third-order* theory (TOT). The TOT was applied to the problem of freezing of hard spheres in three dimensions by Curtin [55]. However, he found that inclusion of a third-order term substantially worsened the prediction of freezing, compared to the result obtained within the SOT. In fact, the prediction of freezing of the SOT and of the TOT rather come as a surprise, since the expansion parameter, $\Delta\rho(\mathbf{r})$, is by no means small in the crystalline phase (for dipolar particles in 2D, we will find $\Delta\rho(\mathbf{r})/\rho \lesssim 100$). The predicting qualities must therefore be due to a cancellation of errors. In two dimensions, however, application of the TOT to the dipolar inverse-power potential, leads to a substantial improvement compared

to the SOT-result (see Chapter 4 for a deeper discussion). We will also use the second-order theory as an input to the nonequilibrium dynamical density functional theory (see Chapter 2) in Chapters 5 and 6.

Another class of approximations to the DFT of freezing comprises non-perturbative approaches (with respect to the homogeneous liquid), which take first- or second- or third-order terms of the infinite sum, Eq. (1.23), properly into account, but contain also contributions of *all* higher-order terms in a non-perturbative fashion. Famous approximations are the *weighted density* approximation or WDA by Tarazona [270], and Curtin and Ashcroft [56], and the *modified weighted density* approximation or MWDA by Denton and Ashcroft [64]. The former amounts to expressing the excess free energy functional,

$$F_{\text{ex}}^{\text{WDA}}[\rho] = \int d\mathbf{r} \rho(\mathbf{r}) f_0(\bar{\rho}(\mathbf{r})) \quad (1.24)$$

in terms of the excess free energy per particle of a homogeneous fluid, $f_0(\bar{\rho}(\mathbf{r})) \equiv F_{\text{ex}}[\rho(\mathbf{r}') = \bar{\rho}(\mathbf{r})]/N$, at a weighted density

$$\bar{\rho}(\mathbf{r}) = \int d\mathbf{r}' \rho(\mathbf{r}') w(|\mathbf{r} - \mathbf{r}'|; \bar{\rho}(\mathbf{r}')), \quad (1.25)$$

which is a local function of the true density $\rho(\mathbf{r})$, weighted with an appropriately chosen weight function w (which is not to be confused with the probability density introduced in Section 1.1). The choice $w(|\mathbf{r} - \mathbf{r}'|) = \delta(|\mathbf{r} - \mathbf{r}'|)$ corresponds to the well-known *local-density* approximation, which, however, leads to poor delta-correlated functional derivatives [117]. Within the WDA the weight function is normalized and chosen to correctly reproduce the correlations of the homogeneous liquid state for any density ρ_0 , i.e.,

$$\lim_{\rho(\mathbf{r}) \rightarrow \rho_0} \left[\frac{\delta^2 F_{\text{ex}}^{\text{WDA}}}{\delta \rho(\mathbf{r}) \delta \rho(\mathbf{r}')} \right] = -\beta^{-1} c_0^{(2)}(\mathbf{r} - \mathbf{r}'; \rho_0). \quad (1.26)$$

By construction, the WDA includes infinitely many higher-order terms in a non-perturbative way as well, which is due to the self-consistent dependence of the weight function on the weighted density in Eq. (1.25). This way of going beyond the SOT has led to substantial improvements of the predictions of hard-sphere crystallization [56, 57], the reference model for comparison with the worse SOT and TOT.

The MWDA, in contrast, is a nonlocal theory, which approximates the excess free energy of an inhomogeneous system by the excess free energy of a homogeneous reference fluid

$$F_{\text{ex}}^{\text{MWDA}}[\rho(\mathbf{r})] = N f_0(\hat{\rho}), \quad (1.27)$$

with the weighted density

$$\hat{\rho} = \frac{1}{N} \iint d\mathbf{r} d\mathbf{r}' \rho(\mathbf{r}) \rho(\mathbf{r}') w(|\mathbf{r} - \mathbf{r}'|; \hat{\rho}). \quad (1.28)$$

Similarly to the WDA, this approach is formulated in a self-consistent fashion rendering it non-perturbative. Also, the weight function is determined by the constraint to reproduce the correlations of the underlying liquid, Eq. (1.26). However, the non-local formulation makes the MWDA computationally much simpler since it amounts to solving algebraic equations rather than nonlinear differential equations as in the WDA (for a derivation of the formalism see reference [64] or Chapter 4). The ease of computation, however, goes along with a restriction of the theory to bulk systems. The treatment of interfaces, for example, is only possible after a modification of the functional to a *hybrid weighted density* approximation, as suggested by Leidl and Wagner [155]. The MWDA has been successfully applied to freezing of hard spheres [64], hard disks [309], Lennard-Jones and inverse-power potentials ($\phi(r) \propto 1/r^\nu$, with $\nu \geq 4$) [149]. Likos and Ashcroft have demonstrated that for the one-component plasma (OCP), characterized by the long-range potential $\phi(r) \propto 1/r$, the MWDA is not a satisfactory theory as it does not predict freezing at all [158]. This failure is due to the vanishing of the coexistence region for inverse-power potentials in the limit of $\nu \rightarrow 1$ [288], i.e., the freezing transition of the OCP is isochoric. This in turn leads to a vanishing three-particle contribution to the excess free energy functional at coexistence, which is otherwise present [158, 159]. They therefore extended the MWDA to reproduce also third-order correlations of the underlying liquid exactly, which is referred to as *extended modified weighted density* approximation or EMA [158, 159]. The second constraint to the functional [next to the first constraint, Eq. (1.26)],

$$\lim_{\rho(\mathbf{r}) \rightarrow \rho} \left[\frac{\delta^3 F_{\text{ex}}^{\text{EMA}}}{\delta \rho(\mathbf{r}) \delta \rho(\mathbf{r}') \delta \rho(\mathbf{r}'')} \right] = -\beta^{-1} c_0^{(3)}(\mathbf{r} - \mathbf{r}', \mathbf{r} - \mathbf{r}''; \rho), \quad (1.29)$$

is fulfilled by introducing a second (three-particle) weight function v for the determination of the weighted density $\hat{\rho}$, which now reads

$$\hat{\rho} = \frac{1}{N} \iint d\mathbf{r} d\mathbf{r}' \rho(\mathbf{r}) \rho(\mathbf{r}') \left[w(|\mathbf{r} - \mathbf{r}'|; \hat{\rho}) + \frac{1}{N} \int d\mathbf{r}'' \rho(\mathbf{r}'') v(\mathbf{r} - \mathbf{r}', \mathbf{r} - \mathbf{r}''; \hat{\rho}) \right]. \quad (1.30)$$

In fact, for long-range power law interactions, $\phi(r) \propto 1/r^\nu$, this approach substantially improves the functional. We will demonstrate in Chapters 3 and 4 that the EMA also yields very accurate results for particles with dipolar interactions [$\phi(r) \propto r^{-3}$] in two dimensions (disregarding the problem of continuous melting, mentioned in the introduction and discussed in Section 1.6).

For a discussion of other density functional approaches to freezing we refer the reader to the already mentioned reviews by Singh [263], Oxtoby [209, 210], Löwen [165, 168], and also to the textbook by Hansen and McDonald [117].

1.5 The search for the optimum crystalline density

At zero external potential, $V(\mathbf{r}) = 0$, i.e., in the bulk, a homogeneous density, $\rho(\mathbf{r}) = \rho_0 = \Lambda^{-3} \exp[\beta(\mu - \mu_{\text{ex}})]$, is always, i.e., for all T and μ , a solution to the variational principle of Eq. (1.7) [or to Eq. (1.14), respectively]. However, for many fluids, below some temperature $T^*(\mu)$ or chemical potential $\mu^*(T)$ (at fixed volume \mathcal{V}), a periodically modulated density field $\rho(\mathbf{r}) = \rho(\mathbf{r} + \mathbf{R})$, with \mathbf{R} a lattice vector of some crystal lattice, also becomes a solution to the equations. According to the theory, the crystal with the minimum grand potential functional among all possible lattice structures is interpreted to be in coexistence with a liquid at that line in the μ - T -plane, at which the grand potential functionals of the liquid and the solid solutions are equal. To find the constant (liquid) solution to Eq. (1.14) is a simple task. On the contrary, to find the crystalline solution to the same equation with the minimum grand potential functional is demanding, since, in principle, infinitely many different crystal geometries with different lattice spacings must be probed. In many practical situations, however, the assumption of stability of simple Bravais lattices (fcc and bcc lattices in three dimensions, and hexagonal lattices in two dimensions) is often reasonable, although we will find in Chapter 7 that the stable post-freezing structure of the cluster-forming particles under study, which interact via bounded potentials, is the non-Bravais lattice of the hexagonally close packed crystal.³

Naively assuming that each lattice site is populated by one single particle, the lattice spacing a is given by the equilibrium average density $\rho = \mathcal{V}^{-1} \int d\mathbf{r} \rho(\mathbf{r})$, $a = c\rho^{-1/D}$ with c some lattice structure-dependent constant. However, the minimum grand potential is most often found at a different, slightly smaller or larger lattice spacing, which is interpreted as a finite concentration of defects such as vacancies or interstitials (see Chapter 4). In fact, it turns out that the lattice spacing turns completely density-independent in the case of cluster-forming particles in the limit of large densities (see Chapter 7), which implies that many particles share the same lattice site and basically sit on top of each other.

Finally, the local shape of the density within a unit cell is *a priori* not given, although an isotropic, Gaussian shape is often justified *a posteriori* [165] (for a detailed discussion see Chapter 4).

1.6 Discussion

A comprehensive discussion of the density functional approach to freezing goes far beyond the scope of this chapter. We must therefore necessarily restrict ourselves

³How to discriminate crystalline from noncrystalline solutions to the DFT in external potentials, in particular, in slit pores, will be discussed in Chapter 7.

here to few subtleties of the theory, which are conceptually relevant for a broader understanding and also for the dynamical density functional theory introduced in the following chapter, but which are discussed in the subsequent chapters only to a small extent. The following points are of order here: in Subsection 1.6.1, we discuss the problem of spontaneous symmetry breaking occurring at a first-order freezing transition, how it is incorporated in the theoretical description, and to what extent fluctuations are in general omitted in approximate density functional approaches. The problem of freezing in two dimensions is expounded in Subsection 1.6.2, in particular, the failure of any approximate DFT to predict continuous melting and a breakdown of translational order on large scales. In Subsection 1.6.3, we discuss the problem of a translation of the original grand canonical into a canonical description, which is pursued by a simple Legendre transform in the thermodynamic limit but which is more subtle in systems of finite size.

1.6.1 Ergodicity breaking and omitted fluctuations

At the first-order liquid-solid transition in the bulk, i.e., for zero external field, $V(\mathbf{r}) = 0$, in three spatial dimensions, the continuous translational and rotational symmetry of the isotropic fluid is spontaneously broken, which is a famous example of ergodicity breaking [100]. Despite ergodicity breaking the DFT, which is in principle based on an unrestricted ensemble average, should always predict a uniform equilibrium density ρ_0 . On the contrary, any known approximate DFT does predict thermodynamical stability of infinitely many crystalline states with different offsets and orientations, which share the same value of the grand potential functional. Therefore, the approximate DFTs do not sample all the fluctuations but only generate restricted ensemble averages. Before suggesting a protocol to overcome this problem, we give here an argument for the better understanding of this failure by doing the following gedankenexperiment.

Let us assume that we have an exact functional, referred to as functional A , which is minimized by a uniform one-particle density ρ_A , which is equal to the correct average density of the crystal in the crystalline regime of the phase diagram. Let us further assume that we have an approximate functional B , which is minimized by an infinite number of periodically modulated density fields, which differ only in offset or orientation. For simplicity, let us arbitrarily choose one periodic field $\rho_B(\mathbf{r})$. Assume further that the total correlation functions of the two completely different density fields are equal, i.e., $h_A(\mathbf{r}, \mathbf{r}') = h_B(\mathbf{r}, \mathbf{r}')$. We now ask the question what external potential $V_A(\mathbf{r})$ is needed in order to render $\rho_B(\mathbf{r})$ the equilibrium density field of functional A . This potential, which pins the density peaks to the lattice vectors, must have the periodicity of the crystal. The important point is now, that its amplitude goes to zero as $k_B T/N$ in the thermodynamic limit, i.e., its total contribution to the Hamiltonian or the free energy is of the order $k_B T$, which is just enough to compensate the entropy gain due to the few D translational and $D - 1$ rotational degrees of freedom of the whole crystal. From this gedankenexperiment

we see that the approximate density functional eventually fails to “see” the small difference in free energy due to additional fluctuations in the center-of-mass motion and rotation of the crystal as a whole (we will come back to this reasoning further down).

This problem can in principle be overcome by two different ways of reasoning, which are, however, a bit flawed: first, we argue that all density fields leading to the same value of the grand potential are in coexistence and therefore appear in an experiment with the same probability; an average over these densities leads to the desired flat density profile. This argument does not only apply to different bulk crystal offsets and orientations but also to the coexistence of different phases at phase boundaries, as discussed in the previous section. Second, the problem can be overcome by breaking the symmetry of the fluid “by hand,” through application of a symmetry breaking external field $V(\mathbf{r})$ (which can, in contrast to the one in the gedankenexperiment above, be limited to a small region in space), calculating the equilibrium density, and then taking the limit $V \rightarrow 0$, although, for practical calculations, this is not necessary.⁴ This “recipe” and also the gedankenexperiment above point at a deeper problem of any approximation to the DFT: as it is typically not clear *a priori*, which fluctuations are physically accessible during an experimental realization and how the ensemble average should be properly restricted in order to yield the same restricted thermodynamics, it is even less clear whether such a restriction is properly accounted for by the approximate DFT, which was in the beginning designed to include all the fluctuations [165]. Still, in the context of bulk freezing, this reasoning has been successfully applied to date.

There have been some attempts to translate this reasoning from the context of spontaneous symmetry breaking to other problems, in which approximate density functionals are known to fail or to perform badly due to important missing fluctuations [11, 229, 262]. In these approaches, effectively, a new partition sum,

$$\Xi^* = M^{-1} \sum_{i=1}^M \exp[-\beta\Omega_i], \quad (1.31)$$

is introduced, in which the Ω_i are the values of the approximate grand potential functional at the constrained density fields ρ_i . The different ρ_i , which do not necessarily minimize the functional even locally, may lead to very different values of the grand potential functional. Reguera *et al.* argue that in the context of nucleation, where DFT is frequently used to estimate nucleation barriers [212, 214], density functionals of critical droplets should rather be interpreted as restricted averages [229]. Singh

⁴Within the dynamical theory introduced in Chapter 2 and applied to crystal growth in Chapter 6, we will replace the mathematical problem of putting the thermodynamic limit and the limit $V \rightarrow 0$ in the right order by an experimentally realizable recipe of preparing a fluid system with an applied external potential V at a high temperature at time $t \rightarrow -\infty$, quenching the system to a low temperature at $t = 0$, turning the external potential off at the same time, and regarding the limit $t \rightarrow \infty$ as the “new” equilibrium state.

et al. construct density fields with artificial point defects, which they then average over [262] in order to find quantitatively better vacancy concentrations of solids. Archer *et al.* split a fluid density field of monodisperse hard spheres artificially into two species and study the constrained density field of the one species in the “free energy landscape” produced by the relaxed density field of the second species in order to estimate the density of the hard-sphere glass transition [11]. Thereby, they actually suppress fluctuations. At best, these exemplarily chosen approaches are justified *a posteriori* by their quantitative predicting capabilities. However, they are not based on fundamental grounds. Reguera *et al.* are aware of this problem and discuss this issue [229].

Although there is no general framework to treat these problems, there is a general tendency of approximate density functionals to miss translational or rotational fluctuations of supra-molecular entities such as crystals, droplets, or clusters as a whole, long-wavelength capillary fluctuations of interfaces, etc., although this is not a strict rule. However, typically the degrees of freedom of the microscopic constituents and the mesoscopic entities are not separated as clearly as, e.g., in the example of a translating droplet. If they are, there are most often effective, coarse-grained theories around, which do a better job in describing these degrees of freedom correctly [157]. Of course, this is not very much different from employing Eq. (1.31) directly. For further discussion we refer the reader also to reference [179] by Marini Bettolo Marconi and Tarazona.

1.6.2 Density functional theory in two dimensions

The problem of missing fluctuations becomes most evident in two spatial dimensions, where the picture is qualitatively different from three dimensions: here, the Goldstone modes of the 2D crystal lead to a *full* breakdown of translational order [91, 92, 100, 185]. In particular, at low temperatures the local crystalline order parameter decays as a power law with distance and only long-range rotational order persists (see also Chapter 4). To date, there is no approximation to the DFT capable of taking this breakdown, i.e., the emergence of the responsible fluctuations, the Goldstone modes, properly into account; all available approximations turn out to be mean-field like in this respect. Also, the two-stage melting transition with an intermediate hexatic phase according to the crystal defect-based KTHNY theory is not captured by the DFT (see Chapters 3 and 4 for a discussion). Since for the dipolar system under study in Chapters 3 and 4 the stability range of the hexatic phase is small and since the translational order parameter decays only slowly with distance, deep inside the crystalline regime, we do not address this question but rather focus on the liquid and the solid phase reasonably far away from the two-stage phase transition. A similar view has been taken for hard disk systems [21, 248, 301, 309] and to the $1/r$ -interaction in 2D [248] where density functional theory of freezing was applied.

We will come back to the problem of missing fluctuations in the next chapter. There, within the context of dynamical density functional theory, we will find *local* minima of approximate density functionals⁵ to be a source of *dynamical* arrest in metastable states, which in experiments or simulations are at best long-lived.

1.6.3 The canonical vs the grand canonical ensemble

Originally, the DFT was formulated in the grand canonical ensemble, at fixed chemical potential μ , which implies the coupling to a particle reservoir. For infinite systems in equilibrium this description is completely equivalent to a canonical description, in which the particle number N is kept fixed, since in the thermodynamic limit fluctuations about the averages of thermodynamic quantities go to zero.⁶ This equivalence breaks down in small systems, where particle number fluctuations become important. It would therefore be highly desirable to construct a canonical-ensemble DFT with a variational principle for a Helmholtz free energy functional. An approximate form of such a variational principle has been suggested by White *et al.* [293, 294].⁷ Their approximation is based on a saddle-point approximation of the grand partition sum of a homogeneous fluid about the corresponding canonical partition sum in terms of the particle number fluctuations $\Delta^2(N) = \langle N^2 \rangle - \langle N \rangle^2$ [310]:

$$-\beta\Omega_{\text{gc}}(\mu) = -\beta F_{\text{c}}(\langle N \rangle) + \beta\mu\langle N \rangle + \frac{1}{2} \ln 2\pi\Delta^2(N),$$

where the indices “gc” and “c” stand for “grand canonical” and “canonical”, respectively. White *et al.* have generalized this concept to inhomogeneous fluids, i.e., the fluctuations $\Delta^2(N)$ become a functional of the density field, $\Delta^2[N; \rho]$. As $\Delta^2[N; \rho]$ is a double integral over the second-order density-density correlation function $H^{(2)}$, it can be obtained via a generalized Ornstein-Zernike equation, similar to Eq. (1.15).

The differences of canonical versus grand canonical equilibrium densities have been shown to be quite pronounced for a small number of hard spheres ($N \lesssim 10$) in small cavities [294], but vanish in the thermodynamic limit. In the following chapter, we will argue that for the dynamical density functional theory a generalization of the concept from *global* to *local* number fluctuations would be desirable (cf. Section 2.2).

⁵That $\Omega[\rho]$ is a convex functional of ρ and therefore should not have more than one local minimum was, e.g., proved by J.-M. Caillol [38].

⁶At phase boundaries, this scaling does not hold, but particle number fluctuations become macroscopic [130].

⁷Later, Hernando and Blum [124] and Hernando [123] constructed a rigorous approach to DFT in the canonical ensemble based on a hierarchy of correlation and distribution functions.

Chapter 2

Colloids in nonequilibrium

After having treated equilibrium fluids and crystals by means of classical density functional theory in the previous chapter, we turn our attention now to theoretical approaches to the overdamped, nonequilibrium dynamics of colloidal particles, which is the basis of our work on relaxation dynamics of crystals and on the motion of active “Brownian swimmers” laid out in Chapters 5, 6, and 8. We will start from the microscopic Langevin equations of motion and the Smoluchowski equation for the time evolution of the probability distribution function [96, 224, 237, 276, 283], ignoring hydrodynamic interactions, in Section 2.1. Deterministic, average quantities are subsequently assessed following two different ways: the first approach is the dynamical density functional theory (DDFT) by Marini Bettolo Marconi and Tarazona (MT) [179, 180], which describes the deterministic dynamics of the time-dependent, average one-particle density of a colloidal system. The DDFT, which is the basis of our assessment of crystal melting (Chapter 5) and growth (Chapter 6), is reviewed in Section 2.2.¹ In particular, we sketch the derivation of the theory starting from the Smoluchowski equation following the references by Archer and Evans [10] and MT [179] in Subsection 2.2.1, we discuss the implications of the approximations made in Subsections 2.2.2 and 2.2.3, we comment on its application to crystal dynamics in Subsection 2.2.4, and review further groundbreaking applications and extensions in Subsection 2.2.5.

The second approach is a non-Hamiltonian rate theory based on the functional integral formalism of the Onsager-Machlup theory [206], which we exploit in Chapter 8 to estimate the long-time diffusion constant of a single, active Brownian particle in two dimensions in a confining channel. This approach is introduced in Section 2.3. As the model under study is $(2 + 1)$ -dimensional, non-Hamiltonian, and even possesses state-dependent mobility coefficients, we embed the derivation of the approximate rate theory into the exposure of the specific dynamics of the model system. In particular, we start, once again, from the Langevin- and Smoluchowski-equations, adapted to particles with an internal orientation in two plus one dimensions (Sub-

¹For another brief review see also reference [300].

section 2.3.1), motivate (Subsection 2.3.2) and introduce (Subsections 2.3.3, 2.3.4) the escape rate approach, discuss the approximation used for the model system at hand (Subsection 2.3.5), and finish with a short discussion (Subsection 2.3.6). Note that in this chapter the particular problems addressed in Chapters 5, 6, and 8 are approached from the theory, or method side, i.e., the specific forms of the theories used are embedded into the general framework of DDFT and rate theories, whereas the physical motivation of the particular problems is largely deferred to the corresponding later chapters.

2.1 Langevin dynamics

We consider the dynamics of a set of N identical, spherical, colloidal particles, immersed in a fluid of viscosity η_0 , on the “Brownian” time scale [67], i.e., we assume that the momenta of the solvent particles *and* of the colloidal particles have already relaxed. The relaxation time of the colloid momenta is given by $m\Gamma$, where m is the particle mass and $\Gamma^{-1} = 3\pi\eta_0\sigma$ is the friction coefficient for a colloidal sphere with diameter σ .² In colloidal suspensions, typical relaxation times of the solvent and of the colloidal particle momenta are of the order 10^{-14} s and 10^{-9} s, respectively [67, 224], whereas typical time scales of interest, e.g., the time, it takes a particle to diffuse its own diameter, are of order $1 \mu\text{s} - 1 \text{s}$ [67, 224]. Assuming further that the particles do not interact via hydrodynamic forces, the N coupled Langevin equations of motion [96, 224, 237, 276, 283] are given by

$$\dot{\mathbf{r}}_i = \Gamma (\mathbf{F}_i + \mathbf{f}_i), \quad i = 1, \dots, N, \quad (2.1)$$

where the dot denotes a time derivative and Γ is the already introduced inverse friction coefficient, which is henceforth referred to as mobility coefficient. State-dependent mobility will be discussed further down (cf. Subsection 2.2.1 for hydrodynamic interactions and Section 2.3 for a coupling to orientational degrees of freedom). For particles, which are embedded in an external field V and interact with each other via the potential energy of interaction U , the deterministic force acting on particle i is given by

$$\mathbf{F}_i(\{\mathbf{r}\}, t) = -\nabla_i [U(\{\mathbf{r}\}) + V(\mathbf{r}_i, t)], \quad (2.2)$$

where we denote the positions of all particles by $\{\mathbf{r}\} = \{\mathbf{r}_1, \dots, \mathbf{r}_N\}$. The Gaussian white noise random forces \mathbf{f}_i originating from the solvent are completely characterized by the first two moments of their distribution function,

$$\overline{\mathbf{f}_i(t)} = \mathbf{0} \quad (2.3)$$

$$\overline{f_{i\alpha}(t)f_{j\beta}(t')} = 2(\Gamma\beta)^{-1}\delta_{ij}\delta_{\alpha\beta}\delta(t-t'), \quad (2.4)$$

²Often, the time scale $m\Gamma$ is referred to as the “Brownian” time τ_B [224]. We will reserve this variable for a different and much larger time scale, $\tau_B = \sigma^2\beta/\Gamma$, which is the time it takes for an isolated particle to diffuse its own diameter (see further down).

which fulfill the well-known Einstein fluctuation-dissipation relation. The bars over the quantities denote a noise average, and Greek indices indicate a component of the cartesian vector.

The Langevin equations of motion are the basis for Brownian dynamics (BD) computer simulations [4], which are used in Chapters 3, 4, and 7 to obtain “exact” structural quantities of fluids in equilibrium and in Chapters 6 and 8 to extract time-dependent quantities of nonequilibrium systems. A straightforward algorithm for the simulation of the continuous-time Langevin equations employing a discrete time step Δt goes back to Ermak [83]. The update equation for the position of particle i reads

$$\mathbf{r}_i(t + \Delta t) = \mathbf{r}_i(t) + \Gamma \Delta t \mathbf{F}_i(\{\mathbf{r}\}, t) + \Delta \mathbf{r}_i + o(\Delta t), \quad (2.5)$$

$$\overline{\Delta \mathbf{r}_i} = \mathbf{0}, \quad \overline{\Delta r_{i\alpha} \Delta r_{j\beta}} = 2\Gamma \beta^{-1} \delta_{ij} \delta_{\alpha\beta} \Delta t, \quad (2.6)$$

where the second line characterizes the Gaussian random displacement $\Delta \mathbf{r}_i$. Equation (2.5) is exact up to order $o(\Delta t)$. Leaving this short excursion to BD computer simulations, we return to the continuous-time description.

The set of coupled, stochastic differential equations (2.1) for the particle coordinates corresponds to a deterministic Fokker-Planck equation for the N -particle probability density $W(\{\mathbf{r}\}, t)$ [96, 224, 237, 276, 283],

$$\dot{W}(\{\mathbf{r}\}, t) = \mathcal{L}_S W(\{\mathbf{r}\}, t), \quad (2.7)$$

$$\mathcal{L}_S = \Gamma \sum_i \nabla_i \cdot [\beta^{-1} \nabla_i - \mathbf{F}_i(\{\mathbf{r}\}, t)], \quad (2.8)$$

which determines the probability to find the set of N particles within a small volume around the positions $\{\mathbf{r}\}$ at time t , given a normalized, initial distribution $W(\{\mathbf{r}\}, t = 0)$. The sum runs over all particles $i = 1, \dots, N$. Eq. (2.7), a continuity equation, which is referred to as Smoluchowski equation, can be formally derived from the Langevin equations, e.g., via a Kramers-Moyal expansion [237]. In Eq. (2.7), we introduced the Smoluchowski-operator \mathcal{L}_S . The probability density $W(\{\mathbf{r}\}, t)$ can be written in terms of the yet unknown conditional probability density $P(\{\mathbf{r}\}, t | \{\mathbf{r}'\}, t')$:

$$W(\{\mathbf{r}\}, t) = \int d^N \mathbf{r}' P(\{\mathbf{r}\}, t | \{\mathbf{r}'\}, 0) W(\{\mathbf{r}'\}, 0),$$

where the short notation $d^N \mathbf{r} = d\mathbf{r}_1 \cdots d\mathbf{r}_N$ was introduced. The conditional probability density obviously fulfills $P(\{\mathbf{r}\}, t | \{\mathbf{r}'\}, t) = \delta(\{\mathbf{r}\} - \{\mathbf{r}'\})$ and obeys the same time evolution as $W(\{\mathbf{r}\}, t)$. We will make use of the short-time solution to the Smoluchowski equation for $P(\{\mathbf{r}\}, t | \{\mathbf{r}'\}, t)$ in the functional integral approach to the time evolution of a single, Brownian rod in Section 2.3. But first, we derive in the following section a dynamical density functional theory for dense fluids, which was developed by MT [179, 180].

2.2 Dynamical density functional theory

For dense, strongly interacting fluids, one is typically not interested in the position of all individual particles but rather in the probability to find *any* particle at a certain vector \mathbf{r} at time t . The corresponding equation of motion for the one-particle density can on the one hand be derived directly from the Langevin equations, Eq. (2.1), via a coordinate transformation $\mathbf{r}_i \rightarrow \hat{\rho}(\mathbf{r})$ and a subsequent noise-average. This way was followed by MT [179], following an earlier approach by Dean [61]. On the other hand, it can be derived from the Smoluchowski equation, Eq. (2.7), an approach adopted by Archer and Evans [10]. In the following subsection, we will follow the latter approach, sketch the derivation and comment on the approximations made. The implications of the use of approximate density functionals as an input to the theory and the so called *adiabatic* approximation (see further down) are discussed in Subsections 2.2.2 and 2.2.3, respectively. In Subsection 2.2.4, we discuss the application of the DDFT to the dynamics of crystals, i.e., melting, crystal growth, and structural relaxation. Further applications, which demonstrate the validity and great value of the theory under many circumstances, and extensions are reviewed in Subsection 2.2.5.

2.2.1 Derivation of the dynamical equation

First, we introduce the time-dependent one- and two-particle densities

$$\rho(\mathbf{r}, t) = \sum_i \overline{\delta(\mathbf{r} - \mathbf{r}_i(t))}, \quad (2.9)$$

$$\rho^{(2)}(\mathbf{r}, \mathbf{r}', t) = \sum_{i,j;i \neq j} \overline{\delta(\mathbf{r} - \mathbf{r}_i(t))\delta(\mathbf{r}' - \mathbf{r}_j(t))}, \quad (2.10)$$

where we dropped the superscript “(1)” on the one-particle density. These densities are equal to the $(N - n)$ -times integrated probability density W ,

$$\rho^{(n)}(\mathbf{r}_1, \dots, \mathbf{r}_n, t) = \frac{N!}{(N - n)!} \int d^{N-n} \mathbf{r} W(\{\mathbf{r}\}, t). \quad (2.11)$$

Note that in equilibrium, where the time-dependent densities turn time-independent, the noise averages in Eqs. 2.9 and 2.10 become equivalent to canonical ensemble averages³ and the one-particle density, Eq. (2.9), turns almost equal to $\rho_0(\mathbf{r})$, given in Eq. (1.4). The important difference is, however, that there we performed a *grand* canonical ensemble average (see also the discussion concerning a canonical vs a grand canonical formulation of the DFT in Subsection 1.6.3 and its importance in the dynamical theory at the end of this subsection and in Subsection 2.2.3). In the following, we restrict ourselves to pairwise interacting particles,⁴ i.e., $U =$

³As we did not prescribe an initial probability density $W(\{\mathbf{r}\}, t_0)$, a noise average might always lead to the same nonergodic state even in the limit of infinitely many different realizations; the corresponding ensemble average must then be restricted (cf. the discussion in Subsection 1.6.1).

⁴An inclusion of higher-order interactions is straightforward [10].

$\frac{1}{2} \sum_{i,j;i \neq j} \phi(|\mathbf{r}_i - \mathbf{r}_j|)$, which are also subject to a in general time-dependent external potential $V(\mathbf{r}_i, t)$. By integration of Eq. (2.7) over the positions of $N - 1$ of the N particles and making use of Eqs. (2.9) and (2.10) we therefore obtain the following continuity equation for $\rho(\mathbf{r}, t)$:

$$\Gamma^{-1} \dot{\rho}(\mathbf{r}, t) = \beta^{-1} \nabla^2 \rho(\mathbf{r}, t) + \nabla \cdot \left[\rho(\mathbf{r}, t) \nabla V(\mathbf{r}, t) + \int d\mathbf{r}' \rho^{(2)}(\mathbf{r}, \mathbf{r}', t) \nabla \phi(\mathbf{r}, \mathbf{r}') \right]. \quad (2.12)$$

For noninteracting particles in zero external field, this equation reduces to Fick's diffusion equation. Also with an external field applied, Eq. (2.12) is in principle exactly solvable. In the interesting case of interacting particles, however, we still need an expression for the time-dependent two-particle density $\rho^{(2)}(\mathbf{r}, \mathbf{r}', t)$. In principle, we can obtain a similar equation for $\rho^{(2)}$ in terms of a three-particle density $\rho^{(3)}$ by $(N - 2)$ -fold integration of Eq. (2.7); this iteration can be continued *ad infinitum* but is of little help. Instead, the time-dependent function $\rho^{(2)}(\mathbf{r}, \mathbf{r}', t)$ is here approximated by its yet unspecified equilibrium counterpart $\rho_0^{(2)}(\mathbf{r}, \mathbf{r}')$, evaluated at a corresponding equilibrium fluid, in which the equilibrium density $\rho_0(\mathbf{r})$ is equal to the instantaneous one-particle density $\rho(\mathbf{r}, t)$ of the nonequilibrium system. In order to render $\rho(\mathbf{r}, t)$ an equilibrium density, an appropriate external potential $v(\mathbf{r})$ must be applied. That such a potential exists, and that it is even a unique functional of the density $\rho_0(\mathbf{r})$, is one of the theorems of DFT, which has been discussed in the beginning of Section 1.1. The approximation of replacing a time-dependent, nonequilibrium correlation function by its equilibrium equivalent, is also referred to as *adiabatic* approximation,⁵ which is equivalent to a protocol of dividing the time evolution into small time intervals $\{t_i, t_i + \Delta\tau\}$, in which the density fully relaxes from $\rho_0[v_i]$ to $\rho_0[v_{i+1}]$ before relaxing towards the next density field, $\rho_0[v_{i+2}]$, etc.

The equilibrium two-particle density, $\rho_0^{(2)}$, was already almost encountered in the previous chapter: in equilibrium, Eq. (2.10) can be rewritten in terms of the density operator $\hat{\rho}$,

$$\rho_0^{(2)}(\mathbf{r}, \mathbf{r}') = \langle \hat{\rho}(\mathbf{r}) \hat{\rho}(\mathbf{r}') \rangle - \rho_0(\mathbf{r}) \delta(\mathbf{r} - \mathbf{r}'), \quad (2.13)$$

where the subscript “0” denotes the equilibrium state. Averages of the density operator have already been introduced as correlation functions obtained by functional differentiation of the grand potential functional in Eq. (1.12). Together with Eq. (1.16), Eq. (2.13) therefore reduces to

$$\rho_0^{(2)}(\mathbf{r}, \mathbf{r}') = H(\mathbf{r}, \mathbf{r}') - \rho_0(\mathbf{r}) \delta(\mathbf{r} - \mathbf{r}') + \rho_0(\mathbf{r}) \rho_0(\mathbf{r}'), \quad (2.14)$$

$$= \rho_0(\mathbf{r}) \rho_0(\mathbf{r}') [h(\mathbf{r}, \mathbf{r}') + 1]. \quad (2.15)$$

A more elegant expression of the integral in Eq. (2.12) is obtained by making use of

⁵The adiabatic approximation was originally suggested for the time evolution of the single-particle distribution function in a dense gas of hard spheres by Enskog [82] and later revised by van Beijeren and Ernst [274].

the following sum rule,

$$-\rho_0(\mathbf{r})\nabla c^{(1)}(\mathbf{r}) = \int d\mathbf{r}' \rho_0^{(2)}(\mathbf{r}, \mathbf{r}') \nabla \beta \phi(\mathbf{r}, \mathbf{r}'), \quad (2.16)$$

which connects the two-particle density $\rho_0^{(2)}$ with the effective one-body potential $\beta^{-1}c^{(1)}$, introduced in the previous chapter. This sum rule is obtained by solving Eq. (1.14) for $c^{(1)}$ and taking the gradient:

$$\nabla c^{(1)}(\mathbf{r}) = \rho_0(\mathbf{r})^{-1} \nabla \rho_0(\mathbf{r}) + \beta \nabla V(\mathbf{r}). \quad (2.17)$$

Equating this relation, which was first obtained by Lovett *et al.* [164], with the first equation of the well-known Yvon-Born-Green hierarchy [117],

$$\nabla \rho_0(\mathbf{r}) + \beta \rho_0(\mathbf{r}) \nabla V(\mathbf{r}) = -\beta \int d\mathbf{r}' \nabla \phi(\mathbf{r}, \mathbf{r}') \rho_0^{(2)}(\mathbf{r}, \mathbf{r}'), \quad (2.18)$$

leads to the sum rule, Eq. (2.16).

Up to a minus sign, the effective one-body potential $\beta^{-1}c^{(1)}$ is equal to the first functional derivative of the excess free energy functional $F_{\text{ex}}[\rho]$ with respect to density [cf. Eq. (1.13)]. Using eq. (2.16), we therefore rewrite Eq. (2.12) as

$$\Gamma^{-1} \dot{\rho}(\mathbf{r}, t) = \beta^{-1} \nabla^2 \rho(\mathbf{r}, t) + \nabla \cdot \left[\rho(\mathbf{r}, t) \nabla V(\mathbf{r}, t) + \rho(\mathbf{r}, t) \nabla \frac{\delta F_{\text{ex}}[\rho(\mathbf{r}, t)]}{\delta \rho} \right]. \quad (2.19)$$

By a simple check it turns out that also the two other terms on the right-hand side of Eq. (2.19) can be written as functional derivatives of the ideal [cf. Eq. (1.10)] and the external [cf. Eq. (1.9)] part of the total Helmholtz free energy, normalized by $\rho(\mathbf{r}, t)$, i.e.,

$$\beta^{-1} \nabla \rho(\mathbf{r}, t) = \rho(\mathbf{r}, t) \nabla \frac{\delta F_{\text{id}}[\rho(\mathbf{r}, t)]}{\delta \rho}, \quad (2.20)$$

$$\rho(\mathbf{r}, t) \nabla V(\mathbf{r}, t) = \rho(\mathbf{r}, t) \nabla \frac{\delta F_{\text{ext}}[\rho(\mathbf{r}, t)]}{\delta \rho}, \quad (2.21)$$

such that eq. (2.19) reduces to

$$\Gamma^{-1} \dot{\rho}(\mathbf{r}, t) = \nabla \cdot \left[\rho(\mathbf{r}, t) \nabla \frac{\delta F[\rho(\mathbf{r}, t)]}{\delta \rho} \right], \quad (2.22)$$

with

$$F[\rho] = \beta^{-1} \int d\mathbf{r} \rho(\mathbf{r}, t) [\ln(\rho(\mathbf{r}, t) \Lambda^D) - 1] + F_{\text{ex}}[\rho] + \int d\mathbf{r} \rho(\mathbf{r}, t) V(\mathbf{r}, t). \quad (2.23)$$

Eq. (2.22) constitutes the fundamental, nonlinear, deterministic equation for the time-evolution of the one-particle density $\rho(\mathbf{r}, t)$ and will be referred to as DDFE

equation henceforth. For time-independent external potentials $V(\mathbf{r})$, the DDFT describes the relaxation dynamics of the density field towards equilibrium at the minimum of the Helmholtz free energy functional $F[\rho_0]$, given an exact canonical excess free energy functional $F_{\text{ex}}[\rho]$. The path in the space of density fields is in general not the one of steepest descent, but is governed by the mass conservation constraint in Eq. (2.22) [179].

The DDFT equation had been suggested earlier on phenomenological grounds by Evans [85] and later by Dieterich *et al.* [68].⁶ However, MT were the first to derive the theory from the microscopic equations of motion and to make clear the contact to static DFT [179, 180]. Actually, very valuable similar attempts had been made by other authors before (Kirkpatrick *et al.* [142], Dean [61], and Kawasaki *et al.* [138, 139]), which turn out, however, to be wrong in confusing of the average density ρ with the density operator $\hat{\rho}$, which in turn leads to an additional noise term on the right-hand-side of Eq. (2.22) and therefore to an overcounting of fluctuations, given an accurate functional $F[\rho]$ (see also the discussions by MT [179], Archer and Rauscher [8], and Löwen [169]).

The DDFT is an approximate theory in several respects: the first and most fundamental approximation is the already introduced assumption of adiabatic relaxation dynamics. In practice, this approximation is most severe in dynamical processes that are fast compared to the diffusive time scales of the system. To our knowledge, this issue has been studied systematically to date only for weak perturbations of a hard-rod fluid in one dimension by Penna and Tarazona [217] (see also Subsection 2.2.3). The lack of systematic studies for more complex systems is understandable, because there is to date no exact functional $F_{\text{ex}}[\rho]$ for any other strongly interacting fluid. The use of approximate free energy functionals is the second fundamental approximation turning out to be severe in many applications (cf. Subsection 2.2.2 and see also the discussion in the previous chapter). Third, we did only consider systems in which hydrodynamic interactions between the particles play no role. The latter assumption can be approximately tackled by allowing for density-dependent mobility constants Γ [245], which is appropriate for long-wavelength fluctuations of the density field, or by taking hydrodynamic interactions on the Rotne-Prager (two-particle) level into account, as was recently demonstrated by Rex and Löwen [233]; this basically amounts to replacing the mobility constant Γ in the Langevin equations (2.1) through the Rotne-Prager diffusion tensor [198, 244].⁷ In the following subsections, we will discuss few of the consequences

⁶The same dynamical equation with the excess free energy functional of Ramakrishnan and Yussouff [119, 226] had been derived by Munakata [194, 195] and extended to non-spherical particles in the context of solvation dynamics by Calef and Wolynes [40], which was later reformulated by Chandra and Bagchi [48, 49]; these equations are referred to as Smoluchowski-Vlasov or *nonlinear diffusion* equations [194], as they are derived from a Vlasov equation [230] with a Fokker-Planck collision operator [194].

⁷The stochastic forces in equations (2.1) have to be modified accordingly; further, depending on the Itô or Stratonovich [96, 237] calculus to the delta-correlated noise, an additional drift term has to be included in the equations [84, 224, 237]. For the corresponding modified Smoluchowski equation, we refer the reader to references [67, 198, 224, 233].

of the use of approximate density functionals (Subsection 2.2.2) and of the adiabatic approximation (Subsection 2.2.3). In the latter subsection, we will also discuss a desirable modification of the DDFT to better account for the short-time dynamics.

2.2.2 Approximate density functionals in the DDFT

Three features of approximate density functionals are to be discussed here in short:

(i) As already extensively commented in the previous chapter, most density functionals, applied to highly correlated fluids, do not give their *exact* equilibrium properties, one famous exception being the grand canonical functional for hard rods in one dimension by Percus [219]. Typical density functionals are based on the first few of a whole hierarchy of correlation functions of the underlying homogeneous fluid; despite often stunning quantitative and qualitative agreement of theory and experiment/simulation, these correlation functions are approximate. As soon as large deviations from the homogeneous state towards highly modulated fluids due to strong external perturbations or due to crystalline ordering take place, density functional theory typically performs even worse. Having said this, the extent of qualitative and quantitative agreement between theory and simulation/experiment also in this highly nonlinear regime is often surprisingly good [168, 299, 300].

(ii) Typical density functionals display local minima in the space of density functions, which is reminiscent of their mean-field character in this respect. However, any exact functional should be convex in density space [38]. Famous examples for such minima are found around phase transitions, which become manifest, e.g., in overheated solids or undercooled liquids typically appearing as long-lived states in experiments and simulations. Employing such kind of density functionals in DDFT might lead to dynamical arrest for infinite time, depending on the initial configuration $\rho(\mathbf{r}, t = 0)$. This infinite arrest is unphysical, as in experiments the system should be able to escape thermodynamically unfavorable “metastable” states by fluctuations, e.g., nucleation. The time scale of this kind of relaxation might be large due to large entropic or energetic barriers compared to the time scale of the bare fluid, the Brownian time scale $\tau_B = \sigma^2\beta/\Gamma$, where σ is the microscopic length scale of the fluid; but for finite barriers the relaxation time should not be infinite. Many authors felt tempted to overcome this problem by imposing random noise on top of Eq. (2.22), but as already argued above, such an additional noise is not justified in the framework of DDFT. MT therefore suggested to simply interpret local minima of the DFT as long-lived states in a relaxation process and to restrict the theoretical analysis to short or intermediate time scales [179]. One way of circumventing the problem is gone by us in Chapter 6 for the specific example of crystallization from the undercooled melt; instead of studying homogeneous nucleation, which is not possible within the strict deterministic framework and with the density functional at hand, we offer a crystalline seed of few pinned particles, which are cut out from a rhombic crystal, to the undercooled melt and study the deterministic growth of the incipient “nucleus.” But also in this example care has to be taken, since the “long”

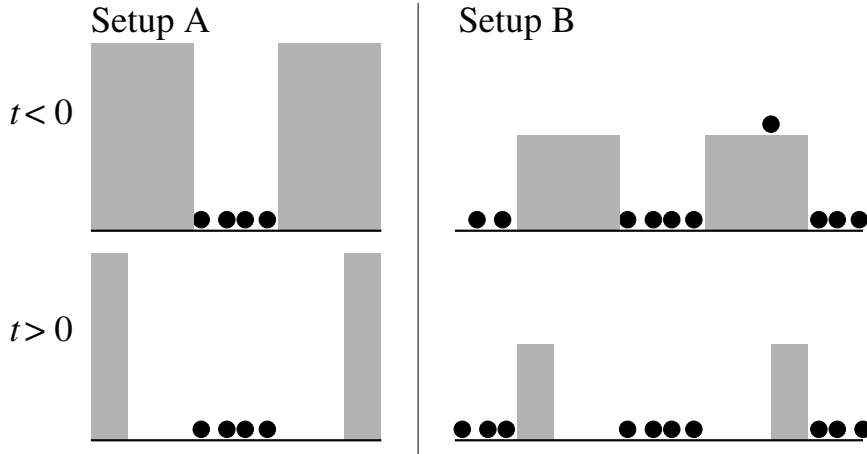


Figure 2.1: Left panel: cartoon of the relaxation dynamics of few hard rods in a closed, one-dimensional cavity after a sudden expansion of the cavity as studied by MT [179] (setup A). Right panel: cartoon of a similar “experiment” (setup B) with the only difference that the cavity walls are not infinitely high, but the particles inside the cavity are coupled to an infinite particle reservoir via high barriers, $\beta\Delta V \gg 1$.

relaxation time scale of the metastable, undercooled melt turns out to be relatively short in the two-dimensional system of dipolar particles under study. Therefore, the treatment of this specific problem with DDFT is only justified for a time window smaller than the mentioned relaxation time.

(iii) As already discussed in Subsection 1.6.3 of the previous chapter, density functionals are typically established in the grand canonical framework. In the DDFT, however, a canonical functional is needed, as the DDFT equation is a continuity equation for the density field. In their groundbreaking work, MT have attributed the failure of the DDFT to predict correctly the relaxation dynamics of few ($N = 8$) hard rods in a one-dimensional, suddenly expanded cavity (for a sketch, see the left panel in Fig. 2.1) mainly to the difference between the applied grand canonical functional and the desired canonical one [179]. In principle, this statement would be worth checking by either employing a more accurate functional, e.g., according to the perturbative scheme suggested by White *et al.* [293, 294], which was reviewed in Subsection 1.6.3, or by studying larger system sizes. For system sizes with particle numbers $N \gtrsim O(10)$, the difference between the functionals and therefore between the equilibrium densities obtained within the canonical or the grand canonical ensemble should disappear [293, 294]. We will come back to the different ensembles at the end of the following subsection.

2.2.3 The adiabatic approximation

The adiabatic approach of replacing the nonequilibrium, time-dependent two-particle density $\rho^{(2)}(\mathbf{r}, \mathbf{r}', t)$ by its equilibrium counterpart $\rho_0^{(2)}(\mathbf{r}, \mathbf{r}')$, evaluated at the same one-particle density $\rho_0(\mathbf{r}) = \rho(\mathbf{r}, t)$, as first suggested by Enskog [82], is an *ad hoc* approximation. The already mentioned systematic study of the relaxation dynamics of small-amplitude perturbations of a one-dimensional fluid of dense hard rods by Penna and Tarazona suggests that the DDFT is a theory that works well on large but transient time scales and for the so called *soft density modes* [217]; the latter are characterized by wave vectors, which are close to the peaks of the equilibrium static structure factor. These soft modes are decaying slowest, as the short-time evolution of a weakly modulated fluid is given by [10]

$$\beta\Gamma^{-1}\dot{\tilde{\rho}}(\mathbf{k}, t) = -k^2 \left[1 - \rho\tilde{c}_0^{(2)}(k) \right] \tilde{\rho}(\mathbf{k}, t), \quad (2.24)$$

where $\tilde{\rho}(\mathbf{k}, t)$ denotes the Fourier transform of the density field and the square bracket on the right hand side is exactly the inverse static structure factor [117]. With “large but transient time scales” Penna and Tarazona refer to a regime, in which the density modes still display the form of the soft modes and have not significantly given rise to the presence of other non-soft modes due to mode coupling in the general eq. (2.22). For many applications, such as the relaxation of a fluid after taking away a wall [75, 232] or crystal growth from a nucleation seed (see Subsection 2.2.4, Chapter 6), the dynamics are mainly governed by the soft modes making the DDFT a suitable tool to study this kind of problems. Still, despite the successful application to many colloidal problems, a systematic test of the adiabatic approximation also for different interaction potentials and in different spatial dimensions remains an open task.

The effect of the adiabatic approximation is expected to become more pronounced for fast relaxation processes of strongly modulated fluids. This was actually observed by MT for a fluid of few hard rods in an expanding cavity (as already cited at the end of the previous subsection and as sketched in Fig. 2.1) or exposed to a periodic, sinusoidal potential [179]. However, they attributed the faster relaxation of the DDFT as compared to BD simulations mainly to the use of the (wrong) grand canonical functional in the DDFT; their argument was the following: in the grand canonical ensemble, the system can relax much faster due to particle exchange with a particle reservoir, whereas in the canonical description it can only do so with the fixed number of particles within the same volume. Let us assume that this argument holds, i.e., that a canonical functional would indeed lead to a better agreement of theoretical and simulation results (this has not been studied so far but would be feasible applying the perturbative scheme by White *et al.* [293, 294], as already commented above). Now, we modify the “experimental setup” of MT, referred to as setup A, by coupling the few particles within the cavity to an infinite particle reservoir through a small “channel of particle exchange” (i.e., separated not by an

infinitely large but only by a *very* large potential barrier, $\beta\Delta V \gg 1$), which we refer to as setup B. Both setups are cartooned in Fig. 2.1. Let us also assume that the number of particles within the cavity in setup B is strictly the same as the one in setup A at $t = 0$, e.g., by applying a deep external potential well for each of the N particles at times $t < 0$, which is turned off at $t = 0$.⁸ Then, it is expected that the dynamics of the density within the cavity, obtained from BD simulations, would be the same for both setups for times smaller than the inverse Kramers rate [147], $\rho_A(x, t) = \rho_B(x, t)$, $0 \leq x \leq L_>$, $t/\tau_B \ll \exp[\beta\Delta V]$, with $L_>$ the width of the cavity after the expansion. On the contrary, clearly, the DDFT results would still differ due to the different functionals for small or infinite particle numbers.

We have made this gedankenexperiment, which would be interesting to study by DDFT and computer simulation *in real*, in order to point out that on short or intermediate time scales a system might be better described as an assembly of effectively closed subsystems, which are treated by means of canonical functionals with few numbers of particles each, and allow for particle exchange between the subsystems only for long times.⁹ So far, this is a very preliminary idea and we can only claim few properties of the local length scale $\lambda(\mathbf{r})$ defining the size of the isolated domains around the position vector \mathbf{r} : $\lambda(\mathbf{r})$ should inversely depend on the rate of density change $\dot{\rho}(\mathbf{r}, t)$, rendering it infinite in equilibrium, and it should grow with increasing diffusion constant Γ/β . Since both quantities are equal to the only characteristic rates in the bulk system (up to some power of a microscopic scale σ , which we regard as the unit length in this subsection), they can only appear as a ratio, i.e., $\lambda(\mathbf{r}, t) \propto f(\beta\Gamma^{-1}\dot{\rho}(\mathbf{r}, t))$. The mobility Γ should eventually be renormalized by a Kramers rate accounting for diffusion limiting energy barriers within the domain of radius λ around the vector \mathbf{r} , which is still the weak point of the idea. A translation of this idea to a proper functional or an additional drift term in the DDFT equation is still missing. However, the approach by White *et al.* [293, 294] describing corrections to the functional through *global* particle number fluctuations might be transferable to a *local* formulation. Note that the dependence of λ on $\dot{\rho}$ turns the DDFT equation nonlinear in time, which could be interpreted as reminiscent of a memory.

2.2.4 Crystal growth and melting

Irrespective of the approximations discussed in the previous subsections, the DDFT is a fully microscopic theory; it is therefore highly qualified for the study of relaxation processes of those colloidal systems for which a good density functional is at hand. One class of systems for which this is certainly the case are colloidal crystals in the

⁸The same external potential should then also be applied in setup A to render the initial density fields equal within the cavity, $\rho_A(x, 0) = \rho_B(x, 0)$, $0 \leq x \leq L_<$, with $L_<$ the width of the cavity before the expansion.

⁹The notion “effective subsystems” denotes an effective number of particles $N(\mathbf{r}, t, \dot{\rho}(\mathbf{r}); [\rho])$, attributed to every point \mathbf{r} at time t .

bulk, in cavities, on walls, or in contact with coexisting liquids [165, 167, 168, 299] (see also the previous chapter and references therein, as well as Chapters 3-7; for further applications of the DDFT, see the next subsection). A study of colloidal crystal growth, melting, or reorganization of the crystal's internal structure, including defect and grain boundary relaxation, with the DDFT is therefore in principle straightforward;¹⁰ this holds in particular because the relevant density modes during the time evolution are typically the aforementioned soft modes, for which the theory has proved to work very well [217] (cf. the previous subsection). However, apart from a stability analysis of undercooled melts towards infinite, periodic density modulations by Bagchi already in 1987 [18] and our work on melting of bulk crystals (Chapter 5) and crystal growth from a small, incipient cluster of crystalline particles (Chapter 6), which are all based on the approximation to the DFT by Ramakrishnan and Yussouff (see previous chapter), there has been no attempt so far to study the diverse problems by means of DDFT, which is still the only fully microscopic, dynamical theory at hand to date.

The reason for the lack of further systematic studies and the restriction to more coarse-grained and phenomenological approaches is basically twofold: first, it is only clear since the work of MT [179] that the DDFT equation (2.22) constitutes a dynamical theory derivable from microscopic grounds, i.e., from the Langevin equations of motion. And second, the computational effort to solving the nonlinear DDFT equation with a nontrivial functional $F_{\text{ex}}[\rho]$ for a translational and rotational symmetry breaking density field, which in turn is furthermore highly modulated and extended over many lattice sites, is immense and only accomplishable with nowadays fast computer technology; even today, studying the time evolution of density fields on large length and time scales is a challenging problem (cf. Chapter 6). Therefore, many research groups concerned with the dynamics of crystals, e.g., the groups around Oxtoby [19, 214], Harrowell [296], Gránásy [105], and Grant [78], have focused on more coarse-grained equations.

In fact, the latter can partly be “derived” from DDFT by further approximations of the still unspecified functional $F_{\text{ex}}[\rho]$ (typically, $F_{\text{id}}[\rho] + F_{\text{ex}}[\rho]$ is reduced to a Cahn-Hilliard function of the local field and its gradient [37]) and by making reasonable assumptions about the modulation and time evolution of the density field, which are then justified *a posteriori*. E.g., by setting the density in front of the functional derivative *ad hoc* to be uniform, the DDFT can be transformed to deterministic Cahn-Hilliard theories [37] for conserved order parameter fields, which are commonly described as “Model B” dynamics in the Halperin and Hohenberg classification scheme [44, 128]; Cahn-Hilliard models are extensively used to study the dynamics of crystals, either on the basis of the average densities of the two coexisting phases within simple *phase field* models [80, 295] or in the context of so-called *phase field crystal* (PFC) models [17, 25, 77, 78], which take into account density oscillations in the crystalline phase on the particle scale, similarly to the DDFT. As

¹⁰For recent reviews on colloidal crystals and their dynamics see, e.g., references [5, 215, 304].

in the literature on the DDFT and its derivatives or predecessors, noise on top of Eq. (2.22) is often included leading to an overcounting of fluctuations for free energy functionals derived from DFT. In principle, by making rather crude approximations or strong assumptions, the DDFT can also be related to “Model A” (time-dependent Ginzburg-Landau theories for non-conserved fields) or “Model C” (two equations for one conserved and one non-conserved field) dynamical equations [44, 128], which are both also widely used for the study of crystal growth [214, 259, 296, 303].

The challenge in treating colloidal crystal dynamics is the nontrivial coupling of a conserved and a non-conserved order parameter, the locally averaged, coarse-grained density and the local crystalline structure, where the latter is typically not simply quantifiable by a single scalar parameter, which renders the description even more complicated. Therefore, to account for the many qualitatively different relaxation processes possible, the problem can either be treated by a multi-variable, coarse-grained description in the form of a “Model C”-dynamics [296, 303] or by means of a microscopic, density-resolved theory, the DDFT or the PFC model [78]. The former “Model C”-approaches have the advantage that all appearing mobilities can be tuned by the respective model-variables; however, this goes at the expense of rather complicated models. The latter, DDFT and PFC models, have the advantage of predicting all dynamical properties of the crystal based on few parameters in the density functional or in the phase field function. Actually, the DDFT does not have any parameter as an input, and also the PFC models can be related to density functionals; however, some freedom in the choice of how to extract the model parameters remains. Consequently, the mobilities, which are an outcome of the respective theory, constitute also a test of the same. The PFC model is based on a very approximate free energy function, whereas the DDFT may be based on highly accurate density functionals. A test of the approximate PFC models with the in general more accurate DDFT is therefore on order. In fact, a direct comparison of the crystal front propagation velocities obtained from the phase field crystal model and from the DDFT is the subject of current work [278] (see also Section 5.5).

In this work, we restrict our analysis to the problems of crystal melting (Chapters 5, 6), growth (Chapter 6), and to the local relaxation of affinely and nonaffinely strained and compressed crystallites (Chapter 6). In future work, it would be highly desirable to extend these studies to the relaxation of defects, e.g., after the mutual convergence of two crystalline domains with different orientations (cf. a study on defects based on the PFC model by Berry *et al.* [26]). Further, a study of the relaxation dynamics of crystals in confinement and on walls would be of uttermost interest (cf. Chapter 7).

Crystal growth typically sets in only after homogeneous or heterogeneous nucleation [15, 104, 105, 246, 257]. Both of these phenomena have been studied with so called *non-classical* nucleation theories based on DFT [98, 133, 134, 211, 212, 268], determining the size and shape of “critical nuclei” and possible nucleation pathways. As discussed in Subsection 1.6.1, the fluctuations needed to drive a system from the undercooled melt into the thermodynamically stable solid phase, are typi-

cally not accounted for by approximate density functional approaches. In this work, we therefore restrict our dynamical studies to relaxation processes, which proceed spontaneously in the DDFT.

2.2.5 Further applications and extensions

In this final subsection, we give a short overview, to what kind of practical problems the DDFT has successfully been applied and what extensions have been made in order to account for problems including hydrodynamic interactions, orientational degrees of freedom, or inertia. In recent years, the number of applications and extensions has rapidly increased; still, as the theory is relatively young, the following short account should give a broad, if not complete, overview of the field.

First, the DDFT was successfully tested for isotropic particles in stationary external potentials [75, 179, 180]—more precisely speaking, after a sudden quench at $t = 0$ from $V(\mathbf{r}, t < 0)$ to $V(\mathbf{r}, t > 0)$. Later, the theory was also applied to driven systems in the steady state [216] or with oscillating (in time) external potentials [227, 232]. Physical problems under study comprise the mentioned relaxation dynamics in oscillating [232] or suddenly expanding [75, 179] cavities, spinodal decomposition [10], sedimentation [245], instabilities in laning phenomena [45, 46], binary phase separation [9], steady states in traveling wave fields [234], and crystal growth (cf. the previous subsection and Chapter 6). Also, glassy dynamics has been addressed via the test-particle approach [11], however, on quite phenomenological grounds. For these problems, different functionals were used ranging from the mean-field [9, 11, 75, 232], via the Ramakrishnan-Yussouff [10, 179] and weighted density approximation [179] to the fundamental measure [233, 245] and Percus [179] functionals, which were all introduced in the previous chapter (except the Percus functional, commented on in Subsection 2.2.2). In all of these approaches, it turned out that the accuracy of the dynamics is directly governed by the accuracy of the underlying free energy functional.

The theory has recently been extended in several ways: first, it was generalized to non-spherical rodlike particles with orientational degrees of freedom by Rex *et al.* [235]¹¹ which amounts to derive a DDFT on the basis of a Fokker-Planck equation for rodlike particles, the so-called Smoluchowski-Perrin equation [67, 72, 220]. For the overdamped dynamics of rods, also non-conservative forces driving the rods in the direction of their own orientation were included in the theory [290], which is the many-body description of a model similar to the “Brownian circle swimmers” studied in Chapter 8 and introduced in the next section. Second, hydrodynamic interactions have been approximately included in the theory [233, 245] (cf. the discussion at the end of Subsection 2.2.1). Third, the most fundamental extension was proposed by

¹¹A similar dynamical density functional theory approach was proposed by Chandra and Bagchi [48, 49] on a phenomenological basis. There, the explicit coupling between orientational and translational diffusion was neglected. Further, a similar model with discrete orientations for platelike particles was suggested by Bier *et al.* [28].

MT [181] and Marini Bettolo Marconi and Melchionna [178] to account for non-overdamped fluids, where inertia plays a crucial role, i.e., not only a one-particle density but also a one-particle current has to be kept track of.¹² Their approach is based on the many body Kramers equation (the equivalent of the Smoluchowski equation, but with inertia [96, 237]) and a multiple time scale analysis.

All of the works cited her, including our own work on crystal relaxation, and also including the extensions to hydrodynamic interactions and to rotational degrees of freedom, describe the dynamics under study astonishingly well. In particular, the time evolution of the soft modes on intermediate times seems to be very accurately taken into account by the theory rendering it most appealing for many applications yet to come.

2.3 Nonequilibrium rate theory for a Brownian swimmer

In the previous section, we were interested in the collective motion of highly correlated fluids, for which the difficulty of the theoretical description was mainly due to the strong correlations among the particles. Now we turn our interest to the motion of a *single* particle in two dimensions, which is *only* interacting with the solvent and an external potential; at first sight, this seems to be a very simple special case of the problems studied above. However, what complicates the model and makes it distinctly different from the problems studied so far, are some novel aspects: first, the particle under study is a rod, i.e., it has an internal orientation ϕ , which is coupled to the translation of its center-of-mass vector \mathbf{r} via anisotropic mobility coefficients rendering even the bare Smoluchowski-Perrin (SP) equation [67, 72, 196, 220] without drift term [Eq. (2.30) with $\mathbf{a}_\alpha = 0$] nonlinear. Second, the particle is permanently driven out of equilibrium by an internal motor, i.e., the particle is *self-propelled*; we therefore refer to the particle as a “swimmer”. The swimming mechanism is represented by an effective, constant force F along the rod orientation and an effective, constant torque M acting on the orientation ϕ (see the left panel of Fig. 2.2). Due to the self-propulsion, the “free” swimmer performs on average a circular motion with a radius $R \propto F/M$.¹³ And third, the swimmer is confined to a narrow, linear channel in the y -direction, which, together with the inherent circular motion, offers two metastable *sliding modes* along either of the channel walls, i.e., the swimmer is trapped in one of two metastable states with constant x - and ϕ -coordinate (cf. the right panel of Fig. 2.2). Since the confining potential renders turning events rare in the low-noise regime, the system can effectively be mapped to a one-dimensional random walk with a typical step length determined by the velocity along the channel,

¹²Earlier, Archer made an attempt to develop a DDFT for atomic liquids based on Newton’s equations of motion [7].

¹³A different model for self-propelled, circular motion in terms of a damped Langevin equation with Rayleigh-friction [256] was recently suggested by Haeggqwist *et al.* [110].

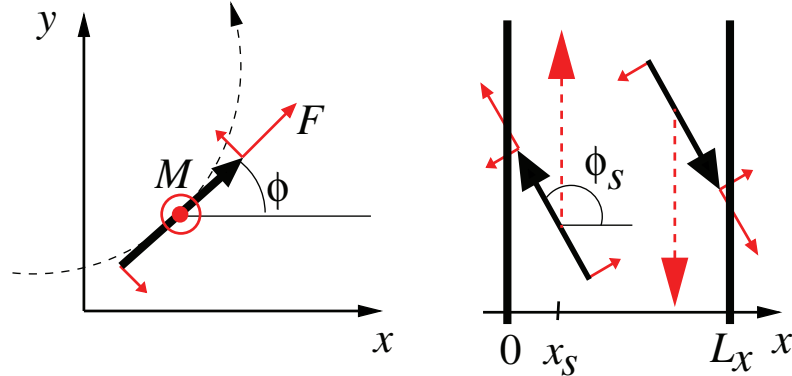


Figure 2.2: Left panel: sketch of the “free” rodlike swimmer in the (x, y) -plane. Indicated are the effective torque M (here, $M > 0$) and the effective force F driving the particle to perform on average a circular motion along the dashed curve (for a sample trajectory from computer simulations see the upper right inset of Fig. 8.1). Right panel: the two metastable sliding modes of the same swimmer along the walls of a confining channel of width L_x , characterized by the x, ϕ -coordinates (x_s, ϕ_s) and $(L_x - x_s, \phi_s + \pi)$, respectively. The dashed arrows indicate the directions of the sliding motion.

i.e., in the y -direction, and by the turning rate γ (for a more detailed characterization of the model features see further down and Chapter 8).

All of these features can be studied by explicitly, i.e., numerically, solving the corresponding non-linear SP equation, similarly to the DDFT for an ensemble of swimmers, suggested by Wensink and Löwen [290];¹⁴ however, because we are in particular interested in the rare events of hopping between the up- and downward motion along the channel, we found it more appropriate to approach the search for the long-time diffusive behavior through a nonequilibrium rate theory valid in the small-noise regime, which is based on Kramers’ *flux-over-population* approach to escape rates in single-variable, equilibrium systems [116, 147]. Rate theories for multi-dimensional and time-dependent problems, which in general violate detailed balance, have been established by several authors, e.g., by Lehmann *et al.* [152–154] and Maier and Stein [177] for oscillating (in time) energy barriers, and also by Maier and Stein [173, 174] for general, non-conservative, but time-independent forces. The work by Lehmann *et al.* [152–154] in turn is based on a functional integral approach to the Fokker-Planck equation, which was first suggested by Onsager and Machlup [206] and later related to the Kramers problem, e.g., by Caroli *et al.* [42] and Weiss [289]. Many other works, including the references by Maier and Stein [171, 173, 174, 176, 177, 197, 255], referred to as *systematic asymptotic expansions*, are based on

¹⁴In reference [290], the rods only experience a force $F\hat{\mathbf{u}}$ along the rod orientation, but no torque M .

a WKB treatment of the Smoluchowski equation, as suggested by Caroli *et al.* [41, 43, 103]. Since we are in Chapter 8 only concerned with the rate determining, exponential Arrhenius factor (see further down),¹⁵ we are free to choose one of the approaches, and we will choose, for convenience, the functional integral approach to a flux-over-population rate.¹⁶

The swimmer under study is far from equilibrium due to its own driving or propulsion mechanism; this gives rise to important effects, such as the mentioned metastability of the sliding modes, which are strictly absent in the corresponding equilibrium system without internal driving; these modes are referred to as *attractors* in the language of rate theories [116]. Different to the nonequilibrium rate theories of Lehmann *et al.* and Maier *et al.* [154, 174] the system under study experiences not only state-dependent, non-conservative—however, time-independent—forces, but also a state-dependent (i.e., ϕ -dependent) mobility matrix, which is a manifestation of the translation-rotation coupling of the bare rod without driving (see further down), and makes the treatment in principle even more complicated. Therefore, as for most multi-dimensional, nonequilibrium problems, the exact escape rates of the swimmer under study need to be evaluated with the help of computer simulations (see Chapter 8).¹⁷

As we do *not* employ a full rate theory in Chapter 8, but instead concentrate on the rate determining, exponential Arrhenius factor, we restrict this introductory section to the derivation of the same factor, however, starting from the exact definition of the Kramers escape rate within the flux-over-population approach and commenting on the relevant approximations made. For detailed derivations of rate theories in equilibrium we refer the reader to excellent textbooks [96, 103, 237, 276], and for nonequilibrium approaches to recent reviews by Hänggi *et al.* [116] and Pollak and Talkner [223], and to the mentioned work by Lehmann *et al.* [152–154] and Maier *et al.* [173, 174, 176, 177]. We embed the derivation of the rate determining Arrhenius factor into the exposure of the specific dynamics of a Brownian, rodlike swimmer in two dimensions. We will therefore start from the Langevin equations and the corresponding Smoluchowski-Perrin equation in Subsection 2.3.1. Subsequently, we motivate and define the flux-over-population escape rate in Subsections 2.3.2 and 2.3.3, and we introduce the necessary probability distribution function as a path integral over the Onsager-Machlup action in Subsection 2.3.4. In Subsection 2.3.5, we introduce an approximation to the rate theory for the swimmer under study, and in the final Subsection 2.3.6 we discuss few points concerning rate theories of non-Hamiltonian systems in general and applied to the particular model system.

¹⁵On the deviations from Arrhenius scaling for non-Hamiltonian systems see, e.g., refs. [175, 176].

¹⁶In order to obtain kinetic prefactors, however, the WKB approach seems to be more appropriate for non-Hamiltonian processes with a continuous symmetry in time [152, 176].

¹⁷In Chapter 8, we perform simple Brownian dynamics simulations, which suffice to obtain accurate data for the desired long-time diffusion constants in the temperature-regime considered. For lower temperatures or different models, however, more refined algorithms, such as *transition path sampling* methods [62], are needed.

2.3.1 The Langevin and the Smoluchowski-Perrin equations for a self-propelled rod

Although we will derive the functional integral formalism from the SP equation, we start again, as in the previous section, with the Langevin equations of motion, in order to see which different forces drive the rodlike swimmer under study. For reasons that will become clear shortly, we write the Langevin equations in a slightly different way as compared to their form in Eq. (2.1) or in Chapter 8 [cf. Eqs. (8.1) and (8.2)]. Introducing the $(2 + 1)$ -dimensional “super vector” $\mathbf{q} = (x, y, \phi)$, the motion of the two-dimensional center-of-mass vector $\mathbf{r}(t) = (x(t), y(t))$ and the orientation $\phi(t)$, which we let run *ad infinitum*, i.e., $-\infty < \phi < \infty$, are given by

$$\dot{\mathbf{q}}_\alpha = \mathbf{a}_\alpha(\mathbf{q}) + \beta^{-1/2} \mathbf{B}_{\alpha\beta}(\phi) \xi_\beta, \quad (2.25)$$

where we employ the Einstein summation convention for Greek indices $\alpha, \beta \in \{x, y, \phi\}$. Here and in the following we use sans-serif letters to represent $(2 + 1)$ -dimensional super vectors (lowercase letters) and $(2 + 1) \times (2 + 1)$ -super matrices (uppercase letters), where letters with or without indices represent a vector/matrix component or the whole object, respectively. The $\mathbf{a}_\alpha(\mathbf{q})$ are the yet to be specified drift coefficients; they will be shortly given in terms of the self-propelling force and torque, and the external potential. $\mathbf{B}_{\alpha\beta}(\phi)$ is the matrix square root of the symmetric, block-diagonal, and ϕ -dependent mobility matrix, i.e.,

$$\mathbf{B}_{\alpha\kappa}(\phi) \mathbf{B}_{\kappa\beta}(\phi) = \Gamma_{\alpha\beta}(\phi), \quad (2.26)$$

which itself is given by [67]

$$\Gamma(\phi) = \beta \left(\begin{array}{c|c} \frac{D_{\parallel}(\hat{\mathbf{u}} \otimes \hat{\mathbf{u}}) + D_{\perp}(\mathbf{I} - \hat{\mathbf{u}} \otimes \hat{\mathbf{u}})}{0} & 0 \\ \hline & D_r \end{array} \right). \quad (2.27)$$

Here, D_{\parallel} and D_{\perp} are the short time longitudinal and transverse translational diffusion constants, $\hat{\mathbf{u}} = (\cos \phi, \sin \phi)$ is the orientation vector, \mathbf{I} the 2×2 -unit tensor, \otimes a dyadic product, and D_r the short time rotational diffusion constant; therefore, the temperature-normalized mobilities $\beta^{-1} \Gamma_{\alpha\beta}$ are also referred to as diffusion coefficients. Note that in the previous section on DDFT we always assumed $\Gamma_{\alpha\beta} = \Gamma \delta_{\alpha\beta}$, where $\delta_{\alpha\beta}$ is the Kronecker delta. The Gaussian random variables fulfill

$$\overline{\xi_\alpha(t)} = 0, \quad \overline{\xi_\alpha(t) \xi_\beta(t')} = 2\delta_{\alpha\beta} \delta(t - t'). \quad (2.28)$$

Since $\mathbf{B}_{\alpha\beta}$ is block-diagonal (as $\Gamma_{\alpha\beta}$), and only the “upper left” block depends on ϕ but not on x or y , whereas $\mathbf{B}_{33} = D_r^{1/2}$ is completely independent of \mathbf{q} , the Itô and Stratonovich calculus to the noise are equivalent in this case, which can also be understood by regarding the motion in the coordinate system of the rod, in

which the diffusion coefficients are state-independent (see also the correspondingly formulated Langevin equations in Chapter 8).¹⁸ The drift coefficients are given by

$$\mathbf{a}_\alpha(\mathbf{q}) = \Gamma_{\alpha\beta}(\phi) [\mathbf{m}_\beta(\phi) - \partial_\beta V(\mathbf{q})] . \quad (2.29)$$

Here, $\mathbf{m}(\phi) = (F\hat{\mathbf{u}}, M)$ is the combined constant *effective* force $F\hat{\mathbf{u}}$, which represents the propulsion mechanism responsible for the deterministic motion in the rod orientation, and the constant *effective* torque M yielding the deterministic circular motion (see sketch in Fig. 8.1).¹⁹ $V(\mathbf{q})$ is an external confining potential, which is characterized more specifically in the next subsection. The Langevin equations (2.25) correspond to a SP equation for the single-particle probability density $W(\mathbf{q}, t)$ [67, 72, 220],

$$\dot{W}(\mathbf{q}, t) = \mathcal{L}_{\text{SP}} W(\mathbf{q}, t) , \quad (2.30)$$

$$\mathcal{L}_{\text{SP}} = -\partial_\alpha \mathbf{a}_\alpha(\mathbf{q}) + \beta^{-1} \Gamma_{\alpha\beta}(\phi) \partial_\alpha \partial_\beta , \quad (2.31)$$

which was first introduced by Perrin [220] for the special case of $\mathbf{a}_\alpha = 0$ and also in three spatial dimensions. Similar to Eq. (2.7) we introduced the SP operator \mathcal{L}_{SP} . Now, it is also clear why we chose the different notation for the Langevin equations; the drift and diffusion coefficients appear explicitly in the SP equation.²⁰

In Chapter 8, we first consider the “free” swimmer, i.e., the case $V(\mathbf{q}) = 0$. Even in this simpler case the SP equation is nonlinear due to the ϕ -dependence of $\Gamma_{\alpha\beta}(\phi)$, which makes an analytical treatment difficult. Recently, Munk *et al.* [196] have given the exact solution of the SP equation in two dimensions with the further constraint $F = M = 0$, i.e., for vanishing drift coefficients. In three dimensions, the equation had been solved by Aragón and Pecora [6] on the same level of simplification. Instead of solving the SP equation for the whole probability distribution $W(\mathbf{q}, t) = P(\mathbf{q}, t | \mathbf{q}_0, 0)$ also for the more general case, $F \neq 0, M \neq 0$, we restrict ourselves to its first and second moments, $\mathbf{r}(t), \mathbf{r}^2(t), \phi(t), \phi^2(t)$, which we obtain exactly by integration and a subsequent noise average of the Langevin equations (2.25); the explicit results are given in Eq. (8.9) of Chapter 8 (see also Fig. 8.1).²¹

2.3.2 Hopping between the sliding modes

With an additional, arbitrary potential $V(\mathbf{q})$ applied, exact analytical integration and averaging of the Langevin equations or the Smoluchowski equation for long times

¹⁸In the computer simulations of Chapter 8, we will employ the Ermak algorithm of Eq. (2.5), which is equivalent to the Itô convention.

¹⁹Both, F and M , can be regarded as representing an internal motor at one of the rod’s tips, which is tilted with respect to the rod orientation.

²⁰The drift and diffusion coefficients are the first and second coefficients of the Kramers-Moyal expansion, mentioned earlier [96, 237].

²¹For the simpler case, $F \neq 0, M = 0$, Han *et al.* [115] have also calculated the first few moments of the probability distribution $P(\mathbf{q}, t | \mathbf{q}_0, 0)$.

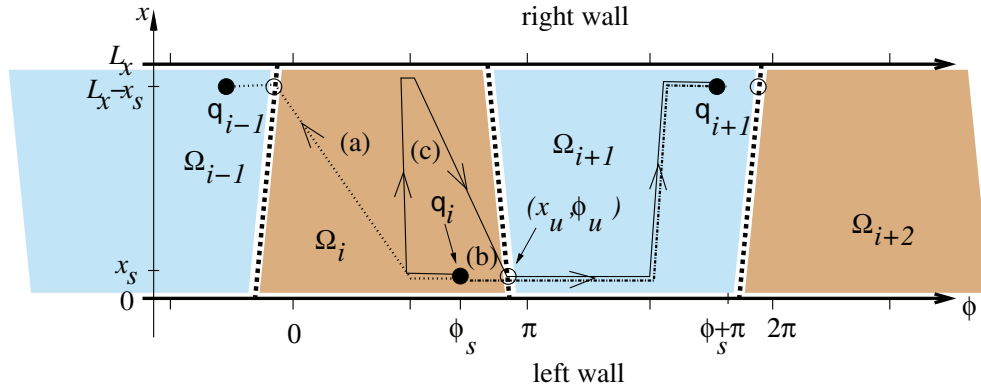


Figure 2.3: Sketch of the (x, ϕ) -plane of the phase space for a swimmer with positive torque $M > 0$. The thick dashed lines denote the separatrices between the domains of attraction. The attractors are marked by filled and the saddles by open circles. The three minimum action paths out of basin i , (a), (b), (c), are indicated schematically by dotted (a), dashed-dotted (b), and solid (c) lines with the arrows indicating the direction of motion (for the trajectories in \mathbf{r} -space see Fig. 8.4).

t is in general impossible. In Chapter 8, we will be concerned with a special external potential, modeling a narrow, infinite, confining channel in the y -direction of width L_x [cf. Eq. (8.11), Figs. 2.3 and 8.2]. The exact form of $V(x, \phi)$ is not needed here; only three characteristics are of importance for the further reasoning: first, $V(x, \phi)$ is independent of y (and time t). Second, $V(x, \phi)$ is symmetric in x about the middle of the channel, situated at $L_x/2$, i.e., $V(x, \phi) = V(L_x - x, \phi)$. And third, depending on the sign of the internal torque M and on the ratio of F/M , the x - and ϕ -coordinates are most of the time fluctuating closely around two symmetric, metastable, and well separated configurations, the attractors $\mathbf{q}_1 = (x_s, y, \phi_s)$ and $\mathbf{q}_2 = (L_x - x_s, y', \phi_s + \pi)$ close to either of the two channel walls, which correspond to the sliding modes in the positive or negative y -direction (see right panel of Fig. 2.2); the values of the respective y -coordinates are growing or shrinking linearly in time, $y \propto (M/|M|)t$ and $y' \propto -(M/|M|)t$, depending on the channel wall and on the sign of the torque M (see Eqs. (8.12), (8.13) for the values of x_s and ϕ_s , which are not important here). To be more precise, the notion that this problem has only two attractors stems from the periodicity of the angle ϕ . If one, however, lets ϕ run from $-\infty$ to $+\infty$, as we do, one gets a set of infinitely many attractors \mathbf{q}_i , of which every other is situated close to the “left” wall ($x = x_s$) and every other close to the “right” wall ($x = L_x - x_s$), i.e., $\mathbf{q}_i = (x_s, y, \phi_s + (i - 1)\pi)$ if i is odd, and $\mathbf{q}_i = (L_x - x_s, y', \phi_s + (i - 1)\pi)$ if i is even. Note that the attractors on either wall $\{\mathbf{q}_i, \mathbf{q}_{i+2}, \dots\}$ are all physically equivalent as they only differ in the angle ϕ by a multiple of 2π . The position of the attractors and the boundaries of the basins of attractions in the (x, ϕ) -plane are sketched in Fig. 2.3.

Hopping between the sliding modes is equivalent to turning by an angle $\Delta\phi =$

$\pm\pi$, and in the limit of small thermal fluctuations the hopping/turning rate γ is proportional to the long-time diffusion constant $D_L \propto \gamma$, which is the quantity of our main interest. The hopping rate γ is equal to the escape rate from the phase space *basin of attraction* around \mathbf{q}_i (basin i , occupying the phase space volume Ω_i) into one of the two neighboring basins of attraction around $\mathbf{q}_{j=i\pm 1}$ (basin j , with phase space volume Ω_j). Here, the basin of attraction i with volume Ω_i is defined by all points $\mathbf{q} \in \Omega_i$, from which the particle would deterministically, i.e., for $\beta^{-1} = 0$, move to the attractor \mathbf{q}_i . Every pair of basins i , $i \pm 1$, is separated by a common boundary $\partial\Omega_{i,i\pm 1}$, on which the particle is indifferent to move into either of the two neighboring basins. The whole boundary of basin i , comprising $\partial\Omega_{i,i-1}$ and $\partial\Omega_{i,i+1}$, which we denote as $\partial\Omega_i$, is referred to as *separatrix* [116].

2.3.3 The escape rate

In the present and the following subsection, we sketch a way of how to obtain an escape rate γ for the problem under study, which is, however, formulated very generally and in principle applicable to many different problems. Following Lehmann *et al.* [154], to quantify the rate γ we introduce the population $P_{\Omega_i}(t)$,

$$P_{\Omega_i}(t) \equiv \int_{\Omega_i} d^3\mathbf{q} P(\mathbf{q}, t | \mathbf{q}_i, 0), \quad (2.32)$$

which is equal to the average number of particles in the basin i at time t , given the particle was at \mathbf{q}_i at $t = 0$.²² Under the assumption of weak noise, i.e., small temperatures β^{-1} , the conditional probability distribution $P(\mathbf{q}', t | \mathbf{q}_i, 0)$, which had already been introduced in Subsection 2.1, reaches a quasi-equilibrium profile in the x - and ϕ -directions shortly after $t = 0$ on a time scale larger than τ_B^* , which is equal to the maximum Brownian diffusion time to “test” the bottom of the basin i (again, in the x - and ϕ -directions) and is assumed to be short with respect to the inverse escape rate.²³ The instantaneous escape rate $\gamma(t)$ is then given by the relative decrease of the population per unit time,

$$\gamma(t) = -\dot{P}_{\Omega_i}(t)/P_{\Omega_i}(t). \quad (2.33)$$

For short, but intermediate times, $\tau_B^* \ll t \ll \gamma^{-1}$, when the probability of finding the particle in basin i is still large, the instantaneous escape rate is independent of time and equal to the desired turning rate γ .²⁴ Assuming therefore $P_{\Omega_i}(t) = 1$ in the denominator of Eq. (2.33), using the SP equation (2.30) and Gauss’s theorem, Eq. (2.33) can be rewritten as a surface integral over the separatrix $\partial\Omega_i$,

$$\gamma(t) = \beta^{-1} \int_{\partial\Omega_i} dS_{\mathbf{q}} \mathbf{n}_{\alpha}(\mathbf{q}) \Gamma_{\alpha\beta}(\phi) \partial_{\beta} P(\mathbf{q}, t | \mathbf{q}_i, 0), \quad (2.34)$$

²²As $P_{\Omega_i}(t = 0) = 1$ it follows that $P_{\Omega_i}(t > 0) \leq 1$.

²³Note that the distribution does not reach a steady state or even quasi equilibrium in the y -direction, as the channel is infinitely long.

²⁴The demand $t \ll \gamma^{-1}$ is to be regarded as a check of consistency.

where $dS_{\mathbf{q}}$ and $\mathbf{n}(\mathbf{q})$ are an infinitesimal surface element and the outer normal unit vector on the separatrix at the point \mathbf{q} . The next step is to obtain an expression for the probability distribution $P(\mathbf{q}, t|\mathbf{q}_i, 0)$ via a functional integral over all possible paths of getting from \mathbf{q}_i at time $t = 0$ to \mathbf{q} at time t .

2.3.4 The probability distribution

Finding the probability distribution $P(\mathbf{q}, t|\mathbf{q}_i, 0)$ is pursued by first solving the SP equation for short times, and afterwards iteratively exploiting the Chapman-Kolmogorov relation for Markov processes [237] in order to decompose the full probability into a sum over products of short-time probabilities. Up to corrections of the order Δt^2 the short time solution of the SP equation (2.30) can be written as

$$P(\mathbf{q}, t + \Delta t|\mathbf{q}', t) = [1 + \mathcal{L}_{\text{SP}}(\mathbf{q}', t)\Delta t] \delta(\mathbf{q} - \mathbf{q}') = \exp[\mathcal{L}_{\text{SP}}(\mathbf{q}', t)\Delta t] \delta(\mathbf{q} - \mathbf{q}') . \quad (2.35)$$

Upon insertion of the SP operator (2.31) and using the Fourier representation of the δ function, this reduces to a Gaussian probability distribution

$$P(\mathbf{q}, t + \Delta t|\mathbf{q}', t) = \frac{1}{(4\pi\Delta t)^{3/2} \det[\beta^{-1}\Gamma(\phi')]^{1/2}} \times \exp\left\{-\frac{1}{4\Delta t} [\mathbf{q}_\alpha - \mathbf{q}'_\alpha - \mathbf{a}_\alpha(\mathbf{q}')\Delta t] \beta \Gamma_{\alpha\beta}^{-1}(\phi') [\mathbf{q}_\beta - \mathbf{q}'_\beta - \mathbf{a}_\beta(\mathbf{q}')\Delta t]\right\} . \quad (2.36)$$

In order to obtain $P(\mathbf{q}, t|\mathbf{q}_i, 0)$ for large times t we make use of the Chapman-Kolmogorov relation for Markov processes [237]

$$P(\mathbf{q}, t|\mathbf{q}', t') = \int d^3\mathbf{q}'' P(\mathbf{q}, t|\mathbf{q}'', t'') P(\mathbf{q}'', t''|\mathbf{q}', t'), \quad t' < t'' < t . \quad (2.37)$$

$N - 1$ -fold decomposition of $P(\mathbf{q}, t|\mathbf{q}_i, 0)$ into small, equidistant time steps $\Delta t = t/N$ yields the desired result

$$P(\mathbf{q}, t|\mathbf{q}_i, 0) = \int \frac{d^3\mathbf{q}_1 \cdots d^3\mathbf{q}_{N-1}}{(4\pi\Delta t)^{3N/2} (D_{\parallel} D_{\perp} D_r)^{N/2}} \exp\left\{-\frac{\beta}{4} S(\mathbf{q}_0, \dots, \mathbf{q}_N)\right\} , \quad (2.38)$$

where the end points, $\mathbf{q}_N = \mathbf{q}$ and $\mathbf{q}_0 = \mathbf{q}_i$, are kept fixed, the determinant of the diffusion matrix, $\det[\beta^{-1}\Gamma] = (D_{\parallel} D_{\perp} D_r)$, has been inserted, and

$$S(\mathbf{q}_0, \dots, \mathbf{q}_N) = \sum_{n=0}^{N-1} \Delta t \left[\frac{\mathbf{q}_{n+1,\alpha} - \mathbf{q}_{n,\alpha}}{\Delta t} - \mathbf{a}_\alpha(\mathbf{q}_n) \right] \Gamma_{\alpha\beta}^{-1}(\phi_n) \left[\frac{\mathbf{q}_{n+1,\beta} - \mathbf{q}_{n,\beta}}{\Delta t} - \mathbf{a}_\beta(\mathbf{q}_n) \right] \quad (2.39)$$

is the discrete-time Onsager-Machlup action [206]. Taking the continuous-time limit $N \rightarrow \infty$, $\Delta t \rightarrow 0$, $N\Delta t = t$, the sum is symbolically written as a path integral

$$P(\mathbf{q}, t|\mathbf{q}_i, 0) = \int_{\mathbf{q}'(0)=\mathbf{q}_i}^{\mathbf{q}'(t)=\mathbf{q}} \mathcal{D}\mathbf{q}'(t') \exp\left\{-\frac{\beta S[\mathbf{q}'(t')]}{4}\right\} . \quad (2.40)$$

Here, $S[\mathbf{q}(t)]$ is the Onsager-Machlup action [206],

$$S[\mathbf{q}'(t')] = \int_0^t dt' L(\mathbf{q}(t'), \dot{\mathbf{q}}(t'), t'), \quad (2.41)$$

with the Lagrangian

$$L(\mathbf{q}, \dot{\mathbf{q}}, t) = [\dot{\mathbf{q}}_\alpha - \mathbf{a}_\alpha(\mathbf{q})] \Gamma_{\alpha\beta}^{-1}(\phi) [\dot{\mathbf{q}}_\beta - \mathbf{a}_\beta(\mathbf{q})]. \quad (2.42)$$

Note that we implicitly employed a prepoint-discretization scheme already in the short-time solution to the SP equation, Eq. (2.35), similar to the $\hat{\text{I}}$ to prescription in Langevin dynamics. Different discretization schemes lead to different path integral forms, which, however, are all equivalent in giving exactly the same Fokker-Planck equation [112, 297]. The freedom in choosing an appropriate discretization scheme makes Eqs. (2.40), (2.41), (2.42) meaningless if the discretization process is not specified. The prepoint-discretization is the simplest form, as it directly leads to the *classical path*, $\dot{\mathbf{q}}_\alpha = \mathbf{a}_\alpha(\mathbf{q})$, in which the particle deterministically follows the force acting on it; however, such a path is possible only for a very limited set of boundary conditions and does not apply for escape problems.

In the low-noise limit, i.e., for small temperatures β^{-1} , the probability determining contribution to the functional integral, Eq. (2.34), is the path $\mathbf{q}_i^*(t')$ with the lowest action among all possible paths $\mathbf{q}'(t')$ leading from \mathbf{q}_i to \mathbf{q} , i.e.,

$$P(\mathbf{q}, t|\mathbf{q}_i, 0) \simeq K(\mathbf{q}, t|\mathbf{q}_i, 0) \exp \left\{ -\frac{\beta S[\mathbf{q}_i^*(t')]}{4} \right\}, \quad (2.43)$$

where $K(\mathbf{q}, t|\mathbf{q}_i, 0)$ is a non-exponential prefactor, and where $\mathbf{q}_i^*(t')$ fulfills

$$S[\mathbf{q}_i^*(t')] \leq S[\mathbf{q}'(t')], \quad \mathbf{q}'(0) = \mathbf{q}_i, \mathbf{q}'(t) = \mathbf{q}.$$

The path $\mathbf{q}_i^*(t')$ is referred to as the *minimum action path* (MAP), and the corresponding exponential factor as Arrhenius factor. The trajectory $\mathbf{q}_i^*(t')$ is determined by the stationary solution to the Onsager-Machlup action, which can be obtained by solving the corresponding Euler-Lagrange equations of motion, respecting the appropriate boundary conditions. For Hamiltonian systems the prefactor $K(\mathbf{q}, t|\mathbf{q}_i, 0)$ can be approximatively determined by a saddle point approximation, which amounts to take Gaussian fluctuations about the MAP into account [42]. In this case, $K(\mathbf{q}, t|\mathbf{q}_i, 0)$ is independent of β , i.e., the scaling of $P(\mathbf{q}, t|\mathbf{q}_i, 0)$ with β is solely determined by the Arrhenius factor. For non-Hamiltonian systems, this is in general not true [175].

2.3.5 An approximate treatment of the escape rate

Let us come back to the rate γ in Eq. (2.34), which is given by an integral over the gradient of the probability distribution $P(\mathbf{q}, t|\mathbf{q}_i, 0)$ with respect to \mathbf{q} . As $P(\mathbf{q}, t|\mathbf{q}_i, 0)$

is simply a sum over exponentials, taking the gradient leads to an additional (nonexponential) prefactor on the integrand in the path integral. In the low-noise limit, the rate determining contribution to the integral over functional integrals, Eq. (2.34), is therefore the MAP, which leads to the lowest saddle point on the separatrix $\partial\Omega_i$ (for exceptions of this rule see the discussion further down). The work presented in Chapter 8 is restricted to the evaluation of the corresponding Arrhenius factor; the prefactors are henceforth ignored, or rather crudely approximated by the inverse Brownian time τ_B^{-1} (see also the discussion in Chapter 8). For Hamiltonian systems, i.e., for $\mathbf{m} = 0$ in Eq. (2.29), the Arrhenius factor is simply given by the potential energy difference between the local minimum at \mathbf{q}_i and the lowest saddle point on the separatrix at \mathbf{q}_i^s , i.e.,

$$\min_{\substack{\mathbf{q}'(0)=\mathbf{q}_i, \\ \mathbf{q}'(t)\in\partial\Omega_i}} S[\mathbf{q}'(t')] = 4[V(\mathbf{q}_i^s) - V(\mathbf{q}_i)]. \quad (2.44)$$

For a derivation we refer the reader to the paper by Onsager and Machlup [207] or, e.g., to reference [205]. For the non-Hamiltonian system under study in Chapter 8, however, we do not only have a potential $V(\mathbf{q})$ but also a non-conservative force \mathbf{m} . We therefore infer the MAP from symmetry arguments and from observed particle trajectories in Brownian dynamics computer simulations. The problem is further simplified by exploiting that orientational fluctuations in ϕ are much more relevant for escaping the attractor than fluctuations in \mathbf{r} .²⁵ We therefore assume that during the MAP the swimmer's translation is determined by the constraint

$$\dot{\mathbf{q}}_{x,y} = \mathbf{a}_{x,y}(\phi).$$

This implies a great simplification to the Lagrangian, which reduces to

$$\tilde{L}(\phi, \dot{\phi}, t) = (\beta D_r)^{-1} \left[\dot{\phi} - \mathbf{a}_\phi(\mathbf{q}[\phi]) \right]^2 = (\beta D_r)^{-1} \left[\dot{\phi} - M + \partial_\phi V(x[\phi], \phi) \right]^2, \quad (2.45)$$

where the tilde on $\tilde{L}(\phi, \dot{\phi}, t)$ denotes the constraint; thereby the swimmer's space coordinate becomes a functional of the orientation $\phi(t)$, i.e., $\mathbf{r}(t) = \mathbf{r}[\phi(t' < t)]$. Note that by imposing this constraint the problem is *not* reduced to one dimension. In fact, different paths $\phi(t)$ lead in general to completely different trajectories in \mathbf{r} -space due to the translation-rotation coupling in the diffusion matrix and—even more important—in the non-conservative forces $\mathbf{m}(\phi)$. However, despite the large number of possible trajectories, it is only a small class of “costly” paths $\phi(t)$ [with the corresponding phase space trajectory $\mathbf{q}(t) = (\mathbf{r}[\phi], \phi(t))$], which lead from the attractor to one of the two saddle points on the separatrix. The latter are situated at $(x_u, \phi_u + (i-1)\pi)$ and $(L_x - x_u, \phi_u + (i-2)\pi)$ if i is odd, and at $(L_x - x_u, \phi_u + (i-1)\pi)$

²⁵This assumption is justified if the rotational diffusion constant is substantially larger than the translational ones, and/or if the self propulsion in the direction of the swimmer F is much larger than the torque M (see also Chapter 8).

and $(x_u, \phi_u + (i - 2)\pi)$ if i is even. The saddle points are indicated by open circles in Fig. 2.3.

The minimization of the action with the simplified Lagrangian, Eq. (2.45), for the swimmer under study is in detail described in Chapter 8. Here, we only mention that not only one, but three different paths $\phi_{ij}^*(t)$, $j = 1, 2, 3$, leading from the attractor \mathbf{q}_i to either of the two saddles are taken into account. Depending on the ratio of the self-propelling forces M/F , one of these paths, which have been identified from computer simulations, is dominating. For the special case $i = 1$ and $M > 0$, the projections of the trajectories on the (x, ϕ) -plane and on the (x, y) -plane are sketched in Figs. 2.3 and 8.4, respectively. Two of the paths [paths (a) and (c) in Figs. 2.3, 8.4] lead to the same, in general, lower saddle, which connects basin i with basin $i + 1$, whereas the third [path (b) in Figs. 2.3, 8.4] leads to another, in general, higher saddle, connecting basins i and $i - 1$. The difference in height is due to the torque M , which renders turning against the ϕ -direction $M/|M|$ difficult according to the Lagrangian, Eq. (2.45). Lacking knowledge about the kinetic prefactors of the three different paths examined, we assume their weight to be simply determined by their respective Arrhenius factor times the inverse Brownian time scale τ_B , which leads to an overall rate

$$\gamma = \tau_B^{-1} \sum_{j=1}^3 \exp \left\{ -\frac{\beta \tilde{S}[\phi_{ij}^*(t)]}{4} \right\}, \quad (2.46)$$

where the tilde on $\tilde{S}[\phi_{ij}^*(t)]$ denotes the use of $\tilde{L}(\phi, \dot{\phi}, t)$ in eq. (2.41), and $\phi_{ij}^*(t)$ describes the respective MAP, given few constraints characterizing the general shape of the corresponding trajectory (for details on how the three different paths (a), (b), and (c) were defined see Chapter 8).

2.3.6 Discussion

In this final subsection, we comment on few points concerning, first, rate theories in general and, second, the Brownian swimmer in particular. Eq. (2.46) is certainly a crude approximation, and it would be highly desirable to obtain approximate expressions for the corresponding kinetic prefactors as well. In fact, many authors have been concerned with the evaluation of the latter in nonequilibrium, non-Hamiltonian systems in more than one dimension [89, 116, 176, 197, 255]. However, already for Hamiltonian systems, in which the MAP can be identified as the “closest” connection between the local minimum and the lowest saddle of the potential $V(\mathbf{q})$, this is a formidable task, as it comprises two steps: at first, a saddle point approximation to characterize the weight of the path in coordinate-space has to be performed [205, 279], and second, a correct treatment of the continuous symmetry in time is needed [42]. This latter problem has not been discussed so far, and deserves a short comment.

The MAP typically describes a process, which is fast, as compared to the inverse escape rate, i.e., the reaction time τ_R it takes the particle to travel from the attractor to the separatrix is given by $\tau_R \ll \gamma^{-1}$. On large times, $t \gg \tau_R$, which we consider, the action $S[\mathbf{q}_i^*(t')]$ is independent of *when* exactly the escape process happens. Naively, one could be tempted to assume, that the probability distribution $P(\mathbf{q}_i^s, t | \mathbf{q}_i, 0)$ would therefore grow linearly with time t , as the chance that such an event, which is also referred to as an *instanton* [42], had already happened before the time t , would increase. However, this is, of course, not the case. Instead, also the relaxation processes of leaving the separatrix either back into the basin i , which is the unsuccessful attempt referred to as an *anti-instanton*, or over the barrier into the other basin, has to be considered. Depending on the curvature of $V(\mathbf{q})$ at the minimum and at the saddle, higher-order combinations of instantons and anti-instantons have to be summed up correctly, which then lead to the correct time-independence of γ [42].

This reasoning points to a different way of approaching escape problems, which is the concept of *mean first passage times* (MFPT) [96, 116]. The MFPT $t_{\Omega_i}(\mathbf{q})$ is the mean time it takes the particle to reach the separatrix *for the first time* having been placed at $\mathbf{q} \in \Omega_i$ at zero time.²⁶ In the spirit of the aforementioned continuous time-symmetry, it is therefore easier, at least conceptually, to assess the corresponding probability distribution, which is a solution to the SP equation with *absorbing* boundary conditions on the separatrix [96], i.e., the probability distribution is not a conserved quantity any more but—by construction—equals zero outside the region Ω_i . Due to the boundary conditions this function has in the weak-noise limit only *one* contribution from a *single* instanton, and the problem of summation over higher-order processes is absent. However, to go beyond this single-instanton approximation is practically very difficult in the framework of path integrals, as the absorbing boundaries are difficult to implement. Instead, the MFPT can be obtained rigorously via the adjoint SP operator [96]²⁷ or as the inverse decay rate of the lowest-eigenvalue eigenfunction to the SP operator, which in turn can be approximately found by a WKB treatment [174]. Both of these approaches form the basis of a class of systematic asymptotic expansions [176, 197, 255] to escape problems, which proved very successful for the determination of escape rates in non-Hamiltonian systems during recent years.

One of the highly non-intuitive outcomes was the following finding: For general non-Hamiltonian systems the *most probable escape path* (MPEP), which is the path taken with the highest probability in the mathematical limit $\beta^{-1} \rightarrow 0$ is not always

²⁶In general, the concept of the MFPT is not limited to applications on basins of attractions but can be formulated for any connected region in phase space [116]. In the weak noise limit and under certain further conditions on $\partial\Omega_i$, the MFPT can be shown to be equal to the inverse of a flux-over-population rate similar to the Kramers rate; for the differences see, e.g., appendix B of ref. [116] or ref. [197].

²⁷ t_{Ω_i} is the solution to the equation $\mathcal{L}^\dagger t_{\Omega_i}(\mathbf{q}) = 1, \mathbf{q} \in \Omega_i$ with boundary condition $t_{\Omega_i}(\mathbf{q}) = 0, \mathbf{q} \notin \Omega_i$.

equal to the MAP, a phenomenon referred to as *saddle point avoidance* [176, 197, 255]. This may in particular happen if two equally high saddles on the separatrix are separated by an unstable fixed point on the separatrix [171]. In our work, this is neither observed nor expected, as the two saddles of the domain Ω_i are situated on different boundaries $\partial\Omega_{i,i-1}$ and $\partial\Omega_{i,i+1}$, respectively.

Due to the torque M the motion in the direction of ϕ and against it is asymmetric. We already saw this becoming manifest in the higher saddle on the border $\partial\Omega_{i,i-1}$ as compared to the one on the border $\partial\Omega_{i,i+1}$, for the case $M > 0$. The swimmer moves therefore on average in the $+\phi$ -direction, whereas in \mathbf{r} -space the particle is equally likely to move in positive as in negative y -direction. Despite the multi-dimensional and non-Hamiltonian character, our model therefore resembles to some extent the problems of tilted periodic potentials in one dimension [116, 237], in which the particle hops from one local minimum of the potential energy to the next, in very rare cases also hopping backwards for short times, but on average walking deterministically in the direction of the tilt.

Chapter 3

Density functional theory of freezing for soft interactions in two dimensions¹

Abstract

A density functional theory of two-dimensional freezing is presented for a soft interaction potential that scales as inverse cube of particle distance. This repulsive potential between parallel, induced dipoles is realized for paramagnetic colloids on an interface, which are additionally exposed to an external magnetic field. An extended modified weighted density approximation which includes correct triplet correlations in the liquid state is used. The theoretical prediction of the freezing transition is in good agreement with experimental and simulation data.

A microscopic theory of freezing and melting is a great challenge in statistical physics. There are two complementary approaches to the liquid-to-solid transition: first, classical density functional theory [165, 209, 263] starts from liquid state and views the solid as a condensation of liquid density modes, hence it is a liquid-based approach. Second, crystal elasticity theory [265] is a solid-based theory where the liquid is viewed as a solid with an accumulation of defects. In three dimensions, the freezing transition is first order and it is known that it is not defect mediated. Here, density functional theory provides a molecular theory for the freezing transition. Crystal elasticity theory is appropriate to two dimensions and predicts a possible scenario of two-stage melting via an intermediate hexatic phase [113, 146, 200, 305].

¹This chapter was published by Sven van Teeffelen, Norman Hoffmann, Christos N. Likos, and Hartmut Löwen in *Europhys. Lett.* 75 (2006), 583 (arXiv:cond-mat/0604422). It is reprinted with permission from EDP Science, Copyright 2006.

The advantage of density functional theory is that it can be used to calculate the structure of the solid, whereas it is not possible to extract the structure of the fluid out of crystal elasticity theory.

An excellent realization of a two-dimensional system is provided by paramagnetic colloidal particles in a pendant water droplet, which are confined to the air-water interface [307]. If an external magnetic field is applied perpendicular to the interface, a magnetic moment is induced in the particles resulting into a tunable, mutual dipolar repulsion between them. The corresponding interaction pair potential $u(r)$ is repulsive and soft, being proportional to $1/r^3$, with r denoting the distance between the particles. The prefactor can easily be tuned by varying the external magnetic field strength. In real-space experiments [282, 306], the two-stage melting process was confirmed with an intermediate hexatic phase which had a tiny stability range bracketed between the fluid and the crystalline phase. There are also computer simulations [111, 166] for freezing in $1/r^3$ system but finite-size effects turn out to become crucial here as was shown in elaborate studies [22].²

In this chapter, we apply density functional theory (DFT) to two-dimensional freezing of soft $1/r^3$ interactions. There are two major difficulties arising in doing so: first, it is known that it is difficult to get a reliable density functional approximation for soft repulsive interaction potentials. While hard sphere freezing serves as standard test case for various approximations and many reliable approximations do exist (e.g. Rosenfeld's fundamental measure theory [240]), the freezing of soft inverse-power law-fluids turns out to be much harder [287]. For the extreme case of the one-component plasma, featuring a $1/r$ interaction, it has been shown by Likos and Ashcroft [158, 159] that an extended modified weighted density approximation (EMA) which contains correct triplet correlation of the fluid yields reliable freezing data. In this chapter, we overcome the first problem in a similar way and generalize the EMA to two dimensions and apply it to the $1/r^3$ interaction. The second, more fundamental problem is linked to the two-dimensional character of the system itself. It is not clear to date how to include the hexatic phase into the density functional language. Here, we do not address this deep question but rather focus on the prediction of the freezing transition point neglecting the tiny stability range of the hexatic phase. A similar view has been taken for hard disk systems [21, 248, 301, 309] and to the $1/r$ interaction in 2D [248] where density functional theory of freezing was applied to.

We demonstrate that the EMA yields excellent freezing data as compared to the standard modified weighted density approximation (MWDA) [64]. Even the relative-mean-square-displacement in the coexisting solid is in reasonable agreement with the experimental data on colloids in a magnetic field.

The Helmholtz free energy density functional is typically split into the ideal gas and an excess part, $F_{\text{tot}}[\rho(\mathbf{r})] = F_{\text{id}}[\rho(\mathbf{r})] + F_{\text{ex}}[\rho(\mathbf{r})]$. Here the ideal part is local and nonlinear, $F_{\text{id}}[\rho(\mathbf{r})] = k_B T \int d\mathbf{r} \rho(\mathbf{r}) \{ \ln [\rho(\mathbf{r}) \Lambda^2] - 1 \}$, with Λ denoting

²A critical survey of finite-size effects to hard disks can be found in reference [137].

the thermal de Broglie wavelength and $k_B T$ the thermal energy. The excess part can only be calculated approximately. Both the MWDA and the EMA approximate the excess free energy of the inhomogeneous system by setting it equal to the excess free energy of a uniform liquid evaluated at an appropriately weighted density $\hat{\rho}$: $F_{\text{ex}}[\rho(\mathbf{r})] \approx F_{\text{ex}}^{\text{MWDA/EMA}}[\rho(\mathbf{r})] = N f_0(\hat{\rho})$, where N is the number of particles in the system and $f_0(\hat{\rho})$ is the excess free energy per particle of the uniform liquid at the weighted density $\hat{\rho}$ determined through:

$$\begin{aligned} \hat{\rho}[\rho(\mathbf{r})] = & \frac{1}{N} \int d\mathbf{r} d\mathbf{r}' \rho(\mathbf{r}) \rho(\mathbf{r}') w(\mathbf{r} - \mathbf{r}'; \hat{\rho}) \\ & + \frac{1}{N^2} \int d\mathbf{r} d\mathbf{r}' d\mathbf{r}'' \rho(\mathbf{r}) \rho(\mathbf{r}') \rho(\mathbf{r}'') v(\mathbf{r} - \mathbf{r}', \mathbf{r} - \mathbf{r}''; \hat{\rho}). \end{aligned} \quad (3.1)$$

Here the second term only appears in the EMA and not in the MWDA. The weight functions $w(\mathbf{r}; \rho)$ and $v(\mathbf{r}, \mathbf{r}'; \rho)$ are determined by requiring that the approximate functional $F_{\text{ex}}[\rho(\mathbf{r})]$ is exact up to second (MWDA) or third (EMA) order in density difference $\Delta\rho(\mathbf{r}) = \rho(\mathbf{r}) - \rho$ in the functional expansion of the excess free energy of the inhomogeneous system about the excess free energy of the fluid. The second weight function v in Eq. (3.1) is chosen to be zero in the MWDA since the third order correlation function does not enter the formalism explicitly; rather, all higher terms are approximately included as a consequence of the self-consistency requirement on the determination of $\hat{\rho}$, appearing on both sides of Eq. (3.1). The EMA, on the other hand, is exact up to third order and, similarly, includes approximate contributions from all higher-order terms. The normalized weight functions have to fulfill the requirements [158, 159]

$$\begin{aligned} \lim_{\rho(\mathbf{r}) \rightarrow \rho} \left[\frac{\delta^2 F_{\text{ex}}^{\text{MWDA/EMA}}}{\delta\rho(\mathbf{r}) \delta\rho(\mathbf{r}')} \right] &= -k_B T c_0^{(2)}(\mathbf{r} - \mathbf{r}'; \rho) \\ \lim_{\rho(\mathbf{r}) \rightarrow \rho} \left[\frac{\delta^3 F_{\text{ex}}^{\text{EMA}}}{\delta\rho(\mathbf{r}) \delta\rho(\mathbf{r}') \delta\rho(\mathbf{r}'')} \right] &= -k_B T c_0^{(3)}(\mathbf{r} - \mathbf{r}', \mathbf{r} - \mathbf{r}''; \rho), \end{aligned} \quad (3.2)$$

where $c_0^{(2)}$ and $c_0^{(3)}$ are the two- and three-particle direct correlation functions of the liquid [117] which are an input to the theory. These conditions uniquely determine the weight functions and lead to simple algebraic equations for v and w that can be found in reference [158, 159].

In order to find the equilibrium one-particle density $\rho_{\text{eq}}(\mathbf{r})$ we minimize the total free energy functional $F_{\text{tot}}^{\text{MWDA/EMA}}[\rho(\mathbf{r})]$ with respect to the inhomogeneous one-particle density $\rho(\mathbf{r})$. We make the Gaussian ansatz, $\rho(\mathbf{r}) = \frac{\alpha}{\pi} \sum_{\mathbf{R}_i} \exp[-\alpha |\mathbf{r} - \mathbf{R}_i|^2]$ where $\{\mathbf{R}_i\}$ is the set of Bravais lattice vectors of a triangular lattice (with average density ρ). For fixed average density ρ we thus end up with only one minimization parameter α which describes the degree of localization. For $\alpha \rightarrow 0$ the density profile becomes flat and the system turns into a homogeneous liquid of number density ρ , whereas increasing α leads to enhanced particle localization around the lattice sites.

With the Gaussian parametrization of the density profiles, we obtain the following self-consistent equation for the weighted density $\hat{\rho}$ as function of the localization parameter α and the average density ρ :

$$\frac{\hat{\rho}(\rho, \alpha)}{\rho} = \left[1 - \frac{k_B T}{2f'_0(\hat{\rho})} \sum_{\mathbf{K} \neq 0} \mu_K^2 \tilde{c}_0^{(2)}(\mathbf{K}; \hat{\rho}) - \frac{\rho k_B T}{6f'_0(\hat{\rho})} \sum_{\substack{\mathbf{K} \neq 0 \\ \mathbf{Q} \neq 0, -\mathbf{K}}} \mu_K \mu_Q \mu_{|\mathbf{K}+\mathbf{Q}|} \tilde{c}_0^{(3)}(\mathbf{K}, \mathbf{Q}; \hat{\rho}) \right], \quad (3.3)$$

where $\mu_k = e^{-k^2/4\alpha}$ are the Fourier coefficients of the Gaussian ansatz for $\rho(\mathbf{r})$ and, likewise, $\tilde{c}_0^{(n)}$, $n = 2, 3$, denote the Fourier transforms of the n -particle direct correlation functions, evaluated at the reciprocal lattice vectors (RLV's) \mathbf{K} and \mathbf{Q} . Primes denote derivatives with respect to density and the three-particle term only appears in the EMA. Whereas F_{id} grows with α , $\hat{\rho}$ decreases with the latter, causing a concomitant decrease in F_{ex} , because the latter is a monotonically increasing function of $\hat{\rho}$. As can be induced from Eq. (3.3) above, the decrease of $\hat{\rho}$ with α is pronounced when the RLV's of the lattice lie close to the maxima of $\tilde{c}_0^{(2)}(k; \hat{\rho})$, a feature that corresponds physically to an inherent tendency of the fluid to enhance density waves at these wavevectors.

We now apply the MWDA/EMA to the inverse-power pair potential $u(r) = u_0/r^3$, where u_0 is a parameter with dimensions of energy \times volume; for the specific realization of two-dimensional paramagnetic colloids of susceptibility χ exposed to a perpendicular magnetic field \mathbf{B} , we have $u_0 = (\chi\mathbf{B})^2/2$ in Gaussian units. The thermodynamics and structure depend, due to simple scaling, only on one relevant dimensionless coupling parameter $\Gamma = u_0\rho^{3/2}/(k_B T)$. Therefore, it is convenient to express all quantities in terms of Γ and consider coupling parameters rather than densities via this scaling relation. Correspondingly, in what follows we employ the weighted coupling constant $\hat{\Gamma}$, related to $\hat{\rho}$ via the scaling relation $\hat{\Gamma}(\Gamma, \alpha) = u_0\hat{\rho}^{3/2}(\rho, \alpha)/(k_B T)$.

In order to obtain the concrete form of the functional approximations, we need the two- and three-particle direct correlation functions and the excess free energy per particle f_0 of the corresponding uniform fluid for a wide range of coupling constants Γ . These quantities are obtained as described below:

(i) The two-particle direct correlation function is obtained by liquid integral equation theory, where we used the hypernetted chain (HNC) [117] or the thermodynamically consistent Rogers-Young (RY) closure [239], adopted to two dimensions [39]. We have also produced ‘‘exact’’ data for the real-space direct two-particle correlation by computer simulation applying a closure suggested by Verlet [280] that inverts the pair-distribution function from a finite simulation box in order to obtain $c_0^{(2)}$. A comparison between the HNC, RY and simulation data for the Fourier transform $\tilde{c}_0^{(2)}$ of the direct correlation function is shown in Fig. 3.1 for the experimentally determined coupling close to freezing. The HNC closure underestimates the structure strongly while the RY closure is closer to the simulation data. The

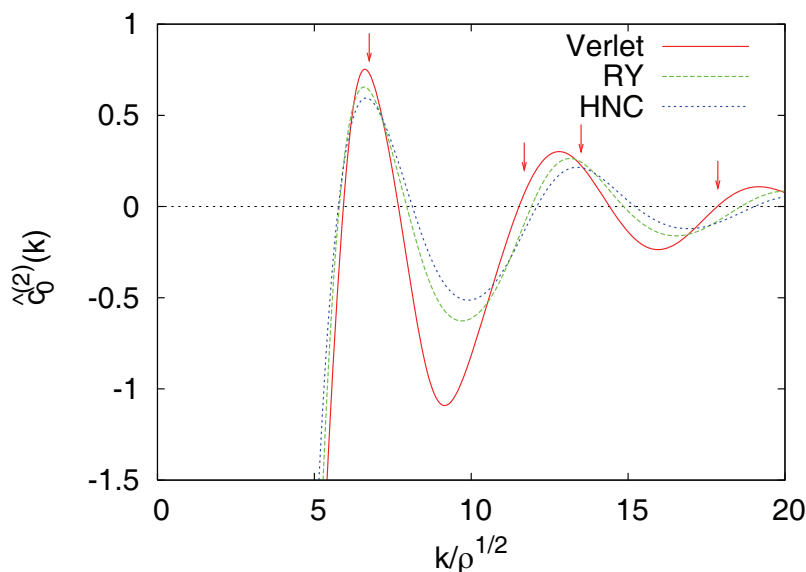


Figure 3.1: The Fourier transform $\rho\tilde{c}_0^{(2)}(k)$ of the two-particle direct correlation function at $\Gamma = 9$, plotted against ka , where $a = \rho^{-1/2}$. Shown are simulation data using the Verlet closure (solid line); liquid integral equation theory using the RY closure (dashed line) and liquid integral equation theory using the HNC closure (dotted line). The arrows indicate the positions of the first four reciprocal lattice vectors of the triangular lattice.

HNC closure is therefore not considered further. We also show the positions of the first four reciprocal lattice vectors of a triangular lattice with same density. The value of $\tilde{c}_0^{(2)}$ at these lattice vectors crucially influences the solid free energies, as can be seen from Eq. (3.3).

(ii) The excess free energy per particle f_0 is obtained from the pair correlation via the compressibility route [117], $[\rho f_0(\rho)]'' = -k_B T \tilde{c}_0^{(2)}(k=0; \rho)$.

(iii) Finally, the three-particle direct correlation function $c_0^{(3)}$ of the underlying fluid is obtained from an approximation by Denton and Ashcroft [63], which is based on a weighted density approximation to the first order direct correlation function of an inhomogeneous system. This approach leads to an analytic expression of $c_0^{(3)}$ in terms of the one- and two-particle correlation functions $c_0^{(1)}$, $c_0^{(2)}$ of the liquid, employing the ‘symmetrized sum’

$$\tilde{c}_0^{(3)}(\mathbf{k}, \mathbf{k}') = \frac{1}{3} \left[\tilde{f}(|\mathbf{k}|, |\mathbf{k}'|) + \tilde{f}(|\mathbf{k}|, |\mathbf{k} + \mathbf{k}'|) + \tilde{f}(|\mathbf{k}'|, |\mathbf{k} + \mathbf{k}'|) \right], \quad (3.4)$$

where

$$\tilde{f}(k, k') = \frac{1}{c_0^{(1)'}} \left[\tilde{c}_0^{(2)}(k) \tilde{c}_0^{(2)'}(k') + \tilde{c}_0^{(2)'}(k) \tilde{c}_0^{(2)}(k') \right] - \frac{c_0^{(1)''}}{[c_0^{(1)'}]^2} \tilde{c}_0^{(2)}(k) \tilde{c}_0^{(2)}(k'). \quad (3.5)$$

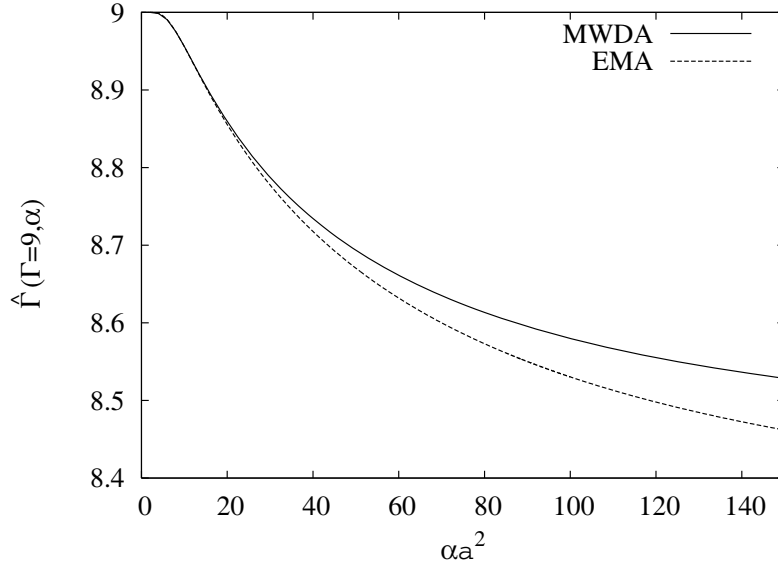


Figure 3.2: The weighted coupling constant $\hat{\Gamma}(\Gamma, \alpha)$ as a function of the localization parameter α within the MWDA (solid line) and within the EMA (dashed line) using the “exact” pair structure from simulation for the strong coupling $\Gamma = 9$.

Results for the approximations proposed are presented in Figs. 3.2 and 3.3. In Fig. 3.2, the weighted coupling constant $\hat{\Gamma}(\Gamma, \alpha)$ is shown versus the localization parameter α for a strong coupling Γ close to freezing. Both the MWDA and the EMA are examined with the simulation pair structure input. Obviously, $\hat{\Gamma}$ coincides with the bare Γ in the fluid ($\alpha = 0$). It can be seen that the MWDA yields a smaller reduction in $\hat{\Gamma}$ relative to Γ than the EMA: explicit inclusion of three-body effects enhances the tendency of the particles to localize. Hence, one expects freezing at lower couplings in the EMA. In fact, in Fig. 3.3, the free energy difference between a solid of localization α and a fluid ($\alpha = 0$) shown versus α reveals that the fluid is much more stable in the MWDA as compared to the EMA. The EMA yields a transition from the fluid to the solid close to $\Gamma = 9.4$: while for $\Gamma = 9.0$ the fluid is stable as indicated by the minimal value at $\alpha = 0$, fluid-solid coexistence is achieved at $\Gamma = 9.4$, see the two equal minima in Fig. 3.3. The solid phase, on the other hand, is clearly stable for $\Gamma = 9.8$. The localization parameter at coexistence is roughly $\alpha_{\min} a^2 = 100$.

The full results of a numerical calculation using Maxwell’s double tangent construction yield a weak first-order transition with a fluid density corresponding to a coupling constant of Γ_f and a solid density corresponding to a coupling constant of Γ_s . There is a small density gap $\Delta\Gamma = \Gamma_s - \Gamma_f$, describing the coexistence region. Table 3.1 summarizes the freezing/melting parameters for the MWDA with RY closure, for the EMA with RY closure, and for the EMA with the “exact” pair

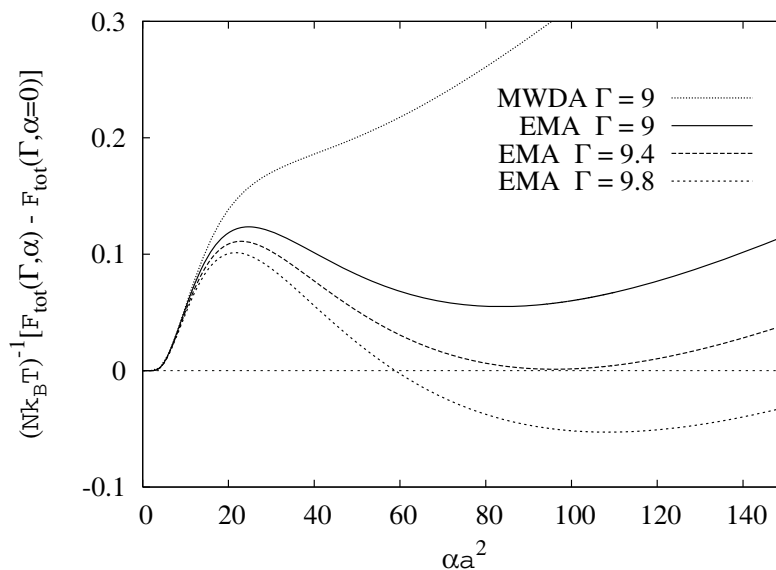


Figure 3.3: Relative free energy per particle $N^{-1} [F_{\text{tot}}(\Gamma, \alpha) - F_{\text{tot}}(\Gamma, \alpha = 0)]$ in units of $k_B T$ as a function of α obtained within the EMA for three different coupling constants $\Gamma = 9, 9.4, 9.8$ (the three lower curves from top to bottom) compared to the same obtained within the pure MWDA for a coupling constant $\Gamma = 9$ (uppermost line). The fluid input is obtained from simulation.

structure obtained from simulation. The data are compared against experimental results obtained from real-space microscopy measurement of magnetic colloids confined to an air-water interface. The experiments give freezing with an intermediate hexatic phase. The liquid-solid transition has also been studied using numerical simulation [111, 166] yielding a slightly higher inverse transition temperature between 12.0 and 12.25 but these investigations suffer from finite size effects.

As becomes evident from Table 3.1, the MWDA is not a quantitatively satisfying theory as it overestimates the freezing coupling by a factor of 4. Note that the overestimation of the freezing coupling is the reason why it is not possible to feed the “exact” pair structure into the MWDA. At such high coupling, no fluid pair structures are available since the fluid spontaneously crystallizes in the simulation. The EMA, on the other hand, yields results in close agreement with experimental data.

More detailed, structural information can be extracted from the localization parameter of the coexisting solid. For all approximations used we find localization parameters at freezing in the range $99 < \alpha_{\text{min}}(\Gamma_f)a^2 < 115$. Strictly speaking, the localization parameter has no counterpart in “real” 2D systems since the particles are not localized due to long range fluctuations. However, if one relates the particle displacements to that of their nearest neighbor, one can define a finite quantity

Table 3.1: Freezing and melting parameters Γ_f and Γ_s , the widths of the coexistence regions $\Delta\Gamma = \Gamma_s - \Gamma_f$, and the relative displacement parameters γ at coexistence obtained within: the MWDA with the RY closure (first row); the EMA with the RY closure (second row); the EMA with the “exact” pair structure from simulation (third row) and experimental parameters for the isotropic-hexatic transition, the hexatic-crystal transition and the Lindemann parameter, obtained from real-space microscopy measurements of magnetic colloids confined to an air-water interface (last row).

	Γ_f	Γ_s	$\Delta\Gamma$	γ
MWDA with RY	41.07	41.13	0.06	0.017
EMA with RY	23.0	23.08	0.09	0.020
EMA with simulation	9.33	9.49	0.16	0.020
Experiment	10.0	10.75	-	0.038

as $\gamma = \rho \langle (\mathbf{u}_i - \mathbf{u}_{i+1})^2 \rangle$, where \mathbf{u}_i and \mathbf{u}_{i+1} are the displacement vectors of neighboring lattice sites. Disregarding nearest-neighbor correlations $\langle \mathbf{u}_i \cdot \mathbf{u}_{i+1} \rangle$, γ can be estimated. Since the nearest-neighbor correlations $\langle \mathbf{u}_i \cdot \mathbf{u}_{i+1} \rangle$ are expected to be positive:

$$\gamma \lesssim 2\rho \langle \mathbf{u}_i^2 \rangle \approx 2/(\alpha_{\min} a^2). \quad (3.6)$$

By this relation, the localization parameter of the coexisting solid gives a prediction for γ which is included in Table 3.1. From experiments, γ is known to be close to $\cong 0.038$ [306]. This was shown to be in accordance with harmonic lattice theory [95]. The EMA yields $\gamma \lesssim 0.020$, i.e. the EMA roughly overestimates the localization of the particles by a factor of 2. γ is *smaller* than the experimental value, contrarily to what was expected from the inequality (3.6). This shows that there is still a need to improve the theories in order to correctly predict localization properties. A similar overestimation of the localization is also common in weighted density approximations in three spatial dimensions [64].

Another quantity of interest, which is directly connected to the Helmholtz free energy is the pressure at coexistence. Within the EMA with the “exact” pair structure we obtain $P(\Gamma_f = 9.33)/(k_B T \rho) = 72.6$.

In conclusion, we have demonstrated that the EMA is able to quantitatively predict the freezing transition of a two-dimensional colloidal system with soft and long-ranged $1/r^3$ -interactions in good agreement with experimental and simulation data. In analogy to three-dimensional systems, the appearance of long-range interactions requires the explicit inclusion of three-particle correlation functions of the liquid in the construction of the weighted density. Furthermore, the predicted transition temperatures are very sensitive towards slight changes of the two-particle correlation functions of the underlying fluid. A highly accurate input of the same is

therefore crucial.

Relying on the good quality of the EMA functional, our results can serve as a platform to treat more challenging problems than bulk transitions [167]. One obvious extension is towards external potentials acting on the particles, such as system walls or gravity. The MWDA can in principle be applied to a fluid near a single wall, but not to a free interface between coexisting phases. Another interesting example is a spatially inhomogeneous magnetic field, which renders the interactions space dependent [94]. Finally, one may employ the scheme of dynamical density functional theory [75, 179] in order to use the EMA functional to study the effect of spatially homogeneous magnetic fields that oscillate in time. Work along these lines is currently under way.

Acknowledgements

This work has been supported by the DFG within the SFB TR6, project section C3.

Chapter 4

Crystallization of magnetic dipolar monolayers: a density functional approach¹

Abstract

We employ density functional theory to study in detail the crystallization of superparamagnetic particles in two dimensions under the influence of an external magnetic field that lies perpendicular to the confining plane. The field induces non-fluctuating magnetic dipoles on the particles, resulting into an interparticle interaction that scales as the inverse cube of the distance separating them. In line with previous findings for long-range interactions in three spatial dimensions, we find that explicit inclusion of liquid-state structural information on the triplet correlations is crucial to yield theoretical predictions that agree quantitatively with experiment. A non-perturbative treatment is superior to the oft-employed functional Taylor expansions, truncated at second or third order. We go beyond the usual Gaussian parametrization of the density site-orbitals by performing free minimizations with respect to both the shape and the normalization of the profiles, allowing for finite defect concentrations.

4.1 Introduction

Classical density functional theory (DFT) is the method of choice to the study of inhomogeneous fluids [85]. Perhaps the most extreme inhomogeneities arise in a crystalline solid, where the density field $\rho(\mathbf{r})$ is both periodic and shows extreme differences between its local values on the lattice sites and in the interstitial regions.

¹This chapter was published by Sven van Teeffelen, Hartmut Löwen, and Christos N. Likos in *J. Phys.: Condens. Matter* 20 (2008), 404217 (<http://www.iop.org/journals/jpcm>; arXiv:0804.3299). It is reprinted with permission from IOP Publishing Ltd., Copyright 2008.

DFT has been successfully applied to the problem of crystallization of a number of different systems [157, 165, 168, 210, 263], *mostly* in three spatial dimensions. Here, the most popular system is the prototype of hard spheres, for which a geometry-based theory [240, 243, 251] has proven quite successful. For soft interactions [55, 56, 59], however, where one cannot assign geometrical measures to the interacting point-particles, one has to resort to other functionals. In particular, it has been shown [158] that for long-range interactions, structural information of the liquid on the pair-level is insufficient and triplet fluid correlations should be allowed to explicitly flow into the construction of the functional. Even less is known for crystallization in two spatial dimensions [241, 272, 309]. Here, we consider a combination of the two above-mentioned cases in considering *long range interactions in two spatial dimensions* and we study in detail the role played by accurate liquid-state information on triplet correlations in determining phase boundaries between a fluid and the coexisting crystal.

In this chapter, we study freezing of a classical two-dimensional model fluid, namely of a fluid of aligned dipoles directed perpendicular to the 2D-plane and repelling each other with a soft $1/r^3$ inverse-power pair potential, with the help of density functional theory (DFT). In Chapter 3 we studied freezing of the the dipolar system with the modified weighted density approximation and its extension to third order correlation functions. Within this chapter we will extend our previous study in several ways: We allow for a finite defect concentration and relax the constraint of Gaussian density peaks in the crystalline phase, as, e.g., suggested for hard sphere crystals in Ref. [203]. Furthermore, we systematically study the influence of perturbative and non-perturbative inclusion of higher order correlation functions of the liquid in the density functional approximation on the freezing transition. We employ two different approximations to the three-particle correlation functions, which lead to substantially different results, therefore signalling the importance of an accurate approximation of the latter.

We use different approximations to the DFT—based on the famous and powerful approach by Ramakrishnan and Yussouff [226], but extending on the latter in taking higher-order terms into account, as will be described below. The quantity to be approximated in the DFT of freezing is the excess Helmholtz free energy functional $F_{\text{ex}}[\rho(\mathbf{r})]$, a unique functional of the inhomogeneous one-particle density $\rho(\mathbf{r})$ of the solid [85]. The uniqueness property implies that the excess free energy can be formally expanded about the excess free energy of a homogeneous fluid at a uniform density ρ in terms of density difference $\Delta\rho(\mathbf{r}) = \rho(\mathbf{r}) - \rho$:

$$\beta F_{\text{ex}}[\rho(\mathbf{r})] = \beta F_{\text{ex}}(\rho) - \sum_{n=1}^{\infty} \frac{1}{n!} \int_V d\mathbf{r}_1 \dots d\mathbf{r}_n c_0^{(n)}(\mathbf{r}_1, \dots, \mathbf{r}_n; \rho) \Delta\rho(\mathbf{r}_1) \dots \Delta\rho(\mathbf{r}_n), \quad (4.1)$$

where $\beta = 1/(k_B T)$ and V is the volume occupied of the system. $F_{\text{ex}}(\rho)$ is the Helmholtz excess free energy and the $c_0^{(n)}$ are the n -particle direct correlation func-

tions of the fluid, which are well known up to second order for dipolar fluids.²

Within the theory of Ramakrishnan and Yussouff this series expansion is truncated at second order. We therefore refer to the theory as “second order theory” (SOT). Part of the reason for this truncation lies in poor knowledge about higher than second order correlation functions; the truncation is not well justified in the problem of freezing, since here $\Delta\rho$ is not a small parameter. In particular, it has been extensively shown that the SOT fails to accurately predict freezing for systems interacting via long-range pair potentials for three-dimensional systems [149, 158]. We will show in this work, that also for the two-dimensional dipolar system the SOT highly underestimates the stability of the crystal. Therefore, several approaches have been employed to include higher than second-order terms in the expansion—in a perturbative [55] or non-perturbative way [56, 64, 158, 159].

The simplest attempt to go beyond the SOT is to explicitly include the third order term in the expansion in Eq. (4.1), which we refer to as “third order theory” (TOT). Employing the TOT demands an approximate form of the three-particle direct correlation function $c_0^{(3)}(\mathbf{r}, \mathbf{r}'; \rho)$ of the fluid. We will show here, that—given an accurate expression for $c_0^{(3)}(\mathbf{r}, \mathbf{r}'; \rho)$ —including this term substantially improves the predicted freezing temperature of the long-range $1/r^3$ -fluid (in line with previous findings for long-range interactions in 3D [20]).

A third approach to the DFT we follow here, is the Modified Weighted-Density Approximation (MWDA) [64] by Denton and Ashcroft which we already presented for the dipolar system in brief in Chapter 3. This approach includes first and second order correlation functions of the fluid *exactly* (as in the SOT) and higher order correlation functions in a non-perturbative, implicit fashion. We find that the MWDA, in two dimensions, slightly shifts the freezing transition to higher temperature as compared to the SOT, still highly underestimating the stability of the solid state. In a fourth approach we employ the so called “extended modified weighted-density approximation” (EMA), as suggested in Refs. [158, 159]. Different from the MWDA, this approximation to the density functional now includes not only first and second, but also third order correlation functions of the fluid *exactly* (as in the TOT). Higher than third-order correlation functions are contained in a non-perturbative, implicit fashion, following a similar scheme as in the MWDA. For the dipolar system we find that this approach leads to a very accurate value of the freezing transition temperature, lying slightly above the one obtained from the simpler TOT. The two-particle correlation functions of the liquid are obtained from liquid state integral equation theory and from simulation. The three-particle correlation functions are obtained applying two approximations, both based on the two-particle correlation functions: The first approximation used is by Denton and Ashcroft (DA) [63], and the second is by Barrat, Hansen, and Pastore (BHP) [21].

We find that the inclusion of higher order correlation functions in a perturbative (TOT) or non-perturbative (EMA) way subsequently increase the freezing transition

²See Chapter 3.

temperature, thus broadening the range of the thermodynamical stability of the crystal. In fact, we find the freezing transition temperature to be in good agreement with experiment [306] and simulation [111, 163, 166]. The importance of inclusion of third order correlation functions is addressed to the long-range nature of the dipole-dipole pair interaction.

The rest of this work is organized as follows: In Section 4.2 we give a brief description of the MWDA and of the EMA. In Section 4.3 we apply the different approximations to the DFT to freezing of monodispers two-dimensional liquids. The theory is adapted to the dipolar system under study in Section 4.4. In Section 4.5 we present the resulting phase diagrams and different structural properties of the crystalline system, and we conclude in Section 4.6.

4.2 Modified weighted-density approximation and its extension to third-order correlation functions

It is well known that the intrinsic Helmholtz free energy of an inhomogeneous system can be divided into an “ideal” and an “excess” part,

$$F[\rho(\mathbf{r})] = F_{\text{id}}[\rho(\mathbf{r})] + F_{\text{ex}}[\rho(\mathbf{r})] . \quad (4.2)$$

The “ideal” term

$$F_{\text{id}}[\rho(\mathbf{r})] = \beta^{-1} \int d\mathbf{r} \rho(\mathbf{r}) \{ \ln [\rho(\mathbf{r})\Lambda^2] - 1 \} , \quad (4.3)$$

is known exactly. In Eq. (4.3) Λ is the thermal de Broglie wavelength. The excess part can only be calculated approximately. In contrast to the SOT and TOT, within the MWDA and EMA the excess free energy of the inhomogeneous system is approximated by setting it equal to the excess free energy of a uniform liquid evaluated at a weighted density $\hat{\rho}$,

$$F_{\text{ex}}[\rho(\mathbf{r})] \approx F_{\text{ex}}^{\text{M/E}}[\rho(\mathbf{r})] = N f_0(\hat{\rho}^{\text{M/E}}) , \quad (4.4)$$

where superscripts denote the approximations to the DFT, MWDA (M) and EMA (E), respectively. N is the number of particles in the system and $f_0(\hat{\rho})$ is the excess free energy per particle of the liquid at the weighted density $\hat{\rho}$. The latter is expressed as

$$\begin{aligned} \hat{\rho}^{\text{M/E}}[\rho(\mathbf{r})] = & \frac{1}{N} \int_V d\mathbf{r} \int_V d\mathbf{r}' \rho(\mathbf{r}) \rho(\mathbf{r}') w(\mathbf{r} - \mathbf{r}'; \hat{\rho}) \\ & + \frac{1}{N^2} \int_V d\mathbf{r} \int_V d\mathbf{r}' \int_V d\mathbf{r}'' \rho(\mathbf{r}) \rho(\mathbf{r}') \rho(\mathbf{r}'') \\ & \times v(\mathbf{r} - \mathbf{r}', \mathbf{r} - \mathbf{r}''; \hat{\rho}) , \end{aligned} \quad (4.5)$$

where the second term only appears in the EMA and not in the MWDA. The weight functions $w(\mathbf{r}; \rho)$ and $v(\mathbf{r}, \mathbf{r}'; \rho)$ are determined in such a way that the approximate functional $F_{\text{ex}}^{\text{M/E}}[\rho(\mathbf{r})]$ is exact up to second (MWDA) or third (EMA) order in density difference $\Delta\rho(\mathbf{r}) = (\rho(\mathbf{r}) - \rho)$, i.e., up to that order Eq. (4.4) and Eq. (4.1) do agree. Note that the weighted density $\hat{\rho}$ is determined self-consistently, as it appears as an argument of both weight functions. In order to obtain equality with Eq. (4.1) up to second or third order in $\Delta\rho$ we demand the weight functions to be normalized, i.e.,

$$\int_V d\mathbf{r} w(\mathbf{r}; \rho) + \frac{1}{V} \int_V d\mathbf{r} \int_V d\mathbf{r}' v(\mathbf{r}, \mathbf{r}'; \rho) = 1. \quad (4.6)$$

and to fulfill the requirements

$$\begin{aligned} \lim_{\rho(\mathbf{r}) \rightarrow \rho} \left[\frac{\delta^2 F_{\text{ex}}^{\text{M/E}}}{\delta\rho(\mathbf{r})\delta\rho(\mathbf{r}')} \right] &= -\beta^{-1} c_0^{(2)}(\mathbf{r} - \mathbf{r}'; \rho), \\ \lim_{\rho(\mathbf{r}) \rightarrow \rho} \left[\frac{\delta^3 F_{\text{ex}}^{\text{E}}}{\delta\rho(\mathbf{r})\delta\rho(\mathbf{r}')\delta\rho(\mathbf{r}'')} \right] &= -\beta^{-1} c_0^{(3)}(\mathbf{r} - \mathbf{r}', \mathbf{r} - \mathbf{r}''; \rho), \end{aligned} \quad (4.7)$$

where $c_0^{(2)}(\mathbf{r}; \rho)$ and $c_0^{(3)}(\mathbf{r}, \mathbf{r}'; \rho)$ are the two- and three-particle correlation functions of the liquid with density ρ which are an input to the theory. These conditions uniquely determine the weight functions. In order to obtain the simple algebraic equations for v and w that can be found in Ref. [159] a further approximation has to be made: The inner integral in the second term of Eq. (4.6) is assumed to be equal to a constant, C (demanding the first term in Eq. (4.6) to be equal to $1 - C$), where C is independent of the fixed space coordinate of the weight function $v(\mathbf{r}, \mathbf{r}'; \rho)$. The weighted density $\hat{\rho}$ in Eq. (4.5) is independent of the choice of C [159].

For non-zero wave vectors ($\mathbf{k} \neq 0, \mathbf{k}' \neq 0$, or $\mathbf{k} + \mathbf{k}' \neq 0$), the Fourier transforms of the weight functions $\tilde{w}(k; \rho)$ and $\tilde{v}(\mathbf{k}, \mathbf{k}'; \rho)$ are simply proportional to the Fourier transforms of the second- and third-order direct correlation functions $\tilde{c}_0^{(2)}(k; \rho)$ and $\tilde{c}_0^{(3)}(\mathbf{k}, \mathbf{k}'; \rho)$, respectively:

$$\begin{aligned} -\beta^{-1} \tilde{c}_0^{(2)}(k; \rho) &= 2f'_0(\rho) \tilde{w}(k; \rho), \\ -\beta^{-1} \tilde{c}_0^{(3)}(\mathbf{k}, \mathbf{k}'; \rho) &= 6f'_0(\rho) \tilde{v}(\mathbf{k}, \mathbf{k}'; \rho). \end{aligned} \quad (4.8)$$

Furthermore, Eq. (4.5), together with Eqs. (4.6) and (4.7) guarantee fulfillment of the sum rules

$$\begin{aligned} \beta^{-1} \tilde{c}_0^{(2)\text{M/E}}(k = 0; \rho) &= 2f'_0(\rho) + \rho f''_0(\rho), \\ \tilde{c}_0^{(3)\text{M/E}}(\mathbf{k}, \mathbf{k}' = 0; \rho) &= \tilde{c}_0^{(3)\text{M/E}}(\mathbf{k}, -\mathbf{k}; \rho) = \frac{\partial \tilde{c}_0^{(2)}(k; \rho)}{\partial \rho}, \end{aligned} \quad (4.9)$$

where the former is the compressibility sum rule, and where the superscripts on the correlation functions indicate that these functions are the Fourier transforms of the

functional derivatives of the approximate excess free energy functionals in the limit of constant average density ρ [c.f. Eq. (4.7)]. The primes on the excess free energy density f_0 denote derivatives with respect to density.

Due to the self-consistency requirement, the approximate excess free energies of both the MWDA and the EMA include contributions from arbitrarily many higher orders. However, if expanded about the excess free energy of a fluid with the same average density as the inhomogeneous system according to Eq. (4.1), the MWDA only gives even order terms and estimates the odd order terms zero. Contrary, the EMA includes, approximately, contributions from all higher order terms. In particular, it includes the exact third-order term, which is an input to the theory.

4.3 Application of the different approximations to the DFT to freezing of monodisperse two-dimensional liquids

In order to find the equilibrium one-particle density $\rho_{\text{eq}}(\mathbf{r})$ of a system at a given average density ρ and temperature T we minimize the approximate total free energy functional $F[\rho(\mathbf{r})]$ of Eq. (4.2) with respect to the inhomogeneous one-particle density $\rho(\mathbf{r})$ for fixed ρ . As described, for example, in Refs. [64, 159] this minimization is pursued in a number of subsequent steps, depending on the kind of approximation: For all approximations to the DFT, first, an appropriate parametrization for the inhomogeneous one-particle density is made (we will employ a free minimization in Section 4.5.3). Within the SOT and TOT, we can now, in a second step, calculate the excess and ideal parts of the Helmholtz free energy according to Eqs. (4.1) and (4.3). However, within the MWDA and EMA, the excess part is given by Eq. (4.4), with the weighted density $\hat{\rho}$ obtained in an intermediate step according to Eq. (4.5). In a final step, minimization is carried out with respect to all free variables in the parametrization of $\rho(\mathbf{r})$.

The crystalline one-particle density which we expect to be in equilibrium for low temperature and/or high density has the symmetry of the triangular crystal—the quadratic lattice is thermodynamically unstable for the whole range of accessible densities/coupling constants and we expect mechanical instability with respect to the triangular lattice for any coupling. We can therefore express $\rho(\mathbf{r})$ as a sum over reciprocal lattice vectors (RLV's) of the triangular lattice:

$$\rho(\mathbf{r}) = \rho \left[1 + \sum_{\mathbf{K} \neq 0} \mu_{\mathbf{K}} e^{i\mathbf{K} \cdot \mathbf{r}} \right], \quad (4.10)$$

where ρ is the average density of the solid, $\{\mathbf{K}\}$ is the set of reciprocal lattice vectors (RLV's), and where the $\mu_{\mathbf{K}}$ are the dimensionless Fourier components. In terms of Fourier components the excess part to the Helmholtz free energy within SOT and

TOT [Eq. 4.1] now reads

$$\begin{aligned} \beta F_{\text{ex}}^{\text{S/T}}[\rho(\mathbf{r})]/N &= \beta f_0(\rho) - \frac{\rho}{2} \sum_{\mathbf{K} \neq 0} \mu_{\mathbf{K}}^2 \tilde{c}_0^{(2)}(k; \rho) \\ &- \frac{\rho^2}{6} \sum_{\mathbf{K} \neq 0} \sum_{\mathbf{K}' \neq 0, -\mathbf{K}} \mu_{\mathbf{K}} \mu_{\mathbf{K}'} \mu_{-(\mathbf{K}+\mathbf{K}')} \tilde{c}_0^{(3)}(\mathbf{K}, \mathbf{K}'; \rho), \end{aligned} \quad (4.11)$$

the superscript referring to the SOT (S) and to the TOT (T), respectively. The third term only appears in the TOT.

Within the MWDA and EMA, the weighted density, Eq. (4.5), now reads

$$\hat{\rho}^{\text{M/E}} = \rho \left\{ 1 + \sum_{\mathbf{K} \neq 0} \mu_{\mathbf{K}}^2 w(K; \hat{\rho}) + \rho \sum_{\mathbf{K} \neq 0} \sum_{\mathbf{K}' \neq 0, -\mathbf{K}} \mu_{\mathbf{K}} \mu_{\mathbf{K}'} \mu_{-(\mathbf{K}+\mathbf{K}')} \left[\frac{v(\mathbf{K}, \mathbf{K}'; \hat{\rho})}{N} \right] \right\} \quad (4.12)$$

As in Eq. (4.5) the three-particle term only appears in the EMA.

Since a free minimization of the approximate Helmholtz free energy with respect to an infinite number of Fourier components $\mu_{\mathbf{K}}$ at all RLV's is intractable, we make a simple ansatz for the one-particle density which is a superposition of normalized Gaussians centered around the lattice sites of the triangular lattice:

$$\rho(\mathbf{r}) = \frac{n_c \alpha}{\pi} \sum_{\mathbf{R}} \exp[-\alpha |\mathbf{r} - \mathbf{R}|^2], \quad (4.13)$$

where α is the localization strength, n_c is the average number of particles occupying a lattice site, yielding a vacancy concentration $n_v = 1 - n_c$, and $\{\mathbf{R}\}$ is the set of Bravais lattice vectors of the triangular lattice with lattice constant $a = (\sqrt{3}n_c/2\rho)^{1/2}$. Thus, the Fourier components $\mu_{\mathbf{K}}$ now simply read

$$\mu_{\mathbf{K}} = e^{-\mathbf{K}^2/4\alpha}. \quad (4.14)$$

The ansatz, Eq. (4.13), was chosen in such a way that the system forms a triangular lattice for any finite α keeping its average density ρ fixed. For $\alpha \rightarrow 0$ the density profile becomes flat and the system turns into a liquid. We thus end up with two minimization parameters α and n_c .

This ansatz disregards a possible partition of the system into coexisting liquid and crystal phases of different densities keeping the overall average density fixed. However, this is accounted for by performing a common-tangent construction to the crystal and liquid volume free energy densities in the end. Furthermore, Eq. (4.13) disregards the spatial anisotropy of the density site profile at each lattice site. We will see in Section 4.5.3, where we relax the constraint on the density peaks, that both, the assumption of isotropy and the Gaussian shape are well justified close to the positions of the Bravais lattice vectors, i.e., where the density is reasonably large ($\rho(r) \gtrsim \rho$).

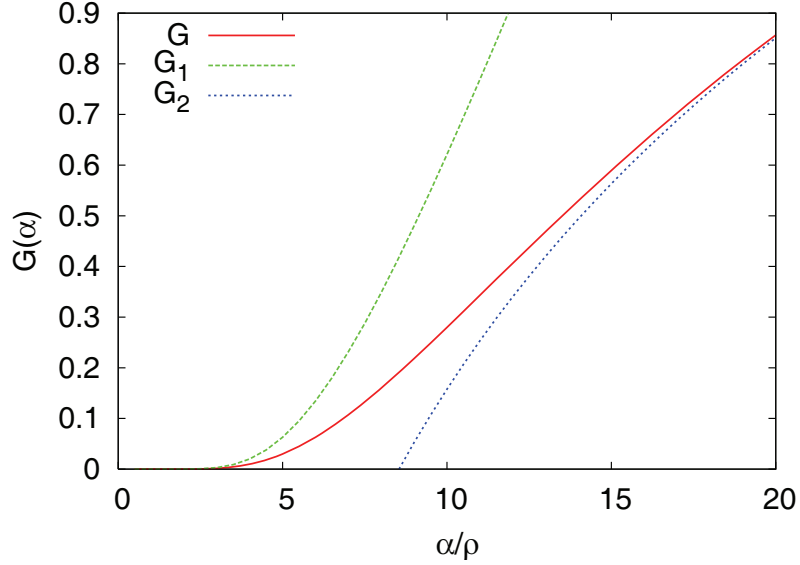


Figure 4.1: The function $G(\alpha/\rho)$ and its analytically known asymptotics for small and large localization strength.

Employing the ansatz of Eq. (4.13) for the inhomogeneous density, the ideal part of the Helmholtz free energy [Eq. (4.3)] can now be written as a function of α and n_c only: $F_{\text{id}}[\rho(\mathbf{r})] = F_{\text{id}}(\alpha, n_c; \rho)$. For $n_c = 1$ it reads

$$\frac{\beta}{N} F_{\text{id}}(\alpha, n_c = 1; \rho) = \text{const} + \ln(\rho L^2) + G(\alpha^*), \quad (4.15)$$

$$G(\alpha^*) = \int_{A_1} d\mathbf{x} \frac{\rho(\mathbf{x}, \alpha^*, n_c = 1)}{\rho} \ln \left[\frac{\rho(\mathbf{x}, \alpha^*, n_c = 1)}{\rho} \right], \quad (4.16)$$

where const is an irrelevant constant and L is a density-independent length scale of the system. $\mathbf{x} = \mathbf{r}\rho^{1/2}$ and $\alpha^* = \alpha/\rho$ are the dimensionless space coordinate and localization strength, respectively, and the integral is performed over the area A_1 of a unit cell. The function $G(\alpha^*)$ is approximated for small and large localization strengths by its analytically known asymptotics

$$G(\alpha^*) \simeq \begin{cases} G_1(\alpha^*) = \sum_{\mathbf{K}_* \neq 0} \exp[-\mathbf{K}_*^2/2\alpha^*], & \alpha^* \ll 1 \\ G_2(\alpha^*) = \ln(\alpha^*/\pi) - 1, & \alpha^* \gg 1, \end{cases} \quad (4.17)$$

where $\mathbf{K}_* = \mathbf{K}/\rho$ are the dimensionless RLV's. For intermediate values of $2 \leq \alpha^* \leq 50$ the function $G(\alpha^*)$ was calculated numerically. The function $G(\alpha^*)$ and the asymptotics of Eq. (4.17) are plotted as a function of α^* in Fig. 4.1.

The ideal free energy for values $n_c \neq 1$ is obtained via the simple scaling relation

$$\frac{\beta}{N} F_{\text{id}}(\alpha, n_c, \rho) = \text{const} + \ln(\rho L^2) + G(n_c \alpha^*). \quad (4.18)$$

4.4 The dipolar system

We now turn to the system of monodisperse particles which repel each other with an inverse-power pair potential $u(r) = u_0/r^3$, where u_0 is a parameter with dimensions of energy \times volume. For the specific realization of two-dimensional paramagnetic colloids of susceptibility χ exposed to a magnetic field \mathbf{B} which is directed perpendicular to the 2D plane, we have $u_0 = (\chi\mathbf{B})^2/2$ in Gaussian units [93]. Here, we assume perfect alignment of the magnetic dipoles with the external field which is well justified for $\chi B^2 \gg k_B T$ [307]. The thermodynamics and structure depend, due to simple scaling, only on one relevant dimensionless coupling parameter [288]

$$\Gamma = \frac{u_0 \rho^{3/2}}{k_B T}. \quad (4.19)$$

Therefore, it is convenient to express all quantities in terms of Γ and consider coupling parameters rather than densities via this scaling relation. Correspondingly, the excess free energy within the SOT and TOT now read

$$\begin{aligned} \beta F_{\text{ex}}^{\text{S/T}}(\Gamma, \alpha)/N &= \beta f_0(\Gamma) - \frac{1}{2} \sum_{\mathbf{K} \neq 0} e^{-K^2/4\alpha} \hat{c}_0^{(2)}(K; \Gamma) \\ &- \frac{1}{6} \sum_{\mathbf{K} \neq 0} \sum_{\mathbf{K}' \neq 0, -\mathbf{K}} e^{-(K^2+K'^2+(\mathbf{K}+\mathbf{K}')^2)/4\alpha} \hat{c}_0^{(3)}(\mathbf{K}, \mathbf{K}'; \Gamma), \end{aligned} \quad (4.20)$$

the third term only appearing in the TOT. Here, Γ is the coupling constant corresponding to the average density ρ according to Eq. (4.19), $\hat{c}_0^{(2)} = \rho \tilde{c}_0^{(2)}$, and $\hat{c}_0^{(3)} = \rho^2 \tilde{c}_0^{(3)}$ are the dimensionless correlation functions of the fluid in reciprocal space, respectively.

For the MWDA and EMA, the weighted coupling constants $\hat{\Gamma}$ now read

$$\begin{aligned} \hat{\Gamma}(\Gamma, \alpha) &= \Gamma \left[1 - \frac{1}{3\beta \hat{\Gamma} f'_0(\hat{\Gamma})} \sum_{\mathbf{K} \neq 0} e^{-K^2/2\alpha} \hat{c}_0^{(2)}(K; \hat{\Gamma}) \right. \\ &\left. - \frac{\Gamma^{2/3}}{9\beta \hat{\Gamma}^{5/3} f'_0(\hat{\Gamma})} \sum_{\mathbf{K} \neq 0} \sum_{\mathbf{K}' \neq 0, -\mathbf{K}} e^{-(K^2+K'^2+\mathbf{K}\mathbf{K}')/2\alpha} \hat{c}_0^{(3)}(\mathbf{K}, \mathbf{K}'; \hat{\Gamma}) \right]^{3/2}, \end{aligned} \quad (4.21)$$

where $f'_0(\Gamma)$ is the derivative of the excess free energy density with respect to coupling constant. As in Eq. (4.12) the third term only appears in the EMA.

In order to solve Eqs. (4.20) and (4.21) we need the two- and three-particle correlation functions $\hat{c}_0^{(2)}(k; \Gamma)$ and $\hat{c}_0^{(3)}(k; \Gamma)$ and the excess free energy density $f_0(\Gamma)$ of the corresponding liquid for a wide range of coupling constants Γ . The two-particle correlation function is obtained with liquid state integral equation theory or from computer simulations. In the first case, following the procedure described

in Ref. [126] we solve the Ornstein-Zernicke (OZ) Eq. [117]

$$\hat{h}(k) = \frac{\hat{c}_0^{(2)}(k)}{1 - \hat{c}_0^{(2)}(k)}, \quad (4.22)$$

which relates the dimensionless Fourier transform $\hat{h}(k) = \rho \tilde{h}(k)$ of the total correlation function $h(r)$ to the direct pair correlation function $\hat{c}_0^{(2)}(k)$, numerically. Note that the density has been absorbed in both the Fourier transform of the total correlation function $\hat{h}(k)$ and in the direct correlation function $\hat{c}_0^{(2)}(k)$. The total correlation function is connected to the pair distribution function via $g(r) = h(r) + 1$.

The solution of Eq. (4.22) for the two unknown quantities $\hat{h}(k)$ and $\hat{c}_0^{(2)}(k)$ demands a constitutive equation, the so called closure relation which for any non-trivial case can only be determined approximatively. Two approaches which proved successful for the description of fluids with long-range interactions will be applied here, the hypernetted chain (HNC) [117] and the Rogers-Young (RY) closure relation [239]. They can both be written as

$$h(r) = e^{-\beta u(r)} \{1 + f(r)^{-1} (e^{\chi(r)f(r)} - 1)\} - 1, \quad (4.23)$$

where $\chi(r) = h(r) - c_0^{(2)}(r)$ is the indirect correlation function. $f(r) = 1 - e^{-\xi r}$ is a ‘mixing function’ with an adjustable parameter $0 \leq \xi \leq \infty$ which is either sent to infinity (HNC)—which is equivalent to letting $f(r) \rightarrow 1$ —or chosen to guarantee thermodynamic consistency between virial and compressibility route to the free energy (RY).

The coupled Eqs. (4.22) and (4.23) are iteratively solved by applying the method of fast Fourier transforms for radially symmetric two-dimensional problems as suggested by Caillol *et al* [39] and as also summarized in appendix A of [126]. In order to reach rapid convergence an iteration procedure for the indirect correlation function $\chi(r)$ is used, since its Fourier transform, $\tilde{\chi}(k)$, decays more rapidly with increasing k than $\tilde{h}(k)$. The iteration scheme now consists of making an ansatz for $c_0^{(2)}$, calculating χ according to Eq. (4.22), obtaining the next estimate of $c_0^{(2)}$ via Eq. (4.23), inserting this into Eq. (4.22), etc., until convergence is obtained.

Applying this procedure we are able to calculate $\hat{c}_0^{(2)}(k; \Gamma)$ for coupling constants Γ much larger than the experimentally known coupling of freezing $\Gamma_f \approx 10$ [306] which enables us to calculate the Helmholtz free energy of the system deep inside the thermodynamically stable crystalline region.

More accurate pair correlation functions can be obtained from computer simulations. We have performed extensive Monte Carlo computer simulations [4] in a quadratic simulation box of size $L \times L$ comprising 900 particles employing periodic boundary conditions in order to measure the pair distribution function $g_s(r) = h_s(r) + 1$, the subscript ‘s’ denoting the simulation result. Since the accessible range of $h_s(r)$ is limited to distances r smaller than a cutoff radius $r_c \lesssim L/2$ we employed an extrapolation technique suggested by Verlet [280] to obtain the complete

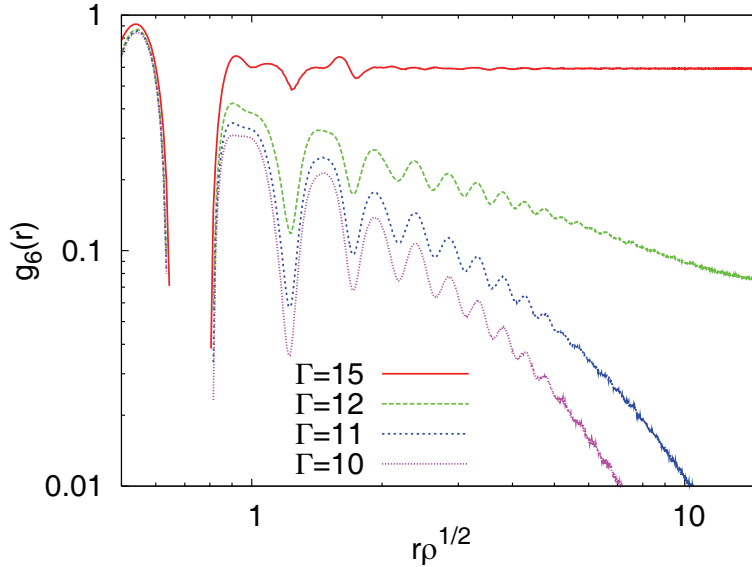


Figure 4.2: The bond-orientational order parameter $g_6(\mathbf{r})$ for different coupling constants Γ as obtained by computer simulation. g_6 decays exponentially for coupling constants $\Gamma \lesssim 11$ indicating the system to be in the fluid state.

pair correlation function: Verlet defined a closure relation to the Ornstein-Zernicke equation

$$\begin{aligned} h(r) &= h_s(r), & r < r_c, \\ c_0^{(2)}(r) &= c_{\text{HNC}}^{(2)}(r), & r > r_c, \end{aligned} \quad (4.24)$$

where $c_{\text{HNC}}(r)$ is given in Eq. (4.23). The Verlet closure relation [Eq. (4.24)] together with the Ornstein-Zernicke equation [Eq. (4.22)] uniquely specify the direct correlation function $c_0^{(2)}(r)$ for all radii r and thus also yield the correlation function in reciprocal space $\hat{c}_0^{(2)}(k)$. As for the HNC and the RY closures the Ornstein-Zernicke equation and the Verlet closure were solved iteratively via the indirect correlation function χ . Furthermore, r_c was chosen the largest root of $h(r)$ still smaller than $L/2$.

For the Verlet data we checked that the simulated system does not crystallize for coupling constants $\Gamma \lesssim 11$. Here, the freezing-criterion was chosen a non-exponential decay of the bond-orientational order parameter $g_6(\mathbf{r}) = \langle \exp[i6[\theta(\mathbf{r}) - \theta(\mathbf{r}')]] \rangle$, where $\theta(\mathbf{r})$ is the angle of the bond connecting two neighboring particles according to the Voronoi construction (see Fig. 4.2). The application of the Verlet closure within the DFT formalism was thus restricted to the range $0 \leq \hat{\Gamma} \lesssim 11$.

The Fourier transforms $\hat{c}_0^{(2)}(k)$ of the two-particle direct correlation functions obtained from the three different closure relations (HNC, RY, Verlet) are shown in Fig. 4.3 for $\Gamma = 9$, which is close to the experimentally determined coupling constant

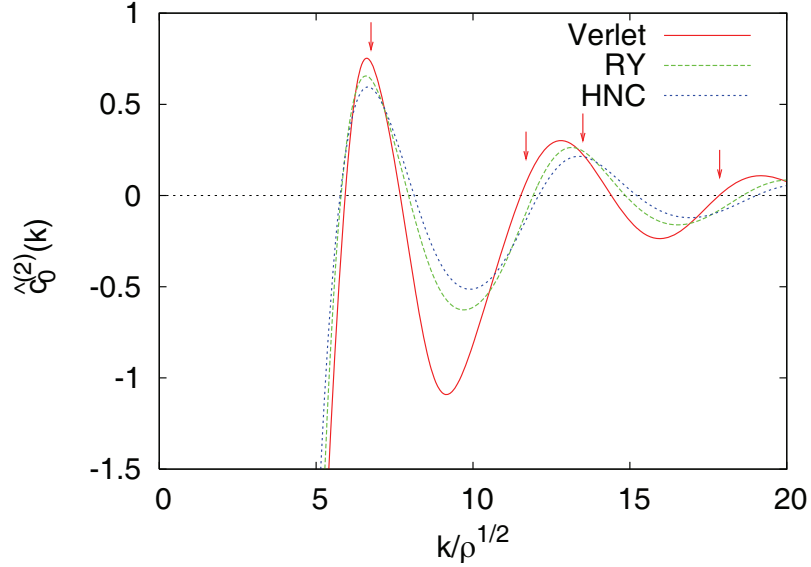


Figure 4.3: The dimensionless Fourier transform $\hat{c}_0^{(2)}(k)$ of the two-particle direct correlation function at $\Gamma = 9$, plotted against $k/\rho^{1/2}$. Shown are simulation data using the Verlet closure, liquid integral equation theory using the RY closure, and liquid integral equation theory using the HNC closure. The arrows indicate the positions of the first four reciprocal lattice vectors of the triangular lattice.

of freezing $\Gamma_f \simeq 10$ [306]. The HNC closure underestimates the pair structure strongly while the RY closure is closer to the simulation data. We also show the positions of the first four reciprocal lattice vectors of the triangular lattice with lattice constant $a = (\sqrt{3}/2\rho)^{1/2}$. The value of $\hat{c}_0^{(2)}$ at these lattice vectors crucially influences the solid free energies, as can be seen from Eqs. (4.20) and (4.21).

Within the RY-approach the excess free energy density f_0 is obtained by integrating the compressibility which is inversely proportional to the static structure factor:

$$\beta f_0(\Gamma) = \frac{2}{3} \int_0^\Gamma \frac{d\Gamma'}{\Gamma'} \left[\frac{\beta P}{\rho} - 1 \right], \quad (4.25)$$

where the pressure P is given by

$$\frac{\beta P}{\rho} - 1 = -\frac{2}{3\Gamma^{2/3}} \int_0^\Gamma \frac{d\Gamma'}{\Gamma'^{1/3}} \hat{c}_0^{(2)}(k=0; \Gamma'). \quad (4.26)$$

In order to obtain the excess free energy density from the simulation data we make use of the relation [23]

$$\beta \langle u_{\text{ex}} \rangle = \beta \frac{\partial \beta f_0}{\partial \beta} = \Gamma \frac{\partial \beta f_0}{\partial \Gamma} \quad (4.27)$$

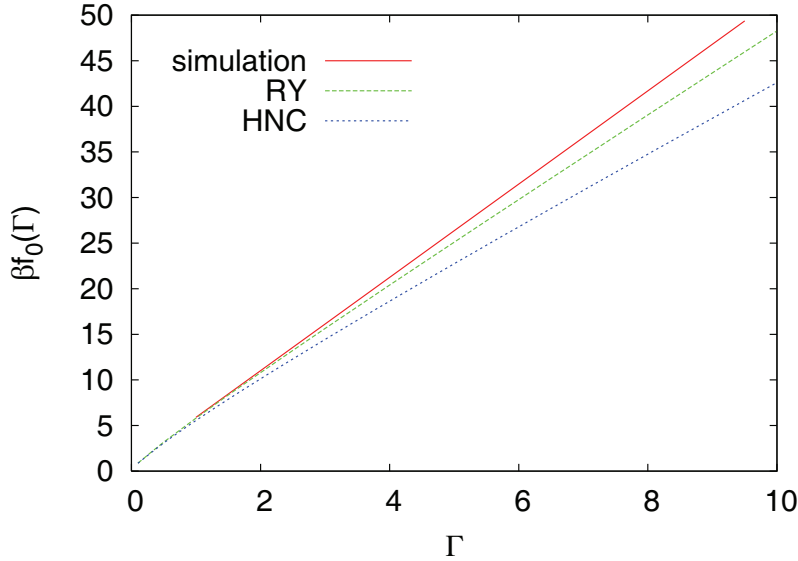


Figure 4.4: The excess free energy density $\beta f_0(\Gamma)$ as a function of coupling constant Γ using the Verlet closure, the RY closure and the HNC closure.

between the average excess energy density $\langle u_{\text{ex}} \rangle = \frac{1}{2} \langle \sum_{i \neq j} u_{i,j} \rangle$ and f_0 and integrate the former. Note that for both of our approaches, the RY and the Verlet closure, the virial and the compressibility route are equivalent. As the energy dominates the free energy in the strong coupling limit, $\Gamma \gtrsim 1$, the excess free energy density scales roughly linearly with coupling constant, as can be seen from Fig. 4.4.

For the EMA we need the three-particle correlation function $\tilde{c}_0^{(3)}(\mathbf{k}, \mathbf{k}'; \rho)$ of the underlying fluid for a wide range of coupling constants. We use here two conceptually different approximations: The first approximation is by Denton and Ashcroft [63] (DA) which is based on a weighted density approximation to the first order direct correlation function $c^{(1)}(\mathbf{r}; \rho(\mathbf{r}))$ of an inhomogeneous system. The DA approach leads to an analytic expression of $\tilde{c}_0^{(3)}$ in terms of the one- and two-particle correlation functions $c_0^{(1)}$, $\tilde{c}_0^{(2)}$ of the liquid and their derivatives with respect to density:

$$\tilde{c}_0^{(3)\text{DA}}(\mathbf{k}, \mathbf{k}') = \frac{1}{3} \left[\tilde{f}^{\text{DA}}(|\mathbf{k}|, |\mathbf{k}'|) + \tilde{f}^{\text{DA}}(|\mathbf{k}|, |\mathbf{k} + \mathbf{k}'|) + \tilde{f}^{\text{DA}}(|\mathbf{k}'|, |\mathbf{k} + \mathbf{k}'|) \right], \quad (4.28)$$

where

$$\tilde{f}^{\text{DA}}(k, k') = \frac{1}{c_0^{(1)'}} \left[\tilde{c}_0^{(2)}(k) \tilde{c}_0^{(2)'}(k') + \tilde{c}_0^{(2)'}(k) \tilde{c}_0^{(2)}(k') \right] - \frac{c_0^{(1)''}}{[c_0^{(1)'}]^2} \tilde{c}_0^{(2)}(k) \tilde{c}_0^{(2)}(k'). \quad (4.29)$$

Here, primes denote derivatives with respect to density, as above. The DA approximation—by construction—fulfills the symmetry condition

$$\tilde{c}_0^{(3)\text{DA}}(\mathbf{k}, \mathbf{k}') = \tilde{c}_0^{(3)\text{DA}}(\mathbf{k}, \mathbf{k} + \mathbf{k}') = \tilde{c}_0^{(3)\text{DA}}(\mathbf{k}', \mathbf{k} + \mathbf{k}'). \quad (4.30)$$

The derivatives $\tilde{c}_0^{(2)'}(k)$ were obtained by applying a simple finite difference method bearing in mind that

$$\rho^2 \tilde{c}_0^{(2)'}(k; \rho) = \frac{1}{2} \left[3\Gamma \frac{\partial \hat{c}_0^{(2)}(k\rho^{-1/2}; \Gamma)}{\partial \Gamma} - k\rho^{-1/2} \frac{\partial \hat{c}_0^{(2)}(k\rho^{-1/2}; \Gamma)}{\partial k\rho^{-1/2}} - 2\hat{c}_0^{(2)}(k\rho^{-1/2}; \Gamma) \right]. \quad (4.31)$$

We calculated $\tilde{c}_0^{(3)\text{DA}}(\mathbf{k}, \mathbf{k}')$ taking the direct correlation function from both the RY and the Verlet closure. As pointed out in Refs. [63, 159, 242] the DA model, although itself not derived from a free energy functional but from an approximate one-particle correlation function, is very similar to different approaches, all based on taking three successive functional derivatives of approximate free energy functionals.

We also employed another approximation for $c_0^{(3)}$, namely a factorization ansatz of Barrat, Hansen and Pastore (BHP) [20]. The approximation reads

$$c_{\text{BHP}}^{(3)}(\mathbf{r}, \mathbf{r}') = t(r)t(r')t(|\mathbf{r} - \mathbf{r}'|). \quad (4.32)$$

The function $t(r)$ can be uniquely determined from the second of the sum rules in Eq. (4.9) which in r -space now reads

$$\int d\mathbf{r}' c_0^{(3)}(\mathbf{r}, \mathbf{r}'; \rho) = \int d\mathbf{r}' t(r)t(r')t(|\mathbf{r} - \mathbf{r}'|) = \frac{\partial c_0^{(2)}(r; \rho)}{\partial \rho}. \quad (4.33)$$

We solved Eq. (4.33) numerically for $t(r)$ applying the method of ‘steepest descent’ as outlined in appendix B of reference [20]. As opposed to the simple finite difference approach above the derivatives $c_0^{(2)'}(k)$ were now obtained by iteratively solving the coupled differentiated Ornstein-Zernicke equation and the differentiated RY closure relation, as outlined in appendix B of [20]. Since it proved difficult to reach convergence of the iteration procedure we did not pursue this method using the Verlet closure. The triplet-correlation function was then obtained by a double Fourier transform of Eq. (4.33) using a standard expansion in Legendre polynomials, as outlined in appendix A of [20].

In the single summation in Eq. (4.21) we consider all RLV’s of absolute value $|\mathbf{K}| \leq 33|\mathbf{K}_1|$, where \mathbf{K}_1 is the smallest RLV of the triangular lattice—this comprises the first 299 stars of RLV’s, which is by far sufficient to reach convergence of the single summation. The double summation is performed over sets of equivalent triangles of RLV’s which are each characterized by the absolute values of the two RLV’s \mathbf{K} and \mathbf{K}' , and by the absolute value of there included angle. For the DA model and for the BHP model we include 42 sets of triangles of RLV’s, where that RLV of the three RLV’s, \mathbf{K} , \mathbf{K}' , $\mathbf{K} - \mathbf{K}'$, with the largest absolute value satisfies $|\mathbf{K}| \leq 4|\mathbf{K}_1|$, which also guarantees convergence of the double sum.

4.5 Results

We first study the influence of the explicit inclusion of the triplet correlation functions obtained with the DA model and with the BHP model on the approximate excess free energy according to the TOT as compared to the simpler SOT, and according to the EMA as compared to the MWDA, respectively. For all six approaches we use the two different closure relations of Rogers and Young [Eq. (4.23)], and of Verlet [Eq. (4.24)], respectively.

4.5.1 Gaussian profiles, no vacancies

In order to keep things simple in the beginning we keep the number of particles occupying a lattice site, n_c , in Eq. (4.13) fixed (i.e., $n_c = 1$) and thus end up with a single order parameter, the dimensionless localization strength $\alpha^* \equiv \alpha/\rho$.

In Fig. 4.5 we show the weighted coupling constant and the associated excess free energy difference per particle between the solid and the liquid state $F_{\text{ex}}(\alpha^*)/N - f_0$, according to Eq. (4.4), as functions of localization strength α^* for a value of $\Gamma = 9$ which is close to the experimentally known value of freezing, $\Gamma_f \simeq 10$ [306], for the MWDA and for the EMA, using the RY or the Verlet approach to the direct correlation function and using the two different approaches for the triplet correlation function, the DA and the BHP model. The latter are both based on the direct correlation functions used for the respective two-particle term. In Fig. 4.6(a) the excess free energy for the simpler SOT and TOT are plotted as a function of α^* for the same approximations to the correlation functions. In Fig. 4.6(b) the non-perturbative and the perturbative approaches are compared. Different interesting features of the different approximations are observed:

(i) For all approaches used except for those where $c_0^{(3)}$ is obtained within the BHP model the excess free energy decreases monotonically with increasing localization strength α^* , reaching a plateau for $\alpha^* \approx 400$ [c.f. Figs. 4.5(b) and 4.6(a)]. However, employing the BHP model to the triplet-correlation function leads to an increase of $\hat{\Gamma}(\alpha^*)$ and $F_{\text{ex}}(\alpha^*)$ for values of $\alpha^* \gtrsim 80$. The former behavior is intuitively expected and has also been observed in the original MWDA [64]—localization is favoured by the excess part of the free energy. Once the density peaks become very narrow, a further increase of α^* does not change the excess free energy further. On the other hand, the rise of $\hat{\Gamma}$ and of F_{ex} within the BHP model is regarded as unphysical. We therefore do not consider the BHP model any further.

(ii) Both within the DA model and within the BHP model (for $\alpha^* \lesssim 80$) the sign of the third term in Eq. (4.21) is negative, i.e., the value of $\hat{\Gamma}$ is decreased as compared to the pure MWDA and thus freezing is favoured. It is also interesting to note, that within the DA model the triplet-part in Eq. (4.21) is much smaller than the second-order term while it is significantly larger within the BHP model. This same behavior had already been found for hard spheres in three dimensions [159].

(iii) Although the direct correlation functions using the RY- and the Verlet-

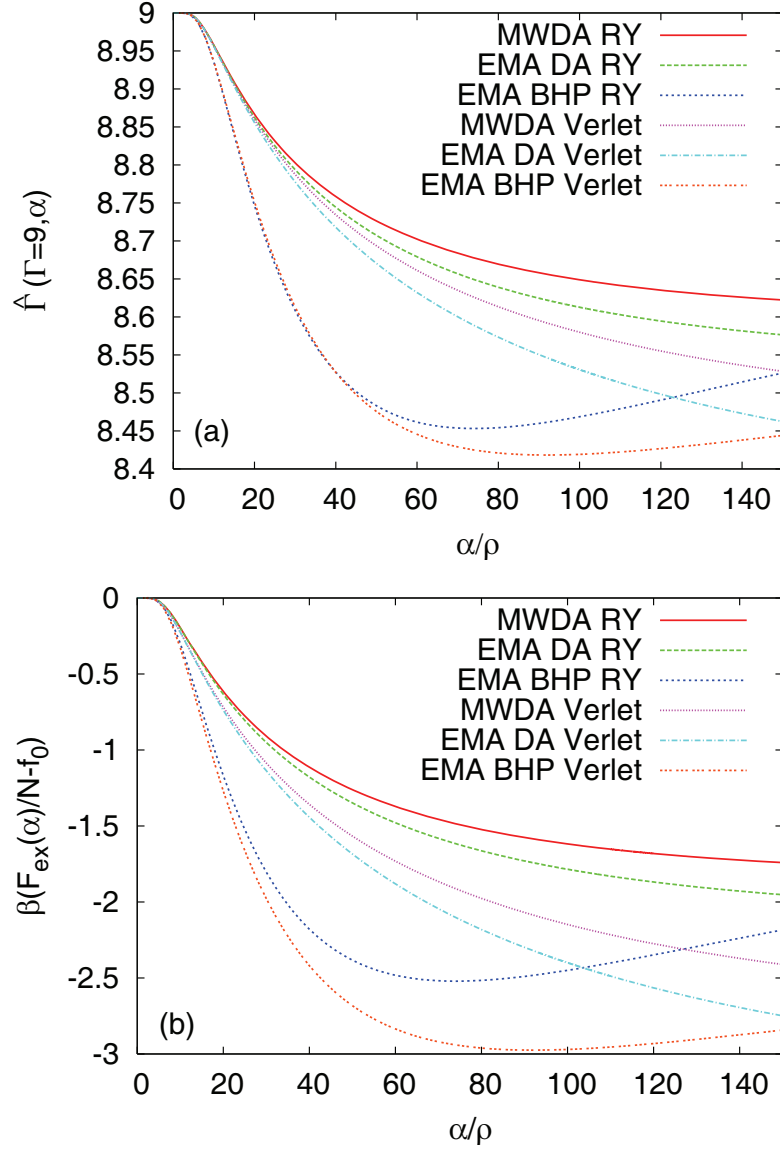


Figure 4.5: (a) The weighted coupling constant as a function of α^* within the MWDA and within the EMA using $c_0^{(2)}$ from the RY and from the Verlet closure, and using $c_0^{(3)}$ from the DA and the BHP model for $\Gamma = 9$. (b) The approximate excess free energy difference per particle $f_0(\hat{\Gamma}(\alpha^*)) - f_0(\Gamma)$ as a function of α^* for the same approximations as in (a).

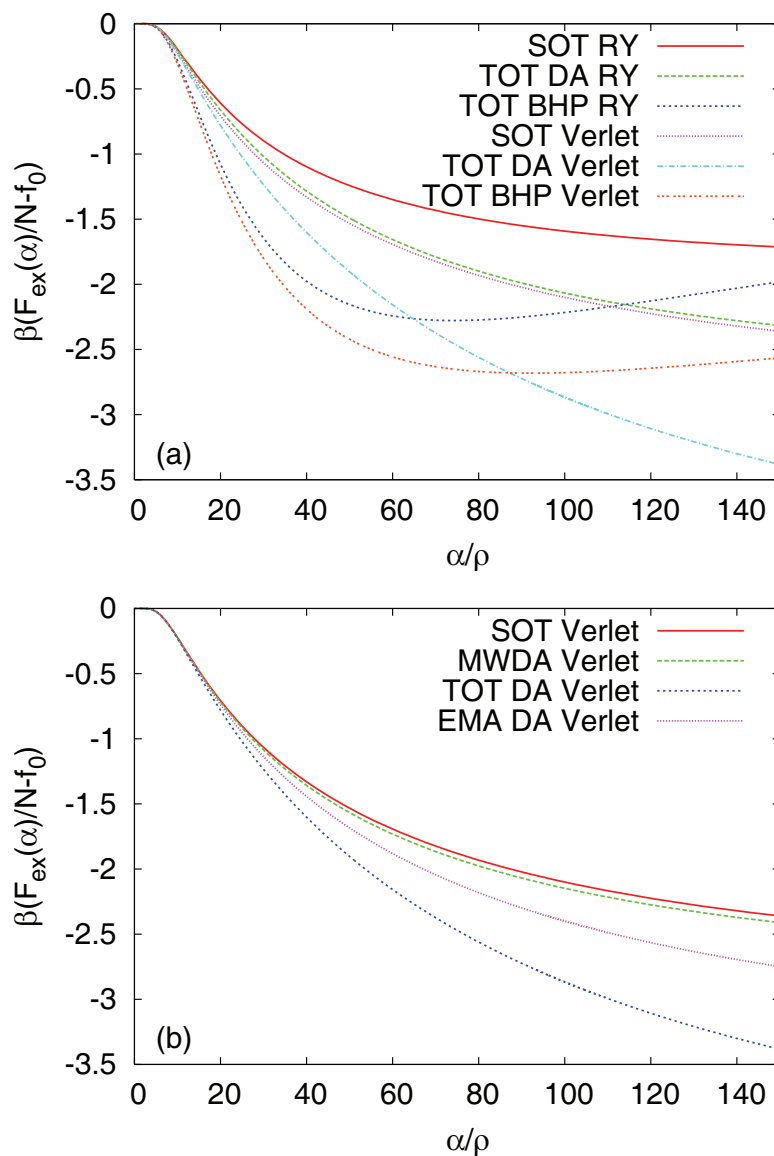


Figure 4.6: (a) The approximate excess free energy difference per particle $F_{\text{ex}}(\alpha^*)/N - f_0(\alpha^* = 0)$ as a function of α^* obtained within the SOT and TOT using the same approximations for the two- and three-particle correlation functions as in Fig. 4.5 for $\Gamma = 9$. (b) Comparison of F_{ex} obtained within the four different approximate theories MWDA, EMA, SOT, and TOT using $c_0^{(2)}$ from the Verlet closure, and using $c_0^{(3)}$ from the DA model for $\Gamma = 9$.

closures do not differ by more than $\sim 10\%$ at the position of the most important first RLV (cf. Fig. 4.4) the difference in $\hat{\Gamma}$ between the two is quite pronounced which is due to the self-consistency relation in Eq. (4.21). Furthermore, as shown in Fig. 4.5(b) the difference in excess free energy is even more enhanced.

(iv) Inclusion of higher than second-order terms in a non-perturbative way within the MWDA reduces the excess free energy as compared to the simpler SOT [c.f. Fig. 4.6(b)]. However, inclusion of higher than third-order terms within the EMA increases the excess free energy with respect to the TOT.

The total Helmholtz free energy per particle is obtained by adding to the excess part F_{ex} the ideal part F_{id} according to Eq. (4.2). The free energy difference per particle $\Delta F/N = [F(\alpha^*; \Gamma) - F(\alpha^* = 0; \Gamma)]/N$ is plotted in Fig. 4.7 as a function of α^* , for the same value of $\Gamma = 9$ as in Fig. 4.5 for the SOT and TOT [Fig. 4.7(a)], and for the MWDA and EMA [Fig. 4.7(b)], respectively, using $c_0^{(2)}$ from the RY and from the Verlet closure, and using $c_0^{(3)}$ obtained within the DA model. It is found that the different curves of $\Delta F/N$ show qualitatively very different behavior for the coupling of $\Gamma = 9$: While the free energy increases monotonically with α^* within the SOT and MWDA and within the TOT and EMA employing the RY closure it displays a local minimum with respect to α^* at a finite value of α^* within the EMA and TOT, employing the Verlet closure, this local minimum even turning the deep global minimum within the TOT at $\alpha^* \approx 213$. The appearance of a global minimum at a finite value of α^* corresponds to a thermodynamically stable crystalline state while the global minimum at $\alpha^* = 0$ indicates a stable fluid system.

In Fig. 4.8, we display the total free energy obtained within the EMA employing the DA model with the Verlet closure for three different values of $\Gamma = 9.0, 9.4, 9.8$. We thus conclude from Fig. 4.8—this has already been presented in Chapter 3—that the EMA employing the Verlet closure and the DA model yields a transition from the fluid to the solid close to $\Gamma = 9.4$: while for $\Gamma = 9.0$ the fluid is stable as indicated by the minimal value at $\alpha^* = 0$, fluid-solid coexistence is achieved at $\Gamma = 9.4$ (see the two equal minima in Fig. 4.8). The solid phase, on the other hand, is clearly stable for $\Gamma = 9.8$. The localization parameter at coexistence is roughly $\alpha_{\text{min}}^* \approx 100$.

The curves always displays a local minimum with respect to α^* at $\alpha^* = 0$. This is in accordance with the mean-field character of any approximation to the DFT, which ignore fluctuations leading to a breakdown of long-range order in one and two dimensions. Therefore, a first-order transition between fluid and solid state is always predicted, i.e., the liquid system always has to overcome a free energy barrier in order to reach the thermodynamically stable crystalline state.

The freezing and melting transition constants for the first-order phase transition predicted by the different approximations to the DFT, Γ_s and Γ_f , respectively, are obtained by using Maxwell's double tangent construction to the fluid and crystal volume free energy densities $\Gamma^{2/3}F/N \propto F/V$, where F denotes the minimum free energy with respect to α , and $\Gamma^{2/3}$ is proportional to the average density ρ

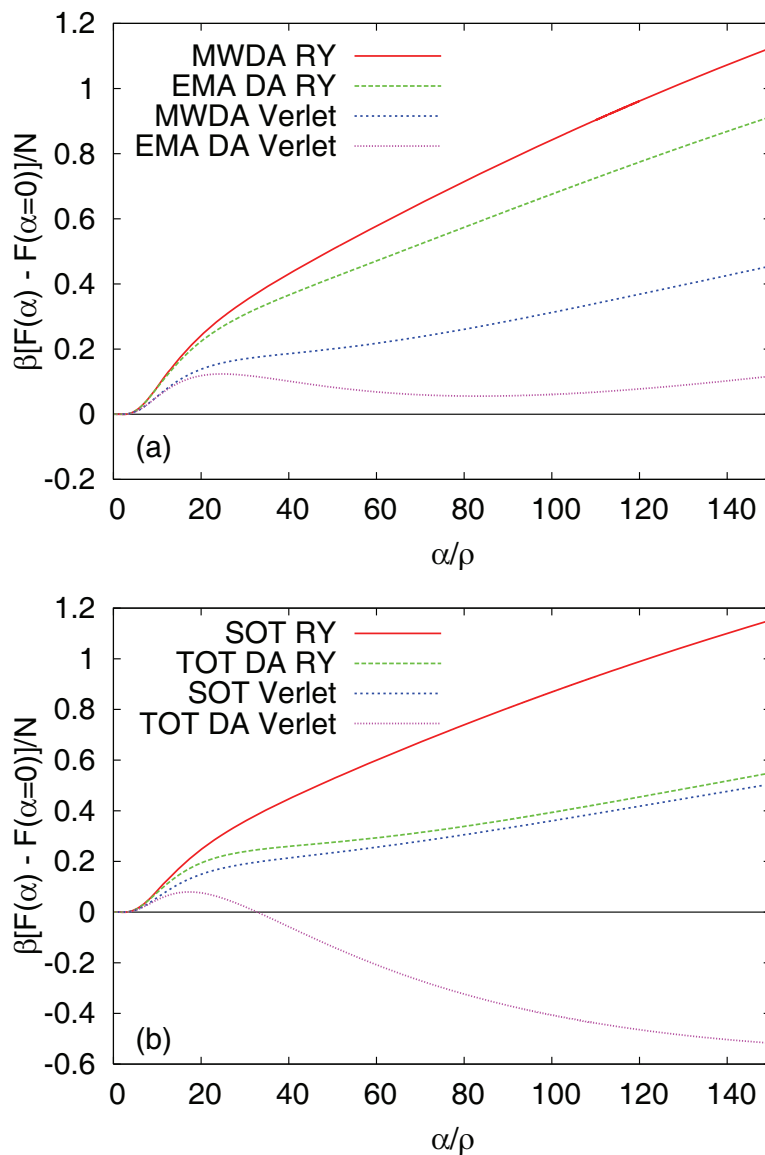


Figure 4.7: The total free energy difference per particle $\Delta F(\Gamma)/N$ as a function of α^* within the MWDA and EMA (a), and within the SOT and TOT (b) using $c_0^{(2)}$ from the RY and from the Verlet closure, and using $c_0^{(3)}$ from the DA model for $\Gamma = 9$.

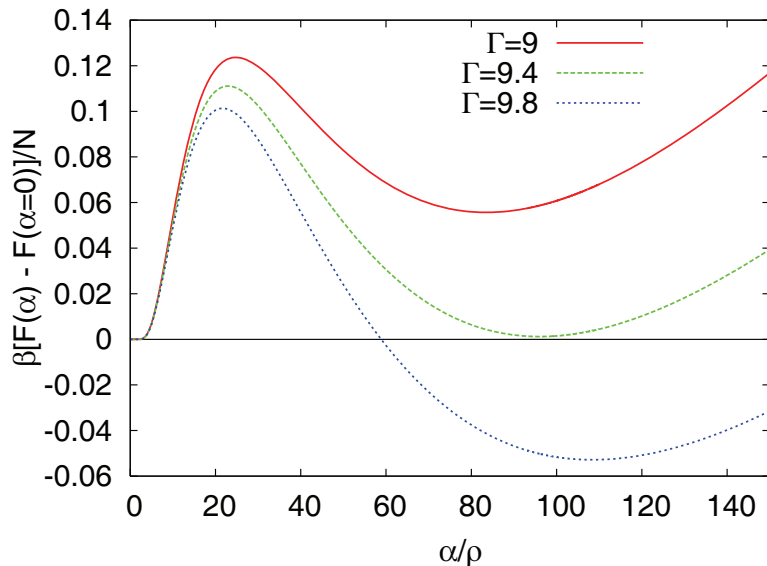


Figure 4.8: The total free energy difference per particle $\Delta F(\Gamma)/N$ as a function of α^* within the EMA using $c_0^{(2)}$ from the Verlet closure, and using $c_0^{(3)}$ from the DA model for $\Gamma = 9, 9.4, 9.8$.

of the system [c.f. Eq. (4.19)]. Γ_s and Γ_f correspond to the freezing and melting densities, ρ_s and ρ_f , respectively. The volume free energy density is exemplarily shown for the EMA using the Verlet closure and the DA model in Fig. 4.9. Within this approximation we obtain freezing and melting with a narrow coexistence gap $\Delta\Gamma = \Gamma_s - \Gamma_f$. Table 4.1 summarizes the freezing/melting parameters for all the approximations made. The data are compared against experimental results obtained from real-space microscopy measurements of magnetic colloids confined to an air-water interface. The experiments give freezing with an intermediate hexatic phase. The liquid-solid transition has also been studied using numerical simulation [111, 166] yielding a slightly higher inverse transition temperature between 12.0 and 12.25 but these investigations suffer from finite size effects.

As becomes evident from Table 4.1, the SOT, TOT, and MWDA are not quantitatively satisfying theories as they either over- or underestimate the freezing coupling. Note that the overestimation of the freezing coupling within SOT and MWDA are the reason why it is not possible to feed the “exact” pair structure into these theories. At such high coupling, no fluid pair structures are available since the fluid spontaneously crystallizes in the simulation. The EMA, on the other hand, yields results in close agreement with experimental data. The TOT obviously underestimates the freezing coupling by a factor of ≈ 2 .

More detailed, structural information can be extracted from the localization parameter of the coexisting solid. For all approximations used we find localization

Table 4.1: Freezing and melting parameters Γ_f and Γ_s , the widths of the coexistence regions $\Delta\Gamma = \Gamma_s - \Gamma_f$, the relative displacement parameters γ , and the pressures P at coexistence obtained within: the SOT with the RY closure (first row); the TOT with the RY closure (second row); the TOT with the Verlet closure (third row); the MWDA with the RY closure (forth row); the EMA with the RY closure (fifth row); the EMA with the Verlet closure (sixth row), where all three-particle correlation functions were obtained with the DA model using the respective pair-correlation function as input. The last row displays experimental parameters for the isotropic-hexatic transition, the hexatic-crystal transition and the Lindemann parameter, obtained from real-space microscopy measurements of magnetic colloids confined to an air-water interface.

	Γ_f	Γ_s	$\Delta\Gamma$	γ	$\beta P(\Gamma_f)/\rho$
SOT with RY	42.85	42.92	0.07	0.017	288.3
TOT with RY	13.49	13.62	0.13	0.021	93.1
TOT with Verlet	6.79	6.97	0.18	0.019	53.1
MWDA with RY	41.07	41.13	0.06	0.017	276.1
EMA with RY	23.0	23.08	0.09	0.020	156.9
EMA with Verlet	9.33	9.49	0.16	0.020	72.6
Experiment	10.0	10.75	-	0.038	-

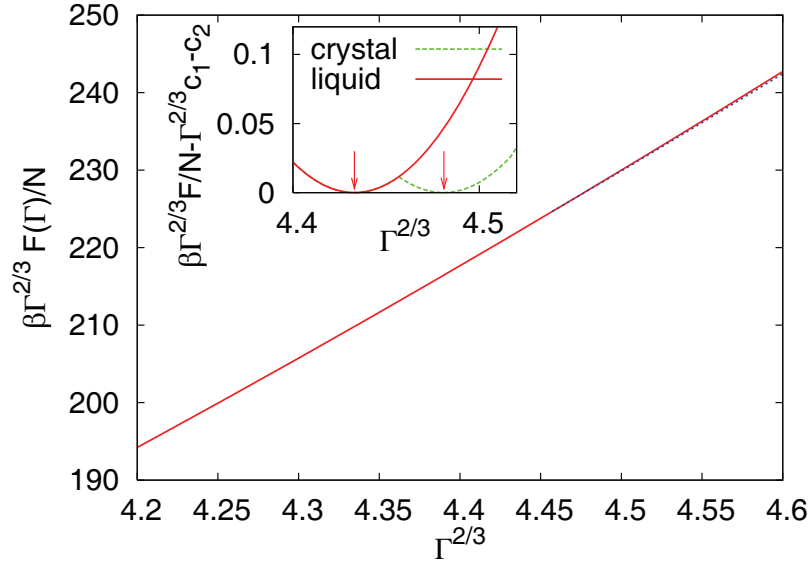


Figure 4.9: The liquid (solid line) and crystal (dotted line) volume free energy densities $\Gamma^{2/3}F/N$ obtained within the EMA using the Verlet closure and the DA model as a function of $\Gamma^{2/3}$. The inset show the tilted free energy densities around the transition values Γ_s , Γ_f , as indicated by arrows.

parameters at freezing in the range $99 < \alpha_{\min}^*(\Gamma_s) < 115$. Strictly speaking, the localization parameter has no counterpart in “real” 2D systems since the particles are not localized due to long range fluctuations. However, if one relates the particle displacements to that of their nearest neighbor, one can define a finite quantity as $\gamma = \rho \langle (\mathbf{u}_i - \mathbf{u}_{i+1})^2 \rangle$, where \mathbf{u}_i and \mathbf{u}_{i+1} are the displacement vectors of neighboring lattice sites. Disregarding nearest-neighbor correlations $\langle \mathbf{u}_i \cdot \mathbf{u}_{i+1} \rangle$, γ can be estimated. Since the nearest-neighbor correlations $\langle \mathbf{u}_i \cdot \mathbf{u}_{i+1} \rangle$ are expected to be positive:

$$\gamma \lesssim 2\rho \langle \mathbf{u}_i^2 \rangle \approx 2/\alpha_{\min}^*. \quad (4.34)$$

By this relation, the localization parameter of the coexisting solid gives a prediction for γ which is included in Table 4.1. From experiments, γ is known to be close to $\cong 0.038$ [306]. This was shown to be in accordance with harmonic lattice theory [95]. The EMA yields $\gamma \lesssim 0.020$, i.e. the EMA roughly overestimates the localization of the particles by a factor of 2. γ is *smaller* than the experimental value, contrarily to what was expected from the inequality (4.34). This shows that there is still a need to improve the theories in order to correctly predict localization properties. A similar overestimation of the localization is also common in weighted density approximations in three spatial dimensions [64].

Another quantity of interest, which is directly connected to the Helmholtz free energy is the pressure at coexistence which is also included in Table 4.1. It is

obtained via the Eqs. (4.25), (4.26), (4.27), depending on whether the RY closure or the simulation data were used.

4.5.2 Gaussian profiles, allowing for vacancies

In this subsection, we relax the constraint of zero vacancy concentration, $1 - n_c = 0$, in Eq. (4.13) and instead minimize the total free energy with respect to the two parameters α and n_c , respectively. However, instead of calculating the phase diagram for all approximations to the DFT and to the pair- and triplet-correlation functions, we focus here on the two non-perturbative approaches, the MWDA using the RY closure and the EMA using the Verlet closure and the DA model. In Fig. 4.10 we plot the approximate total free energy per particle of the EMA as a function of α and n_c for the freezing coupling constant obtained at fixed $n_c = 1$, $\Gamma = 9.49$. The minimum of the total free energy is slightly shifted in n_c and α from ($n_c \approx 1$, $\alpha^* \approx 98.7$) towards ($n_c \approx 0.998$, $\alpha^* \approx 100.5$). As can be seen in Fig. 4.10(a), the difference in total free energy per particle between the two configurations is only of the order $10^{-4}k_B T$, which has no influence on the phase diagram within the accuracy given in Table 4.1.

For the simpler MWDA, however, the vacancy concentration is substantially larger, which has pronounced effects on the phase diagram. In particular, we find the coupling constants of freezing and melting reduced to ($\Gamma_f \approx 37.35$, $\Gamma_s \approx 37.45$), the liquid being in coexistence with the triangular crystal at the parameters $n_c \approx 0.966$, $\alpha^* \approx 200.5$, i.e., the relaxation of n_c improves the prediction of the freezing coupling while the Lindemann parameter $\gamma \approx 0.01$ is by a factor of $\approx 2/3$ smaller than predicted within the simpler theory keeping $n_c = 1$ fixed which—compared to the experiment—is worse than the result from the constrained theory.

4.5.3 Free minimization

In this final subsection we completely remove the constraint of Gaussian density peaks. Instead, we minimize the density functional with respect to a free, periodic density field $\rho(x, y)$, which has the periodicity of the hexagonal lattice with lattice constant $a = (\sqrt{3}n_c/2\rho)^{1/2}$, as above. As laid out in Chapter 5, we minimize the density functional of the SOT with the RY closure with respect to $\rho(\mathbf{r})$ by calculating the overdamped relaxation dynamics of a highly ordered hexagonal crystal with the help of dynamical DFT [10, 75, 179]³ according to

$$\frac{\partial \rho(\mathbf{r}, t)}{\partial t} = \beta D \nabla \cdot \left(\rho(\mathbf{r}, t) \nabla \frac{\delta F[\rho(\mathbf{r}, t)]}{\delta \rho(\mathbf{r}, t)} \right), \quad (4.35)$$

where βD is the mobility coefficient, which sets the Brownian time scale $\tau_B = (\rho D)^{-1}$. Since in this work we are only interested in the equilibrium state reached

³See also Chapter 6.

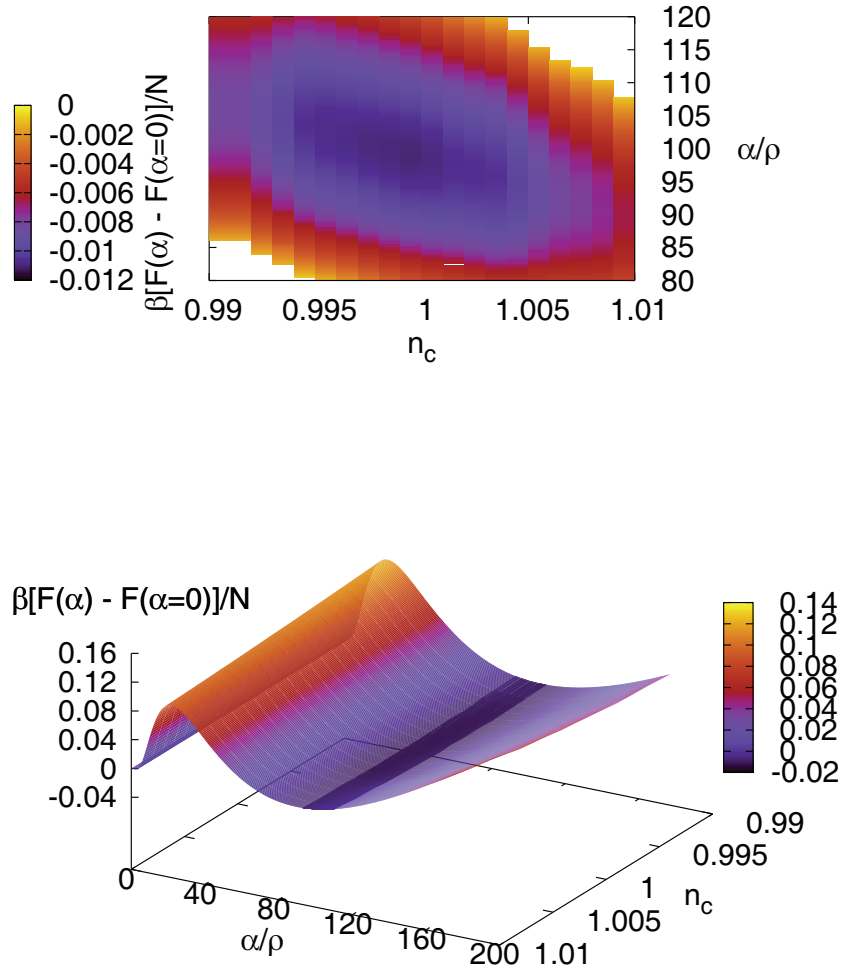


Figure 4.10: The total free energy difference per particle $\Delta F(\Gamma)/N$ as a function of α^* and n_c within the EMA using $c_0^{(2)}$ from the Verlet closure, and using $c_0^{(3)}$ from the DA model for $\Gamma = 9.49$. The upper panel displays a zoom-in of the lower panel.

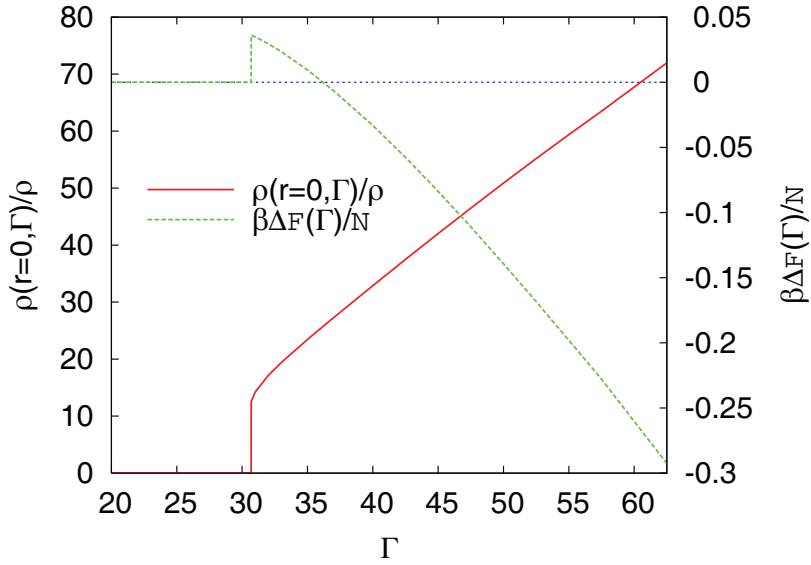


Figure 4.11: Height of the density peak $\rho(\mathbf{r}, \Gamma)$ and difference in free energy $\Delta F(\Gamma)$ as a function of Γ obtained from dynamical DFT using the SOT with the RY closure.

after long time, τ_B is irrelevant in the following considerations, i.e., we use Eq. (4.35) just as a minimization procedure to the static DFT. Starting from an initial density profile $\rho(\mathbf{r}, t = 0)$, Eq. (4.35) is solved numerically for times $(t/\tau_B) \lesssim 10$ applying a finite difference method and keeping the coupling constant Γ fixed. The maximum time is chosen large enough to guarantee convergence towards a (local) minimum of the free energy landscape. The rectangular periodic box of size $L_x \times L_y = \sqrt{3}a \times a$ with a discretization of 256×128 lattice points comprises $2n_c$ particles. Due to lattice symmetry, it suffices to solve the problem in a single elementary cell. For $\rho(\mathbf{r}, t = 0)$ we choose a superposition of sharply localized Gaussians according to Eq. (4.13) with a large localization strength of $\alpha^* = 200$.

At first, we fix $n_c = 1$ and calculate the equilibrium density profiles and the according approximate Helmholtz free energies for various coupling constants $0 < \Gamma \leq 62.5$. In Fig. 4.11 we plot the difference in Helmholtz free energy density $\Delta F(\Gamma)/N = F[\rho(\mathbf{r}, t \rightarrow \infty; \Gamma)]/N - f_0(\Gamma)$ between the final (solid/liquid) and the liquid state as a function of Γ . The system remains crystalline for couplings $\Gamma \gtrsim 30.7$. However, the free energy difference is negative only for $\Gamma \gtrsim 36.2$, which is equivalent with thermodynamic stability. As for the Gaussian parametrization coexistence is found in a narrow gap around $\Gamma \approx 36.2$ which we do not specify here.

In Fig. 4.12(a) we plot the equilibrium density profile $\rho(\mathbf{r}; \Gamma)$ for $\Gamma = 36$ which is close to freezing. In Fig. 4.12(b) the quantity $r^2\rho(\mathbf{r})$, where r is the distance from a lattice vector, is shown along the two directions [11] and [10], corresponding to cuts through the density plane in Fig. 4.12(a) along the x - and the y - axis, respectively,

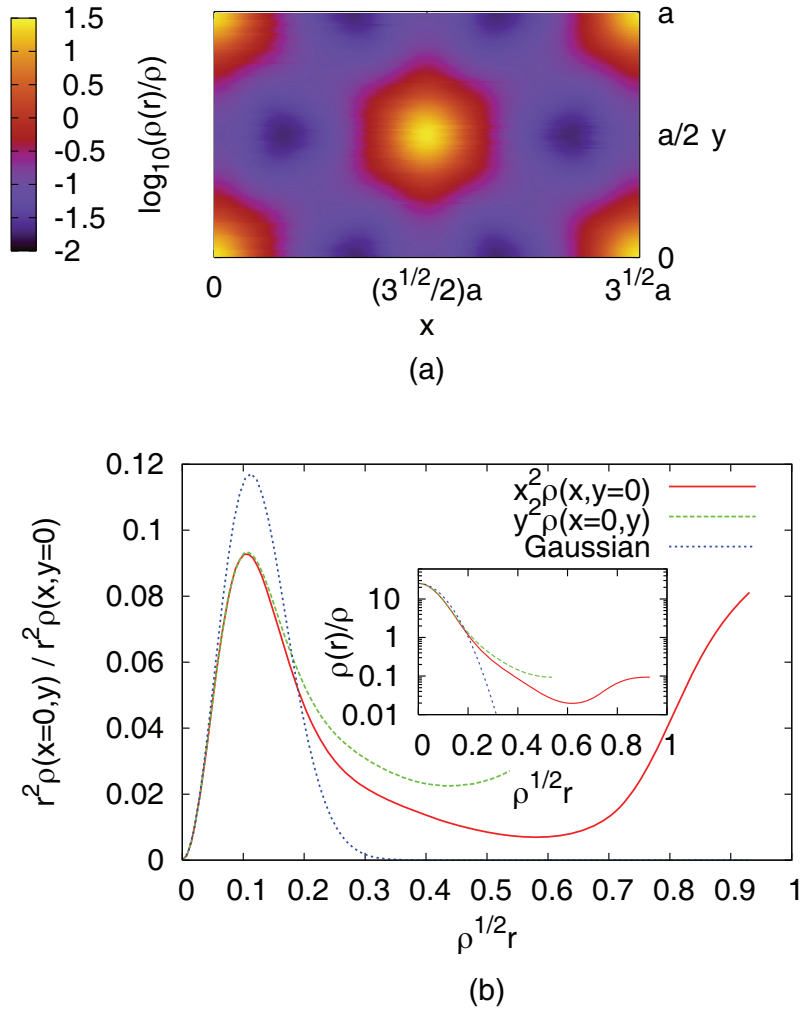


Figure 4.12: (a) The density profile $\rho(\mathbf{r})$ obtained from dynamical DFT using the SOT with the RY closure for $\Gamma = 36$ which is close to freezing. (b) The quantity $r^2\rho(\mathbf{r}; t \rightarrow \infty)$ along the straight line connecting two nearest neighbours [$y^2\rho(x = 0, y; t \rightarrow \infty)$, i.e., in the [10]-direction] and along the line connecting two next-nearest neighbours [$x^2\rho(x, y = 0; t \rightarrow \infty)$, i.e., in the [11]-direction], both drawn from the center to the respective edge of the box in (a). The two curves are compared to a Gaussian of the same amplitude at $\mathbf{r} = 0$. The inset displays the bare density along the same lines and the bare Gaussian.

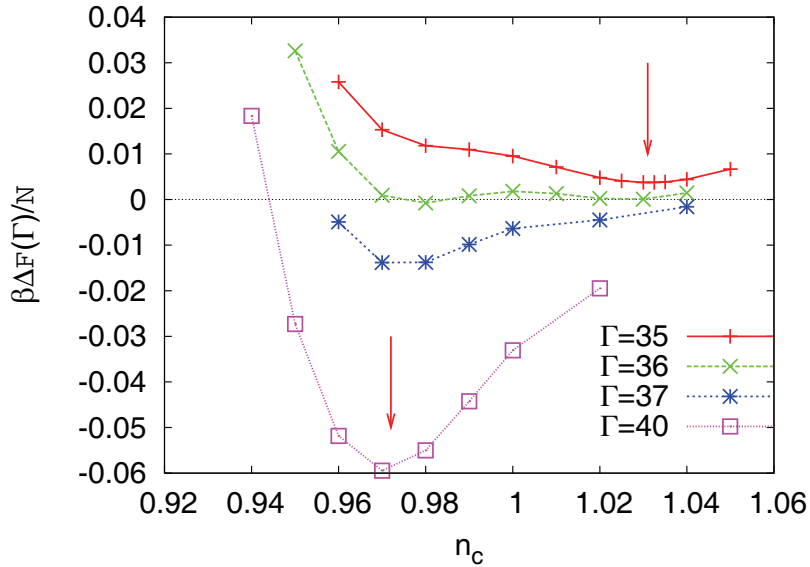


Figure 4.13: The difference in Helmholtz free energy per particle $\Delta F(n_c; \Gamma)/N$ as a function of n_c for different coupling constants $\Gamma = 35, 37, 40$. The arrows indicate the positions of the minima.

which is compared to a Gaussian of the same height as the density peaks. It is found that the density profile has an isotropic Gaussian form for small distances from the origin $r \lesssim 0.1/\rho^{1/2}$. For larger distances, however, i.e., where the density is of the order $\rho(\mathbf{r}) \lesssim \rho$, the density profile significantly deviates from a Gaussian form. In particular, we observe the establishment of “bridges” of higher density between neighbouring lattice sites, whereas the density is significantly lower between next-nearest neighbours. This counter-intuitive behavior was also found applying the MWDA to hard sphere crystals in three spatial dimensions [203]. However, computer simulations revealed that the behavior should be the opposite. Although we did not measure the density profiles of the two-dimensional dipolar system in computer simulations, we expect a similar behavior: The probability density should be enhanced along the [11]-direction as compared to the [10]-direction.

We also performed the minimization procedure for different vacancy concentrations. In Fig. 4.13 we show the free energy difference $\Delta F(n_c; \Gamma)$ as a function of n_c for four different values of Γ . We find, that for crystals in equilibrium, i.e., for $\Gamma \gtrsim 36$, the equilibrium vacancy concentration is $1 - n_c \approx 0.03$. However, the overheated crystal which is metastable for $31 \lesssim \Gamma \lesssim 36$ prefers a vacancy concentration of $1 - n_c \approx -0.03$, implying interstitials instead of vacancies. We note that most of the point defects in the experimental realization of the dipolar system appear in pairs or in pairs of pairs as dislocations or pairs of dislocations, respectively [306].

4.6 Discussion and concluding remarks

In conclusion, we have demonstrated that density functional theory is able to quantitatively predict the freezing transition of a two-dimensional colloidal system with long-range $1/r^3$ -interactions in good agreement with experimental and simulation data. In complete analogy to systems in 3D, the appearance of long-range interactions requires the explicit inclusion of three-particle correlation functions of the liquid in the construction of the weighted density [158, 159]. Furthermore, the predicted transition temperatures are very sensitive towards slight changes of the two- and three-particle correlation functions of the underlying fluid. A highly accurate input of the same is therefore crucial.

The obtained density functional can be used in future studies in order to approach more complicated situations such as crystals in confinement [203], under gravity [27], and crystal-fluid interfaces [203]. By extending the static functional to Brownian dynamics [10, 75, 179],⁴ one may even address nonequilibrium situations. One possible problem to tackle is heterogeneous nucleation upon temperature quenches and subsequent crystal growth as outlined in Chapter 6.

Acknowledgements

We thank Norman Hoffmann for helpful discussions. This work has been supported by the DFG within the Collaborative Research Centre SFB TR6, “Physics of Colloidal Dispersions in External Fields”, project section C3.

⁴See also Chapters 5 and 6.

Chapter 5

Critical nuclei and crystallization in colloidal suspensions¹

Abstract

The aim of this paper is to review and to preview some selected topics of crystal nucleation in colloidal suspensions. First we discuss how the structure of critical nuclei can be calculated by computer simulations, in particular how linear shear flow affects the size and shape of the critical nuclei. Second we preview the possibilities to access heterogeneous crystal nucleation and dynamics of a crystal by using the recent developed formalism of dynamical density functional theory. In particular, data for global crystal heating are presented.

5.1 Introduction

The theoretical prediction of crystal nucleation phenomena is an active and still open area of current research [211]. Classical nucleation theory (CNT) is based on simple thermodynamical consideration of a spherical nucleus covered by an solid-liquid interface which separates the stable crystal phase inside the nucleus from the unstable liquid phase outside. The classical nucleation theory makes explicit predictions for the nucleation rate and the size of the critical nucleus. If the latter is exceeded, growth of the crystallite initiated by the nucleus takes place.

Recently, computer simulation techniques have been applied to extract the size and shape of a critical nucleus in the undercooled melt [15] using the umbrella sampling technique. It was found that the critical nucleus possesses a pretty rough interface and is not spherical in general. The same result has also been extracted from real-space experiments on colloidal suspensions [97].

¹This chapter was published by Hartmut Löwen, Christos N. Likos, Lahcen Assoud, Ronald Blaak, and Sven van Teeffelen in *Philos. Mag. Lett.* 87(2007), 847 (<http://www.informaworld.com>). It is reprinted with permission of Taylor and Francis Ltd., Copyright 2007.

Very recently a microscopic dynamical theory [179, 180] was put forward to describe crystal nucleation which is dynamical analog of the traditional classical density functional theory of freezing [165]. This theory was justified on the basis of the Smoluchowski equation for Brownian systems and allows for a fit-parameter-free description of one-particle density dynamics. This theory can straightforwardly be used to describe the deterministic crystal growth once a heterogeneous nucleus of fixed seed particle is offered to the undercooled melt. This can be experimentally realized in colloidal suspensions [284].

The aim of this paper is twofold: first, we shall review what is known about the critical nucleus in sheared colloidal suspensions. Here computer simulations have been used in nonequilibrium situation to access the size and shape of the critical nucleus and its orientation relative to the shear flow. A convenient generalization of classical nucleation theory including a finite shear rate $\dot{\gamma}$ does describe the data surprisingly well although there is a priori no reason for it to work in nonequilibrium. Second, we shall briefly introduce and describe dynamical density functional theory. We apply it to a situation of gradual and rapid global heating of a bulk solid growth. The relation to the recently proposed phase field crystal is also briefly discussed.

5.2 Homogeneous nucleation of colloidal melts under shear

A model colloidal mixture consisting of a Yukawa fluid which performs Brownian motion at fixed temperature was extensively studied by computer simulations [30, 31]. A linear shear flow was imposed such that a fixed shear rate $\dot{\gamma}$ is prescribed. By generalizing the umbrella sampling technique to nonequilibrium situations [32], the size and shape of the critical crystal nucleus is obtained for different shear rates and “undercoolings”, the meaning of the latter can be rationalized by the pressure difference to the fluid-solid coexistence pressure.

Results are shown in Fig. 5.1 where the number of colloidal particles N^* belonging to the critical cluster is shown as a function of the reduced shear rate $\dot{\gamma}/\kappa^2 D$. Here κ denotes the inverse screening length of the Yukawa interaction and D is the free diffusion constant of the colloidal particles. Data are presented for three different pressures P measured in terms of κ^3/β where β is the inverse thermal energy. The cluster size increases with shear rate. At the same time, the crystallization rate decreases. This implies that shear suppresses crystallization for this particular model. Although classical nucleation theory does not hold a priori in non-equilibrium situations (such as shear), it is tempting to test an ansatz where the shear rate is treated as a thermodynamic variable. Surprisingly good agreement is found, see again the parabolic fits in Fig. 5.1, when the concept of classical nucleation theory is applied.

The anisotropy of the critical nucleus relative to the shear flow direction is shown in Fig. 5.2. It is tilted relative to the shear gradient direction (y axis). The averaged

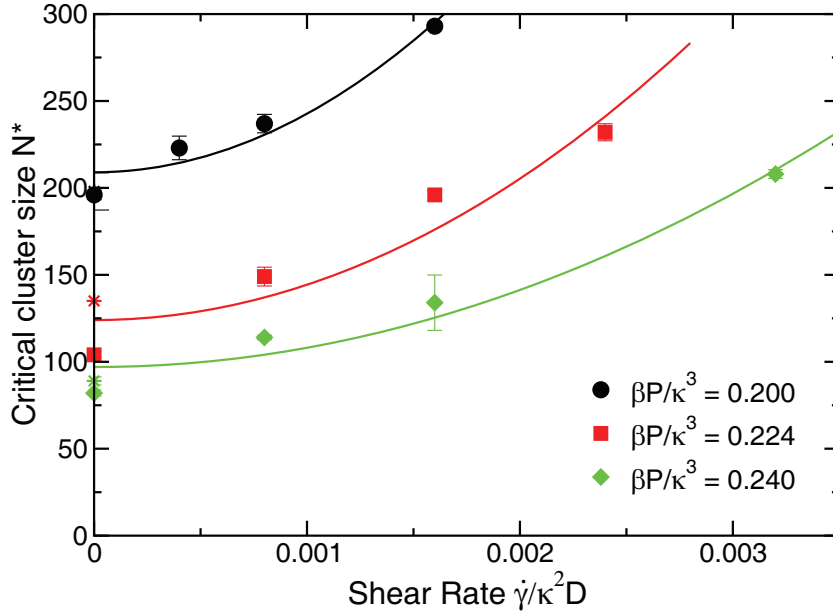


Figure 5.1: The number of particles N^* of the critical nucleus as a function of the dimensionless shear rate $\dot{\gamma}/\kappa^2 D$ and for different pressures P . The solid lines are parabolic fits through the data. The stars are data from equilibrium Monte Carlo simulations without shear.

tilt angle scales linearly with the shear rate.

A detailed comparison with experiments is in principle possible. Data for crystallization rates in charged suspensions are known [254] and individual particles can be tracked and visualized under shear flow [51, 52, 65, 129]. Still the size of the critical nucleus should be measured, by e.g. confocal microscopy [97], in order to verify the simulation predictions of Refs. [30, 31].

5.3 Dynamical density functional theory

Dynamical density functional theory is the generalization of classical density functional theory which is formulated in terms of the static one-particle density field $\rho(\mathbf{r})$ towards an ensemble-averaged time-dependent one-particle density field $\rho(\mathbf{r}, t)$. In the static case [85, 165, 263], a free-energy functional $F[\rho(\mathbf{r}, t)]$ is uniquely defined. The dynamical generalization can be derived from Smoluchowski's approach [10]. The only assumption is that pair correlations in nonequilibrium are replaced by their corresponding equilibrium expression, an assumption whose validity is amply confirmed by extended studies [75, 231, 232]. Then the following dynamical equation for $\rho(\mathbf{r}, t)$ is derived:

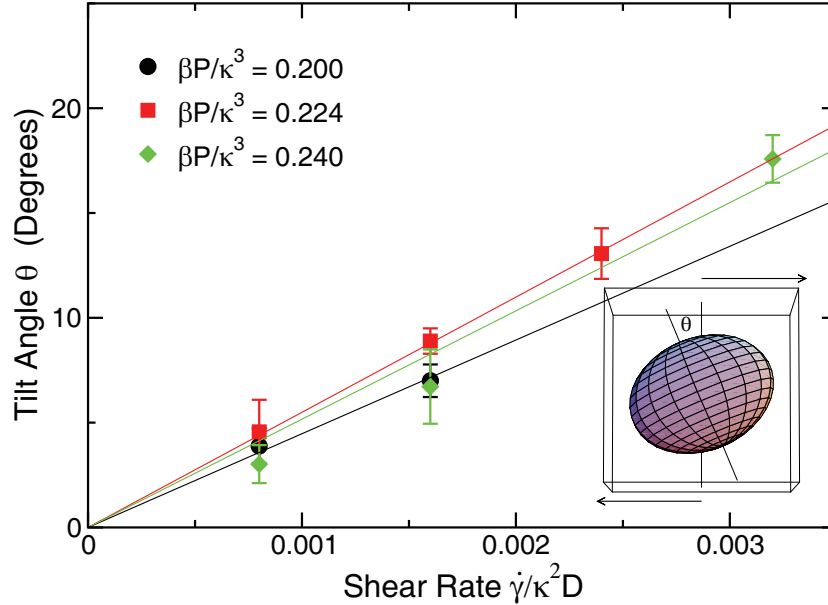


Figure 5.2: The tilt angle θ of the principal moment of inertia with respect to the y -axis. The inset shows a schematic representation of the preferred orientation of the nucleus with respect to the shear direction indicated by the arrows.

$$\frac{\partial \rho(\mathbf{r}, t)}{\partial t} = \beta D \nabla \cdot \left(\rho(\mathbf{r}, t) \nabla \frac{\delta F[\rho(\mathbf{r}, t)]}{\delta \rho(\mathbf{r}, t)} \right) \quad (5.1)$$

This is a deterministic equation without noise (see the comment of Ref. [8]) which is microscopic in principle since all molecular correlations are included in the functional $F[\rho(\mathbf{r}, t)]$. Note that the mobility coefficient βD is not a phenomenological fit parameter (as typically for order parameter dynamics) but has a precise microscopic meaning. Three remarks are in order: i) The uniqueness proof of the dynamical functional can be performed also for dynamical density functional theory, see Ref. [47]. ii) Mode coupling theory can be brought into relation with dynamical density functional theory, see Ref. [7]. iii) There are alternate ways of deriving dynamical density functional theory on microscopic grounds [179, 180].

The dynamical density functional theory has been tested against Brownian dynamics computer simulations for strongly inhomogeneous fluids and very good agreement has been found, see e.g. Ref. [231, 232]. Hence it is tempting to use the dynamical density functional approach also for crystallization. The conventional static density functional theory provides a microscopic approach to freezing. For a given particle interaction, it is in principle possible to predict to full phase diagram of the system including freezing and melting. The inhomogeneous density profile of the crystal consists of periodic peaks around the solid lattice positions. For a functional $F[\rho(\mathbf{r}, t)]$ which predicts freezing, the full dynamical of a crystal out of a given start-

ing density profile can be then predicted. Since the dynamical density functional theory works well for strongly inhomogeneous liquids it is expected that it describes the dynamics of freezing as well.

The following problems of herogeneous nucleation and microstructure formation can be addressed, at least in principle:

- 1) Heterogeneous nucleation at an external planar wall, e.g. by a system boundary.
- 2) Crystal growth out of an undercooled melt if a piece of crystal with a cleaved front is offered to the fluid. If there is no mass transport necessary, a steady-state growth velocity should be obtained [278].
- 3) Heterogeneous nucleation and subsequent growth starting from a germ of prescribed structure.

Homogeneous nucleation requires an additional careful treatment of fluctuations (see again Ref. [8]) but is also contained in the framework of dynamical density functional theory.

5.4 Application of DDFT to gradual versus sudden solid heating

An example for how dynamical density functional theory works for freezing and melting is shown for a two-dimensional system interacting via an inverse power potential $u(x) = \epsilon/x^3$. Here $x = \rho^{1/2}r$ denotes particle distance, where ρ is the average density. In this case reliable equilibrium functionals $F[\rho(\mathbf{r}, t)]$ are known [226] (see also Chapters 3, 4) which describe freezing in quantitative accordance with experiments [306].

Here, we use the approximation of Ramakrishnan and Yussouf [226] to the equilibrium density functional. Starting from an initial density profile $\rho_0(\mathbf{r}, t = 0)$, Eq. (5.1) is numerically solved for times $(t/\tau_B) \lesssim 100$, where $\tau_B = (\rho D)^{-1}$ is the Brownian time scale. In this case the rectangular periodic box with $L_x/L_y = \sqrt{3}$ comprises 2 solid particles. Due to lattice symmetry, it suffices to solve the problem in a single elementary cell.

As a first application, we study melting of a highly ordered two-dimensional, infinite triangular crystal which is in equilibrium for a low temperature $T_0 = 0.016\epsilon/k_B < T_m$, where $T_m \simeq 0.028\epsilon/k_B$ is the melting temperature, at higher temperatures.

In a first Gedanken experiment we adiabatically increase the temperature T , i.e. we increase the temperature by a small step, let the system equilibrate, increase the temperature again, etc. and we proceed like that until the crystal melts to the fluid state. In Fig. 5.3 we plot the amplitude of the such obtained equilibrium density peaks $\rho_a^*(T) = \rho_a(\mathbf{r} = \mathbf{R}; T)$ and the difference in Helmholtz free energy density $\Delta F(T)/N = F[\rho_a(\mathbf{r}; T), T]/N - F_1(T)/N$, where $F_1(T) = F[\rho(\mathbf{r}) = \rho, T]$ is the free energy of the fluid, and where N is the number of particles as a function of T . We

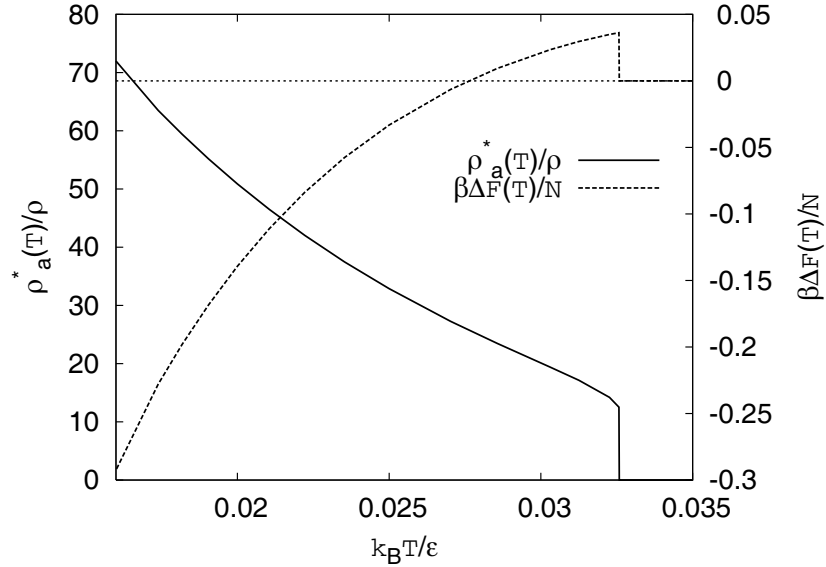


Figure 5.3: Height of the peak $\rho_a^*(T)/\rho = \rho_a(\mathbf{r} = \mathbf{r}; T)/\rho$ and difference in free energy $\beta\Delta F(T)/N = \beta F[\rho_a(\mathbf{r}; T), T]/N - \beta F_1(T)/N$ as a function of $k_B T/\epsilon$ during an adiabatic temperature decrease from $T_0 = 0.016\epsilon/k_B$.

find that for temperatures $T \leq T_o \simeq 0.033\epsilon/k_B$ the system remains crystalline but only for $T \leq T_m \simeq 0.028\epsilon/k_B$ is the free energy difference negative and thus the crystal in thermodynamic equilibrium. For $T_m < T < T_o$ the free energy difference is positive implying the crystal is metastable and therefore overheated as can be seen in Fig. 5.3. The system is not able to overcome the free energy barrier which would lead to a favorable liquid state. For $T > T_o$ the crystal immediately melts into the fluid state.

In order to see whether the system upon increasing the temperature is able to surround the free energy barrier by choosing a different pathway through the free energy landscape we perform a second Gedanken experiment: Starting from the same initial density profile $\rho_0(\mathbf{r}, t = 0)$ as above we heat the system instantaneously to a temperature $T_q > T_0$ and monitor time evolution of the density profile. In Fig. 5.4 we plot the amplitude of the density peaks $\rho_q^*(t; T_q) = \rho_q(\mathbf{r} = \mathbf{r}, t; T_q)$ for different quench temperatures T_q as a function of time. We find that the system reaches the same density profiles as above, i.e. $\rho_q(\mathbf{r}, t \rightarrow \infty; T_q) = \rho_a(\mathbf{r}; T_q)$. Therefore we conclude that upon heating the system, the heating rate does not affect the final density profile $\rho(\mathbf{r}, t \rightarrow \infty; T)$.

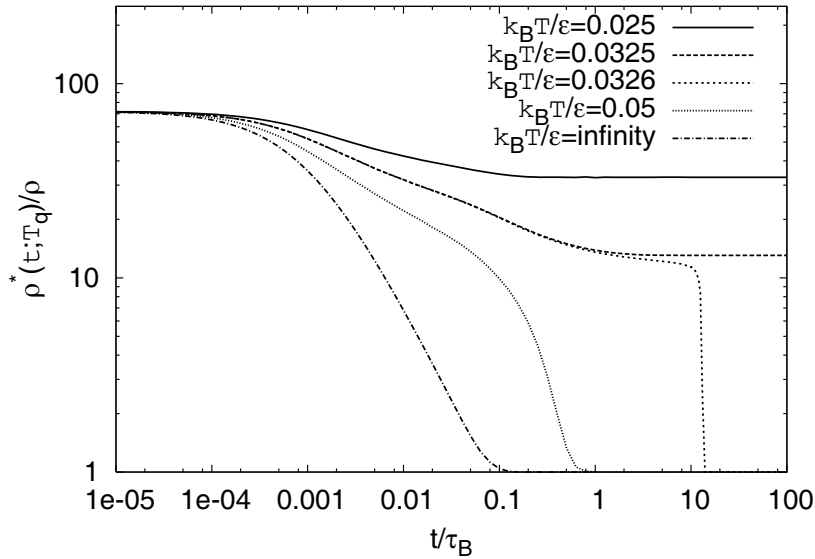


Figure 5.4: Height of the peak $\rho_q^*(t; T_q)/\rho = \rho_q(\mathbf{r} = \mathbf{r}, t; T)/\rho$ as a function of time t/τ_B after a temperature quench to different temperatures T_q at time $t = 0$.

5.5 Relation to phase-field models

Phase-field models are derived on a more phenomenological (coarse-grained) level for order-parameter dynamics [80]. The resulting equations for the dynamics of the order parameter are similar to Eq. (5.1) if the corresponding functional is replaced by a square-gradient functional of the order parameter in the spirit of Ginzburg-Landau theory. These dynamical equations of the phase-field model are then solved numerically. There are numerous applications of phase-field dynamics to various circumstances of crystal growth and nucleation [81, 105].

Phase field models have been refined to incorporate more microscopic information from the solid phase. One important development in this direction is the description of so-called phase-field crystal by suitable order parameters [78]. The phase-field crystal approach can also be generalized to include elastic distortions in the growing solid phase [2, 77, 101, 264]. Dynamical density functional theory, on the other hand, operates on the full microscopic level without any phenomenological parameters. It is a challenge to derive the phase-field model from dynamical density functional theory. Then one should get insight into the levels of different approximations which are included in the phase-field approach (including the phase-field crystal). For the static density functional theory this has been performed [170, 172], but the extension towards dynamical situations is still missing.

5.6 Conclusions

In conclusion, computer simulations and dynamical density functional theory are ideal tools to study nucleation on a microscopic level, i.e. on molecular length and time scales. In particular, dynamical density function theory which is still in its infancy as far as applications of crystallization is concerned is expected to play a major role as a microscopic theory for any crystallization and nucleation event. At the same time real-space experiments on colloidal suspensions will give direct insight into the birth and growth of crystals such that of mutual cross-fertilization of experiment, simulation and theory is expected in this research area [167].

Chapter 6

Colloidal crystal growth at externally imposed nucleation clusters¹

Abstract

We study the conditions under which and how an imposed cluster of fixed colloidal particles at prescribed positions triggers crystal nucleation from a metastable colloidal fluid. Dynamical density functional theory of freezing and Brownian dynamics simulations are applied to a two-dimensional colloidal system with dipolar interactions. The externally imposed nucleation clusters involve colloidal particles either on a rhombic lattice or along two linear arrays separated by a gap. Crystal growth occurs after the peaks of the nucleation cluster have first relaxed to a cutout of the stable bulk crystal.

While important steps towards a quantitative understanding of homogeneous crystal nucleation out of the melt have been made in the past decade (for recent reviews, see [15, 246]), work on the molecular principles of heterogeneous nucleation is still at its infancy [104, 105, 257]. Colloidal suspensions have served as excellent model systems for nucleation, since the crystallization process is typically much slower than in their molecular counterparts and the critical nucleus can be detected in real space [97]. By using external fields, e.g., optical tweezers, it is possible to fix a cluster of colloidal particles and watch directly its impact on the rest of the colloidal

¹This chapter was published by Sven van Teeffelen, Christos N. Likos, and Hartmut Löwen in *Phys. Rev. Lett.* 100 (2008), 108302 (arXiv:0802.2235). It is reprinted with permission from the American Physical Society, Copyright 2008.

suspension. If the crystal phase is slightly off-coexistence and the fluid is stable, it is possible to generate crystalline layers around such a cluster [36, 121, 285].

In this chapter we study crystal growth processes into a metastable fluid. A cluster of fixed colloidal particles, which could act as a seed for heterogeneous crystal nucleation is arranged within the metastable melt. Whereas in homogeneous nucleation such clusters spontaneously form by means of thermal fluctuations, here they are externally imposed. We investigate whether they serve as initiators of crystal growth processes. Our motivation for this study is twofold: first, by imposing a seed cluster one can steer the crystallization behavior. Second, offering complex cluster structures could lead to unexpected dynamical scenarios of crystal growth.

We approach the problem using classical density functional theory (DFT) of freezing which is a microscopic approach to crystallization [263, 299]. DFT can be extended to describe dynamics in strongly inhomogeneous Brownian fluids [10, 75, 179].² Here it is put forward as the first full microscopic approach to the dynamics of crystallization. Our DFT results are backed by Brownian dynamics (BD) computer simulations. In principle, the dynamical DFT is superior to phase-field crystal theories of nucleation [78], which operate on more coarse-grained length and time-scales and need phenomenological mobilities as an input. Therefore our results provide benchmark data to test the validity of more approximate theories.

In detail, we study a model for a two-dimensional suspension of superparamagnetic colloids, exposed to an external magnetic field which tunes their parallel dipole moments [111, 307]. By using additional fields, such as optical tweezers, certain particles can be fixed in the suspension [145, 221, 222]. We first consider a stable fluid phase, realized for a weak magnetic field. In this fluid suspension, colloidal particles are placed by optical tweezers into prescribed positions forming a cluster. Then the magnetic field is suddenly increased rendering the fluid metastable with respect to the stable hexagonal crystal and the tweezers are released. Two different kinds of cluster geometries are considered: In the first setup we study hexagonal clusters that are cut out of a perfect rhombic lattice while in the second setup two sets of linear crystalline arrays, separated by a gap, are examined.

As a result, we observe that the kinetic pathway of the system is a *two-stage* dynamical process: first, on a sub-Brownian time scale, the peak positions of the externally imposed nucleation cluster relax towards a cutout of the stable bulk crystal. Then, on a Brownian time scale, there are two further possibilities: either the relaxed cluster acts as a nucleation seed for further complete crystal growth or it dies out completely without stimulating further crystallization. Whether crystal growth occurs or not depends delicately on the compatibility of the initial cluster geometry with that of the stable bulk crystal in terms of strain energy.

Our system is characterized by the pairwise interaction potential $u(r) = u_0/r^3$, where u_0 is the interaction strength. For the specific realization of two-dimensional

²A stability analysis of undercooled fluids in three spatial dimensions with respect to periodic density waves was performed by B. Bagchi [18].

paramagnetic colloids of susceptibility χ exposed to a perpendicular magnetic field \mathbf{B} , we have $u_0 = (\chi\mathbf{B})^2/2$. The thermodynamics and structure depend only on one dimensionless coupling parameter $\Gamma = u_0\rho^{3/2}/k_B T$, where ρ is the average one-particle density and $k_B T$ is the thermal energy.

It has been shown [10, 75, 179] that the static, classical DFT can be given an extension to dynamics to describe overdamped, time-dependent, out-of-equilibrium systems in terms of a deterministic, time-dependent, and ensemble averaged one-particle density $\rho(\mathbf{r}, t)$. The time evolution of $\rho(\mathbf{r}, t)$ is then governed by the continuity equation

$$\frac{\partial\rho(\mathbf{r}, t)}{\partial t} = \frac{D}{k_B T} \nabla \cdot \left[\rho(\mathbf{r}, t) \nabla \frac{\delta F[\rho(\mathbf{r}, t)]}{\delta\rho(\mathbf{r}, t)} \right]. \quad (6.1)$$

Here, $D/k_B T$ is the mobility coefficient originating from the solvent, ignoring hydrodynamic interactions.

The equilibrium phase diagram of the system under study has been obtained using classical DFT,³ which provides the intrinsic Helmholtz free energy functional $F[\rho(\mathbf{r})]$, a unique functional of the static one-particle density $\rho(\mathbf{r})$ of the system. The functional $F[\rho(\mathbf{r})]$ is minimized by the equilibrium one-particle density, where it takes the value of the system's intrinsic Helmholtz free energy. The density functional is typically split into the ideal gas, an excess, and an external part,

$$F[\rho(\mathbf{r})] = F_{\text{id}}[\rho(\mathbf{r})] + F_{\text{ex}}[\rho(\mathbf{r})] + F_{\text{ext}}[\rho(\mathbf{r})]. \quad (6.2)$$

The ideal part is

$$F_{\text{id}}[\rho(\mathbf{r})] = k_B T \int d\mathbf{r} \rho(\mathbf{r}) \{ \ln [\rho(\mathbf{r})\Lambda^2] - 1 \}, \quad (6.3)$$

with Λ denoting the thermal de Broglie wavelength. F_{id} is of completely entropic nature and leads to a simple diffusion term in Eq. (6.1). The excess part F_{ex} , originating from the correlations between the particles, is in this chapter approximated by the ansatz of Ramakrishnan and Yussouff to the DFT [226]. It is expanded up to second order in terms of density difference $\Delta\rho = \rho(\mathbf{r}) - \rho$ around a reference fluid, where the fluid density ρ is chosen as the average density of the inhomogeneous system:

$$F_{\text{ex}}[\rho(\mathbf{r})] \simeq F_{\text{ex}}(\rho) - \frac{1}{2}k_B T \iint d\mathbf{r}d\mathbf{r}' \Delta\rho(\mathbf{r})\Delta\rho(\mathbf{r}')c_0^{(2)}(\mathbf{r} - \mathbf{r}'; \rho). \quad (6.4)$$

Here $F_{\text{ex}}(\rho)$ and $c_0^{(2)}(\mathbf{r}; \rho)$ are the excess free energy and the direct correlation function of the reference fluid of density ρ , respectively. Finally, the external part is simply given by $F_{\text{ext}}[\rho(\mathbf{r})] = \int d\mathbf{r} \rho(\mathbf{r})V(\mathbf{r})$, where $V(\mathbf{r})$ is the total external potential.

³See Chapters 3, 4.

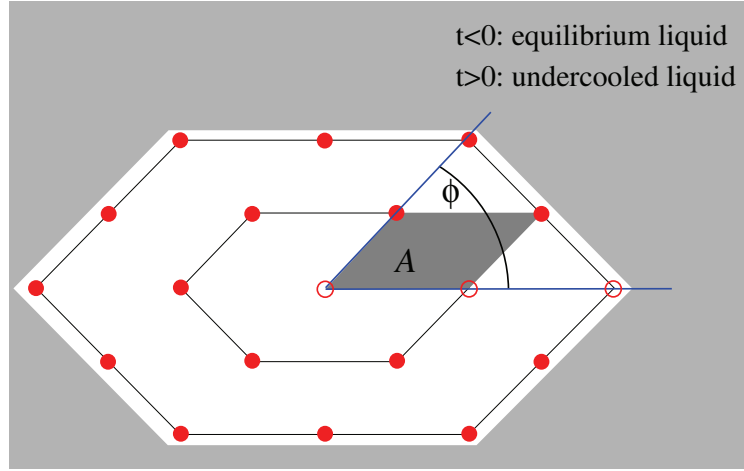


Figure 6.1: Sketch of the imposed, rhombic nucleation cluster of 19 particles surrounded by a gray fluid. The angle ϕ between the spanning basis vectors and the area of a unit cell A are also shown.

For both setups under study, the clusters of tagged particles are first, i.e., for times $t < 0$, held fixed in a thermodynamically stable, equilibrated fluid of density ρ at a coupling constant of $\Gamma_{<} = 10$, which is well below the freezing transition at $\Gamma \simeq 35.7$,⁴ obtained within the theory. For the equilibration of the fluid, Eq. (6.1) is numerically solved fixing the tagged particles by deep parabolic external potentials at the tagged particle positions—in an experiment this could be achieved by using optical tweezers [145]. At time $t = 0$ we turn the external pinning potential off and, at the same time, instantaneously quench the system to a coupling constant $\Gamma_{>} = 62.5$, which is well above the freezing transition and we observe the time evolution of the density field for times $(t/\tau_B) \lesssim 10$, where $\tau_B = (\rho D)^{-1}$ is the Brownian time scale. Eq. (6.1) is numerically solved applying a finite difference method. The dimensions $L_x \times L_y = n_x a \times n_y (\sqrt{3}/2)a$ of the rectangular periodic box considered are chosen integer multiples n_x, n_y of the lattice spacing $a = (2/\sqrt{3})^{1/2} \rho^{-1/2}$ of the perfectly ordered hexagonal crystal.

The first setup under study comprises a rhombic nucleation seed of 19 tagged particles, arranged in a hexagon, as sketched in Fig. 6.1. The nucleus is characterized by the strain parameters A , the area of a unit cell which in the perfectly ordered hexagonal crystal equals $A = 1/\rho$, and ϕ , the angle spanned by two of the nucleus axes. The size of the periodic rectangular box is $16a \times 16(\sqrt{3}/2)a$. In Fig. 6.2 snapshots of the time-evolving density field are shown exemplarily for two clusters cut out from two compressed hexagonal crystals with parameters $(A\rho = 0.7, \cos \phi = 0.5)$ and $(A\rho = 0.6, \cos \phi = 0.5)$, respectively, at times $t/\tau_B = 0, 0.001, 0.1, 1.0$.

While the former, less strongly compressed cluster grows into the equilibrium

⁴See Chapter 5.

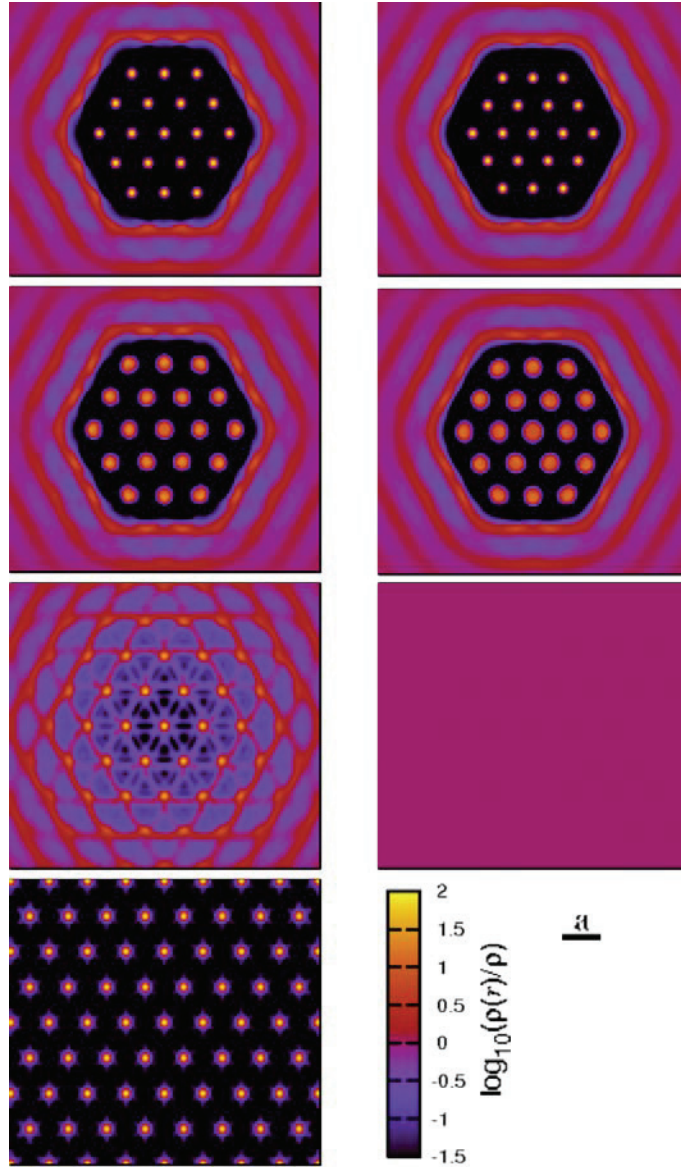


Figure 6.2: Snapshots of the central region of the dimensionless density field $\rho(\mathbf{r}, t)/\rho$ of two colloidal clusters with strain parameters $A\rho = 0.7, \cos \phi = 0.5$ (left panel) and $A\rho = 0.6, \cos \phi = 0.5$ (right panel) at times $t/\tau_B = 0, 0.001, 0.1, 1.0$ (from top to bottom; $t/\tau_B = 1.0$ only for $A\rho = 0.7$; see EPAPS Document No. E-PRLTAO-100-032811 for movies of the time evolution of $\rho(\mathbf{r}, t)$). Note that the images display only the system's central region of dimensions $L_x/2 \times L_y/2$.

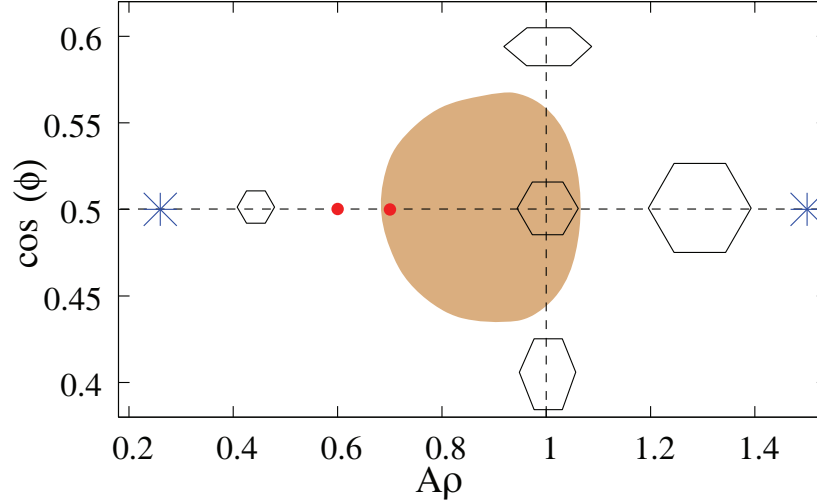


Figure 6.3: Stability “island” of the imposed nucleation cluster of 19 particles according to Fig. 6.1. The shaded region separates the growth from the no-growth situation. The (blue) stars display the according boundaries for fixed $\cos \phi = 0.5$ obtained from BD computer simulation. The hexagon symbols indicate the way the seeds are deformed in the different regions of the parameter space. The (red) dots indicate the configurations for the snapshots in Fig. 6.2.

crystalline state, the latter collapses back into an undercooled, metastable fluid within $t/\tau_B \lesssim 0.1$. The growth dynamics of the stable nucleus is a two-stage process: In the first stage—on a sub-Brownian time scale $t \lesssim 0.002$ —the positions of the seed’s density peaks move to a cutout of the thermodynamically stable bulk crystal. In the second stage—on the Brownian time scale—the system crystallizes out of the relaxed cluster.

Fig. 6.3 displays the “island” of growth in the $(A, \cos \phi)$ -parameter space, i.e., the set of parameters, for which the nucleus grows for $t > 0$. It is found that the “island” is nearly symmetric in $\cos \phi$, relative to the equilibrium value of $\cos \phi = 0.5$ while it is asymmetric in unit cell area A about the ideal value of $A = 1/\rho$. This asymmetry is qualitatively validated by BD simulations.⁵⁶

⁵In the Brownian dynamics simulations, the following cluster criterion for crystal growth was chosen. A particle is defined to be crystalline if it has six nearest neighbours according to the Voronoi construction. Neighbouring particles i and j are assigned to the same crystalline cluster if $|\text{Re}[\Psi_6^i \Psi_6^{j*}]|/|\Psi_6^i \Psi_6^{j*}| \lesssim 0.32$, where Ψ_6^i is particle i ’s complex bond order parameter. Crystal growth is defined if the average number of crystalline particles belonging to the cluster which contains the seed’s innermost particle at $t/\tau_B = 0.1$, N_c , exceeds $N_{\min} = 23$. For the strain parameters $\cos \phi = 0.5$, $\rho A = 0.2, 0.4, 0.6, 0.8, 1, 1.2, 1.4, 1.6$ we performed 10.000 independent runs each and measured N_c as a function of A . By linear interpolation the boundaries of the stability island for $\cos \phi = 0.5$ were determined $A_{\min} \simeq 0.26$, $A_{\max} \simeq 1.5$.

⁶Since freezing in the simulation sets in at $\Gamma \simeq 12$ [111] we quench the simulated system from $\Gamma_{<} = 5$ to $\Gamma_{>} = 20$.

Within the second setup we study the time evolution of a nucleation seed of two equal linear arrays along the y -direction, each comprising three infinite rows of hexagonally crystalline particles, which are separated by a gap, as can be seen from the density map for $t = 0$ in Fig. 6.4. These arrays, corresponding to an equilibrium crystal generated via a suitable external potential, are displaced relative to each other in y -direction by half a lattice spacing $\Delta y = a/2$. In between the two crystalline arrays there is an empty stripe of width $\Delta x = \sqrt{3}a$ corresponding to one missing row of crystalline particles. In contrast to the first setup, the second setup corresponds to a configuration with a huge local, non-affine strain relative to a perfect cutout of a bulk crystal due to the gap.

In order to keep the gap free of particles during the equilibration of the surrounding fluid for times $t < 0$ we employ an additional strong external potential in the region of the gap. The dimensions of the periodic box within which Eq. (6.1) is solved numerically are now given by $L_x \times L_y = 64(\sqrt{3}/2)a \times a$. Snapshots of the central region of the density field $\rho(\mathbf{r}, t)$ are shown in Fig. 6.4 for times $t/\tau_B = 0, 0.01, 0.1, 0.63, 1.0$ after the quench.

Again, a two-stage dynamical scenario is observed: On a sub-Brownian time-scale of about $0.02 \tau_B$, the positions of the peaks drift to those of a perfect cutout of the stable bulk crystal. This leads to a rapid filling of the gap. Then crystallization occurs on a Brownian time-scale. In Fig. 6.5 we plot the distances $x_i(t)$ of the three crystalline density peaks and the distance of the crystal front $x_f(t)$ with respect to the center of the gap as a function of time. The latter is taken as the inflection point of the envelope function of the y -averaged density field. The theoretical curves are compared to BD simulation data of the same setup⁷ obtained by averaging over the particle positions of 24000 independent simulation runs. The two-stage picture is clearly confirmed.

In conclusion, we have investigated by dynamical density functional theory whether and how an externally imposed cluster of fixed particles acts as a nucleation seed for crystal growth if the particles are released and the system is quenched instantaneously from a stable to a metastable bulk fluid. If the imposed cluster is not too much strained relative to a cutout of the stable bulk crystal, it induces global crystallization. The kinetic pathway of the imposed cluster exhibits a two-stage scenario: the cluster structure first relaxes towards an appropriate cutout of the bulk crystal before further growth. This two-stage process is unexpected since it is reversed in larger clusters which contain quite a large portion of the stable bulk crystal. In the latter case crystal growth starts at the edges but the inner elastic distortion anneals on a much larger time scale. For higher undercoolings, i.e., larger $\Gamma_>$, the size of the stability island (Fig. 3) increases.

Our predictions can be verified by real-space experiments on two-dimensional superparamagnetic colloidal particles confined to the air-water interface in an ex-

⁷Since freezing in the simulation sets in at $\Gamma \simeq 12$ [111] we quench the simulated system from $\Gamma_< = 5$ to $\Gamma_> = 20$.

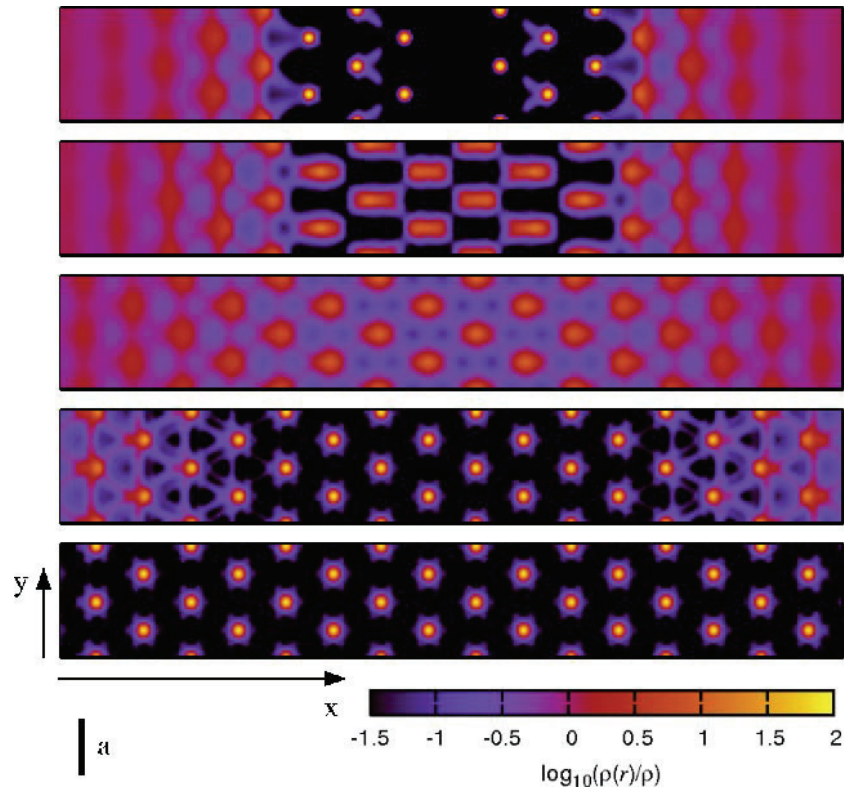


Figure 6.4: Snapshots of the central region of the dimensionless density field $\rho(\mathbf{r}, t)/\rho$ of a linear nucleus of two times three infinite rows of hexagonally crystalline particles, separated by a gap, at times $t/\tau_B = 0, 0.01, 0.1, 0.63, 1.0$ (from top to bottom; see EPAPS Document No. E-PRLTAO-100-032811 for movies of the time evolution of $\rho(\mathbf{r}, t)$). Note that the images display twice the system's central region of dimensions $L_x/4 \times 2L_y$ for better visibility.

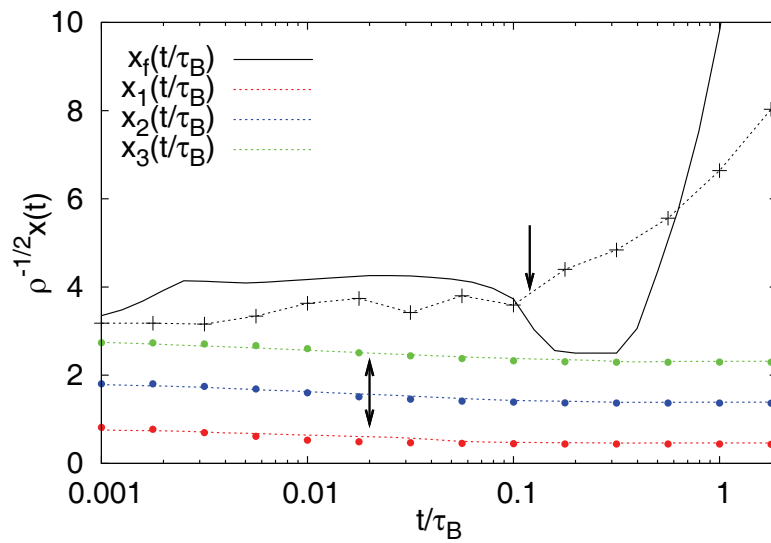


Figure 6.5: Time evolution of the distance of the linear array's three density peaks $x_i(t)$ and of the crystal front $x_f(t)$ with respect to the center of the gap as a function of time. Dynamical density functional theory results (lines) are compared against Brownian dynamics simulation data (symbols; the dashed line connecting the crosses is a guide to the eye). The arrows indicate the typical time scales on which the relaxation of the x_i is occurring and on which the crystal growth sets in, respectively.

ternal magnetic field [111, 307]. Qualitatively similar scenarios are expected for different repulsive interactions and in three spatial dimensions, which are relevant for nucleation and growth experiments in sterically and charge stabilized suspensions [60, 253, 285, 292]. In three dimensions, one may even induce the growth of metastable crystals and quasi-crystals imposed by suitable nucleation seeds [308].

Acknowledgements

We thank N. Hoffmann, R. Blaak, M. Rex, and A. van Blaaderen for helpful discussions. This work has been supported by the DFG through the SFB TR6 (project section C3) and the DFT priority program SPP 1296.

Chapter 7

Cluster crystals in confinement¹

Abstract

A large class of fluids of particles interacting via ultrasoft, repulsive pair potentials crystallize into cluster crystals. Here, we employ density functional theory and computer simulations to study the behavior of a system of particles that repel each other with a $\exp(-r^8)$ -potential [A. J. Moreno and C. N. Likos, Phys. Rev. Lett. 99 (2007), 107801] under planar confinement. We compare the behavior for purely repulsive to that for attractive slit walls. In particular, we present the phase diagram and we show that for repulsive walls the system freezes from the middle, whereas for attractive ones crystallization sets in at the walls and proceeds to the middle. For large wall-wall-separations we find continuous growth of a fluid or crystalline layer on the wall, depending on the wall-particle interaction, which is interrupted by capillary melting or freezing close to the bulk crystallization transition. An asymptotic scaling analysis of the width of the liquid or crystalline films growing at the walls indicate complete wetting in both cases.

7.1 Introduction

The influence of slit pore confinement and of single planar walls on freezing and melting has been studied for many different atomic and colloidal systems [3, 50, 98, 165] by means of computer simulation [53, 54, 70, 88, 109, 114, 131], theory [58, 202, 204], and experiment [50, 90, 275]. In general, two limiting cases of planar confinement are to be distinguished in terms of the pore size: In narrow pores of the width of one or few particle diameters, crystallization of the quasi-2D system is strongly influenced by the wall-particle interaction and by packing effects [88, 208, 249, 250]. For monolayers or even a few hard-sphere layers in planar confinement, the otherwise

¹This chapter is accepted for publication in *Soft Matter* by Sven van Teeffelen, Angel J. Moreno, and Christos N. Likos, *Soft Matter*, DOI:10.1039/b813916d (arXiv:0808:1363). It is reprinted with permission of the Royal Chemical Society, Copyright 2008.

first-order Kosterlitz-Thouless phase transition becomes continuous [225, 302]. On the other hand, for large confinement widths, freezing and melting is dominated by the 3D bulk phase behavior and by single-wall properties, i.e., crystal/fluid wetting [53, 54, 70]. For large confinement widths, two possible scenarios are observed upon approaching the bulk liquid-solid transition, depending on the different interactions between the wall, the liquid, and the crystal: In the first scenario, the walls induce melting, which becomes manifest in a fluid layer growing on the walls, already under conditions in which the crystal is stable in the bulk, a situation referred to as *premelting* [58, 90, 202, 204]. In the second scenario, the walls induce freezing, which is due to the presence of a crystalline slab under conditions in which the fluid is stable in the bulk, denoted as *prefreezing* [53, 54, 70, 88, 131]. The former mechanism is responsible for surface melting, which prevents the persistence of overheated crystalline states [90]. On the other hand, the latter mechanism prevents undercooling of the fluid state; after a quench from a high to a low temperature it is responsible for heterogeneous nucleation on the walls [14] which is often much more likely than homogeneous nucleation deep in the (bulk) fluid state.

Despite a host of literature on experiments, simulation studies, and phenomenological theories, there have been only few attempts to study confinement-induced freezing or melting by means of *microscopic* theories [3], in which the only input should be the particle-particle and the wall-particle interaction potentials. The method of choice is, evidently, classical density functional theory (DFT) [85, 86, 165, 209, 263]. DFT is an *exact* reformulation of the statistical mechanics of many-body systems, uniform and nonuniform alike, based on the equilibrium one-particle density $\rho_{\text{eq}}(\mathbf{r})$ of the system. As such, it treats fluids ($\rho_{\text{eq}}(\mathbf{r}) = \rho$, a prescribed constant) and crystals ($\rho_{\text{eq}}(\mathbf{r})$ is a periodically modulated space field) on equal footing. In fact, several of the commonly used liquid-state theories can be derived from a DFT formulation [117], whereas the DFT-treatment of crystals can be traced back to the pioneering work of Ramakrishnan and Yussouff [226]. Concomitantly, DFT offers also a tool to study bulk phase coexistence, a prerequisite for the subsequent investigations of fluid-solid interfaces [182]. There have been DFT calculations for surface melting of Lennard-Jones particles [202, 204], for hard spheres on hard walls [204], for hard spheres in very thin slit pores [252], and also for hard spheres sedimenting onto hard walls [186]. Hard spheres in slit pores have been examined by means of macroscopic, thermodynamically-inspired arguments [140] as well as by computer simulations in a system similar to the one that is the subject of this work, in the sense that it also forms clusters, albeit of a different nature than the ones we consider here [135]. Quite a bit of theoretical work and simulation studies have been carried out for liquid-gas separation and wetting phenomena of fluids in confinement [29, 86]. However, to the best of our knowledge, the effect of *varying* confinement-width on crystallization has not been systematically studied by means of DFT to-date.

In this work, we study the influence of planar confinement on a special class of colloidal particles, which interact via bounded and purely repulsive pairwise additive potentials. In particular, these pair potentials do not diverge at zero particle

distance. These so called *ultrasoft, repulsive particles* are realized in nature and experiment by a large class of complex molecules, such as branched or non-branched polymers that possess a vast number of internal degrees of freedom, a property which allows them to share their (center-of-mass) position with another particle or even several other particles of their kind [157]. The effective interaction of such complex molecules is highly tunable by choosing different architectures and solvabilities of the respective polymer monomers, model amphiphilic dendrimers being a concrete example [192]. Recent interest in such potentials has grown not only on the basis of their physical relevance but also due to some beautiful mathematical properties they possess, allowing for the determination of *exact* ground states [266, 267] and the application of generalized duality relations to such systems [273].

The rest of this work is organized as follows: In Section 7.2 we introduce the model interaction and briefly review its properties. In Section 7.3 we give a short description of the DFT, whereas in Section 7.4 we describe the numerical simulation technique used. The bulk phase behavior is discussed in Section 7.5. The system confined between repulsive walls is studied in Section 7.6, whilst the attractive walls are studied in Section 7.7. Finally, in Section 7.8 we summarize and draw our conclusions.

7.2 The model: ultrasoft, repulsive particles

The particles considered here interact by means of a *non-negative* and *bounded* pair interaction potential, $0 \leq \phi(r) < \infty$, that is integrable and possesses a Fourier transform $\tilde{\phi}(k)$, and are termed *ultrasoft, repulsive particles*. Such interactions have been divided into two categories, the so called Q^\pm - and the Q^+ -class [160]. The former classifies potentials for which $\tilde{\phi}(k)$ has an oscillatory decay about zero, while interaction potentials in systems of the latter kind fulfill the condition $\tilde{\phi}(k) \geq 0$. The drosophila of bounded pair potentials is the generalized exponential model of index n (GEM- n), which is defined by

$$\phi(r) = \epsilon \exp[-(r/\sigma)^n], \quad (7.1)$$

where r is the particle distance, σ is the interaction range (typically a measure of the particle's size), and ϵ is the interaction strength. In the following, we will set $\epsilon = 1$, $\sigma = 1$ as well as $k_B = 1$, the latter being Boltzmann's constant. It has been shown [161] that $\phi(r)$ of Eq. (7.1) belongs to the Q^+ -class for $n \leq 2$ and to the Q^\pm -class for $n > 2$. Moreover, it has been established [160] that the distinction of Q^\pm - and Q^+ -particles goes along with two different principle features of the topologies of the respective bulk phase diagrams: Systems of the Q^\pm -kind display freezing for arbitrarily high temperatures and densities into so called cluster crystals [161, 188, 190, 192] while systems of the Q^+ -kind are characterized by reentrant-melting and a maximum freezing temperature [150]. In this chapter, we concentrate on the class of Q^\pm -particles and their behavior in confinement.

Cluster crystallization is highly distinct from crystallization of “conventional/ordinary” colloids: It implies that at high densities several particles share the same lattice site of a periodic crystal. In fact, it has been shown for the GEM-4 model that upon increasing the density, the lattice constant of the stable fcc crystal, $a = \sqrt{2}d$, where d is the nearest-neighbor distance, approaches a density- and temperature-independent constant [192]. The above implies that the average number of particles sharing a lattice site, n_c , grows linearly with density. In this work, we investigate the phase behavior of GEM-8-particles, i.e., representative ones of the Q^\pm -species, which show a tendency to cluster at a lower density than the GEM-4-particles do, due to a deeper minimum of the respective Fourier-transformed pair potential [161]. Freezing is studied with the help of mean field density functional theory (MFA-DFT) and with simulation for different wall-particle interactions and for different wall-wall separation L_z . MFA-DFT has proved to be highly accurate to reproduce the bulk phase behavior of the GEM-4 model [188], and will be shown here to accurately predict the equilibrium phase diagram of the GEM-8 in the bulk and in confinement.

The main focus of this work is in the behavior of the GEM-8 model in slit pores. Two kinds of planar confinement are considered: In a first setup we study the effect of purely repulsive Yukawa-walls on the structure and phase diagram of the system while in a second setup the influence of attractive Lennard-Jones walls is examined. The Yukawa potential has been shown to model the interaction of dendrimers with hard walls [102, 156]. In order to model attractive walls we introduce a 9-3-Lennard-Jones potential. The latter interaction is not based on microscopic grounds but is introduced to model the influence of attractive wall potentials in general. However, recent simulation results [156] have shown that dendrimers on walls with core-monomer-wall attractions show very similar effective interaction potentials. We demonstrate that the first setup leads to premelting: the system is molten at the walls and crystallizes at the center, while for the second setup the opposite happens, i.e., there the walls induce prefreezing [3, 98]. Furthermore, we argue that both setups display complete wetting [69] which is deduced from a continuous, logarithmic growth of the fluid/crystalline wetting layer down/up to the point of capillary melting/freezing.

A salient property that distinguishes the behavior of clustering particles from non-clustering ones in confinement, is the ability to locally adjust the average occupation number of the clusters, n_c , without distorting the crystal structure through point defects such as vacancies or interstitials. Remarkably, although there is incessant hopping of particles from one site to the other, rendering these crystals *ergodic* and endowing them with a non-vanishing long-time diffusivity, the underlying crystal structure remains intact. In fact, this happens not *despite* the hopping mechanism but *because* of it. For details, see Ref. [162, 193].

7.3 Density functional theory

Density functional theory is based on a variational grand canonical functional $\tilde{\Omega}[\rho(\mathbf{r})]$, a unique functional of the static one-particle density $\rho(\mathbf{r}) = \left\langle \sum_{i=1}^N \delta(\mathbf{r} - \mathbf{r}_i) \right\rangle$ of the system, where \mathbf{r}_i , $i = 1 \dots N$ are the particle coordinates and $\langle \dots \rangle$ denotes the according grand canonical average [85]. The functional $\tilde{\Omega}[\rho(\mathbf{r})]$ is minimized by the equilibrium one-particle density $\rho_{\text{eq}}(\mathbf{r})$, where it takes the value of the system's grand potential, $\Omega[\rho(\mathbf{r})]$. The density functional is typically split into the ideal gas, an excess, and an external part,

$$\begin{aligned} \tilde{\Omega}[\rho(\mathbf{r})] &= F_{\text{id}}[\rho(\mathbf{r})] + F_{\text{ex}}[\rho(\mathbf{r})] \\ &+ \int d\mathbf{r} \rho(\mathbf{r}) (V(\mathbf{r}) - \mu), \end{aligned} \quad (7.2)$$

where $V(\mathbf{r})$ is the external potential and μ is the chemical potential. The integral runs over the system volume. The ideal part reads as

$$F_{\text{id}}[\rho(\mathbf{r})] = \beta^{-1} \int d\mathbf{r} \rho(\mathbf{r}) [\ln \rho(\mathbf{r}) - 1] + 3 \langle N \rangle \beta^{-1} \ln \Lambda, \quad (7.3)$$

with $\beta^{-1} = T$, $\langle N \rangle = \int d\mathbf{r} \rho(\mathbf{r})$ being the average particle number and Λ the thermal de Broglie wavelength. The last term in Eq. (7.3) above is thermodynamically irrelevant and will be ignored henceforth. The excess part is given very accurately for sufficiently high temperatures and/or densities by the mean-field expression [161]

$$F_{\text{ex}}[\rho(\mathbf{r})] = \frac{1}{2} \iint d\mathbf{r} d\mathbf{r}' \rho(\mathbf{r}) \rho(\mathbf{r}') \phi(\mathbf{r} - \mathbf{r}'). \quad (7.4)$$

It is pertinent, at this point, to shortly comment on the accuracy of the expression (7.4) above. In Ref. [161], it has been shown that this functional form rests on the validity of the approximation $c(r) = -\beta\phi(r)$ for the direct correlation function $c(r)$ of the fluid (uniform) phase. Within the framework of linear response theory and employing the Percus identity, it can be shown that the relation $c(r) = -\beta\phi(r)$ holds *asymptotically* in regions of space for which the potential $\phi(r)$ caused by a test particle held fixed at the origin is much weaker than the other two energy scales of the problem: the thermal energy T and/or the average potential energy per particle caused by all other particles in a fluid of density ρ [117]. For diverging potentials, this relationship *must* break down at sufficiently small r -values.² However, for ultra-soft, bounded potentials, it can and it indeed does hold approximately true for *all separations* r provided T and/or ρ are sufficiently high, so that the thermal and/or the potential energy per particle dominate over $\phi(r)$. In previous work [160, 161] it was demonstrated that the conditions $T \gtrsim 1$ and/or $\rho \gtrsim 1$ are sufficient for the relationship $c(r) = -\beta v(r)$ to be fulfilled to a satisfactory degree of approximation.

²In fact, exact diagrammatic expansions show that $c(r)$ remains finite for all r , whereas diverging potentials do not at $r = 0$. Thus, $c(r) = -\beta\phi(r)$ must break down in such case.

Minimization of $\tilde{\Omega}[\rho(\mathbf{r})]$ is pursued by demanding its functional derivative with respect to density to vanish. This amounts to numerically solving the self-consistent equation

$$\rho_{\text{eq}}(\mathbf{r}) = \exp \left\{ \beta\mu - \beta V(\mathbf{r}) - \int d\mathbf{r}' \beta \phi(|\mathbf{r} - \mathbf{r}'|) \rho_{\text{eq}}(\mathbf{r}') \right\}, \quad (7.5)$$

for $\rho_{\text{eq}}(\mathbf{r})$ in an iterative fashion, on a periodic rectangular grid of $N_x \times N_y \times N_z$ grid points, where the convolution integral is evaluated with the help of fast Fourier transform. We chose a grid of $N_\alpha \approx 16L_\alpha$, $\alpha = x, y, z$ which is fine enough to reach numerical convergence for all state points under study. For the study of crystalline states the x - and y -dimensions of the box are chosen to be commensurable with the expected lattice spacings in plane with the confining walls (see Section 7.5). The lattice spacing of crystalline GEMs in the bulk is well known to be relatively insensitive towards density/chemical potential and temperature. This is also found for the GEM-8 in confinement, as will be shown below.

7.4 Simulation

We simulated a system of several thousand particles, N , interacting through a GEM-8 potential $\phi(r) = \exp(-r^8)$. For the case of confinement, they also experience an external wall potential $V(z)$ presented in Sections 7.6 and 7.7. Simulation results presented here are obtained by means of Brownian dynamics. The equation of motion for the position vector \mathbf{r}_i of a particle i is given by:

$$\dot{\mathbf{r}}_i(t) = -\Gamma \nabla_{\mathbf{r}_i} \left[V(\mathbf{r}_i) + \sum_{j \neq i} \phi(|\mathbf{r}_i - \mathbf{r}_j|) \right] + \mathbf{w}_i(t), \quad (7.6)$$

where Γ is a mobility constant (we set $\Gamma = 1$) and $\mathbf{w}_i(t)$ is a stochastic Gaussian noise term. The latter represents the random collisions with the much faster solvent molecules, which are not explicitly included in the model. The noise fulfills the statistical properties [4]

$$\overline{\mathbf{w}_i(t)} = 0, \quad \overline{w_i^\alpha(t) w_j^\beta(t')} = 2\beta^{-1} \delta_{\alpha\beta} \delta_{ij} \delta(t - t'), \quad (7.7)$$

where α, β are the Cartesian x, y, z -components and the bars over the quantities denote a noise average.

We implemented periodic boundary conditions for the simulation cell of volume $V_c = L_x \times L_y \times L_z$. Periodicity was applied in the x, y -directions in all cases, and also in the z -direction for the bulk case. We employed a cubic cell of size $L_x = L_y = L_z = 18.57$ for the bulk system. In the confined system, we set $L_x = L_y = 20.43$ for slits of thickness $L_z \leq 8$. We also carried out simulations on the confined system for thickness $L_z = 24$, with $L_x = L_y = 9.285$.

The Brownian dynamics simulations were performed at constant N, V_c , and T , and the equations of motion (7.6) were integrated via the Ermak's algorithm [4, 83],

with a timestep $\Delta\tau = 10^{-4}\tau_B$. Here, $\tau_B = \beta$ is the Brownian time scale. The system was prepared by randomly placing the particles in the simulation cell. In this way, crystallization occurs spontaneously at sufficiently high density. An equilibration run of typically 10^6 timesteps was performed before the production run of typically 3×10^6 timesteps. During the production run, configurations were periodically saved for computation of observables. Density profiles and radial distribution functions (see below) were averaged over typically 30 configurations, the interval between two consecutive configurations of the latter being 100 000 timesteps. In this time scale, the particle mean displacement is of at least one molecular diameter for all the investigated systems, guaranteeing that the former configurations are uncorrelated. At high densities, a few independent runs were also performed for some fixed state points (ρ, T, L_z) , starting from different configurations of the particles, in order to check that the final values of the former observables are independent of the initial conditions.

7.5 The bulk phase diagram

The phase behavior in confinement is determined by two factors, the interaction of the particles with the walls and the behavior in the bulk; in particular, the location of the considered thermodynamic point (μ, T) with respect to bulk phase boundaries plays a decisive role in influencing the density profiles in confinement and related surface phase transitions. Before presenting the phase diagram of the system in confinement we therefore provide the bulk phase behavior, as obtained from the DFT, which serves as a reference point.

Solving Eq. (7.5) within the minimum rectangular unit cell of the body centered cubic (bcc), the face centered cubic (fcc) and the hexagonal close packed (hcp) lattices of variable lattice spacing, we find that for temperatures $0.5 \leq T \leq 4$ the system undergoes two subsequent first-order transitions upon increasing the chemical potential μ , first from the liquid to a hcp cluster crystal at μ_f , and at higher μ , a subsequent structural phase change from a hcp to a fcc cluster crystal. This scenario is in contrast to other GEM- n models with smaller n where at first a post-freezing bcc cluster phase is found, preceding a $\text{bcc} \rightarrow \text{fcc}$ transformation at higher values of ρ (or μ) [188, 190]. We have not carried out a search of other non-Bravais lattices than the hcp-one. Thus it cannot be ruled out that there are other stable phases of non-Bravais lattices at freezing or at higher μ . However, we can clearly state that within the DFT the post-freezing lattice is *not* a Bravais lattice.

For $T = 1$, which is the temperature for all confinement studies throughout this work, we locate the freezing transition in the bulk at a chemical potential $\mu_f = 12.09$. Here, a fluid of density $\rho_f = 2.96$ coexists with the hcp cluster crystal of density $\rho_s = 3.48$. The latter crystal consists of polydisperse clusters that contain on average $n_c \cong 6.02$ particles each, corresponding to an equilibrium nearest neighbor distance of $d = 2^{1/6}(n_c/\rho_s)^{1/3} \cong 1.347$. The second transition towards the fcc crystal takes

place at a chemical potential $\mu = 20.03$. Here, already deep in the crystalline phase, an hcp lattice of average density $\rho = 7.80$, average occupation number $n_c = 11.96$, and nearest neighbor distance $d = 1.295$ coexists with a fcc lattice of average density $\rho = 7.82$, occupation number $n_c = 11.85$, and nearest-neighbor distance $d = 1.289$ implying a lattice constant of $a = \sqrt{2}d = 1.823$. We anticipate that, similar to the GEM-4-model, there is a triple point at which liquid, hcp crystal and fcc crystal coexist.

The detailed investigation of the bulk phase behavior of the GEM-8-model is not the purpose of this work, yet a few comments are of order. First, the stability of the hcp lattice with respect to the fcc comes as a surprise, since the latter features a larger distance to the third-nearest neighbors of a given particle than the first. On energetic grounds, one would thus expect the fcc to win, and it indeed does so at $T = 0$. But very much like the bcc-lattice is the post-freezing structure above the triple point of the GEM-4-model on entropy grounds, the hcp achieves a lower free energy than the fcc due to an entropically more favorable arrangement of the density profiles around the crystal sites [277]. As density grows, however, so does also the cluster population n_c . The inter-site interaction energy, which scales as n_c^2 , becomes increasingly important, energy takes over and fcc wins over hcp. There are indications from the simulations in confinement that at post-freezing densities the ordered state indeed has the propensity to undertake a hcp-like ordering, i.e., an $ABAB \dots$ stacking of hexagonal arrays, as opposed to the $ABCABC \dots$ stacking of the fcc, as shown in Fig. 7.1. However, in bulk simulations the system spontaneously forms a bcc lattice at freezing. The determination of accurate phase boundaries and crystal phases could be pursued by means of the novel simulation technique of Mladek, *et al.* [189, 192]. This task goes beyond the scope of this work and will be the subject of further investigations.

For the rest of this chapter, we sidestep thus the issue of the stability of the hcp-lattice and the associated question of the possible existence of other non-Bravais lattices and restrict our theoretical studies to Bravais crystals *only*. The reasons for doing this are twofold: first, as mentioned above, because it is not clear which other non-Bravais lattices might be competitive. Second, we expect that our results are generic, since the physics is dictated by the tendency of the model to form cluster crystals and is not dependent on the detailed spatial arrangement of the same on a specific lattice. Therefore, we focus on the bulk results for the phase boundary between a liquid and a fcc crystal, ignoring any other candidate periodic arrangement; among all Bravais lattices, the fcc lattice is the most stable one. The bulk freezing transition for the same temperature $T = 1$ within the DFT is found at a slightly higher chemical potential than for the liquid-hcp transition, namely $\mu_f = 12.13$. Here, a fluid of density $\rho_f = 2.97$ coexists with the fcc cluster crystal of density $\rho_s = 3.50$. The fcc crystal consists of polydisperse clusters that contain on average $n_c \cong 6.04$ particles each, corresponding to an equilibrium lattice constant

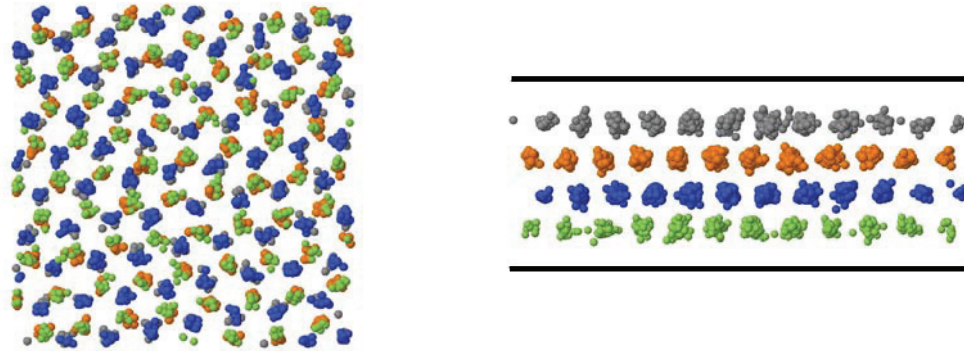


Figure 7.1: Left panel: simulation snapshot of the four crystalline layers of a confined GEM-8-model at temperature $T = 1$ and density $\rho = 4.2$, view of one quarter of the xy -periodic box from the bottom (lower wall). The two repulsive walls have a separation $L_z = 5.2$ and are lying parallel to the page. The layers of clusters are color-coded, from bottom to top: green, blue, orange, and gray. An $ABAB\dots$ stacking of the hexagonal layers can be seen. Right panel: same as the left but now from the side view.

of $a = (4n_c/\rho_s)^{1/3} \cong 1.905$. The equilibrium lattice constant exceeds the value

$$a^* = 2\sqrt{3}\pi/k^* = 1.859, \quad (7.8)$$

where $k^* = 5.855$ is the wavenumber for which $\tilde{\phi}(k)$ attains its minimum, negative value, by a factor 1.025. The lattice constant a^* corresponds to a nearest-neighbor distance $d^* = 2^{-1/2}a^* = 1.314$ and to a distance of adjacent layers of hexagonally crystalline particles in the 111-direction of the fcc crystal $c^* = a^*/\sqrt{3} = 1.073$ [13]. The result of Eq. (7.8) stems from a simplified version of the MFA-DFT, which takes only the first reciprocal lattice vector (RLV) of the fcc lattice into account and results into the outcome that the length of the first shell of RLVs of the fcc crystal should coincide with k^* *at all densities* [161]. The equilibrium lattice constant of the fcc crystal resulting from the *full* DFT-minimization is relatively insensitive towards temperature changes. Furthermore, as is known for the GEM-4 as well, it is almost independent of μ . In particular, for $T = 1$, a decays as a function of μ towards a plateau of $a = 0.94a^*$ which it reaches at $\mu \sim 50$, as can be seen in Fig. 7.2.

In view of the aforementioned insensitivity of a with respect to the state point in the phase diagram, we can simplify the calculation by fixing it to a constant value $a = a^*$ for all state points (μ, T) and recalculate the bulk phase diagram under this constraint. Thereby, a slightly higher chemical potential at freezing is obtained: For $T = 1$, the value $\mu_f = 12.25$, with coexistence densities of $\rho_f = 3.00$ and $\rho_s = 3.58$, and average cluster occupancy $n_c \cong 5.74$ results. The chemical potential μ_f and the

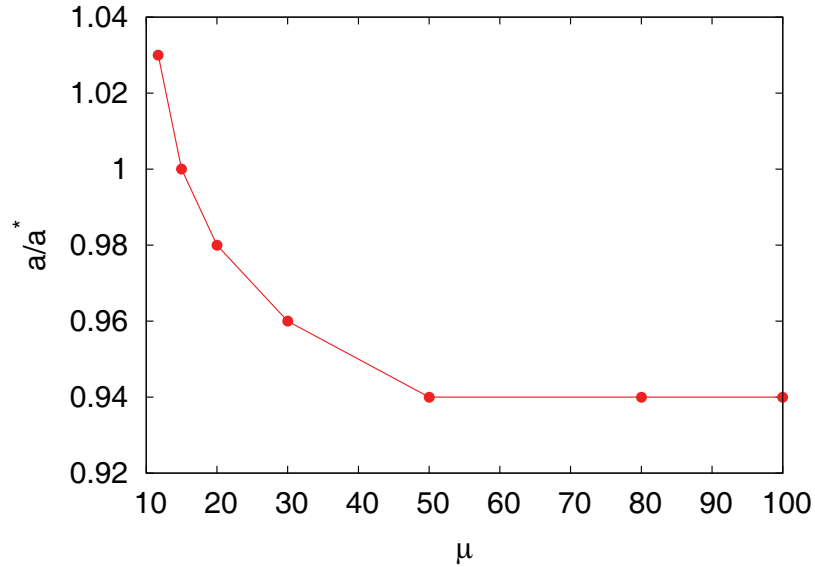


Figure 7.2: The equilibrium lattice constant for the fcc crystal in the bulk as a function of chemical potential for $T = 1$.

densities of coexistence are plotted versus temperature in Fig. 7.3.³

Another constraint to the lattice geometry, which becomes important for the confinement studies, is the following: The distance of neighboring layers of hexagonally crystalline particles in the 111-direction of the fcc crystal c is free to vary whereas the nearest-neighbor distance of particles within each plane is fixed to $d = d^*$. If we minimize the grand potential in this partially constrained fashion ($d = d^*$ only in the xy -plane of confinement), we obtain yet a third value for the bulk freezing chemical potential, $\mu_f = 12.19$, which lies in-between the two bulk values $\mu_f = 12.13$ (free lattice constant a) and $\mu_f = 12.25$ (fixed lattice constant $a = a^*$). The optimal distance of neighboring layers was then found to be given by $c = 1.113$ which exceeds the corresponding distance c^* in an isotropic fcc-crystal with lattice constant a^* by a factor 1.038. The bulk freezing parameters obtained by DFT under the various constraint conditions on the minimization procedure are summarized in Table 7.1.

³By fixing the lattice constant to a^* there is actually a stable bcc-phase intervening between the liquid-fcc-crystal phase transition, which is not persistent when relaxing the constrained of fixed lattice constant. We therefore ignore this subtlety here.

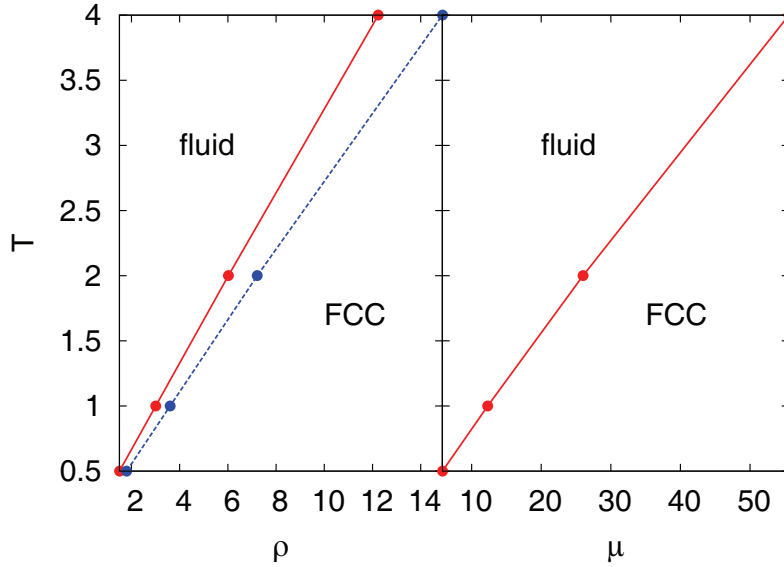


Figure 7.3: The (constrained) bulk phase diagram for fixed lattice constant a^* and for the fixed fcc-lattice. Left panel: The phase diagram at the (ρ, T) -representation. The lines are the loci of the coexisting liquid- and fcc-densities and the gap in-between denotes the coexistence region. Right panel: same as the left one but at the (μ, T) -representation.

7.6 Repulsive slit pores

In the first setup we study the effect of the repulsive confining walls. The latter are characterized by the external potential

$$V_Y(\mathbf{r}) = 10 \left[\frac{e^{-z}}{z} + \frac{e^{-(L_z-z)}}{L_z-z} \right], \quad 0 < z < L_z, \quad (7.9)$$

where z is the component of the particle coordinate \mathbf{r} perpendicular to the wall, measured with the origin on one of the walls. The Yukawa form is motivated on the basis of results for the interactions of athermal dendrimers (GEM-2-particles) with model planar walls [102] and is confirmed by recent results of Lenz, *et al.* [156]. The prefactor 10 in Eq. (7.9) is so far arbitrary but should roughly scale linearly with the number of monomers of a dendrimer.

In the DFT, the xyz -periodic box for the density field has the dimensions of $L_x \times L_y \times (L_z + 1)$, where neighboring slits in the z -direction are separated by a large additional barrier of width 1, which is wide enough to obviate any mutual particle interactions across the wall. The system volume itself is only of size $L_x \times L_y \times L_z$, excluding the barrier. The dimensions parallel to the walls, L_x and L_y , are chosen to be commensurate with the fcc-lattice of lattice constant a^* either at the 100- or the 111-direction perpendicular to the walls (100: $L_x = L_y = a^*$, 111: $L_x = 2^{-1/2}a^*$,

Table 7.1: Freezing parameters for the liquid-solid transition in the bulk obtained within mean field density functional theory for different constraints to the lattice types of the crystalline phase (hcp, fcc, distorted fcc) and for different unit cell dimensions (fixed vs variable spacing of neighboring hexagonal layers c and fixed vs variable nearest-neighbor distance within each plane d). The freezing parameters are the chemical potential μ_f , the densities of the coexisting liquid (ρ_f) and solid (ρ_s), the in-plane nearest neighbor distance d , the distance of neighboring planes c , and the average occupancy n_c .

lattice	minimization	μ_f	ρ_f	ρ_s	d/d^*	c/c^*	n_c
hcp	free	12.09	2.96	3.48	1.025	1.025	6.02
fcc	free	12.13	2.97	3.50	1.025	1.025	6.04
fcc	constrained ^a	12.25	3.00	3.58	1	1	5.74
distorted fcc	constrained ^b	12.19	2.98	3.54	1	1.038	5.89

^a The (isotropic) lattice constant is held fixed ($a = a^*$).

^b The nearest-neighbor distance within a plane of hexagonally crystalline particles is held fixed ($d = d^*$) but the inter-plane distance c is allowed to relax freely (cf. text).

$L_y = \sqrt{3/2}a^*$). The 110-orientation is unfavorable due to inefficient packing and is therefore not considered. As already mentioned in the determination of the bulk phase diagram, we did not vary the nearest neighbor distance in the x - and y -direction in the slit pore geometry. However, we left the system freedom in adjusting its lattice constant in the z -direction, i.e., perpendicularly to the walls.

In confinement, freezing is defined at the point in which a fully modulated density field $\rho(\mathbf{r})$ yields a grand potential lower than that of the z -modulated fluid with density $\rho(z)$: $\Omega[\rho(\mathbf{r}); L_z] < \Omega[\rho(z); L_z]$ ⁴ and it occurs at a corresponding freezing chemical potential in confinement, $\mu_f(L_z)$. It will be shortly demonstrated that due to the repulsive nature of the Yukawa walls, the bulk freezing chemical potential μ_f can be independently obtained as $\mu_f = \mu_f(L_z \rightarrow \infty)$ by an appropriate extrapolation procedure. Since we minimize the grand potential in a partially constrained fashion (fixed $d = d^*$ only in the xy -plane, which will turn out to be perpendicular to the 111-direction of the equilibrium fcc-crystal in slit pores of large widths), the asymptotic value of $\mu_f(L_z \rightarrow \infty)$ should coincide with the bulk freezing chemical potential $\mu_f = 12.19$ as obtained by applying the partially constrained minimization procedure in Section 7.5 (cf. Table 7.1, line 4). The coincidence of the results obtained by two independent routes for the determination of μ_f serves as a confirmation of the

⁴Here and in the following, we denote the local minima of $\tilde{\Omega}[\rho(\mathbf{r})]$ with respect to the density field $\rho(\mathbf{r})$ by $\Omega[\rho(\mathbf{r})]$, although the grand potential is, of course, given by the minimum value of *all* local minima.

validity of the extrapolation procedure to be employed.

In DFT, symmetry does not break spontaneously. To avoid getting trapped in metastable minima of the free energy landscape in our search for the true equilibrium configuration, we iteratively solve Eq. (7.5) starting from different initial density fields. In particular, we start *both* from a purely z -modulated density field, which always leads to a stable or metastable fluid state *and* from highly modulated fields, which possess the symmetry of the fcc crystal everywhere but very close to the confining walls, trying different orientation and offsets. To be precise, we start from 111- and 100-oriented crystals (with respect to the walls), which have either a particle layer centered about the middle of the box ($z = L_z/2$) or a particle layer shifted by half an inter-plane distance from $z = L_z/2$. The 111-oriented fcc crystal always leads to a stacking of hexagonally ordered clusters in the *ABCABC*-fashion. The *ABAB*-stacking resulting from an hcp-crystal is not tested within the theory (see the above discussion of the bulk phase behavior).

Due to the slow exponential decay of the wall-particle potential, the clusters in the layers closest to the walls are less populated and blurred compared to the middle of the slit. This can be seen from the plots of the x - and y -averaged density field $\rho_{xy}(z) \equiv (L_x L_y)^{-1} \iint dx dy \rho(\mathbf{r})$ for different average densities $\rho = L_z^{-1} \int dz \rho_{xy}(z)$ in Fig. 7.4(a), as obtained from the DFT. We therefore introduce the notion that *the crystal freezes from the middle* under the influence of the repulsive, Yukawa walls. For comparison, we present in Fig. 7.4(b) results from BD computer simulations for the same parameters as in the DFT, which show the same quantitative behavior for $\rho = 2$ and the same qualitative behavior for $\rho = 4$. For $\rho = 3$, the DFT predicts a crystalline state whereas the system remains fluid in the simulation. The difference in the density profiles for the states at $\rho = 3, 4$ is associated with a difference in the bulk liquid/solid coexistence densities which has already been observed for the GEM-4 model when applying the compressibility route to the Helmholtz free energy [191].

The pronounced crystallinity in the central region of the simulation box can be observed not only in the density profiles but is also confirmed by measurements of the restricted pair-distribution function [3] in the xy -plane,

$$g_{2D}^{(k)}(r_{\parallel}) \equiv \frac{V_k}{N_k^2} \overline{\sum'_{i,j(i \neq j)} \delta(\mathbf{r}_{\parallel} - |\mathbf{r}_{i\parallel} - \mathbf{r}_{j\parallel}|)}. \quad (7.10)$$

Here, \mathbf{r}_{\parallel} denotes the lateral projection (onto the slit plane), i.e., $\mathbf{r}_{\parallel} \equiv \mathbf{r} - (\mathbf{r} \cdot \hat{\mathbf{e}}_z)\hat{\mathbf{e}}_z$, where $\hat{\mathbf{e}}_z$ is the unit vector in the z -direction. The double sum in Eq. (7.10) runs over all N_k particles i and j lying in the k th layer from the wall (this restriction being denoted by the prime) with volume V_k . Particles belong to the same layer if their position lies between the same two consecutive minima of the respective laterally-averaged density profile $\rho_{xy}(z)$. We show $g_{2D}^{(k)}(r_{\parallel})$ for the first three layers from either wall, $k = 1, 2, 3$, in Fig. 7.5. Peaks and minima of the pair distribution function clearly become more pronounced for increasing distance of the layer from the wall.

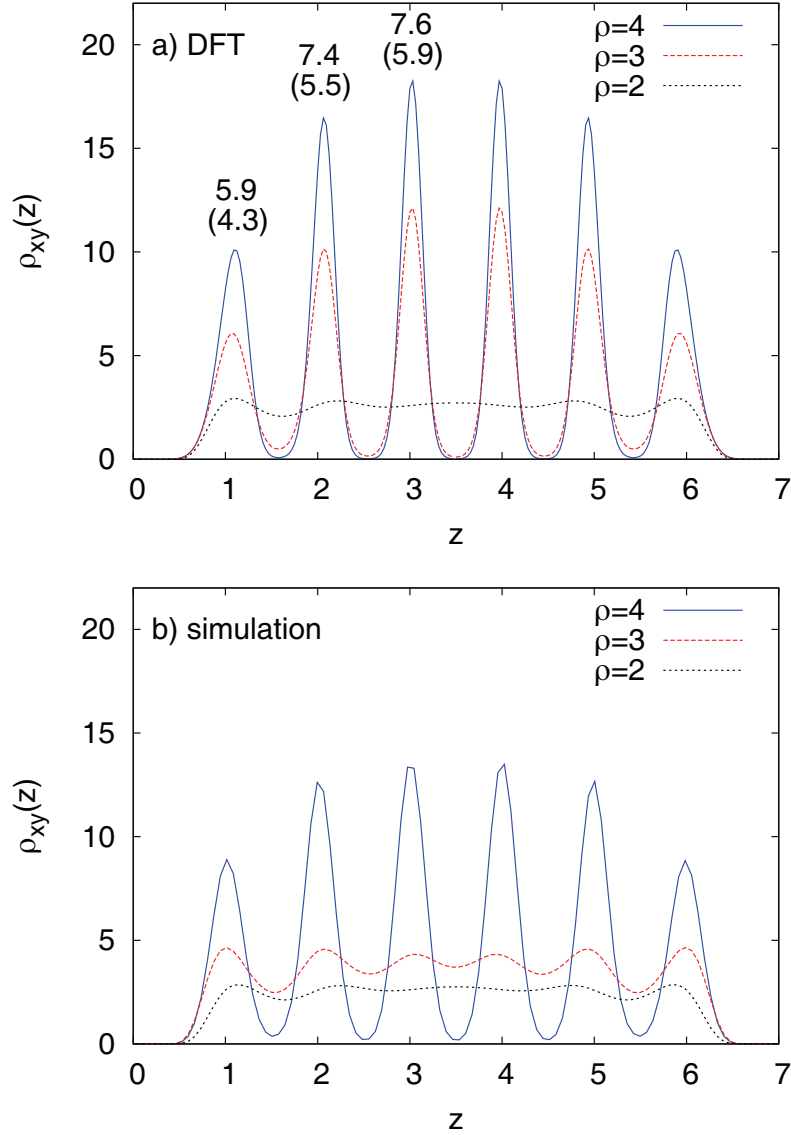


Figure 7.4: Yukawa walls: Laterally-averaged density profiles $\rho_{xy}(z)$ for different average densities ($\rho = 4, 3, 2$ from top to bottom) for $L_z = 7$ as obtained from the DFT, (a), and the simulation, (b). (a) The fcc crystal in the DFT has the 100-orientation. The numbers over the peaks denote the average number of particles, n_c , occupying a cluster, for $\rho = 4$ (top value) and $\rho = 3$ (bracketed, lower value) from the DFT. (b) The lateral dimensions of the periodic simulation box are $L_x = L_y = 20.43$.

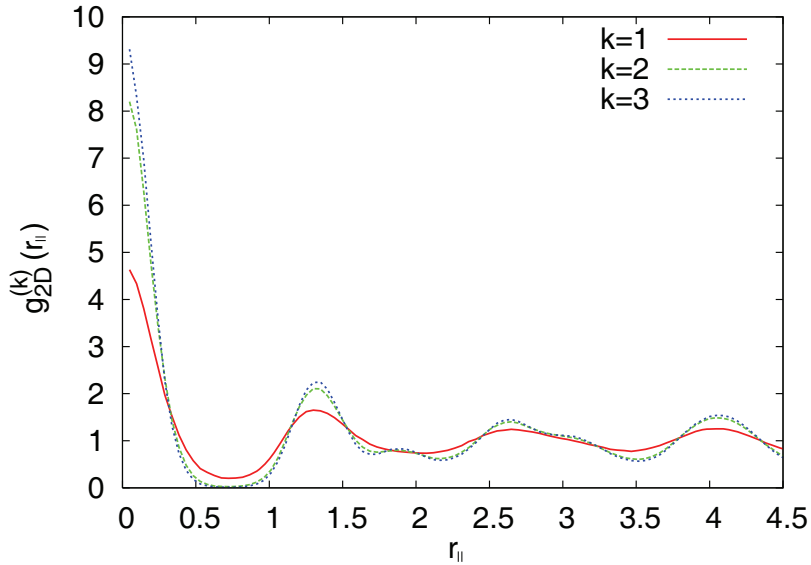


Figure 7.5: Yukawa walls: The lateral pair distribution function $g_{2D}^{(k)}(r_{||})$ for the first three layers of clusters on either of the wall (k is counted from the wall) for the same confinement as in Fig. 7.4 at average density $\rho = 4$ (for the definition of layers see main text).

Also, the appearance of a shoulder at the third peak of $g_{2D}^{(2)}$ and $g_{2D}^{(3)}$ indicates the strong crystallinity of the clusters within the respective layers.

It is important to note that the ability of the particles to form clusters has two profound consequences for the interpretation of the density field $\rho(\mathbf{r})$, qualitatively distinguishing them from ordinary colloidal crystals: First, the decreased sharpness of the density peaks close to the walls as compared to the central region of the slit is not only to be interpreted as a fluctuation of the clusters' center-of-mass position but also and rather as an increase of the cluster radii, i.e., an increase of the mean distance of the particles from their cluster's center of mass. Second, as was already mentioned in the introduction, the different average numbers of particles occupying the cluster peaks indicated by the numbers in Fig. 7.4, do not go along with distortions of the lattice structure. In contrast to freezing of usual colloidal systems in confinement, even for the smallest average densities above freezing the average number of particles occupying a cluster is substantially larger than 1. In fact, it is these features which make the system very amenable to a mean field DFT-treatment.

For all confinement lengths $2 \leq L_z \leq 48$ studied, the freezing chemical potential in confinement is higher than in the bulk, $\mu_f(L_z) > \mu_f$, see Fig. 7.6; freezing is hindered by the confining Yukawa walls. On the other hand, the fluid and the fcc solid average densities $\rho_f(L_z)$ and $\rho_s(L_z)$ at coexistence are smaller than the respective

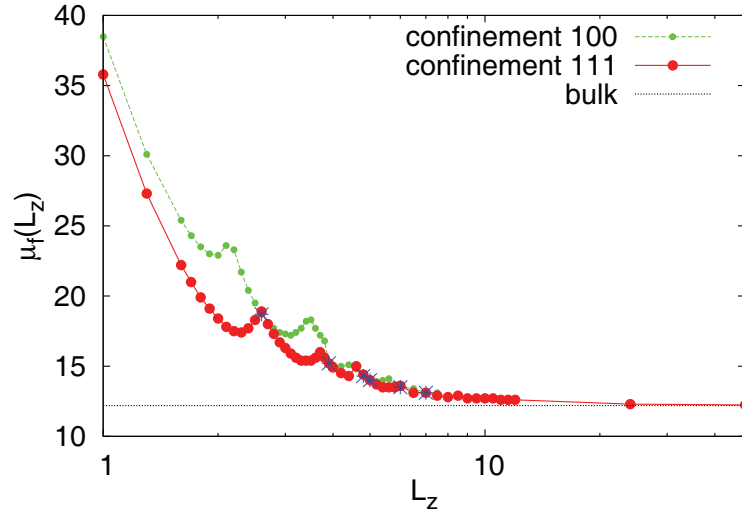


Figure 7.6: Yukawa walls: Freezing chemical potential $\mu_f(L_z)$ as a function of the confinement width L_z for the 111-orientation (red/solid) and the 100-orientation (green/dashed). The (blue) stars mark those points where the 100-orientation is stable versus the 111-orientation. The horizontal line displays the respective freezing value of the bulk system, $\mu_f = 12.19$.

bulk values for $L_z \gtrsim 1$, as can be seen in Fig. 7.7. The reason lies in the decreased probability density to find a particle close to the walls. Both freezing chemical potential and fluid/solid densities at coexistence display pronounced oscillations while approaching the respective bulk values with increasing L_z . This effect is clearly more pronounced for small wall-wall separations. After each spike of $\mu_f(L_z)$ in Fig. 7.6, a new layer of crystalline clusters is introduced into the box. The local minima of $\mu_f(L_z)$ correspond to crystalline states with optimal layer spacing in the z -direction. Concomitantly, the wavelength of the oscillations equals the bulk value of the distance of the crystalline particle layers in the 111-direction, $c = 1.04c^* = 1.113$ (cf. Table 7.1, line 4). This finding is qualitatively validated by the computer simulations (see Fig. 7.7). Here, a simple criterion to separate crystalline from non-crystalline states was based on the value of the first minimum of the laterally averaged pair distribution functions $g_{2D}^{(k)}(r_{\parallel})$ of the most central layer k , which always freezes first among all layers. The simulation points in Fig. 7.7 display the states of constant minimum $g_{2D}^{(k)}(r_{\min}) = 0.15$.

The confining walls have a profound influence on the grand potential of the system, especially for small values of L_z . Despite the lower average density within the slit pores, the grand potential density $\omega(\mu; L_z) \equiv \Omega[\rho_{\text{eq}}(\mathbf{r}; \mu, L_z)]/V$, plotted as a function of μ for different confinement lengths L_z in Fig. 7.8, is higher in confinement than in the bulk. In Fig. 7.8, $\omega(\mu; L_z)$ is represented both for the solid and the fluid

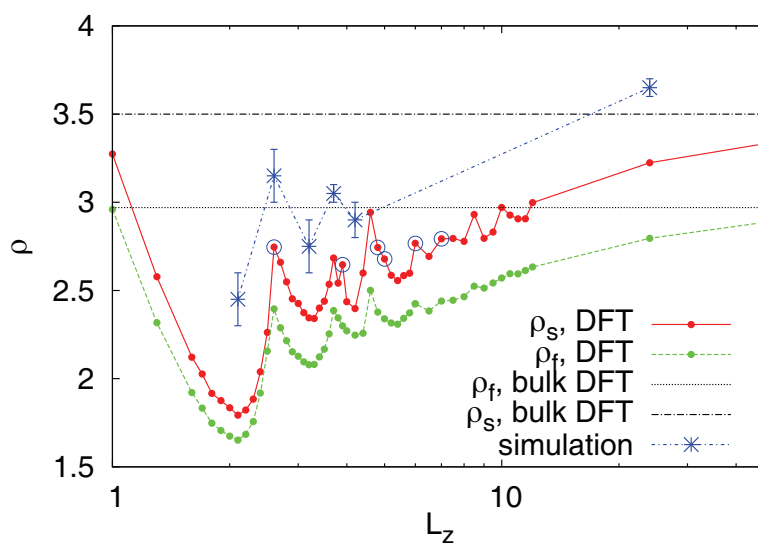


Figure 7.7: Yukawa walls: Fluid and solid densities $\rho_f(L_z)$, $\rho_s(L_z)$ at coexistence. The open circles display the crystalline states which possess a 100-orientation with respect to the walls. Shown are also the respective bulk values. The DFT-results for the confined case are compared against the locus of constant $g_{2D}^{(k)}(r_{\min}) = 0.15$ from the simulation, where k refers to the most central layer (see main text).

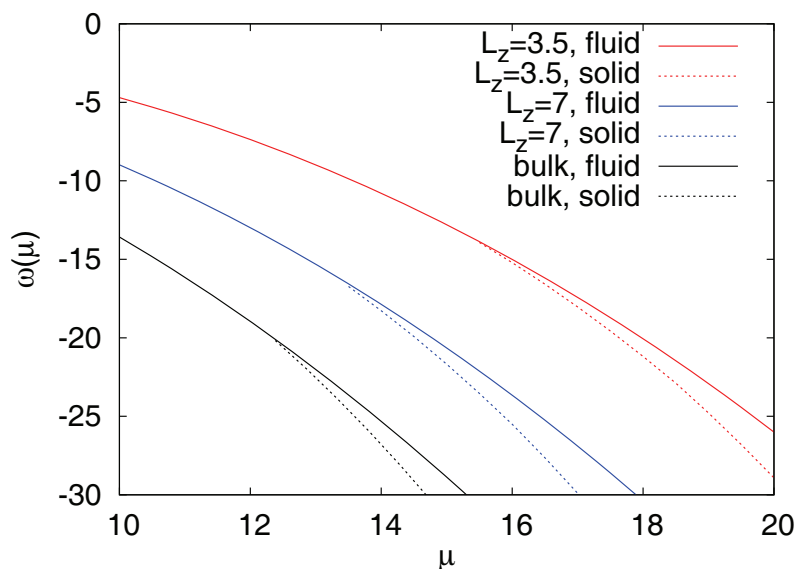


Figure 7.8: Yukawa walls: Grand potential density $\omega(\mu)$ in the fluid (solid lines) and the solid state (dashed lines) as a function of chemical potential for $T = 1$ for different confinement lengths $L_z = 3.5, 7$ and for the bulk (from top to bottom).

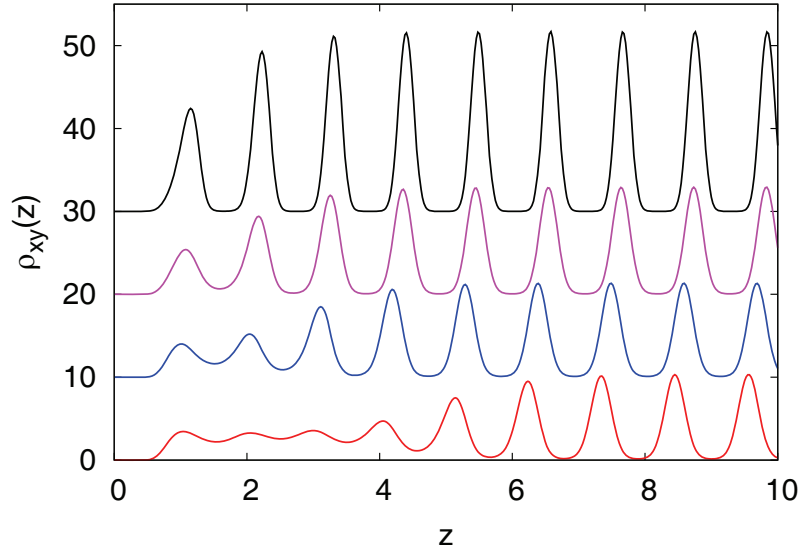


Figure 7.9: Yukawa walls: Laterally-averaged density profiles $\rho_{xy}(z)$ close to the left wall for $L_z = 48$ for different chemical potentials $\mu = 16, 13, 12.5, 12.24$ (from top to bottom).

state, the fluid being stable for $\mu < \mu_f(L_z)$ and metastable for $\mu > \mu_f(L_z)$.

For the case of small confinement lengths, $L_z \lesssim 7$, the favorite orientation of the compressed/expanded fcc crystal is, except within some tiny L_z -intervals, the 111-orientation. As a consequence, the chemical potential at freezing for the 100-crystal which is metastable within the DFT, is almost always equal or higher than for the 111-crystal (cf. Fig. 7.6), within the accuracy of the DFT calculation. This signifies that the system favors to have a layer of hexagonally crystalline clusters close to the walls, this layer being clearly visible in the simulation snapshots in Fig. 7.1. We note exemplary for $L_z = 7$, for which we find a stable 100-oriented crystal, that under consideration of the non-Bravais hcp lattice, the latter is thermodynamically stable in comparison to the fcc one, albeit with a small difference in grand potential, leading again to a hexagonal cluster arrangement on the walls. The stability of the hcp versus the 100-oriented fcc lattice is also most likely to be found for the other confinement lengths but we did not check this in our study. For very large L_z , the difference in grand potential density between the 100- and the 111-orientations is decreasing and we focus on the 111-orientation for $L_z \geq 24$.

For large wall-wall separations, $L_z \gg 1$, as the bulk freezing chemical potential is approached from above ($\mu > \mu_f = 12.19$), the blurred clusters on the walls melt and a fluid layer grows on each wall. The walls enforce the growth of a liquid film, a property referred to as premelting. The number of molten layers N_m on each wall increases continuously with decreasing difference in chemical potential $\Delta\mu \equiv \mu - \mu_f$,

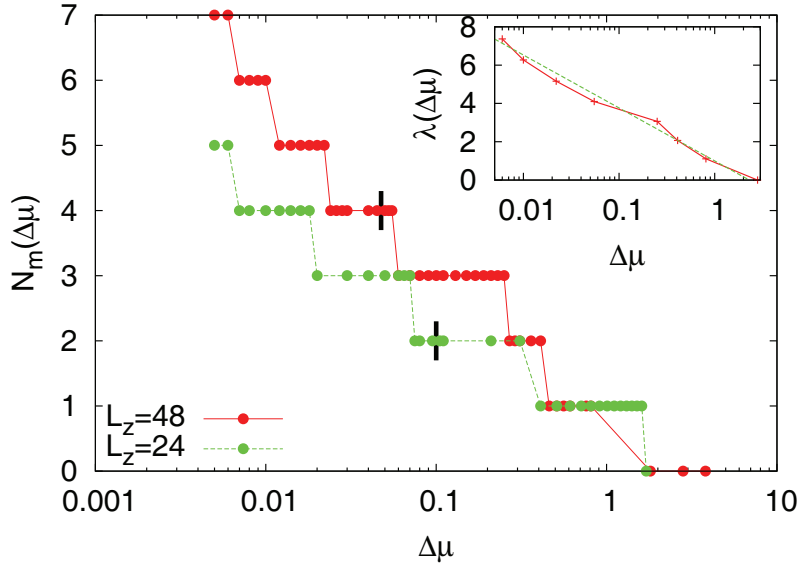


Figure 7.10: Yukawa walls: The number of molten layers $N_m(\Delta\mu)$ on either Yukawa-wall as a function of the difference in chemical potential $\Delta\mu$. The black bars indicate the points of capillary melting, $\mu_f(L_z)$. The points to the left of the bars correspond to metastable crystalline states with the minimum grand potential among all possible crystalline states. We did display N_m only for those chemical potentials for which at least one other still crystalline state with a higher number of molten layers was found to be metastable (see main text). Inset: The corresponding width $\lambda(\Delta\mu)$ of the fluid system close to the wall for $L_z = 48$, evaluated at the kinks of $N_m(\Delta\mu)$. The dashed line is the least-square logarithmic fit $-\xi_f \ln(\Delta\mu) + \text{const}$.

as can be seen from the xy -averaged density profiles in Fig. 7.9 for the confinement length of $L_z = 48$. In Fig. 7.10, we show the number of molten layers on the walls as a function of $\Delta\mu$ for two different confinement lengths, $L_z = 24$ and $L_z = 48$. Here, a layer of what used to be crystalline clusters, is defined to be molten once the density within it exceeds the threshold value of $\rho(\mathbf{r}) > 0.15$ for all x and y . This criterion has been used for the absence of knowledge about the pair-correlations, which was the basis for the simulation-results above. The z -position of a layer is defined by the z -position of the respective maximum of the x - and y -averaged density field. After growing up to a maximum finite number of molten layers on each wall, $N_m^c(L_z)$, the system turns completely fluid due to capillary melting at $\mu_f(L_z)$, as is also visualized in Fig. 7.10 by the black vertical bars. At the melting transition, the number of molten layers at each wall is still substantially smaller than the number of crystalline layers in the central region of the slit. In particular, we find for the maximum wall-wall-separation under study, $L_z = 48$, that $N_m^c(L_z = 48) = 4$ which is still microscopic. For $L_z = 24$ we find $N_m^c(L_z = 24) = 2$.

The occurrence of capillary filling when a system close to its bulk phase transition is confined between two parallel walls is a well-known phenomenon in the context of liquid-gas phase coexistence of ordinary fluids [69, 86]. Here, we establish the existence of capillary melting from the walls for a system that forms crystalline layers in the middle of the slit pore. For the liquid-gas coexistence, capillary condensation precludes the wetting transition that takes place between two semi-infinite bulk phases [86]. Wetting can be studied within DFT if one employs a semi-infinite system with the appropriate boundary condition at a distance $z \rightarrow \infty$ from the wall and it is straightforward to implement for the case of uniform phases [12]. In our case, however, this would correspond to fixing a periodic crystal at $z \rightarrow \infty$, whilst the chemical potential μ is lowered towards its bulk value μ_f from above. This renders the DFT-calculation very complicated, therefore we will resort to a different approach in arguing that in the limit of infinite wall-wall separation, the fluid completely wets the Yukawa wall as $\mu \rightarrow \mu_f^+$. The approach is based on general, thermodynamic considerations that lead to scaling laws for the width of the wetting layer, which diverges at the bulk phase transition. Thus, the walls drive the system to the molten state.

In the limit of large wall-wall separation and for macroscopically thick fluid films of width $1 \ll \lambda(\Delta\mu) \ll L_z$ on either wall, the grand potential per unit surface area A of the short-range interacting system can be written as [16, 69]

$$\frac{\Omega(\Delta\mu)}{A} = 2(\gamma_{fw} + \gamma_{fs}) + \omega(\mu_f)L_z + 2\epsilon_1 \exp\left[-\frac{\lambda}{\xi_f}\right] - [(L_z - 2\lambda)\rho_s + 2\lambda\rho_f] \Delta\mu + O(\Delta\mu^2), \quad (7.11)$$

where γ_{fw} is the fluid-wall surface tension, γ_{fs} is the fluid-solid surface tension, and ϵ_1 is the prefactor of the interaction between the fluid-wall and the fluid-solid interfaces, which decays exponentially on the range of the correlation length of the fluid that wets the wall [16, 69]. As thermodynamic quantities on the right-hand side are evaluated at phase coexistence, use has been made of the identity $\partial\omega_{f,s}/\partial\mu = -\rho_{f,s}$, where $\omega_{f,s}$ are the grand potential densities of the fluid and the crystal at coexistence, respectively. The correlation length ξ_f of the fluid is obtained as the inverse of the smallest imaginary part of the pole of the static structure factor $S(k) = [1 - \rho_f\tilde{\phi}(k)]^{-1}$ closest to the real axis, i.e., $\xi_f = [\text{Im}(k)]^{-1} = 1.20$, where k fulfills $1 - \rho_f\tilde{\phi}(k) = 0$ [12]. In the case of complete wetting, i.e., for

$$\gamma_{sw} = \gamma_{fw} + \gamma_{fs}, \quad (7.12)$$

where γ_{sw} is the wall-solid surface tension, two scaling behaviors follow from this ansatz. At first, upon approaching μ_f from above, the width of the fluid film $\lambda(\Delta\mu)$ grows logarithmically as a function of $\Delta\mu$:

$$\lambda(\Delta\mu) \simeq -\xi_f \ln(\Delta\mu) + \text{const}, \quad (7.13)$$

as long as $\lambda \ll L_z$ holds, i.e., as long as both walls behave each as single walls in contact with a semi-infinite crystal. Growth is indeed observed in our results but it is interrupted at the freezing transition $\mu_f(L_z)$ by capillary melting, which leads us to the second scaling relation: at the point of capillary melting, the net contribution of the fluid region in the middle of the slit pore to the grand potential per unit area, $(\omega_f - \omega_s)(L_z - 2\lambda)$ equals twice the liquid-solid surface tension γ_{fs} , which yields the following relation:

$$L_z - 2\lambda(\mu_f(L_z)) \simeq \frac{2\gamma_{fs}}{(\rho_s - \rho_f)(\mu_f(L_z) - \mu_f)}. \quad (7.14)$$

For the maximum confinement-width studied ($L_z = 48$), we found $N_m^c = 4$ at $\mu = \mu_f(L_z) \cong 12.24$ corresponding to $\lambda \cong 4.1$, which is too small to accurately be fitted to a logarithmic function and to extract $\mu_f(L_z)$. Nevertheless, within the DFT it is possible to avoid the transition to the stable, capillary-molten phase, and remain instead in a partly crystalline setup also for $\mu < \mu_f(L_z)$ by iterating Eq. (7.5) with an appropriate initial density field $\rho(\mathbf{r})$, which already has a given number of molten layers. For a single wall, in which case capillary melting is absent, the system will choose the crystalline state with the lowest value of $\tilde{\Omega}[\rho(\mathbf{r})]$. Accordingly, we focus on the state that fulfills the same condition, among all metastable crystalline states, in the presence of two walls. However, we do consider only those chemical potentials for which at least one other state, which is still crystalline and has a higher number of molten layers, was found to be metastable, i.e., non-collapsed to a fluid. In this way, further growth of the fluid layer is observed up to a point where the crystalline slab in the middle of the slit becomes unstable towards collapse (see Fig. 7.10). By performing a least-square fit of the whole growth (between $N_m = 1$ and $N_m = 6$) to the logarithmic growth of Eq. (7.13), we obtain the bulk freezing chemical potential $\mu_f = 12.19$ independently of the already known value from Section 7.5 (see inset of Fig. 7.10). In fact, the width $\lambda(\Delta\mu)$ was taken to be the distance of the most distant molten layer from the wall. As expected, for large numbers of molten layers we find $\lambda(\Delta\mu) \simeq cN_m(\Delta\mu)$, with the layer separation $c = 1.04c^* = 1.113$, as discussed above. The independently obtained freezing chemical potential $\mu_f = 12.19$ agrees perfectly with the freezing chemical potential obtained from the partly constrained bulk measurement in Section 7.5. This finding constitutes a strong confirmation of the validity of the complete wetting scenario.

The second scaling relation, Eq. (7.14), serves as a check, again for the largest confinement length $L_z = 48$. The ingredient we are still missing is the surface tension γ_{fs} at coexistence. The latter quantity can be obtained within DFT by comparing the grand potential Ω of a bulk system at $\mu = \mu_f$ with that of a system that contains stripes of equally sized liquid and crystalline parts that form two planar liquid-solid interfaces within the periodic 'box' of size $L_x \times L_y \times L_z$. We have performed this calculation using a box with the same x - and y -dimensions as in the confining case and a longer z -length, $L_z = 96$; clearly, there is no external potential in this case. In this way, we obtain $\gamma_{fs} \cong 0.49$, where the crystal is oriented in the 111-

direction at the interface. Insertion of γ_{fs} , together with $\rho_s - \rho_f = 0.56$ and $\mu_f(L_z = 48) - \mu_f = 0.05$ into Eq. (7.14), yields $L_z - 2\lambda \cong 35.3$, which agrees reasonably well with $L_z - 2\lambda \cong 39.9$ from the direct comparison of the grand potential densities of the capillary-molten or crystalline states in confinement. It must be noted that we disregarded widths of the interfaces in our crude, ‘sharp-kink’ treatment of the interfaces that led to Eq. (7.14). In reality, the widths of the fluid-wall and of the fluid-solid interfaces are of the order of $\sim 2\sigma$, which helps in explaining the discrepancy.

Capillary melting is a first-order phase transition, which comprises the possibility of non-equilibrium states close to or at the transition remaining metastable. In the DFT calculations, the metastability of non-molten states beyond equilibrium capillary melting has already been exploited for extracting the logarithmic growth of the wetting layer [see Fig. 7.10 and Eq. (7.13)]. In computer simulations of systems in the NVT -ensemble, metastable states may persist in small periodic simulation boxes and for average densities lying within two coexisting densities of a first-order phase transition. Here, free energy contributions of phase-separating interfaces are comparable or larger than bulk contributions.⁵ This behavior is also observed in computer simulations of the GEM-8 model in a relatively large planar confinement of $L_z = 24$, where the lateral dimensions of the xy -periodic simulation box $L_x = L_y = 9.29$ are comparatively small. Consequently, by continuously varying the density of the system a continuous growth of a liquid layer on each Yukawa wall up to complete filling of the box is observed (see Fig. 7.11). Snapshots of the simulation are exemplarily shown for three different average densities $\rho = 3.5, 3.7, 4.0$ in Fig. 7.12.

The average number of molten layers on each wall, $N_m(\rho)$ in Fig. 7.11, has been determined by analyzing the lateral pair distribution function $g_{2D}(r_{\parallel})$ (not shown here) for a total of 22 crystalline layers in parallel to the walls, occurring for large densities. As for the narrow confinement of $L_z = 7$ above, the range of each layer in the z -direction is determined by two consecutive minima of the respective density profile $\rho_{xy}(z)$ (also not shown here). A layer is defined to be molten/crystalline once the first minimum of $g_{2D}(r_{\parallel})$ is larger/smaller than 0.15. Clearly, the system separates along the z -axis and does not show an indication of capillary melting. However, and as already argued above, we have strong evidence that the observation of states with a large number of molten layers is a finite-size effect in the simulations.

⁵Strictly speaking, these states are *in equilibrium* due to the (small) finite size but only for larger sizes they would be metastable.

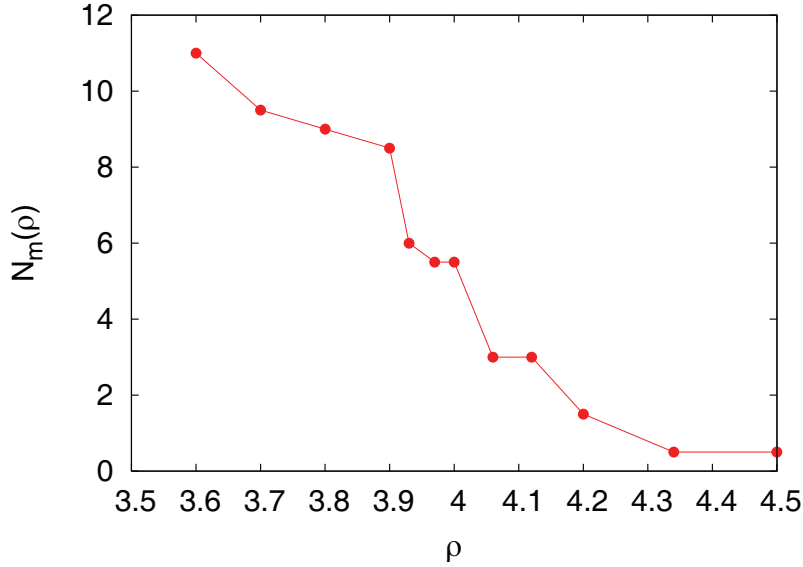


Figure 7.11: Yukawa-walls: The average number of molten layers on each wall for the same confinement as in Fig. 7.12 as a function of average density ρ , and as obtained from the computer simulations. The averages are performed over the left and the right wall.

7.7 Attractive walls

In the second setup, we study the effect of attractive Lennard-Jones walls. The corresponding external potential is taken to have the form

$$V_{\text{LJ}}(\mathbf{r}) = 10 \left[\frac{1}{z^9} - \frac{1}{z^3} + \frac{1}{(L_z - z)^9} - \frac{1}{(L_z - z)^3} \right], \quad (7.15)$$

$$0 < z < L_z.$$

Recent numerical simulations by Lenz *et al* [156] have indeed shown that amphiphilic dendrimers of the second generation, demonstrated to be GEM-particles of the Q^\pm -class in ref. [192], together with an attractive core wall-particle interaction lead to very similar effective interaction potentials. The precise shape of the wall potential depends, of course, on the different molecular interaction parameters. However, a range of the attraction of the order of σ and a depth of the order of few $k_B T$ is certainly a reasonable assumption. Here, the minimum value of the Lennard-Jones potential for large L_z is $V_{\text{LJ}}(z_{\text{min}} \cong 1.2) \cong -3.85$.

In contrast to the setup with repulsive, Yukawa walls of Section 7.6, the system now *freezes at the walls before freezing in the middle region* of the confinement, as can be seen for $L_z = 7$ in Fig. 7.13. Note the big difference of cluster population close to the wall and in the middle of the slit by more than 2 particles per cluster. As for the

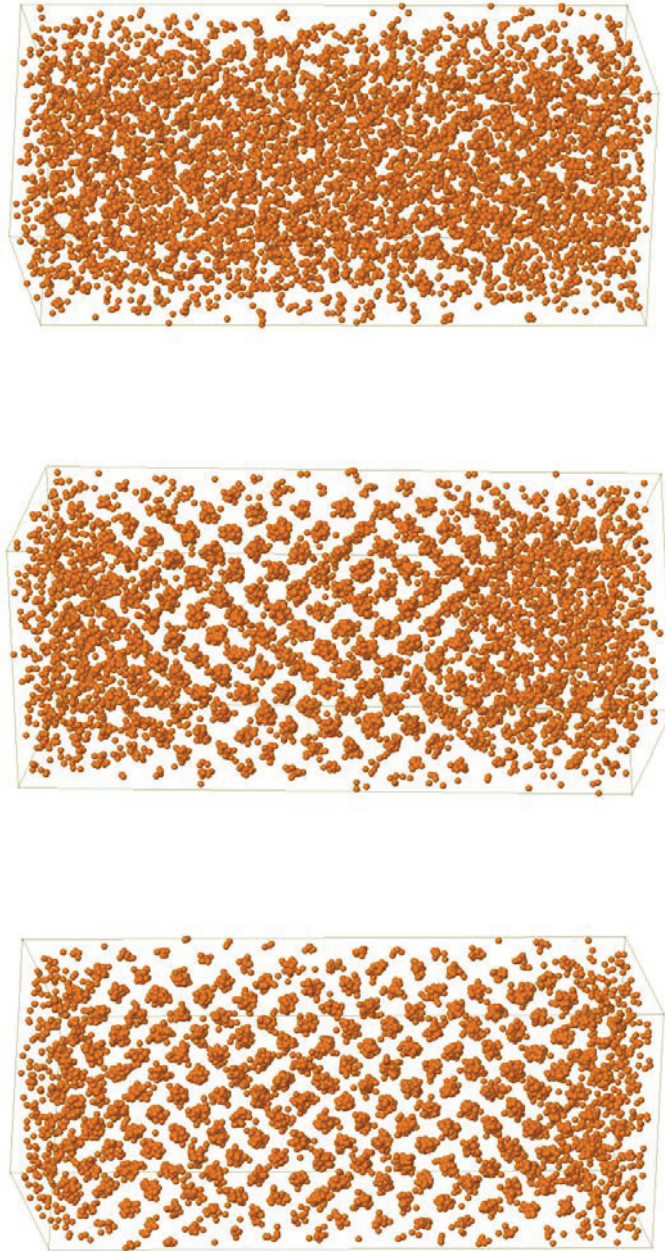


Figure 7.12: Yukawa walls: Simulation snapshots for $L_z = 24$ and average densities of $\rho = 3.5, 3.7, 4.0$ (from top to bottom). The boundaries of the box ($L_x = L_y = 9.29$) are indicated by thin lines. The Yukawa-walls are situated at the left and at the right boundaries, respectively. The simulation boxes are oriented differently for better visibility of the crystalline region in the middle of the box.

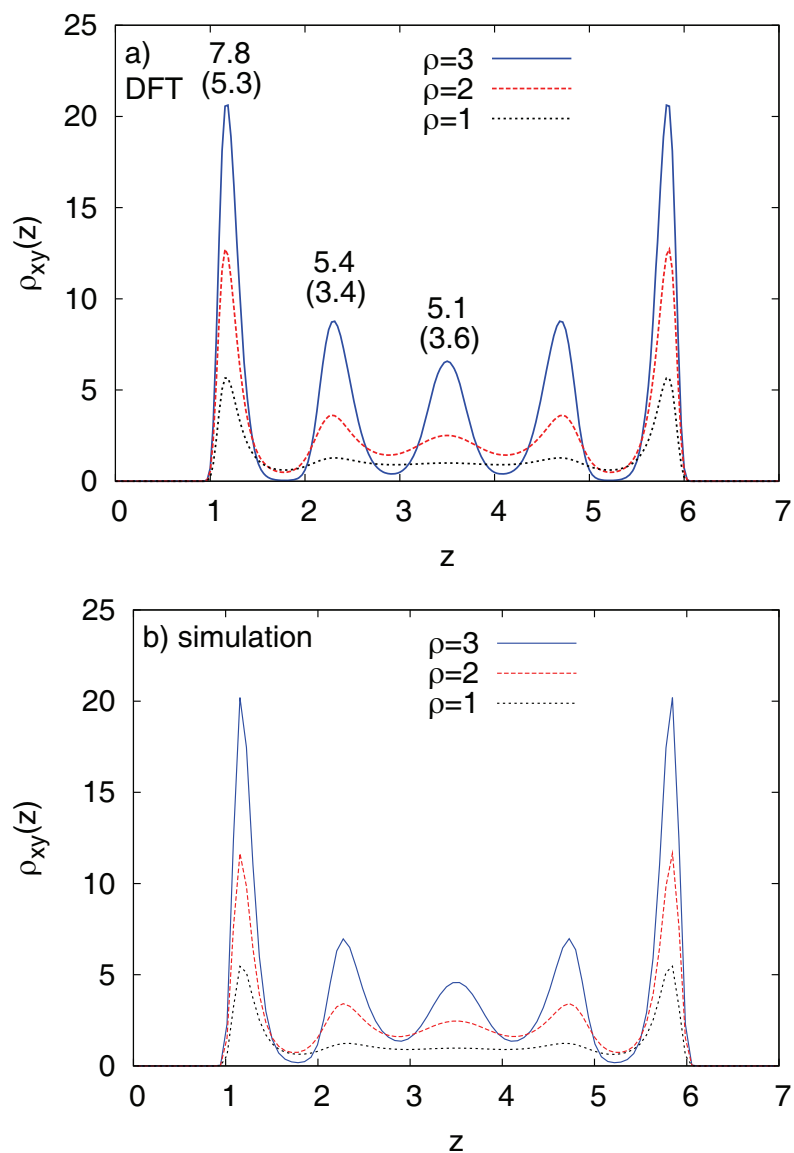


Figure 7.13: Lennard-Jones walls: Laterally-averaged density profiles $\rho_{xy}(z)$ for three different densities above ($\rho = 2, 3$) and below ($\rho = 1$) the freezing transition for $L_z = 7$ as obtained from the DFT, (a), and the simulation, (b). The numbers over the peaks denote the average number of particles, n_c , occupying a cluster, for $\rho = 3$ (top value) and $\rho = 2$ (in parentheses, lower value). (b) The lateral dimensions of the periodic simulation box are $L_x = L_y = 20.43$.

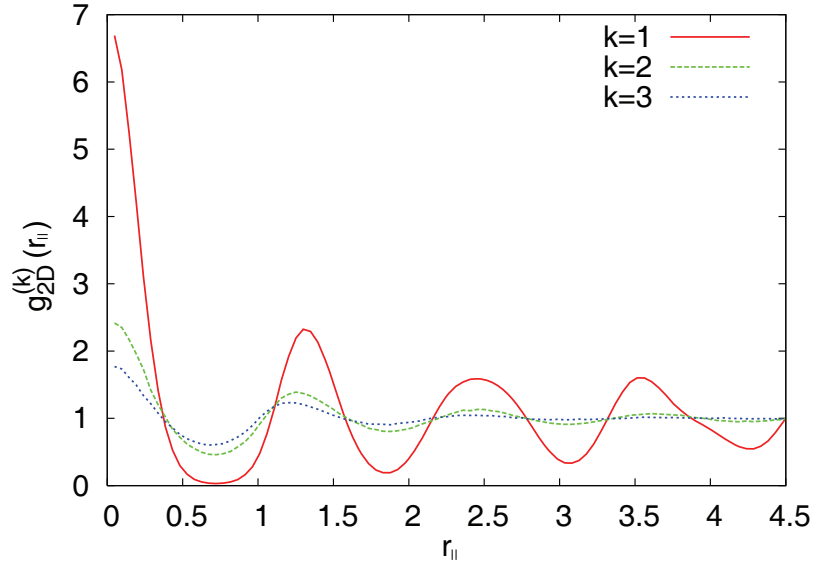


Figure 7.14: Lennard-Jones walls: The lateral pair distribution function $g_{2D}^{(k)}(r_{||})$ for the first three layers of clusters on either of the wall (k is counted from the wall) for the same confinement as in Fig. 7.13 at average density $\rho = 3$ (for the definition of layers see main text).

Yukawa setup, we present in Fig. 7.13(b) results from BD computer simulations for the same parameters as in the DFT, which show the same quantitative behavior for $\rho = 1$ and the same qualitative behavior for $\rho = 2, 3$. The reversal of the dependence of crystallinity on the layer-distance from the walls is confirmed by measurements of the restricted pair-distribution function, $g_{2D}^{(k)}(r_{||})$, Eq. (7.10), shown for the first three layers from either wall in Fig. 7.14. Peaks and minima of the pair distribution function clearly become less pronounced for increasing distance of the layer from the wall.

Freezing in terms of breaking the xy -symmetry of the system is now mainly a single-wall effect, which is slightly disturbed by the interaction of the two crystalline layers on either wall with each other. This is at odds with freezing at the Yukawa setup, which is a bulk-dominated phenomenon disturbed by the walls. On these grounds, we denote the surface freezing chemical potential for the Lennard-Jones setup as $\mu_f^s(L_z)$, in order to distinguish it from the respective capillary freezing chemical potential $\mu_f(L_z)$ (see below). The bulk phase diagram only enters the stage once the bulk freezing chemical potential, μ_f , is approached *from below*. Interactions between crystalline layers on either wall are subdominant for wall separations as small as $L_z \approx 5$. This can be ascertained from the dependence of the surface-freezing chemical potential $\mu_f^s(L_z)$ on L_z , Fig. 7.15, which monotonically approaches a plateau value of $\mu_f^s \equiv \mu_f^s(L_z \rightarrow \infty)$ already from $L_z = 5$ on. By extrapolating

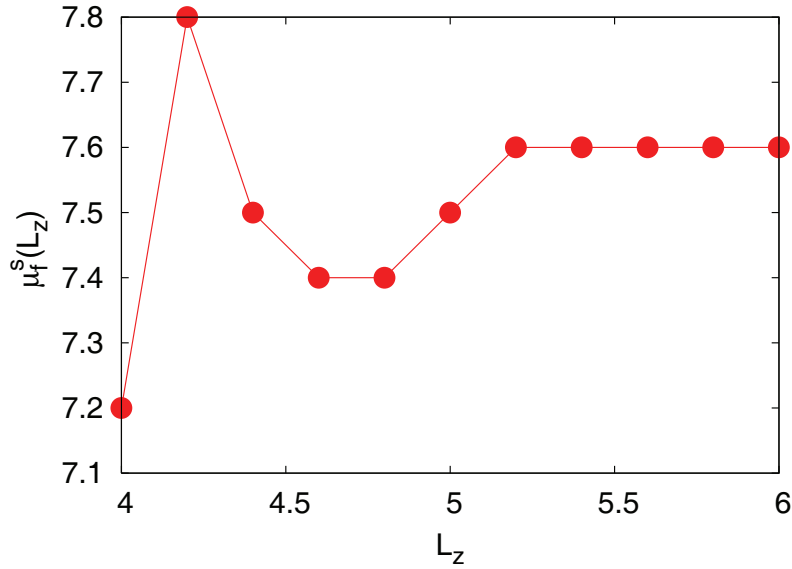


Figure 7.15: Lennard-Jones walls: Surface freezing chemical potential $\mu_f^s(L_z)$ as a function of the confinement width L_z for the attractive Lennard-Jones walls.

the phase diagram of Fig. 7.15 to $L_z \rightarrow \infty$ we find $\mu_f^s \cong 7.7$ which corresponds to a bulk fluid density of $\rho \cong 1.90$. This value, of course, depends on the depth of the external potential.

Contrary to Yukawa walls, this setup shows capillary freezing from the walls. Whereas at $\mu_f^s(L_z)$ surface-induced freezing sets in, capillary freezing occurs at a significantly higher value $\mu_f(L_z)$, which now approaches μ_f from below as L_z grows, i.e., $\mu_f(L_z \rightarrow \infty) = \mu_f$. We note also that freezing on the walls is not only observed for the prefactor 10 in Eq. (7.15) but for any prefactor, i.e., for a vanishing attractive part of $V_{LJ}(\mathbf{r})$, implying that surface-induced freezing is an intricate effect which sensitively depends on the nature of the wall-particle interaction. In particular, for the system under study the question whether surface-induced freezing or melting is observed, seems to be mostly a matter of the range or softness of the wall-particle potential. Our results suggest that there is surface-induced freezing for a hard wall (as for the Lennard-Jones walls) whereas there is surface-induced melting for a soft wall (as for the Yukawa-walls).

For small values of L_z , the two minima of the external potential merge and the system behaves qualitatively the same as for the repulsive Yukawa walls. We therefore restrict our analysis to $L_z \geq 4$. Due to the relatively strong attraction of the walls, the system favors a hexagonal pattern of clusters on the planar surfaces. The equilibrium orientation of the (distorted) fcc lattice in confinement is therefore always the 111-orientation. As the chemical potential is increased beyond $\mu_f^s(L_z)$ and as the bulk freezing chemical potential μ_f is approached from below, the number

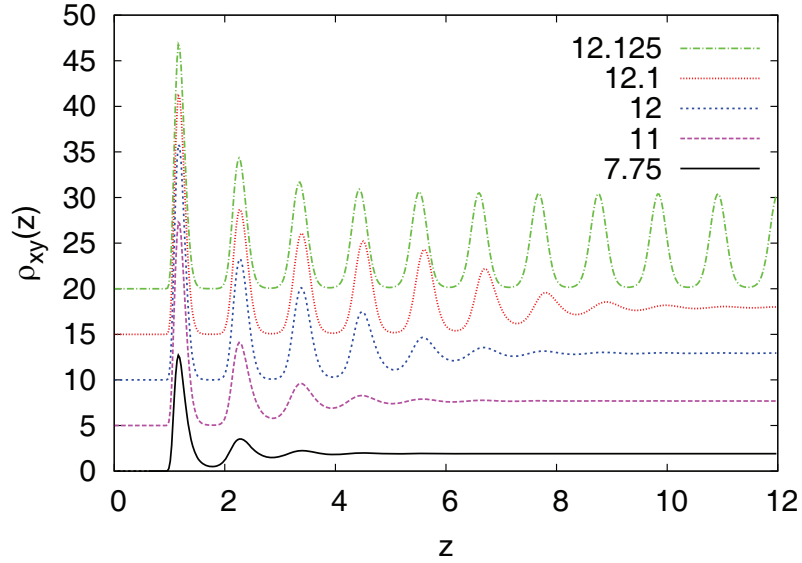


Figure 7.16: Lennard-Jones walls: Laterally-averaged density profiles $\rho_{xy}(z)$ close to the left wall for $L_z = 48$ for different chemical potentials $\mu = 12.125, 12.1, 12, 11, 7.75$ (from top to bottom).

of crystalline layers on either wall grows continuously, as can be seen from the density profiles for $L_z = 24$ in Fig. 7.16.

Upon approaching μ_f from below, we find for the Lennard-Jones walls that the number of crystalline layers on the walls, $N_c(\mu)$, grows continuously and nearly logarithmically with $|\Delta\mu| = |\mu - \mu_f|$ (cf. Fig. 7.17 for $L_z = 24, 48$). This growth is eventually interrupted by capillary freezing, which occurs at a chemical potential $\mu_f(L_z)$. The surface- and bulk-freezing chemical potentials for attractive walls order as $\mu_f^s(L_z) \lesssim \mu_f^s \ll \mu_f(L_z) \lesssim \mu_f$.

As for the case of the Yukawa walls, we studied two large confinement lengths $L_z = 24$ and $L_z = 48$. We found $\mu_f(L_z = 24) = 12.12$ and $\mu_f(L_z = 48) = 12.16$. In the limit of large L_z and large crystalline film thickness λ , still substantially smaller than $L_z/2$, the (local) density of the fluid in the middle of the confining region is very close to the fluid density of a semi-infinite fluid reservoir on a single Lennard-Jones wall at infinity, which allows us to define the adsorption as

$$\gamma = \int_0^{L_z/2} dz [\rho_{xy}(z) - \rho_{xy}(L_z/2)], \quad (7.16)$$

which is plotted as a function of $|\Delta\mu|$ in the inset of Fig. 7.17.

Following the same reasoning as for the Yukawa walls, the slopes of the logarithmic growths of N_c and γ are now given by the correlation length of the (bulk) solid

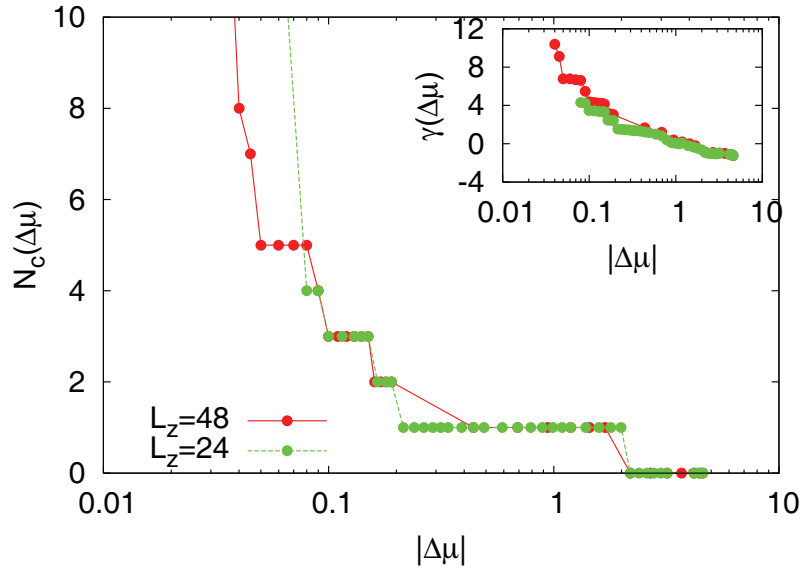


Figure 7.17: Lennard-Jones walls: The number of crystalline layers on the walls, $N_c(\mu)$, as a function of the difference between the bulk freezing chemical potential, $\Delta\mu$ and for two different confinement widths. Note that $\mu_f > \mu$ here. Inset: the adsorption of a crystal layer γ , Eq. (7.16), as a function of $|\Delta\mu|$.

phase ξ_s that wets the wall:

$$N_c \simeq -\frac{\xi_s}{c} \ln(|\Delta\mu|) + \text{const}, \quad (7.17)$$

$$\gamma \simeq -(\rho_s - \rho_f)\xi_s \ln(|\Delta\mu|) + \text{const}, \quad (7.18)$$

where $c = 1.113$ is the distance of neighboring layers of the constrained bulk fcc crystal, again. By fitting a logarithmic curve to the N_c -data at intermediate N_c we roughly obtain $\xi_s \cong 2$, roughly twice as large as the fluid correlation length ξ_f . As for the specular case of the Yukawa-walls, we cannot rule out the possibility of a non-continuous growth of the crystalline layer in a single-wall setup. However, our results for the two confinement widths of $L_z = 24, 48$ suggest that the crystal completely wets the Lennard-Jones walls and that the growth of the crystalline film is only interrupted by capillary freezing.

We present snapshots of BD-computer simulations of the system in planar Lennard-Jones confinement of $L_z = 24$ for different average densities in Fig. 7.18. For the smallest density of $\rho = 2.5$ the system is only crystalline on the walls. For intermediate density, $\rho = 4.0$, the system displays two equally large crystalline layers on both walls, and for $\rho = 5.0$ the system turns completely crystalline. This behavior is again quantified through the analysis of $g_{2D}^{(k)}(r_{\parallel})$ for all crystalline/fluid layers parallel to the confining walls, as in Section 7.6. The resulting average number of

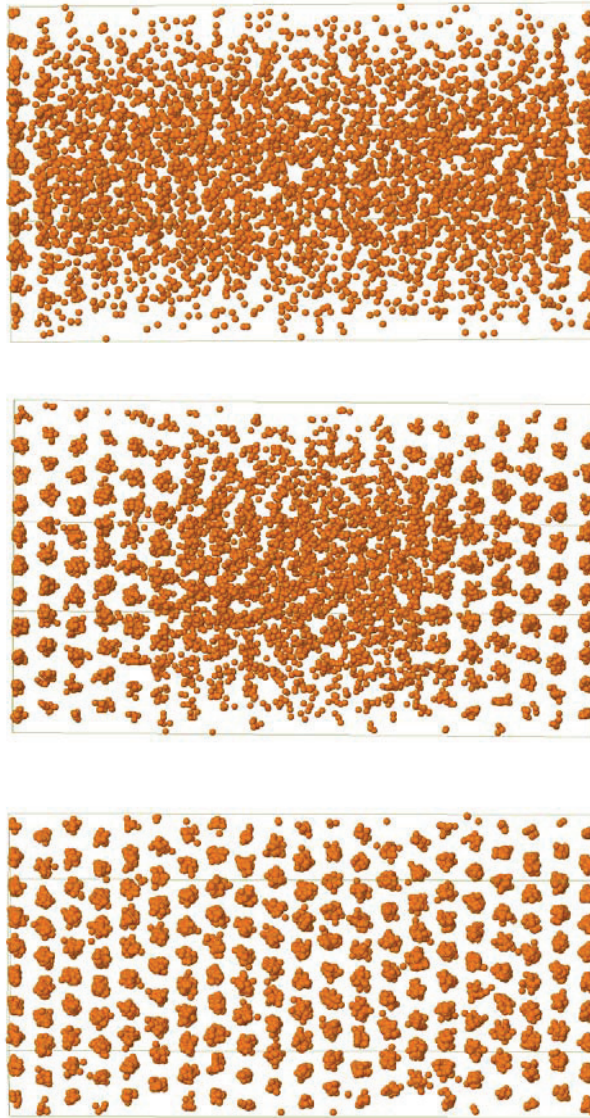


Figure 7.18: Lennard-Jones walls: Simulation snapshots for $L_z = 24$ and average densities $\rho = 2.5, 4.0, 5.0$ (from top to bottom). The boundaries of the box ($L_x = L_y = 9.29$) are indicated by thin lines. The Lennard-Jones walls are situated at the left and at the right boundaries, respectively. The simulation boxes are oriented differently for better visibility of the crystalline region in the middle of the box.

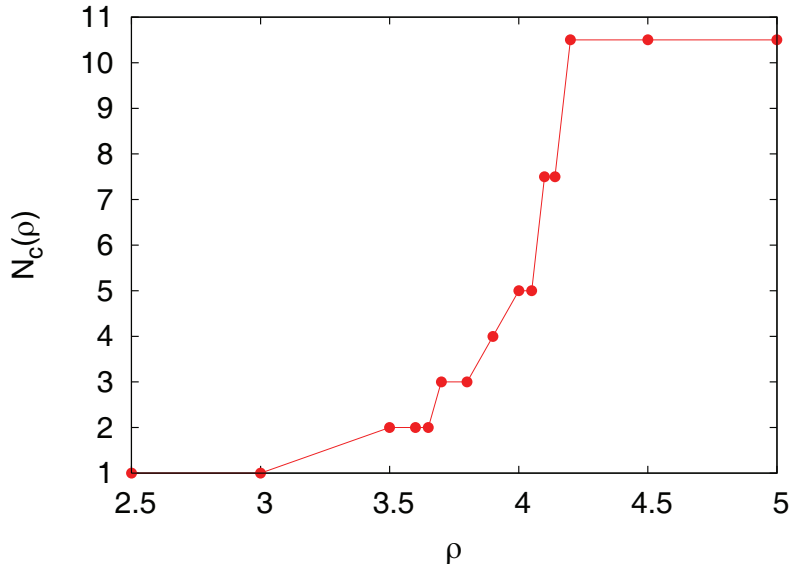


Figure 7.19: Lennard-Jones-walls: The average number of crystalline layers on each wall for the same confinement as in Fig. 7.18, as a function of average density ρ , and as obtained from the computer simulations. The averages are performed over the left and the right wall.

crystalline layers on each wall, $N_c(\rho)$, is plotted as a function of average density in Fig. 7.19.

7.8 Conclusions

In conclusion, we studied the effect of repulsive and attractive slit-pore confinement on freezing and melting of cluster-forming, ultrasoft, repulsive particles of the GEM-8-class. For repulsive Yukawa-walls we found that the system freezes from the middle of the slit whereas for attractive Lennard-Jones walls it freezes at the walls before freezing in the middle. For small confinement-widths the respective freezing chemical potentials and liquid-solid coexistence densities display strong oscillations with varying slit width—the wavelength being equal to the distance of crystal layers in the bulk. However, whereas the oscillations are very pronounced for $L_z \lesssim 15$ in the case of the Yukawa-walls, they are damped already for $L_z \approx 5$ in the case of the Lennard-Jones walls. In the case of large confinement-widths we could find strong indications that upon approaching the bulk freezing chemical potential from *above* the Yukawa-walls are completely wetted by fluid whereas upon approaching the bulk freezing chemical potential from *below* the Lennard-Jones walls are completely wetted by the crystal.

Different modifications to the slit-pore geometry and to the particle-wall interac-

tions are of interest: Whereas in this work both confining walls were of the same kind, it would be interesting to study the influence of “competing walls” [29]. Further, the crystal arrangement at the walls is very sensitive towards structured/patterned substrates [33, 118, 121, 122]. Moreover, slit pore confinement is a reference model for more complicated geometries such as porous media [141]. Confinement has also intriguing implications for the diffusive dynamics in and out of equilibrium. For equilibrium fluids in planar confinement, it has been recently demonstrated that both lateral and perpendicular diffusivities, D_{\parallel} and D_{\perp} , are enhanced at z -positions of higher average one-particle density $\rho_{xy}(z)$ as compared to the regions of lower density [99, 187]. For cluster-forming, GEM- n particles, diffusive dynamics features novel characteristics, since even crystals now display nonzero long-time diffusivities, due to the presence of activated hopping processes [162, 193]. It would be interesting to examine the behavior of D_{\parallel} and D_{\perp} in confinement, calculated separately for each layer, for the case at hand. Bulk studies [162, 193] have revealed an essentially Arrhenius-type behavior, $D \sim \exp(-\beta E_A)$, of the long-time diffusivity, with an activation energy E_A proportional to ρ . It is interesting to find out to what extent this law holds also locally for each layer formed in slit-pore confinement. Recently, the relaxation dynamics of a fluid of Gaussian particles in a temporally oscillating, spherical, harmonic trap has been studied using computer simulations and dynamical density functional theory [232]. The latter method is an extension of the DFT to overdamped non-equilibrium dynamics [10, 75, 179], which has recently also been used to study crystal growth in 2D.⁶ It would be interesting to employ dynamical density functional theory to study the relaxation of cluster crystals upon sudden or temporally periodic changes of the slit-pore confinement.

Acknowledgements

The authors would like to thank Hartmut Löwen and Bianca Mladek for helpful discussions. This work has been supported by the DFG within the SFB TR6, project section C3 and by the EU Network of Excellence “Softcomp”. CNL wishes to thank the Erwin Schrödinger International Institute for Mathematical Physics (ESI, Vienna), where parts of this work have been carried out, for a Senior Research Fellowship and for its hospitality. AJM acknowledges support from 2007-60I201 (CSIC, Spain).

⁶See Chapter 6.

Chapter 8

Dynamics of a Brownian circle swimmer¹

Abstract

Self-propelled particles move along circles rather than along a straight line when their driving force does not coincide with their propagation direction. Examples include confined bacteria and spermatozoa, catalytically driven nanorods, active, anisotropic colloidal particles and vibrated granulates. Using a non-Hamiltonian rate theory and computer simulations, we study the motion of a Brownian “circle swimmer” in a confining channel. A sliding mode close to the wall leads to a huge acceleration as compared to the bulk motion, which can further be enhanced by an optimal effective torque-to-force ratio.

Active particles, which are self-propelled by their own motor, exhibit a wealth of novel and fascinating nonequilibrium effects such as giant density fluctuations [261], swarming [281], and swirling [148]. Examples are found in quite different areas of physics and include micro-organisms propelled by flagella in a fluid [24, 71, 125, 236, 298], man-made colloidal swimmers [73], catalytically driven nanorods or Janus particles [66, 286], vibrated granulates of polar rods [148, 199], and pedestrians [120]. Typically it is assumed that the swimmers move along their symmetry axis such that the force and the particle orientation are in line. This leads to a motion along a straight line just perturbed by random (e.g., Brownian) fluctuations.

¹This chapter was published by Sven van Teeffelen and Hartmut Löwen in *Phys. Rev. E* 78 (2008), 020101(R) (arXiv:0803.2008). It is reprinted with permission from the American Physical Society, Copyright 2008. It was selected for publication in the September 2008 issue of the Virtual Journal of Nano Science & Technology (<http://www.vjnano.org/>).

Here we study the case in which the internal force propelling a colloidal particle does not coincide with the particle orientation. In the absence of Brownian fluctuations, this will lead to an overdamped motion along a closed circle, therefore we refer to this particle as a “circle swimmer.” Even a slight misalignment of the drive direction will result in circle swimming, which is thus the generic case of self-propulsion. Circle swimmers with a pronounced curved trajectory are realized in nature and can be artificially prepared: In fact, it has been shown that certain bacteria [24, 71, 125, 151] and spermatozoa [236, 298], when confined to two dimensions, swim in circles. Moreover, catalytically driven nanorods [66, 286] and colloidal particles [73] can be prepared with a tilted motor, and a vibrated polar rod [148] on a planar substrate with an additional left-right asymmetry will move along circles. Last but not least, the trajectories of completely blinded and ear-plugged pedestrians have a significant circular form [201]. Despite their practical importance, the Brownian dynamics of a circle swimmer has not yet been addressed by theory and simulation either in the bulk or under confinement.²

In this chapter, we propose a simple model for Brownian motion of a circle swimmer in two spatial dimensions arising from the combined actions of an internal self-propelling force and a torque. We solve the Langevin equation of a two-dimensional circle swimmer analytically in the bulk providing a suitable reference model. The averaged position falls on a *spira mirabilis*, and a crossover from an oscillatory ballistic to a diffusive behavior is found in the mean-squared displacement. We then identify the modes of propagation of a circle swimmer in confining channels with repulsive walls using computer simulations and a non-Hamiltonian rate theory. In symmetric channels, the long-time self-diffusion coefficient D_L is significantly enhanced mediated by an efficient *sliding mode* of a tilted rod close to a wall. Furthermore, D_L is nonmonotonic in the torque. Finally, in asymmetric channels which are lacking a left-right symmetry (e.g., due to gravity [145]), the sliding mode of the circle swimmer yields a *ballistic* motion along the wall.

Neglecting hydrodynamic interactions, the overdamped motion of the Brownian circle swimmer in two dimensions is governed by the Langevin equations for the rod center-of-mass position

$$\dot{\mathbf{r}} = \beta \mathbf{D} \cdot [F \hat{\mathbf{u}} - \nabla V(\mathbf{r}, \phi) + \mathbf{f}] \quad (8.1)$$

and for the rod orientation

$$\dot{\phi} = \beta D_r [M - \partial_\phi V(\mathbf{r}, \phi) + \tau] , \quad (8.2)$$

respectively, where dots denote time derivatives and $\beta^{-1} = k_B T$ is the thermal energy. The rod’s short time diffusion tensor

$$\mathbf{D} = D_{\parallel} (\hat{\mathbf{u}} \otimes \hat{\mathbf{u}}) + D_{\perp} (\mathbf{I} - \hat{\mathbf{u}} \otimes \hat{\mathbf{u}}) \quad (8.3)$$

²We note that in three spatial dimensions misalignment of internal direction and force leads to motion along spirals which has been observed for bacteria, see ref. [260].

is given in terms of the short time longitudinal (D_{\parallel}) and transverse (D_{\perp}) translational diffusion constants, with $\hat{\mathbf{u}} = (\cos \phi, \sin \phi)$, \mathbf{I} the unit tensor and \otimes a dyadic product. D_r is the short time rotational diffusion constant. $F\hat{\mathbf{u}}$ is a constant *effective* internal force that represents the propulsion mechanism responsible for the deterministic motion in the rod orientation, and M is a constant *effective* internal or external torque yielding the deterministic circular motion (see the sketch in Fig. 8.1). $V(\mathbf{r}, \phi)$ is an external confining potential. \mathbf{f} and τ are the zero mean Gaussian white noise random force and random torque originating from the solvent, respectively. Their variances are given by

$$\overline{f_{\parallel}(t)f_{\parallel}(t')} = 2\delta(t-t')/(\beta^2 D_{\parallel}) \quad (8.4)$$

$$\overline{f_{\perp}(t)f_{\perp}(t')} = 2\delta(t-t')/(\beta^2 D_{\perp}) \quad (8.5)$$

$$\overline{\tau(t)\tau(t')} = 2\delta(t-t')/(\beta^2 D_r), \quad (8.6)$$

where f_{\parallel} , f_{\perp} are the components of \mathbf{f} parallel and perpendicular to $\hat{\mathbf{u}}$, respectively. The bars over the quantities denote a noise average. We remark that for an active self-propelled particle, F and M are *effective* net forces that could be determined in the bulk from the forward and angular velocities $F = |\dot{\mathbf{r}}|/(\beta D_{\parallel})$ and $M = |\dot{\phi}|/(\beta D_r)$, respectively, but are not necessarily directly connected to the internal propulsion mechanism [228].

At first we consider the free circle swimmer, i.e., we set $V(\mathbf{r}, \phi) = 0$. In the limit of zero temperature, the rod center of mass would describe a perfect circle of radius $R = (D_{\parallel}F)/(D_rM)$, with the circular frequency $\omega \equiv \beta D_r M$. For finite temperature all moments of \mathbf{r} and ϕ can be calculated exactly. The first and second moments of $\phi(t)$ are simply given by

$$\overline{\phi} = \phi_0 + \omega t, \quad (8.7)$$

$$\overline{\Delta\phi^2} = \overline{[\phi(t) - \phi_0]^2} = (\omega t)^2 + 2D_r t, \quad (8.8)$$

where $\phi_0 = \phi(t=0)$, and where we let ϕ run ad infinitum. The first two moments of $\Delta\mathbf{r} \equiv \mathbf{r}(t) - \mathbf{r}(0)$ are given by

$$\begin{aligned} \overline{\Delta\mathbf{r}} &= \lambda \left[D_r \hat{\mathbf{u}}_0 + \omega \hat{\mathbf{u}}_0^{\perp} - e^{-D_r t} \left(D_r \overline{\hat{\mathbf{u}}} + \omega \overline{\hat{\mathbf{u}}^{\perp}} \right) \right] \\ \overline{\Delta\mathbf{r}^2} &= 2\lambda^2 \left\{ \omega^2 - D_r^2 + D_r (D_r^2 + \omega^2) t \right. \\ &\quad \left. + e^{-D_r t} \left[(D_r^2 - \omega^2) \cos(\omega t) - 2D_r \omega \sin(\omega t) \right] \right\} \\ &\quad + 2(D_{\parallel} + D_{\perp})t, \end{aligned} \quad (8.9)$$

with $\lambda = \beta D_{\parallel} F / (D_r^2 + \omega^2)$, $\hat{\mathbf{u}}_0 = (\cos \phi_0, \sin \phi_0)$, $\hat{\mathbf{u}}_0^{\perp} = (-\sin \phi_0, \cos \phi_0)$, $\overline{\hat{\mathbf{u}}} = (\cos \overline{\phi}, \sin \overline{\phi})$, and $\overline{\hat{\mathbf{u}}^{\perp}} = (-\sin \overline{\phi}, \cos \overline{\phi})$, i.e., $\overline{\Delta\mathbf{r}}$ describes a *spira mirabilis*.

We consider a very thin rod of length L , where $D_r/D_{\parallel} = 3/(2L^2)$, $D_{\perp} = D_{\parallel}/2$. We will denote all times in units of $\tau_B = L^2/D_{\parallel}$, lengths in units of L , and energies

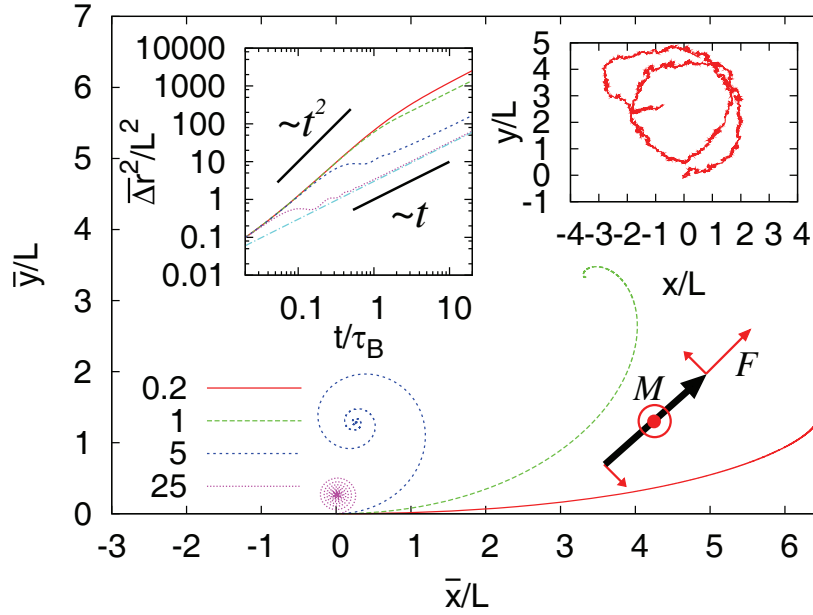


Figure 8.1: Trajectories of the mean position $\bar{\mathbf{r}}$ of the self-propelling rod for fixed $\beta FL = 10$, $\beta M = 0.2, 1, 5, 25$ ($\mathbf{r}_0 = \mathbf{0}, \phi_0 = 0$). Left inset: the mean-square displacement $\overline{\Delta \mathbf{r}^2}$ for the same force and torques, but also for $\beta FL = 0$, $\beta M = 0$ (lowermost curve). Right inset: a typical trajectory of the rod for $\beta FL = 25$, $\beta M = 10$, for times $0 < t < \tau_B$. Lower right inset: Sketch of the self-propelled circle swimmer.

in units of β^{-1} . Different regimes are distinguished in terms of the dimensionless quantities D_r/ω and βFL . The latter determines whether the rod's erratic motion is dominated by the kicks of the solvent particles or by the self-propulsion. The former is the ratio of the ballistic over the random turning rate. In Fig. 8.1, we show $\overline{\Delta \mathbf{r}}$ for different internal torques M and a typical trajectory of the rod position during two complete turns. In the second inset of Fig. 8.1 we display $\overline{\Delta \mathbf{r}^2}$, which shows deterministic behavior for $t \lesssim 1/D_r$ while for large times the swimmer moves in a random fashion according to $\overline{\Delta \mathbf{r}^2} \propto t$.

Next, we introduce a confining, integrated segment-wall power-law potential in the x direction,

$$V(x, \phi) = \int_0^L dl v[x'(l)] + kx \quad (8.10)$$

with

$$v(x') \equiv (\beta L)^{-1} \left\{ \left[\frac{L}{x'} \right]^n + \left[\frac{L}{(L_x - x')} \right]^n \right\}, \quad (8.11)$$

where L_x is the channel width, $n = 24$ is a large exponent, and $x'(l)$ is the x position of the rod segment at contour length l (see the right inset of Fig. 8.2). In case the

solvent is confined as well, hydrodynamic interactions between the particle and the wall lead in principle to an x -dependent diffusion tensor [74], which is ignored in our model. An additional gravitational force in the x direction [145] of strength k will be applied later, but we focus first on the symmetric case $k = 0$. At zero temperature, for a not too large ratio M/LF and under appropriate initial conditions (\mathbf{r}_0, ϕ_0) , the tilted swimmer performs a steady-state *sliding motion* along either of the two walls with a constant x -position close to the wall and with a constant angle ϕ determined by the steady-state conditions $\dot{x} = 0$, and $\dot{\phi} = 0$, respectively. Without loss of generality, we consider the case $M > 0$, i.e., the rod rotates counterclockwise, such that it slides upwards along the left wall (see the sketch in Fig. 8.2). In the limit of hard walls ($n \rightarrow \infty$), the two solutions to the set of steady-state equations can be given explicitly as

$$x_{s/u} = L \left(1 - \frac{1}{2} \cos \phi_{s/u} \right), \quad (8.12)$$

i.e., the front rod tip sits on the wall, and

$$\cos^2 \phi_{s/u} = \frac{1 - 2 \left(\frac{M}{LF}\right)^2 \mp \sqrt{1 - 8 \left(\frac{M}{LF}\right)^2}}{2 + 2 \left(\frac{M}{LF}\right)^2}, \quad \cos \phi_{s/u} < 0, \quad (8.13)$$

where the minus sign corresponds to the stable (ϕ_s) and the plus sign to the unstable (ϕ_u) solution. Clearly, for $2\sqrt{2}M/LF > 1$ there is no solution to the steady-state conditions, but the rod keeps on rotating. For large exponents n , the asymptotic steady-state velocity in the y direction is given by $v_y \simeq D_{\parallel} F \sin \phi_s / (1 + \cos^2 \phi_s)$.

The sliding mode is also present at finite temperature. However, by thermal fluctuations the rod eventually leaves the wall and reaches the opposite wall under an appropriate angle for the respective sliding mode in the opposite y direction, which we refer to as “flipping.” Consequently, the circle swimmer moves diffusively according to $\overline{\Delta \mathbf{r}^2} \simeq 2D_L t$, with D_L the long-time translational diffusion coefficient. This picture is clearly confirmed by Brownian dynamics computer simulations, averaged over 1000 independent simulation runs, as shown in Fig. 8.2.

For large βFL , large βM , and a channel width of the order of the circle radius ($L_x \lesssim R$), the average time the swimmer spends in its stable mode on either of the walls is large as compared to the duration of a flip. Thus, the swimmer effectively performs a one-dimensional random walk with a typical step length $a \simeq v_y / \gamma$, where γ is the flipping rate. This random walk leads to a long-time diffusion coefficient of $D_L \simeq v_y^2 / \gamma$, which we display as a function of internal torque M for different wall-wall separations L_x in Fig. 8.3.

It is clearly seen from the simulations [Fig. 8.3(a)] that the diffusion in the channel is strongly enhanced as compared to the diffusivity of the free swimmer. In particular, this strong enhancement is already observed for $M = 0$, as the narrow walls constantly align the rod in the y direction. However, the diffusion eventually slows with increasing wall-wall separation L_x . For intermediate $M/LF \approx 0.15$,

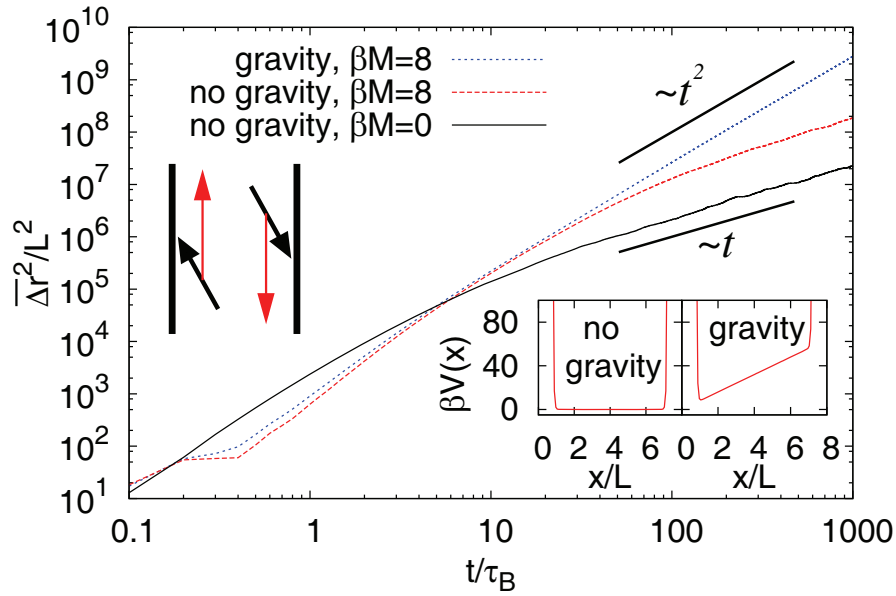


Figure 8.2: Mean-square displacement $\overline{\Delta \mathbf{r}^2}$ in confinement ($\beta FL = 60$, $L_x = 8L$) without gravity and with zero torque (black), without gravity and with finite torque (red), and with torque and gravity (blue). The left inset displays the rod sliding along the walls. The right inset shows the confining potential without (left) and with (right) gravity.

diffusion is enhanced even further—in the simulations [Fig. 8.3(a)] by an order of magnitude—displaying a much smaller dependence on L_x . This non-monotonic behavior of D_L as a function of M is due to the stability of the sliding mode.

To understand the nontrivial interplay of F , M , and L_x in more detail, we identified from the simulations three different paths, (a), (b), and (c), dominating the flipping rate γ . They all describe the transition from a stable mode at the left wall (ϕ_s, x_s) to another at the right wall ($\phi_s + \pi, L_x - x_s$) due to fluctuations in the rod orientation ϕ , whereas the translational motion just follows the internal force F and the confining potential $V(\mathbf{r}, \phi)$.³ These three different paths are sketched in Fig. 8.4 and are described as follows: The rod can slip out of its stable sliding mode by fluctuating in the direction of the torque [path (a)] or by fluctuating against it [path (b)]. In path (a), detachment from the (left) wall, which amounts to overcoming a barrier in the torque/angle from ϕ_s to ϕ_u , most likely also leads to finding the stable mode on the other (right) wall (for $L_x \lesssim R$). Path (b), however, is only successful if the rod orientation is subject to strong and fast fluctuations which enable it to make a turn of an angle $(-\pi + \phi_u - \phi_s)$ before reaching the other wall. This explains why

³This assumption is clearly justified for large ratios D_r/D_{\parallel} , $D_r/D_{\perp} \gg 1/L^2$, and $FL/M \gg 1$.

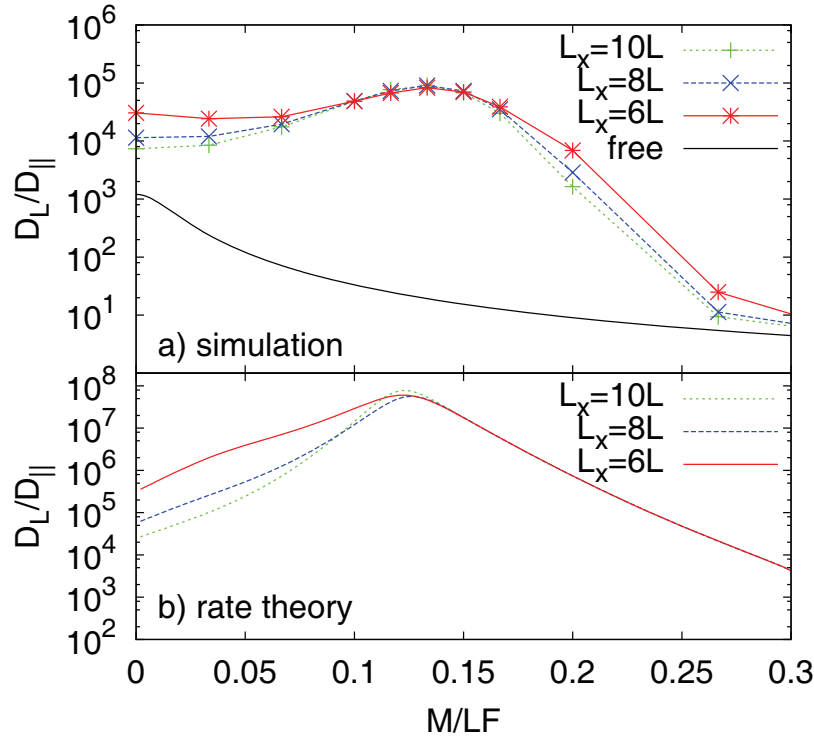


Figure 8.3: Long-time diffusion coefficient D_L as a function of the torque M for the swimmer in the bulk and in confinement for $\beta FL = 60$ and $L_x = 6, 8, 10L$. (a) Computer simulation, (b) rate theory.

for intermediate torques and small L_x , another important three-stage path (c) is dominating. This path is initiated by a small fluctuation of the orientation against the direction of the torque, from ϕ_s toward $\pi/2$ on the (left) wall. In a second stage, the swimmer approaches the other (right) wall at a small, constant turning velocity $\dot{\phi}$, reaching it after only a short time due to its strong internal force. By the other (right) wall it is reoriented in an upward direction before, in a third stage, turning quickly in the direction of the torque such that it reaches the original (left) wall at an angle ϕ_u . The flipping rate is now given by the path integral

$$\gamma \propto \int D\phi \exp(-\beta S[\mathbf{r}, \phi]/4), \quad (8.14)$$

keeping initial and final configurations of ϕ and x appropriately fixed. Here, the Onsager-Machlup action [206]⁴ is given by

$$S[\mathbf{r}, \phi] = \int_0^\infty dt' |\partial_{t'}\phi(t') - M + \partial_\phi V(\mathbf{r}(t'), \phi(t'))|^2, \quad (8.15)$$

⁴For a recent generalization of the Onsager-Machlup theory to non-equilibrium steady states, see ref. [269].

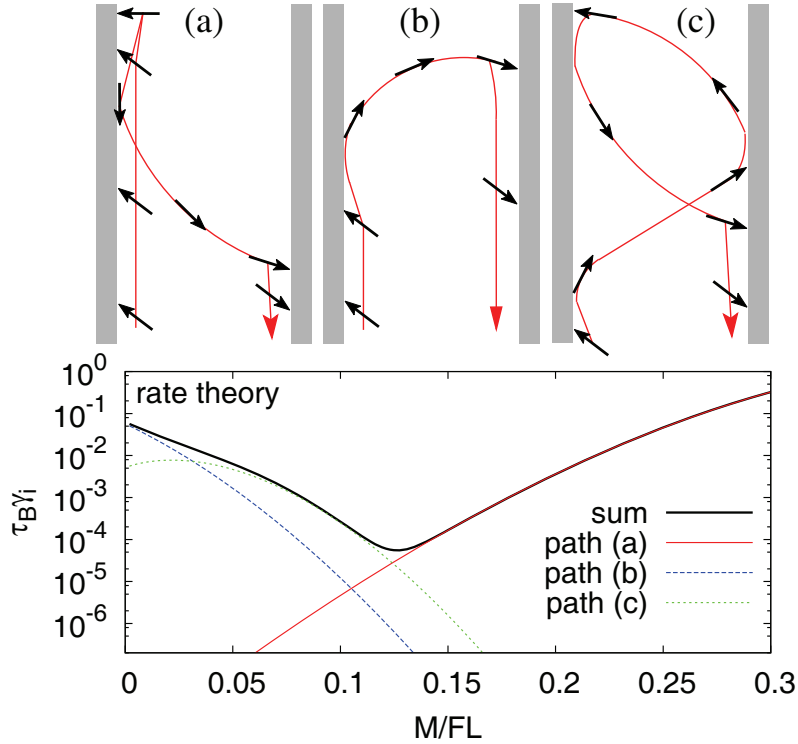


Figure 8.4: Top panel: the paths governing the flipping rate: (a) turning in the direction of the torque, (b) turning against the direction of the torque, (c) three-stage event—first, turning in the direction of the torque and then turning against it. Bottom panel: The rates of the three different paths as a function of M/FL for $\beta FL = 60$, $L_x = 8L$.

with $t' = \beta D_r t$ the normalized time. Note that our system is non-Hamiltonian due to the internal driving force and the translation-rotation coupling. Hence, the least action path cannot be found as the minimum energy path in some energy landscape, as vastly studied in the literature [205, 279]. In contrast, we now construct a non-Hamiltonian rate theory by assuming that—in the limit of large forces βFL —the flipping rate γ is dominated by either of the three paths [$i = (a), (b), (c)$], identified in the simulation. The respective minimum actions are given by $S_i[\mathbf{r}_i, \phi_i]$, with $\phi_i(t')$ minimizing the action subject to the constraints $[\phi_i(0) = \phi_s, x_i(0) = x_s]$ and $[\phi_i(\infty) = \phi_s \pm \pi, x_i(\infty) = L_x - x_s]$, where the plus sign corresponds to paths (a) and (c), and the minus sign to path (b). Paths (a) and (b) [(c)] are further constrained by the condition not to reach (to reach) the initial wall between the initial and the final stage.

In order to calculate the associated actions for the different paths, we divide the trajectories into parts where the front rod tip sits on the original (left) wall and into parts where the rod moves at a constant turning velocity $\dot{\phi}_i$ in between the walls. The

former parts can then be expressed as the barrier heights $4 \int_{\phi_s}^{\phi_m} d\phi |M - \partial_\phi V|$ [205], with $\phi_m = \phi_u$ for path (a) and $\phi_m = \pi/2$ for paths (b), (c), whereas the latter are simply given by $|\partial_{t'}\phi_i - M|^2 t'_{\max}$, t'_{\max} being the normalized time it takes to swim from one wall to the other (t'_{\max} is chosen to minimize the action). The individual rates are roughly given by

$$\gamma_i \approx \tau_B^{-1} \exp[-\beta S_i/4], \quad (8.16)$$

where the kinetic prefactors are crudely approximated by $1/\tau_B$, and plotted in Fig. 8.4. Summation over the individual rates yields the long-time diffusion coefficient

$$D_L \approx v_y^2 \gamma^{-1}, \quad \gamma \simeq \sum_i \gamma_i, \quad (8.17)$$

plotted as a function of M for different L_x in Fig. 8.3(b). The rate theory reproduces clearly the L_x dependence and the nonmonotonicity of D_L as a function of M and attributes it to different rates of the paths (a) and (c). Moreover, the maximum in D_L is predicted to be weakly dependent on L_x in agreement with the simulations. However, the actual values of the rate theory differ from the simulation data due to the crude approximation made for the kinetic prefactors.

Finally, we study the effect of an additional gravitational field in the x direction ($k > 0$), breaking the symmetry of the channel potential (see the right inset of Fig. 8.2). On average, the swimmer is now situated more on the left than on the right channel wall, such that the sliding mode becomes *ballistic* (see Fig. 8.2).

In conclusion, we have studied the dynamic behavior of a self-propelled Brownian rod performing circular motion. In the bulk, the analytical solution reveals long-time diffusive behavior. In channel confinement, an efficient stable sliding mode was identified that strongly enhances the long-time diffusion along the channel as obtained by computer simulation and a non-Hamiltonian rate theory. If the channel is asymmetric, the sliding mode leads to ballistic long-time motion.

The sliding motion of circle swimmers can be verified in experiments with different set-ups: First, catalytically driven nanorods [66, 286] and self-propelled magnetic colloidal rods confined to a microchannel [145] will exhibit sliding [183]. Second, confined bacteria [24, 71, 125] and spermatozoa [236, 298] move in two dimensions along circles. In fact, the typical radius of the observed circular motion is in the range of $10 - 1000 \mu\text{m}$ for spermatozoae [236, 298] and of the order of $50 \mu\text{m}$ for *Escherichia coli* bacteria [24]. Therefore, the radii are typically larger but comparable with the particle sizes. When these particles are exposed to microchannels of similar widths as the observed radii, as realized for the bacteria [71], the predicted huge acceleration behavior should be observed, as has already been seen in 3D [24]. Third, vibrated polar granular rods [148] with an additional left-right asymmetry perform circle motions. When placed into a slit geometry, a sliding effect may be observed here as well.

Accelerating the dynamics in the channel by tuning the torque may be exploited as a mechanism to separate a certain species out of a crowded solution of different active particles. If a microfluidic channel is connected to a bulk mixture, the species moving quickest along the channel will arrive first at the channel end and can efficiently be removed. This might be more efficient than traditional separation techniques such as capillary electrophoresis [238].

Acknowledgments

We thank U. Zimmermann, H. H. Wensink, A. Wynveen and W. C. K. Poon for helpful discussions. This work has been supported by the DFG through the SFB TR6 (project C3).

Bibliography

- [1] ACEDO, L., AND SANTOS, A. The penetrable-sphere fluid in the high-temperature, high-density limit. *Phys. Lett. A* 323 (2004), 427.
- [2] ACHIM, C. V., KARTTUNEN, M., ELDER, K. R., GRANATO, E., ALANISSILA, T., AND YING, S. C. Phase diagram and commensurate-incommensurate transitions in the phase field crystal model with an external pinning potential. *Phys. Rev. E* 74 (2006), 021104.
- [3] ALBA-SIMIONESCO, C., COASNE, B., DOSSEH, G., DUDZIAK, G., GUBBINS, K., RADHAKRISHNAN, R., AND SLIWINSKA-BARTKOWIAK, M. Effects of confinement on freezing and melting. *J. Phys.: Condens. Matter* 18 (2006), R15.
- [4] ALLEN, M. P., AND TILDESLEY, D. J. *Computer Simulation of Liquids*. Clarendon Press, Oxford, 1987.
- [5] ANDERSON, V. J., AND LEKKERKERKER, H. N. W. Insights into phase transition kinetics from colloid science. *Nature* 416 (2002), 811.
- [6] ARAGÓN, S. R., AND PECORA, R. General theory of dynamic light scattering from cylindrically symmetric particles with translational-rotational coupling. *J. Chem. Phys.* 82 (1985), 5346.
- [7] ARCHER, A. Dynamical density functional theory for dense atomic liquids. *J. Phys.: Condens. Matter* 18 (2006), 5617.
- [8] ARCHER, A., AND RAUSCHER, M. Dynamical density functional theory for interacting Brownian particles: stochastic or deterministic? *J. Phys. A.: Math. Gen.* 37 (2004), 9325.
- [9] ARCHER, A. J. Dynamical density functional theory: binary phase-separating colloidal fluid in a cavity. *J. Phys.: Condens. Matter* 17 (2006), 1405.
- [10] ARCHER, A. J., AND EVANS, R. Dynamical density functional theory and its application to spinodal decomposition. *J. Chem. Phys.* 121 (2004), 4246.

-
- [11] ARCHER, A. J., HOPKINS, P., AND SCHMIDT, M. Dynamics in inhomogeneous liquids and glasses via the test particle limit. *Phys. Rev. E* 75 (2007), 040501(R).
- [12] ARCHER, A. J., LIKOS, C. N., AND EVANS, R. Binary star-polymer solutions: bulk and interfacial properties. *J. Phys.: Condens. Matter* 14 (2002), 12031.
- [13] ASHCROFT, N. W., AND MERMIN, N. D. *Solid State Physics*. Holt, Rinehart and Winston, New York, 1976.
- [14] AUER, S., AND FRENKEL, D. Line tension controls wall-induced crystal nucleation in hard-sphere colloids. *Phys. Rev. Lett.* 91 (2003), 015703.
- [15] AUER, S., AND FRENKEL, D. Numerical simulation of crystal nucleation in colloids. *Adv. Polym. Sci.* 173 (2005), 149.
- [16] AUKRUST, T., AND HAUGE, E. Van der Waals theory of wetting with exponential interactions. *Physica A* 141 (1987), 427.
- [17] BACKOFEN, R., RATZ, A., AND VOIGT, A. Nucleation and growth by a phase field crystal (PFC) model. *Philos. Mag. Lett.* 87 (2007), 813.
- [18] BAGCHI, B. Stability of a supercooled liquid to periodic density waves and dynamics of freezing. *Physica A* 145 (1987), 273.
- [19] BAGDASSARIAN, C. K., OXTOBY, D. W., AND SHEN, Y. C. Crystal nucleation and growth from the undercooled liquid: A nonclassical piecewise parabolic free-energy model. *J. Chem. Phys.* 100 (1993), 2139.
- [20] BARRAT, J.-L., HANSEN, J.-P., AND PASTORE, G. On the equilibrium structure of dense fluids. Triplet correlations, integral equations and freezing. *Mol. Phys.* 63 (1988), 747.
- [21] BARRAT, J.-L., XU, H., HANSEN, J.-P., AND BAUS, M. Freezing of binary hard-disc alloys: I. The equation of state and pair structure of the fluid phase. *J. Phys. C.* 21 (1988), 3165.
- [22] BATES, M. A., AND FRENKEL, D. Influence of vacancies on the melting transition of hard disks in two dimensions. *Phys. Rev. E* 61 (2000), 5223.
- [23] BAUS, M., AND HANSEN, J.-P. Statistical mechanics of simple Coulomb systems. *Phys. Rep.* 59 (1980), 1.
- [24] BERG, H. C., AND TURNER, L. Chemotaxis of bacteria in glass-capillary arrays. *Biophys. J.* 58 (1990), 919.

- [25] BERRY, J., ELDER, K. R., AND GRANT, M. Simulation of an atomistic dynamic field theory for monatomic liquids: Freezing and glass formation. *Phys. Rev. E* 77 (2008), 061506.
- [26] BERRY, J., GRANT, M., AND ELDER, K. R. Diffusive atomistic dynamics of edge dislocations in two dimensions. *Phys. Rev. E* 73 (2006), 031609.
- [27] BIBEN, T., OHNESORGE, R., AND LÖWEN, H. Crystallization in sedimentation profiles of hard spheres. *Europhys. Lett.* 28 (1994), 665.
- [28] BIER, M., AND VAN ROIJ, R. Relaxation dynamics in fluids of platelike colloidal particles. *Phys. Rev. E* 76 (2007), 021405.
- [29] BINDER, K., HORBACH, J., VINK, R., AND DE VIRGILIIS, A. Confinement effects on phase behavior of soft matter systems. *Soft Matter* 4 (2008), 1555.
- [30] BLAAK, R., AUER, S., FRENKEL, D., AND LÖWEN, H. Crystal nucleation of colloidal suspensions under shear. *Phys. Rev. Lett.* 93 (2004), 068303.
- [31] BLAAK, R., AUER, S., FRENKEL, D., AND LÖWEN, H. Homogeneous nucleation of colloidal melts under the influence of shearing fields. *J. Phys.: Condens. Matter* 16 (2004), S3873.
- [32] BLAAK, R., AND LÖWEN, H. Umbrella sampling in non-equilibrium computer simulations. *Computer Physics Communications* 169 (2005), 64.
- [33] BOHLEN, H., AND SCHOEN, M. Effect of fluid-substrate attraction and pore geometry on fluid adsorption. *J. Chem. Phys.* 123 (2005), 124714.
- [34] BORN, M. Thermodynamics of crystals and melting. *J. Chem. Phys.* 7 (1939), 591.
- [35] BOYER, L. L. Theory of melting based on lattice instability. *Phase Transit. (UK)* 48 (1985), 1.
- [36] CACCIUTO, A., AND FRENKEL, D. Simulation of colloidal crystallization on finite structured templates. *Phys. Rev. E* 72 (2005), 41604.
- [37] CAHN, J. W., AND HILLIARD, J. E. Free energy of a nonuniform system. I. Interfacial free energy. *J. Chem. Phys.* 28 (1958), 258.
- [38] CAILLOL, J.-M. The density functional theory of classical fluids. *J. Phys. A.: Math. Gen.* 35 (2002), 4189.
- [39] CAILLOL, J. M., LEVESQUE, D., AND WEIS, J.-J. Theoretical determination of the dielectric constant of a two-dimensional dipolar fluid. *Mol. Phys.* 44 (1981), 733.

- [40] CALEF, D. F., AND WOLYNES, P. G. Smoluchowski-Vlasov theory of charge solvation dynamics. *J. Phys. C* 78 (1983), 4145.
- [41] CAROLI, B., CAROLI, C., AND ROULET, B. Diffusion in a bistable potential: A systematic WKB treatment. *J. Stat. Phys.* 21 (1980), 415.
- [42] CAROLI, B., CAROLI, C., AND ROULET, B. Diffusion in a bistable potential: The functional integral approach. *J. Stat. Phys.* 26 (1981), 83.
- [43] CAROLI, B., CAROLI, C., ROULET, B., AND GOUYET, J. F. A WKB treatment of diffusion in a multidimensional bistable potential. *J. Stat. Phys.* 22 (1980), 515.
- [44] CHAIKIN, P. M., AND LUBENSKY, T. C. *Principles of condensed matter physics*. Cambridge University Press, Cambridge, 1995.
- [45] CHAKRABARTI, J., DZUBIELLA, J., AND LÖWEN, H. Dynamical instability in driven colloids. *Europhys. Lett.* 61 (2003), 415.
- [46] CHAKRABARTI, J., DZUBIELLA, J., AND LÖWEN, H. Reentrance effect in the lane formation of driven colloids. *Phys. Rev. E* 70 (2004), 012401.
- [47] CHAN, G., AND FINKEN, R. Time-dependent density functional theory of classical fluids. *Phys. Rev. Lett.* 94 (2005), 183001.
- [48] CHANDRA, A., AND BAGCHI, B. A molecular theory of collective orientational relaxation in pure and binary dipolar liquids. *J. Chem. Phys.* 91 (1989), 1829.
- [49] CHANDRA, A., AND BAGCHI, B. Collective orientational relaxation in a dense liquid of ellipsoidal molecules. *Physica A* 169 (1990), 246.
- [50] CHRISTENSON, H. K. Confinement effects on freezing and melting. *J. Phys.: Condens. Matter* 13 (2001), R95.
- [51] COHEN, I., DAVIDOVITCH, B., SCHOFIELD, A. B., BRENNER, M. P., AND WEITZ, D. A. Slip, yield, and bands in colloidal crystals under oscillatory shear. *Phys. Rev. Lett.* 97 (2006), 215502.
- [52] COHEN, I., MASON, T. G., AND WEITZ, D. A. Shear-induced configurations of confined colloidal suspensions. *Phys. Rev. Lett.* 93 (2004), 046001.
- [53] COURTEMANCHE, D. J., PASMORE, T. A., AND VAN SWOL, F. A molecular dynamics study of prefreezing—hard spheres at a smooth hard wall. *Mol. Phys.* 80 (1993), 861.
- [54] COURTEMANCHE, D. J., AND VAN SWOL, F. Wetting state of a crystal-fluid system of hard spheres. *Phys. Rev. Lett.* 69 (1992), 2078.

- [55] CURTIN, W. A. Freezing in the density functional approach: Effect of third-order contributions. *J. Chem. Phys.* *88* (1988), 7050.
- [56] CURTIN, W. A., AND ASHCROFT, N. W. Weighted-density-functional theory of inhomogeneous liquids and the freezing transition. *Phys. Rev. A* *32* (1985), 2909.
- [57] CURTIN, W. A., AND ASHCROFT, N. W. Density-functional theory and freezing of simple liquids. *Phys. Rev. Lett.* *56* (1986), 2775.
- [58] DE COL, A., MENON, G. I., GESHKENBEIN, V. B., AND G, B. Surface melting of the vortex lattice. *Phys. Rev. Lett.* *96* (2006), 177001.
- [59] DE KUIJPER, A., VOS, W. L., BARRAT, J.-L., HANSEN, J.-P., AND SCHOUTEN, J. A. Freezing of simple systems using density functional theory. *J. Chem. Phys.* *93* (1990), 5187.
- [60] DE VILLENEUVE, V. W. A., DULLENS, R. P. A., AARTS, D. G. A. L., GROENEVELD, E., SCHERFF, J. H., KEGEL, W. K., AND LEKKERKERKER, H. N. W. Colloidal hard-sphere crystal growth frustrated by large spherical impurities. *Science* *309* (2005), 1231.
- [61] DEAN, D. S. Langevin equation for the density of a system of interacting Langevin processes. *J. Phys. A.: Math. Gen.* *29* (1996), L613.
- [62] DELLAGO, C., BOLHUIS, P., AND GEISSLER, P. Transition path sampling. *Adv. Chem. Phys.* *123* (2002), 1.
- [63] DENTON, A. R., AND ASHCROFT, N. W. High-order direct correlation functions of uniform classical liquids. *Phys. Rev. A* *39* (1989), 426.
- [64] DENTON, A. R., AND ASHCROFT, N. W. Modified weighted-density-functional theory of nonuniform classical liquids. *Phys. Rev. A* *39* (1989), 4701.
- [65] DERKS, D., WISMAN, H., VAN BLAADEREN, A., AND IMHOF, A. Confocal microscopy of colloidal dispersions in shear flow using a counter-rotating cone-plate shear cell. *J. Phys.: Condens. Matter* *16* (2004), S3917.
- [66] DHAR, P., FISCHER, T. M., WANG, Y., MALLOUK, T. E., PAXTON, W. F., AND SEN, A. Autonomously moving nanorods at a viscous interface. *Nano Lett.* *6* (2006), 66.
- [67] DHONT, J. K. G. *An Introduction to Dynamics of Colloids*. Elsevier, Amsterdam, 1996.

- [68] DIETERICH, W., FRISCH, H. L., AND MAJHOFFER, A. Nonlinear diffusion and density functional theory. *Z. Phys. B* 78 (1990), 317.
- [69] DIETRICH, S. Wetting phenomena. In *Phase Transitions and Critical Phenomena*, C. Domb and J. Lebowitz, Eds., vol. 12. Academic Press, London, 1988, p. 1.
- [70] DIJKSTRA, M. Capillary freezing or complete wetting of hard spheres in a planar hard slit? *Phys. Rev. Lett.* 93 (2004), 108303.
- [71] DILUZIO, W. R., TURNER, L., MAYER, M., GARSTECKI, P., WEIBEL, D. B., BERG, H. C., AND WHITESIDES, G. M. Escherichia coli swim on the right-hand side. *Nature* 435 (2005), 1271.
- [72] DOI, M., AND EDWARDS, S. F. *The Theory of Polymer Dynamics*. Clarendon Press, Oxford, 1986.
- [73] DREYFUS, R., BAUDRY, J., ROPER, M. L., FERMIGIER, M., STONE, H. A., AND BIBETTE, J. Microscopic artificial swimmers. *Nature* 437 (2005), 862.
- [74] DUFRESNE, E. R., SQUIRES, T. M., BRENNER, M. P., AND GRIER, D. G. Hydrodynamic coupling of two Brownian spheres to a planar surface. *Phys. Rev. Lett.* 85 (2000), 3317.
- [75] DZUBIELLA, J., AND LIKOS, C. N. Mean-field dynamical density functional theory. *J. Phys.: Condens. Matter* 15 (2003), L147.
- [76] EBNER, C., SAAM, W. F., AND STROUD, D. Density-functional theory of classical systems. *Phys. Rev. A* 14 (1976), 226.
- [77] ELDER, K. R., AND GRANT, M. Modeling elastic and plastic deformations in nonequilibrium processing using phase field crystals. *Phys. Rev. E* 70 (2004), 051605.
- [78] ELDER, K. R., KATAKOWSKI, M., HAATAJA, M., AND GRANT, M. Modeling elasticity in crystal growth. *Phys. Rev. Lett.* 88 (2002), 245701.
- [79] ELDER, K. R., PROVATAS, N., BERRY, J., STEFANOVIC, P., AND GRANT, M. Phase-field crystal modeling and classical density functional theory of freezing. *Phys. Rev. B* 75 (2007), 064107.
- [80] EMMERICH, H. *The Diffuse Interface Approach in Materials Science*. Springer, Heidelberg, 2003.
- [81] EMMERICH, H., AND SIQUIERI, R. Investigating heterogeneous nucleation in peritectic materials via the phase-field method. *J. Phys.: Condens. Matter* 18 (2006), 11121.

- [82] ENSKOG, D. Kinetic theory of heat conductivity, viscosity, and diffusion in certain condensed gases and liquids. *K. Sven. Vetenskapsakad. Handl.* 63 (1922), 4 (English translation in Brush, S., *Kinetic Theory*, vol. 3, Pergamon Press, London, New York, 1972).
- [83] ERMAK, D. L. A computer simulation of charged particles in solution. I. Technique and equilibrium properties. *J. Chem. Phys.* 62 (1975), 4189.
- [84] ERMAK, D. L., AND MCCAMMON, J. A. Brownian dynamics with hydrodynamic interactions. *J. Chem. Phys.* 69 (1978), 1352.
- [85] EVANS, R. The nature of the liquid-vapour interface and other topics in the statistical mechanics of non-uniform, classical fluids. *Adv. Phys.* 28 (1979), 143.
- [86] EVANS, R. Fluids adsorbed in narrow pores: phase equilibria and structure. *J. Phys.: Condens. Matter* 2 (1990), 8989.
- [87] EVANS, R. Density functionals in the theory of nonuniform fluids. In *Fundamentals of Inhomogeneous Fluids* (New York, 1992), D. Henderson, Ed., Dekker, p. 85.
- [88] FORTINI, A., AND DIJKSTRA, M. Phase behaviour of hard spheres confined between parallel hard plates: manipulation of colloidal crystal structures by confinement. *J. Phys.: Condens. Matter* 18 (2006), L371.
- [89] FREIDLIN, M. I., AND WENTZELL, A. D. *Random Perturbations of Dynamical Systems*, 2nd ed. Springer, New York, Berlin, 1998.
- [90] FRENKEN, J. W. M., AND VAN DER VEEN, J. F. Observation of surface melting. *Phys. Rev. Lett.* 54 (1985), 134.
- [91] FRÖHLICH, J., AND PFISTER, C.-E. On the absence of spontaneous symmetry breaking and of crystalline ordering in two-dimensional systems. *Commun. Math. Phys.* 81 (1981), 277.
- [92] FRÖHLICH, J., AND PFISTER, C.-E. Absence of crystalline ordering in two dimensions. *Commun. Math. Phys.* 104 (1986), 697.
- [93] FROLTSOV, V. A., BLAAK, R., LIKOS, C. N., AND LÖWEN, H. Crystal structures of two-dimensional magnetic colloids in tilted external magnetic fields. *Phys. Rev. E* 68 (2003), 061406.
- [94] FROLTSOV, V. A., LIKOS, C. N., AND LÖWEN, H. Magnetic colloids in inhomogeneous external magnetic fields: particle tweezing, trapping and void formation. *J. Phys.: Condens. Matter* 16 (2004), S4103.

-
- [95] FROLTSOV, V. A., LIKOS, C. N., LÖWEN, H., EISENMANN, C., GASSER, U., KEIM, P., AND MARET, G. Anisotropic mean-square displacements in two-dimensional colloidal crystals of tilted dipoles. *Phys. Rev. E* 71 (2005), 031404.
- [96] GARDINER, C. W. *Handbook of Stochastic Methods for Physics, Chemistry and in the Natural Sciences*. Springer, Berlin, 1994.
- [97] GASSER, U., WEEKS, E. R., SCHOFIELD, A., PUSEY, P. N., AND WEITZ, D. A. Real-space imaging of nucleation and growth in colloidal crystallization. *Science* 292 (2001), 258.
- [98] GELB, L. D., GUBBINS, K. E., RADHAKRISHNAN, R., AND SLIWINSKA-BARTKOWIAK, M. Phase separation in confined systems. *Rep. Prog. Phys.* 61 (1999), 1573.
- [99] GOEL, G., KREKELBERG, W. P., ERRINGTON, J. R., AND TRUSKETT, T. M. Tuning density profiles and mobility of inhomogeneous fluids. *Phys. Rev. Lett.* 100 (2008), 106001.
- [100] GOLDENFELD, N. *Lectures on Phase Transitions and the Renormalization Group*. Addison-Wesley, Reading, MA, 1992.
- [101] GOLDENFELD, N., ATHREYA, B. P., AND DANTZIG, J. A. Renormalization group approach to multiscale simulation of polycrystalline materials using the phase field crystal model. *Phys. Rev. E* 72 (2005), 020601.
- [102] GÖTZE, I. O., ARCHER, A. J., AND LIKOS, C. N. Structure, phase behavior, and inhomogeneous fluid properties of binary dendrimer mixtures. *J. Chem. Phys.* 124 (2006), 084901.
- [103] GRAHAM, R. L. In *Theory of Continuous Fokker-Planck Systems* (Cambridge, 1989), vol. 1 of *Noise in Nonlinear Dynamical Systems*, Cambridge University Press, p. 225.
- [104] GRÁNÁSY, L., PUSZTAI, T., BORZSONYI, T., TOTH, G., TEGZE, G., WARREN, J. A., AND DOUGLAS, J. F. Phase field theory of crystal nucleation and polycrystalline growth: A review. *J. Mater. Res.* 21 (2006), 309.
- [105] GRÁNÁSY, L., PUSZTAI, T., AND WARREN, J. A. Modelling polycrystalline solidification using phase field theory. *J. Phys.: Condens. Matter* 16 (2004), R1205.
- [106] GREWE, N., AND KLEIN, W. Rigorous derivation of Kirkwood-Monroe equation for small activity. *J. Math. Phys.* 17 (1976), 699.

- [107] GREWE, N., AND KLEIN, W. Kirkwood-Salsburg equations for a bounded stable Kac potential. I. General theory and asymptotic solutions. *J. Math. Phys.* 18 (1977), 1729.
- [108] GREWE, N., AND KLEIN, W. Kirkwood-Salsburg equations for a bounded stable Kac potential. II. Instability and phase transitions. *J. Math. Phys.* 18 (1977), 1735.
- [109] GRZELAK, E. M., AND ERRINGTON, J. R. Computation of interfacial properties via grand canonical transition matrix Monte Carlo simulation. *J. Phys. C.* 128 (2008), 014710.
- [110] HAEGGQWIST, L., SCHIMANSKY-GEIER, L., SOKOLOV, I. M., AND MOSS, F. Hopping on a zig-zag course. *Eur. Phys. J. Special Topics* 157 (2008), 33.
- [111] HAGHGOOIE, R., AND DOYLE, P. S. Structure and dynamics of repulsive magnetorheological colloids in two-dimensional channels. *Phys. Rev. E* 72 (2005), 011405.
- [112] HAKEN, H. Generalized Onsager-Machlup function and classes of path integral solutions of the Fokker-Planck equation and the Master equation. *Z. Phys. B* 24 (1976), 321.
- [113] HALPERIN, B. I., AND NELSON, D. R. Theory of two-dimensional melting. *Phys. Rev. Lett.* 41 (1978), 121.
- [114] HAMADA, Y., KOGA, K., AND TANAKA, H. Phase equilibria and interfacial tension of fluids confined in narrow pores. *J. Chem. Phys.* 127 (2007), 084908.
- [115] HAN, Y., ALSAYED, A. M., NOBILI, M., ZHANG, J., LUBENSKY, T. C., AND YODH, A. G. Brownian motion of an ellipsoid. *Science* 314 (2006), 626.
- [116] HÄNGGI, P., TALKNER, P., AND BORKOVEC, M. Reaction rate theory: 50 years after Kramers. *Rev. Mod. Phys.* 62 (1990), 251.
- [117] HANSEN, J.-P., AND MCDONALD, I. R. *Theory of simple liquids*, 3rd ed. Academic Press, London, 2006.
- [118] HARNAU, L., PENNA, F., AND DIETRICH, S. Colloidal hard-rod fluids near geometrically structured substrates. *Phys. Rev. E* 70 (2004), 021505.
- [119] HAYMET, A. D. J., AND OXTOBY, D. W. A molecular theory for the solid-liquid interface. *J. Chem. Phys.* 74 (1981), 2559.
- [120] HELBING, D. Traffic and related self-driven many-particle systems. *Rev. Mod. Phys.* 73 (2001), 1067.

- [121] HENI, M., AND LÖWEN, H. Surface freezing on patterned substrates. *Phys. Rev. Lett.* *85* (2000), 3668.
- [122] HENI, M., AND LÖWEN, H. Precrystallization of fluids induced by patterned substrates. *Phys. Rev. E* *13* (2001), 4675.
- [123] HERNANDO, J. A. Density functional formalism in the canonical ensemble: I. General formalism. *J. Phys.: Condens. Matter* *14* (2002), 303.
- [124] HERNANDO, J. A., AND BLUM, L. Density functional formalism in the canonical ensemble. *J. Phys.: Condens. Matter* *13* (2001), L577.
- [125] HILL, J., KALKANCI, O., MCMURRY, J. L., AND KOSER, H. Hydrodynamic surface interactions enable *Escherichia coli* to seek efficient routes to swim upstream. *Phys. Rev. Lett.* *98* (2007), 068101.
- [126] HOFFMANN, N., LIKOS, C. N., AND LÖWEN, H. Microphase structuring in two-dimensional magnetic colloid mixtures. *J. Phys.: Condens. Matter* *18* (2006), 10193.
- [127] HOHENBERG, P., AND KOHN, W. Inhomogeneous electron gas. *Phys. Rev.* *136* (1964), B864.
- [128] HOHENBERG, P. C., AND HALPERIN, B. I. Theory of dynamic critical phenomena. *Rev. Mod. Phys.* *49* (1977), 435.
- [129] HOLMQVIST, P., LETTINGA, M. P., BUITENHUIS, J., AND DHONT, J. K. G. Crystallization kinetics of colloidal spheres under stationary shear flow. *Langmuir* *21* (2005), 10976.
- [130] HUANG, K. *Statistical mechanics*, 2nd ed. Wiley, New York, 1987.
- [131] HUG, J. E., VAN SWOL, F., AND ZUKOSKI, C. F. The freezing of colloidal suspensions in confined spaces. *Langmuir* *11* (1995), 111.
- [132] HUNTER, R. J. *Foundations of Colloid Science*, 2nd ed. Oxford University Press, Oxford, 1989.
- [133] HUSOWITZ, B., AND TALANQUER, V. Nucleation on cylindrical plates: Sharp transitions and double barriers. *J. Chem. Phys.* *122* (2005), 194710.
- [134] HUSOWITZ, B., AND TALANQUER, V. Nucleation in cylindrical capillaries. *J. Chem. Phys.* *121* (2004), 8021.
- [135] IMPERIO, A., AND REATTO, L. Microphase morphology in two-dimensional fluids under lateral confinement. *Phys. Rev. E* *76* (2007), 040402(R).

- [136] JONES, R. A. L. *Soft Condensed Matter*. Oxford University Press, Oxford, 2002.
- [137] K., B., S., S., AND P., N. The liquid-solid transition of hard discs: first-order transition or Kosterlitz-Thouless-Halperin-Nelson-Young scenario? *J. Phys.: Condens. Matter* *14* (2002), 2323.
- [138] KAWASAKI, K. Stochastic model of slow dynamics in supercooled liquids and dense colloidal suspensions. *Physica A* *208* (1994), 35.
- [139] KAWASAKI, K., AND MIYAZIMA, S. Path integral formulation of dynamical density functional equation for dense fluids. *Z. Phys. B* *103* (1997), 423.
- [140] KEGEL, W. K. Freezing of hard spheres in confinement. *J. Chem. Phys.* *115* (2001), 6538.
- [141] KHOKHLOV, A., VALIULLIN, R., KÄRGER, J., STEINBACH, F., AND FELDHOFF, A. Freezing and melting transitions of liquids in mesopores with ink-bottle geometry. *New J. Phys.* *9* (2007), 272.
- [142] KIRKPATRICK, T. R. Random solutions from a regular density functional Hamiltonian: a static and dynamical theory for the structural glass transition. *J. Phys. A.: Math. Gen.* *22* (1989), L149.
- [143] KIRKWOOD, J. G. Statistical mechanics of fluid mixtures. *J. Chem. Phys.* *3* (1935), 300.
- [144] KIRKWOOD, J. G., AND MONROE, E. Statistical mechanics of fusion. *J. Chem. Phys.* *9* (1941), 514.
- [145] KÖPPL, M., HENSELER, P., ERBE, A., NIELABA, P., AND LEIDERER, P. Layer reduction in driven 2D-colloidal systems through microchannels. *Phys. Rev. Lett.* *97* (2006), 208302.
- [146] KOSTERLITZ, J. M., AND THOULESS, D. J. Ordering, metastability and phase transitions in two-dimensional systems. *J. Phys. C.* *6* (1973), 1181.
- [147] KRAMERS, H. A. Brownian motion in a field of force and the diffusion model of chemical reactions. *Physica* *7* (1940), 284.
- [148] KUDROLLI, A., LUMAY, G., VOLFSO, D., AND TSIMRING, L. S. Swarming and swirling in self-propelled polar granular rods. *Phys. Rev. Lett.* *100* (2008), 058001.
- [149] LAIRD, B. B., AND KROLL, D. M. Freezing of soft spheres: A critical test for weighted-density-functional theories. *Phys. Rev. A* *42* (1990), 4810.

- [150] LANG, A., LIKOS, C. N., WATZLAWEK, M., AND LÖWEN, H. Fluid and solid phases of the Gaussian core model. *J. Phys.: Condens. Matter* 12 (2000), 5087.
- [151] LAUGA, E., DILUZIO, W. R., WHITESIDES, G. M., AND STONE, H. A. Swimming in circles: Motion of bacteria near solid boundaries. *Biophys. J.* 90 (2006), 400.
- [152] LEHMANN, J., REIMANN, P., AND HÄNGGI, P. Surmounting oscillating barriers. *Phys. Rev. Lett.* 84 (2000), 1639.
- [153] LEHMANN, J., REIMANN, P., AND HÄNGGI, P. Surmounting oscillating barriers: Path-integral approach for weak noise. *Phys. Rev. Lett.* 62 (2000), 6282.
- [154] LEHMANN, J., REIMANN, P., AND HÄNGGI, P. Activated escape over oscillating barriers: The case of many dimensions. *phys. stat. sol. (b)* 237 (2003), 53.
- [155] LEIDL, R., AND WAGNER, H. Hybrid WDA: A weighted-density approximation for inhomogeneous fluids. *J. Phys. C.* 98 (1993), 4142.
- [156] LENZ, D., BLAAK, R., AND LIKOS, C. N. unpublished.
- [157] LIKOS, C. N. Effective interactions in soft condensed matter physics. *Phys. Rep.* 348 (2001), 267–349.
- [158] LIKOS, C. N., AND ASHCROFT, N. W. Self-consistent theory of freezing of the classical one-component plasma. *Phys. Rev. Lett.* 69 (1992), 316.
- [159] LIKOS, C. N., AND ASHCROFT, N. W. Density-functional theory of nonuniform classical liquids: An extended modified weighted-density approximation. *J. Chem. Phys.* 99 (1993), 9090.
- [160] LIKOS, C. N., LANG, A., WATZLAWEK, M., AND LÖWEN, H. Criterion for determining clustering versus reentrant melting behavior for bounded interaction potentials. *Phys. Rev. E* 63 (2001), 031206.
- [161] LIKOS, C. N., MLADEK, B. M., GOTTWALD, D., AND KAHL, G. Why do ultrasoft repulsive particles cluster and crystallize? Analytical results from density functional theory. *J. Chem. Phys.* 126 (2007), 224502.
- [162] LIKOS, C. N., MLADEK, B. M., MORENO, A. J., GOTTWALD, D., AND KAHL, G. Cluster-forming systems of ultrasoft repulsive particles: statics and dynamics. *Computer Physics Communications* 179 (2008), 71.

- [163] LIN, S. Z., ZHENG, B., AND TRIMPER, S. Structure and dynamics of repulsive magnetorheological colloids in two-dimensional channels. *Phys. Rev. E* *73* (2006), 066106.
- [164] LOVETT, R., MON, C. Y., AND BUFF, F. P. The structure of the liquid-vapor interface. *J. Chem. Phys.* *65* (1976), 570.
- [165] LÖWEN, H. Melting, freezing and colloidal suspensions. *Phys. Rep.* *237* (1994), 249.
- [166] LÖWEN, H. Dynamical criterion for two-dimensional freezing. *Phys. Rev. E* *53* (1996), R29.
- [167] LÖWEN, H. Colloidal soft matter under external control. *J. Phys.: Condens. Matter* *13* (2001), R415.
- [168] LÖWEN, H. Density functional theory of inhomogeneous classical fluids: recent developments and new perspectives. *J. Phys.: Condens. Matter* *14* (2002), 11897.
- [169] LÖWEN, H. Density functional theory: from statics to dynamics. *J. Phys.: Condens. Matter* *15* (2003), V1.
- [170] LÖWEN, H., BEIER, T., AND WAGNER, H. Multiple order parameter theory of surface melting: A van der Waals approach. *Z. Phys. B* *79* (1990), 109.
- [171] LUCHINSKY, D. G., MAIER, R. S., MANNELLA, R., MCCLINTOCK, P. V. E., AND STEIN, D. L. Observation of saddle-point avoidance in noise-induced escape. *Phys. Rev. Lett.* *82* (1999), 1806.
- [172] LUTSKO, J. F. Ginzburg-Landau theory of the liquid-solid interface and nucleation for hard spheres. *Phys. Rev. E* *74* (2006), 021603.
- [173] MAIER, R. S., AND STEIN, D. L. Transition-rate theory for nongradient drift fields. *Phys. Rev. Lett.* *69* (1992), 3691.
- [174] MAIER, R. S., AND STEIN, D. L. Escape problem for irreversible systems. *Phys. Rev. E* *48* (1993), 931.
- [175] MAIER, R. S., AND STEIN, D. L. A scaling theory of bifurcations in the symmetric weak-noise escape problem. *J. Stat. Phys.* *83* (1996), 291.
- [176] MAIER, R. S., AND STEIN, D. L. Limiting exit location distributions in the stochastic exit problem. *SIAM J. Appl. Math.* *57* (1997), 752.
- [177] MAIER, R. S., AND STEIN, D. L. Noise-activated escape from a sloshing potential well. *Phys. Rev. Lett.* *86* (2001), 3942.

- [178] MARCONI, U. M. B., AND MELCHIONNA, S. Phase-space approach to dynamical density functional theory. *J. Chem. Phys.* *126*, 184109 (2007).
- [179] MARCONI, U. M. B., AND TARAZONA, P. Dynamic density functional theory of fluids. *J. Chem. Phys.* *110* (1999), 8032.
- [180] MARCONI, U. M. B., AND TARAZONA, P. Dynamic density functional theory of fluids. *J. Phys.: Condens. Matter* *12* (2000), A413.
- [181] MARCONI, U. M. B., AND TARAZONA, P. Nonequilibrium inertial dynamics of colloidal systems. *J. Chem. Phys.* *124* (2006), 164901.
- [182] MARR, D. W., AND GAST, A. P. Planar density-functional approach to the solid-fluid interface of simple liquids. *Phys. Rev. E* *47* (1993), 1212.
- [183] MERKT, F. S., ERBE, A., AND LEIDERER, P. Capped colloids as light-mills in optical traps. *New J. Phys.* *8* (2006), 216.
- [184] MERMIN, N. D. Thermal properties of the inhomogeneous electron gas. *Phys. Rev.* *137* (1964), A1441.
- [185] MERMIN, N. D. Crystalline order in two dimensions. *Phys. Rev.* *176* (1968), 250.
- [186] MINGQING, L., MICHAEL, A. B., AND DAVID, M. F. Interfacial colloidal sedimentation equilibrium. II. Closure-based density functional theory. *J. Chem. Phys.* *127* (2007), 164709.
- [187] MITTAL, J., TRUSKETT, T. M., ERRINGTON, J. R., AND HUMMER, G. Layering and position-dependent diffusive dynamics of confined fluids. *Phys. Rev. Lett.* *100* (2008), 145901.
- [188] MLADEK, B. M., CHARBONNEAU, P., AND FRENKEL, D. Phase coexistence of cluster crystals: Beyond the Gibbs phase rule. *Phys. Rev. Lett.* *99* (2007), 235702.
- [189] MLADEK, B. M., CHARBONNEAU, P., LIKOS, C. N., FRENKEL, D., AND KAHL, G. Multiple-occupancy crystals formed by purely repulsive, soft particles. to appear in *J. Phys.: Condens. Matter* (2008).
- [190] MLADEK, B. M., GOTTWALD, D., KAHL, G., NEUMANN, M., AND LIKOS, C. N. Formation of polymorphic cluster phases for a class of models of purely repulsive soft spheres. *Phys. Rev. Lett.* *96* (2006), 045701.
- [191] MLADEK, B. M., GOTTWALD, D., KAHL, G., NEUMANN, M., AND LIKOS, C. N. Clustering in the absence of attractions: Density functional theory and computer simulations. *J. Phys. Chem. B* *111* (2007), 12799.

- [192] MLADEK, B. M., KAHL, G., AND LIKOS, C. N. Computer assembly of cluster-forming amphiphilic dendrimers. *Phys. Rev. Lett.* *100* (2008), 028301.
- [193] MORENO, A. J., AND LIKOS, C. N. Diffusion and relaxation dynamics in cluster crystals. *Phys. Rev. Lett.* *99* (2007), 107801.
- [194] MUNAKATA, T. Liquid instability and freezing. Reductive perturbation approach. *J. Phys. Soc. Jap.* *43* (1977), 1723.
- [195] MUNAKATA, T. Velocity correlation and relative diffusion in simple liquids. II. *J. Phys. Soc. Jap.* *43* (1977), 1762.
- [196] MUNK, T., HÖFLING, F., FREY, E., AND FRANOSCH, T. Effective Perrin theory for the anisotropic diffusion of a strongly hindered rod. *arXiv.org arXiv:0808.0450* (2008).
- [197] NAEH, T., KŁOSEK, M. M., MATKOWSKY, B. J., AND SCHUSS, Z. A direct approach to the exit problem. *SIAM J. Appl. Math.* *50* (1990), 595.
- [198] NÄGELE, G. On the dynamics and structure of charge-stabilized suspensions. *Phys. Rep.* *272* (1996), 215.
- [199] NARAYAN, V., RAMASWAMY, S., AND MENON, N. Long-lived giant number fluctuations in a swarming granular nematic. *Science* *317* (2007), 105.
- [200] NELSON, D. R., AND HALPERIN, B. I. Dislocation-mediated melting in two dimensions. *Phys. Rev. B* *19* (1979), 2457.
- [201] OBATA, T., SHIMIZU, T., OSAKI, H., OSHIMA, H., AND HARA, H. Fluctuations in human's walking (II). *J. Korean Phys. Soc.* *46* (2005), 713.
- [202] OHNESORGE, R., LÖWEN, H., AND WAGNER, H. Density-functional theory of surface melting. *Phys. Rev. A* *43* (1991), 2870.
- [203] OHNESORGE, R., LÖWEN, H., AND WAGNER, H. Density distribution in a hard-sphere crystal. *Europhys. Lett.* *22* (1993), 245.
- [204] OHNESORGE, R., LÖWEN, H., AND WAGNER, H. Density-functional theory of crystal fluid interfaces and surface melting. *Phys. Rev. E* *50* (1994), 4801.
- [205] OLENDER, R., AND ELBER, R. Yet another look at the steepest descent path. *J. Mol. Struct.: THEOCHEM* *63* (1997), 398.
- [206] ONSAGER, L., AND MACHLUP, S. Fluctuations and irreversible processes. *Phys. Rev.* *91* (1953), 1505.
- [207] ONSAGER, L., AND MACHLUP, S. Fluctuations and irreversible processes. II. Systems with kinetic energy. *Phys. Rev.* *91* (1953), 1512.

- [208] OSTERMAN, N., BABIČ, D., POBERAJ, I., DOBNIKAR, J., AND ZIHERL, P. Observation of condensed phases of quasiplanar core-softened colloids. *Phys. Rev. Lett.* 99 (2007), 248301.
- [209] OXTOBY, D. W. New perspectives on freezing and melting. *Nature* 347 (1990), 725.
- [210] OXTOBY, D. W. Crystallization of liquids: A density functional approach. In *Liquids, Freezing and the Glass Transition* (Amsterdam, 1991), vol. Session LI (1989) of *Les Houches Summer Schools of Theoretical Physics*, North Holland, p. 147.
- [211] OXTOBY, D. W. Phase transitions. Catching crystals at birth. *Nature* 406 (2000), 464.
- [212] OXTOBY, D. W., AND EVANS, R. Nonclassical nucleation theory for the gas-liquid transition. *J. Chem. Phys.* 89 (1988), 7521.
- [213] OXTOBY, D. W., AND HAYMET, A. D. J. A molecular theory of the solid-liquid interface. II. Study of bcc crystal-melt interfaces. *J. Chem. Phys.* 76 (1982), 6262.
- [214] OXTOBY, D. W., AND SHEN, Y. C. Density functional approaches to the dynamics of phase transitions. *J. Phys.: Condens. Matter* 8 (1996), 9657.
- [215] PALBERG, T. Crystallization kinetics of repulsive colloidal spheres. *J. Phys.: Condens. Matter* 11 (1999), R323.
- [216] PENNA, F., DZUBIELLA, J., AND TARAZONA, P. Dynamic density functional study of a driven colloidal particle in polymer solutions. *Phys. Rev. E* 68 (2003), 061407.
- [217] PENNA, F., AND TARAZONA, P. Dynamical correlations in Brownian hard rods. *J. Chem. Phys.* 124 (2006), 164903.
- [218] PERCUS, J. K. The pair distribution function in classical statistical mechanics. In *The Equilibrium Theory of Classical Fluids* (New York, 1964), H. L. Frisch and J. L. Lebowitz, Eds., Benjamin, pp. II-33-II-170.
- [219] PERCUS, J. K. Equilibrium state of a classical fluid of hard rods in an external field. *J. Stat. Phys.* 15 (1976), 505.
- [220] PERRIN, F. Brownian movement of an ellipsoid II. Free rotation and depolarization of fluorescence. Translation and diffusion of ellipsoidal molecules. *J. Phys. Radium* 7 (1936), 1.

- [221] PERTSINIDIS, A., AND LING, X. S. Diffusion of point defects in two-dimensional colloidal crystals. *Nature* 413 (2001), 147.
- [222] PERTSINIDIS, A., AND LING, X. S. Equilibrium configurations and energetics of point defects in two-dimensional colloidal crystals. *Phys. Rev. Lett.* 87 (2001), 098303.
- [223] POLLAK, E., AND TALKNER, P. Reaction rate theory: What it was, where is it today, and where is it going? *CHAOS* 15 (2005), 026116.
- [224] PUSEY, P. N. Colloidal suspensions. In *Liquids, Freezing and the Glass Transition* (New York, 1991), J. P. Hansen, D. Levesque, and J. Zinn-Justin, Eds., Elsevier, p. 763.
- [225] RADHAKRISHNAN, R., GUBBINS, K. E., AND SLIWINSKA-BARTKOWIAK, M. Existence of a hexatic phase in porous media. *Phys. Rev. Lett.* 89 (2002), 076101.
- [226] RAMAKRISHNAN, T. V., AND YUSSOUFF, M. First-principles order-parameter theory of freezing. *Phys. Rev. B* 19 (1979), 2775.
- [227] RAUSCHER, M., DOMÍNGUEZ, A., KRÜGER, M., AND PENNA, F. A dynamic density functional theory for particles in a flowing solvent. *J. Phys. C.* 127, 24 (2007).
- [228] RAZ, O., AND AVRON, J. E. Swimming, pumping and gliding at low Reynolds numbers. *New J. Phys.* 9 (2007), 437.
- [229] REGUERA, D., AND WEISS, H. The role of fluctuations in both density functional and field theory of nanosystems. *J. Chem. Phys.* 120 (2004), 2558.
- [230] R'ESBOIS, P., AND DELEENER, M. *Classical Kinetic Theory of Fluids*. John Wiley, New York, 1977.
- [231] REX, M., LIKOS, C. N., AND LÖWEN, H. Soft colloids driven and sheared by traveling wave fields. *Phys. Rev. E* 72 (2005), 021404.
- [232] REX, M., LIKOS, C. N., LÖWEN, H., AND DZUBIELLA, J. Ultrasoft colloids in cavities of oscillating size or sharpness. *Mol. Phys.* 104 (2006), 527.
- [233] REX, M., AND LÖWEN, H. Dynamical density functional theory with hydrodynamic interactions and colloids in unstable traps. *arXiv.org arXiv:0803.2009* (2008).
- [234] REX, M., LÖWEN, H., AND LIKOS, C. N. Soft colloids driven and sheared by traveling wave fields. *Phys. Rev. E* 72 (2005), 021404.

- [235] REX, M., WENSINK, H. H., AND LÖWEN, H. Dynamical density functional theory for anisotropic colloidal particles. *Phys. Rev. E* 76, 021403 (2007).
- [236] RIEDEL, I. H., KRUSE, K., AND HOWARD, J. A self-organized vortex array of hydrodynamically entrained sperm cells. *Science* 309 (2005), 300.
- [237] RISKEN, H. *The Fokker-Planck Equation, Methods of Solution and Applications*, 2nd ed. Springer, Berlin, 1989.
- [238] RODRIGUEZ, M. A., AND ARMSTRONG, D. W. Separation and analysis of colloidal/nano-particles including microorganisms by capillary electrophoresis: a fundamental review. *J. Chromatography B* 800 (2004), 7.
- [239] ROGERS, F. J., AND YOUNG, D. A. New, thermodynamically consistent, integral equation for simple fluids. *Phys. Rev. A* 30 (1984), 999.
- [240] ROSENFELD, Y. Free-energy model for the inhomogeneous hard-sphere fluid mixture and density-functional theory of freezing. *Phys. Rev. Lett.* 63 (1989), 980.
- [241] ROSENFELD, Y. Free-energy model for the inhomogeneous hard-sphere fluid in D dimensions: Structure factors for the hard-disk (D=2) mixtures in simple explicit form. *Phys. Rev. A* 42 (1990), 5978.
- [242] ROSENFELD, Y., LEVESQUE, D., AND WEIS, J.-J. Free-energy model for the inhomogeneous hard-sphere fluid mixture: Triplet and higher-order direct correlation functions in dense fluids. *J. Chem. Phys.* 92 (1990), 6818.
- [243] ROSENFELD, Y., SCHMIDT, M., LÖWEN, H., AND TARAZONA, P. Fundamental-measure free-energy density functional for hard spheres: Dimensional crossover and freezing. *Phys. Rev. E* 55 (1997), 4245.
- [244] ROTNE, J., AND PRAGER, S. Variational treatment of hydrodynamic interaction in polymers. *J. Chem. Phys.* 1969 (50), 4831.
- [245] ROYALL, C. P., DZUBIELLA, J., SCHMIDT, M., AND VAN BLAADEREN, A. Nonequilibrium sedimentation of colloids on the particle scale. *Phys. Rev. Lett.* 98 (2007), 188304.
- [246] RUCKENSTEIN, E., AND DJIKAEV, Y. S. Recent developments in the kinetic theory of nucleation. *Adv. Colloid Interface Sci.* 118 (2005), 51.
- [247] RUSSEL, W. B., SAVILLE, D. A., AND SCHOWALTER, W. R. *Colloidal Dispersions*. Cambridge University Press, Cambridge, 1989.
- [248] RYZHOV, V. N., AND TAREYEVA, E. E. Two-stage melting in two dimensions: First-principles approach. *Phys. Rev. B* 51 (1995), 8789.

- [249] SALAMACHA, L., PATRIKIEJEW, A., SOKOLOWSKI, S., AND BINDER, K. Lennard-Jones fluids confined in nanoscopic slits: Evidence for reentrant filling transitions. *Eur. Phys. J. E* 13 (2004), 261.
- [250] SALAMACHA, L., PATRIKIEJEW, A., SOKOLOWSKI, S., AND BINDER, K. The structure of fluids confined in crystalline slitlike nanoscopic pores: Bilayers. *J. Chem. Phys.* 120 (2004), 1017.
- [251] SCHMIDT, M. Geometry-based density functional theory: an overview. *J. Phys.: Condens. Matter* 15 (2003), S101.
- [252] SCHMIDT, M., AND LÖWEN, H. Phase diagram of hard spheres confined between two parallel plates. *Phys. Rev. E* 55 (1997), 7228.
- [253] SCHÖPE, H. J., BRYANT, G., AND VAN MEGEN, W. Two-step crystallization kinetics in colloidal hard-sphere systems. *Phys. Rev. Lett.* 96 (2006), 175701.
- [254] SCHÖPE, H. J., AND PALBERG, T. A study on the homogeneous nucleation kinetics of model charged sphere suspensions. *J. Phys.: Condens. Matter* 14 (2002), 11573.
- [255] SCHUSS, Z., AND SPIVAK, A. The exit distribution on the stochastic separator in Kramers' exit problem. *SIAM J. Appl. Math.* 62 (2002), 1698.
- [256] SCHWEITZER, F. *Brownian Agents and Active Particles*. Springer Series in Synergetics. Springer, Berlin, 2003.
- [257] SEAR, R. P. Nucleation: theory and applications to protein solutions and colloidal suspensions. *J. Phys.: Condens. Matter* 19 (2007), 033101.
- [258] SEAR, R. P., AND GELBART, W. M. Microphase separation versus the vapor-liquid transition in systems of spherical particles. *J. Chem. Phys.* 110 (1999), 4582.
- [259] SHEN, Y. C., AND OXTOBY, D. W. Density functional theory of crystal growth: Lennard-Jones fluids. *J. Chem. Phys.* 104 (1996), 4233.
- [260] SHENOY, V. B., TAMBE, D. T., PRASAD, A., AND THERIOT, J. A. A kinematic description of the trajectories of *listeria monocytogenes* propelled by actin comet tails. *PNAS* 104 (2007), 8229.
- [261] SIMHA, R. A., AND RAMASWAMY, S. Hydrodynamic fluctuations and instabilities in ordered suspensions of self-propelled particles. *Phys. Rev. Lett.* 89 (2002), 058101.
- [262] SINGH, S. P., KAUR, C., AND DAS, S. P. Optimum vacancy concentration in a crystal. *Phys. Rev. E* 72 (2005), 021603.

- [263] SINGH, Y. Density-functional theory of freezing and properties of the ordered phase. *Phys. Rep.* 207 (1991), 351.
- [264] STEFANOVIC, P., HAATAJA, M., AND PROVATAS, N. Phase-field crystals with elastic interactions. *Phys. Rev. Lett.* 96 (2006), 225504.
- [265] STRANDBURG, K. J. Two-dimensional melting. *Rev. Mod. Phys.* 60 (1988), 161.
- [266] SÜTŐ, A. Crystalline ground states for classical particles. *Phys. Rev. Lett.* 95 (2005), 265501.
- [267] SÜTŐ, A. From bcc to fcc: Interplay between oscillating long-range and repulsive short-range forces. *Phys. Rev. B* 74 (2006), 104117.
- [268] TALANQUER V, O. D. Formation of droplets on nonvolatile soluble particles. *J. Chem. Phys.* 119 (2003), 9121.
- [269] TANIGUCHI, T., AND D. COHEN, E. G. Onsager-Machlup theory for nonequilibrium steady states and fluctuation theorems. *J. Stat. Phys.* 126 (2007), 1.
- [270] TARAZONA, P. Free-energy density functional for hard spheres. *Phys. Rev. A* 31 (1985), 2672.
- [271] TARAZONA, P. Density functional for hard sphere crystals: A fundamental measure approach. *Phys. Rev. Lett.* 84 (2000), 693.
- [272] TEJERO, C. F., AND CUESTA, J. A. Hard-sphere and hard-disk freezing from the differential formulation of the generalized effective liquid approximation. *Phys. Rev. E* 47 (1993), 490.
- [273] TORQUATO, S., AND STILLINGER, F. H. New duality relations for classical ground states. *Phys. Rev. Lett.* 100 (2008), 020602.
- [274] VAN BEIJEREN, H., AND ERNST, M. H. The modified Enskog equation. *Physica* 68 (1973), 437.
- [275] VAN BLAADEREN, A. Colloids under external control. *MRS Bulletin* 29 (2004), 85.
- [276] VAN KAMPEN, N. G. *Stochastic Processes in Physics and Chemistry*. North-Holland, Amsterdam, 1992.
- [277] VAN TEEFFELEN, S. unpublished.
- [278] VAN TEEFFELEN, S., LÖWEN, H., BACKOFEN, R., AND VOIGT, A. Comparison between dynamical density functional and phase field crystal theory for colloidal solidification. unpublished.

- [279] VANDEN-EIJNDEN, E., AND HEYMANN, M. The geometric minimum action method for computing minimum energy paths. *J. Chem. Phys.* *128* (2008), 061103.
- [280] VERLET, L. Computer “experiments” on classical fluids. II. Equilibrium correlation functions. *Phys. Rev.* *165* (1968), 201.
- [281] VICSEK, T., CZIRÓK, A., BEN-JACOB, E., COHEN, I., AND SHOCHET, O. Novel type of phase transition in a system of self-driven particles. *Phys. Rev. Lett.* *75* (1995), 1226.
- [282] VON GRÜNBERG, H. H., KEIM, P., ZAHN, K., AND MARET, G. Elastic behavior of a two-dimensional crystal near melting. *Phys. Rev. Lett.* *93* (2004), 255703.
- [283] VON SMOLUCHOWSKI, M. Über Brownsche Molekularbewegung unter Einwirkung äußerer Kräfte und deren Zusammenhang mit der verallgemeinerten Diffusionsgleichung. *Ann. Phys. (Leipzig)* *353* (1916), 1103.
- [284] VOSSEN, D. L. J., AND VAN BLAADEREN, A. to be published.
- [285] VOSSEN, D. L. J., VAN DER HORST, A., DOGTEROM, M., AND VAN BLAADEREN, A. Optical tweezers and confocal microscopy for simultaneous three-dimensional manipulation and imaging in concentrated colloidal dispersions. *Rev. Sci. Instr.* *75* (2004), 2960.
- [286] WALTHER, A., AND MÜLLER, A. H. E. Janus particles. *Soft Matter* *4* (2008), 663.
- [287] WANG, D. C., AND GAST, A. P. Crystallization of power-law fluids: A modified weighted density approximation model with a solid reference state. *J. Chem. Phys.* *110* (1999), 2522.
- [288] WEEKS, J. D. Volume change on melting for systems with inverse-power-law interactions. *Phys. Rev. B* *24* (1981), 1530.
- [289] WEISS, U. Decay of unstable states in macroscopic systems. *Phys. Rev. A* *25* (1982), 2444.
- [290] WENSINK, R., AND LÖWEN, H. Aggregation of self-propelled colloidal rods near confining walls. *arXiv.org arXiv:0809.0633* (2008). to be published in *Phys. Rev. E*.
- [291] WERTHEIM, M. S. Integral equations in the theory of classical fluids. *J. Math. Phys.* *8* (1967), 927.

- [292] WETTE, P., SCHÖPE, H. J., AND PALBERG, T. Microscopic investigations of homogeneous nucleation in charged sphere suspensions. *J. Chem. Phys.* *123* (2005), 174902.
- [293] WHITE, J. A., AND GONZÁLEZ, A. The extended variable space approach to density functional theory in the canonical ensemble. *J. Phys.: Condens. Matter* *14* (2002), 11907.
- [294] WHITE, J. A., GONZÁLEZ, A., ROMÁN, F. L., AND VELASCO, S. Density-functional theory of inhomogeneous fluids in the canonical ensemble. *Phys. Rev. Lett.* *84* (2000), 1220.
- [295] WILD, R., AND HARROWELL, P. Density-functional theory of the kinetics of crystallization of hard-sphere suspensions: Single conserved order parameter. *Phys. Rev. E* *56* (1997), 3265.
- [296] WILD, R., AND HARROWELL, P. Density functional theory of the kinetics of crystallization of a hard sphere suspension: Coupling structure to density. *J. Chem. Phys.* *114* (2001), 9059.
- [297] WISSEL, C. Manifolds of equivalent path integral solutions of the Fokker-Planck equation. *Z. Phys. B* *35* (1979), 185.
- [298] WOOLLEY, D. M. Motility of spermatozoa at surfaces. *Reproduction* *126* (2003), 259.
- [299] WU, J. Density functional theory for chemical engineering: From capillarity to soft materials. *AIChE J.* *52* (2006), 1169.
- [300] WU, J. Density-functional theory for complex fluids. *Annu. Rev. Phys.* *58* (2007), 85.
- [301] XU, H., AND BAUS, M. Freezing of binary hard-disc alloys. II. The fluid-disordered crystal transition. *J. Phys.: Condens. Matter* *2* (1990), 5885.
- [302] XU, X., AND RICE, S. Liquid-to-hexatic phase transition in a quasi-two-dimensional colloid system. *Phys. Rev. E* *78* (2008), 011602.
- [303] YEON, D.-H., HUANG, Z.-F., ELDER, K. R., AND THORNTON, K. unpublished.
- [304] YETHIRAJ, A. Tunable colloids: control of colloidal phase transitions with tunable interactions. *Soft Matter* *3* (2007), 1099.
- [305] YOUNG, A. P. Melting and the vector Coulomb gas in two dimensions. *Phys. Rev. B* *19* (1979), 1855.

- [306] ZAHN, K., LENKE, R., AND MARET, G. Two-stage melting of paramagnetic colloidal crystals in two dimensions. *Phys. Rev. Lett.* 82 (1999), 2721.
- [307] ZAHN, K., MÉNDEZ-ALCARAZ, J. M., AND MARET, G. Hydrodynamic interactions may enhance the self-diffusion of colloidal particles. *Phys. Rev. Lett.* 79 (1997), 175.
- [308] ZANDER, D., JANLEWING, R., RÜDIGER, A., AND KÖSTER, U. Nucleation of quasicrystals in bulk glass forming Zr-Cu-Ni-Al alloys. *Mater. Sci. Forum* 307 (1999), 25.
- [309] ZENG, X. C., AND OXTOBY, D. W. Applications of modified weighted density functional theory: Freezing of simple liquids. *J. Chem. Phys.* 93 (1990), 2692.
- [310] ZUBAREV:74. *Nonequilibrium Statistical Thermodynamics*. Plenum, New York, 1974, Sec. 13.

Die hier vorgelegte Dissertation habe ich eigenständig und ohne unerlaubte Hilfe angefertigt. Die Dissertation wurde in der vorgelegten oder in ähnlicher Form noch bei keiner anderen Institution eingereicht. Ich habe bisher keine erfolglosen Promotionsversuche unternommen.

Düsseldorf, den 16.09.2008

(Sven van Teeffelen)